Breton, Helene (2017) *Petrology and geochemistry of the Nakhlite meteorites: Tracking complex igneous and aqueous processes on Mars during the Amazonian.* PhD thesis.

https://theses.gla.ac.uk/8888/

# Petrology and Geochemistry of the nakhlite meteorites: Tracking complex igneous and aqueous processes on Mars during the Amazonian

Thesis submitted in fulfilment of the requirements
for the degree of Doctor of Philosophy
by
Helene Breton

**School of Geographical & Earth Sciences**

**College of Science & Engineering**

**University of Glasgow**

November, 2016

# ABSTRACT

The overarching science question being addressed by this research project was the geological history of the nakhlite group of Martian meteorites as representative of a young Amazonian Martian crust. This included the magmatic processes and mechanism of emplacement at the origin of the meteorites but also the nature of a young Amazonian Martian aquifer that circulated throughout the nakhlites bedrock from its chemistry, origin and longevity. Answering these questions are fundamental to understand the physical and chemical properties and chronological evolution of Mars sub-surface environment over the last billion year with implication for astrobiology and current and future Mars exploration. For this project, a large set of nakhlite meteorites (probably the most comprehensible) have been assembled. It included NWA 5790, NWA 817, NWA 998, MIL 03346, Y 000593/000749, Lafayette and Nakhla. The mineralogy and mineral texture and chemistry of each meteorite have been fully characterized at the $\mu$m- and nm-scale using Electron Microscopy techniques (SEM and TEM) and Raman Spectroscopy at the University of Glasgow and Mass Spectroscopy (LA ICP-MS) at the University of Durham.

The nakhlites are differentiated basaltic rocks formed by accumulation of augite in a sub-surface environment. The chemical composition of both cumulus augites (the liquidus phase) and their multiphase and glass inclusions representing trapped magma during augite growth indicate that the parent magmas at the origin of the meteorites were not primitive but residua of progenitors that experienced cryptic fractional crystallization processes in the deep basaltic plumbing system. The nakhlites have similar mineralogy but each meteorite has mineral phases with distinct properties which indicates that the rocks experienced each their own crystallization history. The nakhlites probably crystallized within separate igneous bodies/batches. Compositional variability of the nakhlites' parent magmas cannot be explained by a differentiation of a single pulse of magma that solidified through continuous fractional crystallization of augite and olivine alone in a shallow magma chamber.

Aqueous alteration of the nakhlites is limited but the presence of small quantities of clay minerals from the smectite family with carbonate, sulphate, halite and Fe-oxide demonstrates the existence of briny crustal water in the young Martian basaltic crust at least at the site sampled by the nakhlites. Variations in mineral assemblages provide evidences for contrasting conditions in the aqueous environments ranging from neutral-to-acidic (with a deposition of sulfate and halite) to near neutral-to-alkaline (with a precipitation of carbonate) apparently associated with a temporal evolution of the brines' property. The texture and chemistry of the secondary mineral assemblages are consistent with a deposition from discrete aqueous events fading away over time.

# ACKNOWLEDGEMENTS

I would like to thank Mr Peter Chung, Mr John Gilleece, Mr Robert MacDonald, Mr Colin How and Mr William Smith at the University of Glasgow for their technical support and guidance with sample preparation and analyses. Dr Chris Dale, Dr Christ Otley and Dr George Cooper at the University of Durham are also thanked for their assistance with the LA ICP-MS analyses.

I would like particularly to acknowledge Dr Paula Lindgren, Mrs Margaret Jackson and Ms Jacqueline McKie for additional assistance and their unshakeable support.

The financial support received from the Science and Technology Facilities Council (STFC) during my research studentship is gratefully acknowledged.

Finally, I would like to thank every teacher of mine from my Bachelor to my Master that has provided me with the opportunity to learn so much about science and continue my journey with this PhD.

# AUTHOR'S DECLARATION

I declare that this dissertation is the result of my own work and has not been submitted for any other degree at the University of Glasgow or any other institution.

Helene Breton

Hélène Breton

# CONTENTS

1. *Introduction to Mars' surface geology during the Amazonian* . . . . . . . 2
    - 1.1 Understanding of the Martian surface and its evolution . . . . . . . 2
    - 1.2 The nakhlite meteorites . . . . . . . . . . . . . . . . . . . . . . . . . . 8
        - 1.2.1 Young basaltic rocks from Mars . . . . . . . . . . . . . . . . . 8
        - 1.2.2 Discovery of the nakhlite meteorites: Where, when, and how 9
        - 1.2.3 Current understanding of the nakhlites's geological context and history . . . . . . . . . . . . . . . . . . . . . . . . . . . 10
    - 1.3 Thesis context and outline . . . . . . . . . . . . . . . . . . . . . . . . 13
        - 1.3.1 Determination of science questions, aims and limitations . . 13
        - 1.3.2 Sample set . . . . . . . . . . . . . . . . . . . . . . . . . . . . . 16
        - 1.3.3 Thesis outline . . . . . . . . . . . . . . . . . . . . . . . . . . . 17

2. *Methodology 1: Theory and application of Electron Microscopy* . . . . . 22
    - 2.1 Introduction: Electron microscopy . . . . . . . . . . . . . . . . . . . . 22
    - 2.2 Electron-matter interactions and their application in Electron Microscopy . . . . . . . . . . . . . . . . . . . . . . . . . . . . . . . . 23
        - 2.2.1 Introduction . . . . . . . . . . . . . . . . . . . . . . . . . . . . 23
        - 2.2.2 The different electron-matter interactions . . . . . . . . . . . 23
    - 2.3 Scanning Electron Microscopy (SEM) . . . . . . . . . . . . . . . . . 26
        - 2.3.1 Introduction . . . . . . . . . . . . . . . . . . . . . . . . . . . . 26
        - 2.3.2 SEM instrument . . . . . . . . . . . . . . . . . . . . . . . . . 26
        - 2.3.3 SEM sample requirement and preparation . . . . . . . . . . 27
        - 2.3.4 Electron Backscattered Diffraction (EBSD) . . . . . . . . . . 28
        - 2.3.5 Qualitative and quantitative analyses using Energy Dispersive X-ray Spectroscopy . . . . . . . . . . . . . . . . . . . . 29
        - 2.3.6 SEM analyses of the nakhlites: Analytical procedure and standardization . . . . . . . . . . . . . . . . . . . . . . . . . 30
    - 2.4 Transmission Electron Microscopy (TEM) . . . . . . . . . . . . . . 30
        - 2.4.1 TEM instrument . . . . . . . . . . . . . . . . . . . . . . . . . 31
        - 2.4.2 TEM technique . . . . . . . . . . . . . . . . . . . . . . . . . . 33
        - 2.4.3 Specimen preparation for TEM investigations . . . . . . . . 41

3. *Methodology 2: Raman Spectroscopy and Mass Spectrometry* . . . . . . 46
    - 3.1 Raman spectroscopy . . . . . . . . . . . . . . . . . . . . . . . . . . . 46
        - 3.1.1 Introduction to Raman spectroscopy . . . . . . . . . . . . . 46
        - 3.1.2 Raman spectroscopy instrument and technique . . . . . . . . 47
        - 3.1.3 Raman spectroscopy application and configuration for sample analyses . . . . . . . . . . . . . . . . . . . . . . . . . . . . 47
    - 3.2 Laser Ablation Inductively-Coupled Mass Spectrometry (LA ICP-MS) 48

- 3.2.1 LA ICP-MS technique and instrument . . . . . . . . . . . . 48
- 3.2.2 LA ICP-MS limitations and quantitative analyses . . . . . . 50
- 3.2.3 Analytical procedure and operating conditions . . . . . . . . 51

*4. Basaltic petrogenesis of the nakhlites* . . . . . . . . . . . . . . . . . . . . . 53

- 4.1 Introduction . . . . . . . . . . . . . . . . . . . . . . . . . . . . . . . . 53
- 4.2 The nakhlites petrography: Mineral texture, chemistry and characteristics . . . . . . . . . . . . . . . . . . . . . . . . . . . . . . . . 55
  - 4.2.1 Augite . . . . . . . . . . . . . . . . . . . . . . . . . . . . 55
  - 4.2.2 Olivine . . . . . . . . . . . . . . . . . . . . . . . . . . . . 59
  - 4.2.3 Low-Ca pyroxene . . . . . . . . . . . . . . . . . . . . . . 63
  - 4.2.4 Mesostasis . . . . . . . . . . . . . . . . . . . . . . . . . . 65
  - 4.2.5 Magmatic inclusions . . . . . . . . . . . . . . . . . . . . . 73
- 4.3 Bulk chemical composition . . . . . . . . . . . . . . . . . . . . . . . 75
  - 4.3.1 Major element composition . . . . . . . . . . . . . . . . . . 75
  - 4.3.2 Trace element composition . . . . . . . . . . . . . . . . . . 75
- 4.4 Fractional crystallization-driven magmatic differentiation . . . . . . 85
  - 4.4.1 The nakhlites are complex basaltic rocks . . . . . . . . . . . 85
  - 4.4.2 Fractional crystallization . . . . . . . . . . . . . . . . . . . 85
- 4.5 Magmatic inclusions: A key for better understanding early magma composition . . . . . . . . . . . . . . . . . . . . . . . . . . . . . . . . 92
  - 4.5.1 Mono-phase inclusions in augite, olivine and magnetite . . . 93
  - 4.5.2 Poly-phase inclusions in augite and olivine . . . . . . . . . . 94
  - 4.5.3 Origin of compositional variations of melt inclusions . . . . . 99
- 4.6 Crystallization of reactive low-Ca pyroxenes during late stage magmatic processes . . . . . . . . . . . . . . . . . . . . . . . . . . . . . . 100
  - 4.6.1 A complex magmatic history from basaltic to silicic magma composition . . . . . . . . . . . . . . . . . . . . . . . . . . 101
  - 4.6.2 Petrographic observations of reactive low-Ca pyroxenes . . . 104
  - 4.6.3 Low-Ca pyroxenes: Mineralogical re-equilibration from what? 108
- 4.7 Constraint on the nakhlites magmatic history using trace elements . 111
  - 4.7.1 Trace element geochemistry . . . . . . . . . . . . . . . . . 111
  - 4.7.2 Tracking magma composition and differentiation through trace elements composition in separate mineral phases . . . . . . . 119
- 4.8 Estimation of the REE compositions of the nakhlites' parent magmas 137
  - 4.8.1 Summary of crystallization sequences and history . . . . . . 146
- 4.9 Conclusions . . . . . . . . . . . . . . . . . . . . . . . . . . . . . . . . 146

*5. Mineralogy and hydrochemistry of a young Martian aquifer* . . . . . . . . 154

- 5.1 Introduction . . . . . . . . . . . . . . . . . . . . . . . . . . . . . . . . 154
- 5.2 Aqueous alteration: Definition and comprehensive model . . . . . . 155
  - 5.2.1 General understanding of water-rock reactions . . . . . . . . 155
  - 5.2.2 Understanding of the nakhlites aqueous environment from the atom scale: What to expect . . . . . . . . . . . . . . . . . 159
- 5.3 Recent hydrologic activity on Mars: Evidences from the Nakhlites . 161
- 5.4 Aqueous alteration textures: Tracking fluid-rock interactions in the nakhlites . . . . . . . . . . . . . . . . . . . . . . . . . . . . . . . . . 162
  - 5.4.1 Olivine phenocryst alteration . . . . . . . . . . . . . . . . . 163

5.4.2 Mesostasis alteration . . . 168
5.5 Secondary mineralogy and elemental composition . . . 170
5.5.1 NWA 817 . . . 171
5.5.2 MIL 03346 . . . 176
5.5.3 Y 000749 . . . 178
5.5.4 Y 000593 . . . 181
5.5.5 Nakhla . . . 184
5.5.6 Lafayette . . . 186
5.5.7 NWA 998 . . . 188
5.6 Chemistry of the nakhlites mineralising brines . . . 191
5.6.1 Fine phyllosilicate . . . 191
5.6.2 Salts-phyllosilicate admixture . . . 193
5.6.3 The unique alteration products of Lafayette . . . 195
5.7 Terrestrial contaminations . . . 195
5.8 Insights into the dynamic, structure and geological history of the Nakhlites aquifer . . . 199
5.8.1 Early mineral-water reactions and deposition of material precursor of smectite-group minerals . . . 200
5.8.2 Complex evolution of the nakhlites aquifer and crystallization of salt and clay mineral assemblage . . . 202
5.8.3 Mineralogical evidence for multiple fluid pulses . . . 203
5.8.4 Spatio-temporal evolution of environmental conditions in the nakhlites aquifer . . . 207
5.9 Conclusions . . . 210

*6. Summary* . . . 213

*Appendices* . . . 231

*A.* . . . 232

# LIST OF FIGURES

1.1 *Global topographic map of Mars and major surface features labelled. Image from the MGS MOLA (Mars Global Surveyor Mars Orbiter Laser Altimeter Team, https://attic.gsfc.nasa.gov/mola/images.html). The ancient high plateaux of Mars forming the South hemisphere are much more heavily cratered than the plains forming the young Martian terrains.* . . . . . 3

1.2 *Global geological map of Mars with its principal geological units from the Early and Late (E and L) Noachian, Hesperian and Amazonian (N, H and A respectively). Map taken from Nimmo and Tanaka (2005).* 5

1.3 *Estimates of the total amount of water stored near the Martian surface recalculated from hydrogen distribution identified by instruments aboard NASA's Mars Odyssey spacecraft. Water are mostly present in the circumpolar regions, below the dry ice polar caps and around the Tharsis bulge, http://www.spaceref.com/news/viewnews.html?id=740.* 6

1.4 *Total alkalis vs. silica diagram for Martian meteorites, analyses of soils and rocks at robotic landing sites, and chemical information from orbiting spacecraft (TES and GRS). All data cluster around the basalt field, showing the basaltic nature of the Martian crust (McSween et al., 2009).* . . . . . 8

1.5 *Photographs of a thin section of the Theo's Flow pyroxenite layer and Nakhla taken from Friedman-Lentz et al. (1999). The textural and mineralogical similarity between both rocks suggest that the nakhlites may have formed in a similar environment, a thick cumulate pile emplaced in a sub-surface environment.* . . . . . 11

1.6 *Cumulate pile model of Mikouchi et al. (2012) showing the relative stratigraphic position of the nakhlites based on proportion of olivine, augite and rock matrix and mineral zoning.* . . . . . 12

1.7 *Photograph and photomicrograpgh of NWA 817 taken with a visible light microscope (reflective light). The brownish-yellowish product on the photograph are secondary minerals, easily recognisable with their natural porosity. Pyroxene (px) have a green color while olivine (ol) have a yellowish-greenish color due to alteration. The dark crystals in the mesostasis are Fe-oxides/sulfides.* . . . . . 17

1.8 *Photograph and photomicrograpgh of MIL 03346 taken with a visible light microscope (reflective light). The large green crystals are pyroxene while the dark crystals in the mesostasis are Fe-oxides/sulfides.* 18

1.9 *Photomicrograph of our thin section of lafayette. The green crystals are pyroxene and olivine. The brown product surrounding the crystals are alteration products while the dark grains are Fe-oxides/sulfides.* 18

1.10 *Photomicrograph of two polished rock mounts of NWA 998 taken with a visible light microscope (reflective light). The rock is fully crystallized. On the pictures, a distinction between pyroxene and olivine is difficult but olivine grains still appear slightly more brownish probably due to their alteration by aqueous fluids during secondary processing. The dark grains are Fe-oxides/sulfides. The brownish tint of the rock testifies of aqueous alteration.* . . . . . . . . . . . . . . . . . . . . . . . . 19
1.11 *BSE images of the different nakhlites analysed in this study in their relative position in the cumulate pile model of Mikouchi et al. (2012).* 20

2.1 *Signals generated during electron-matter interactions (unknown author). Primary processes include diffraction and backscattering of electrons from the electron beam while secondary processes comprise the generation of secondary and auger electrons, X-rays and cathodoluminescence.* . . . . . . . . . . . . . . . . . . . . . . . . . . . . . . . . 24
2.2 *Physical interaction between an electron beam and the electron cloud of an atom. The electron from the electron cloud is ejected while the beam electron is deflected from its initial trajectory, (http://mcswiggen.com).* 24
2.3 *Effect of topography on the release of secondary electrons from the surface of a sample. Topographic highs appear brighter on virtual images because more secondary electrons are released (greater surface) which saturates the detector screen, whereas topographic lows appear darker because the secondary electrons are absorbed by the sample (http://mcswiggen.com).* . . . . . . . . . . . . . . . . . . . . 25
2.4 *Schema of an SEM with its different components (unknown author).* 27
2.5 *Schematic arrangement of a sample in an SEM for EBSD analyses relative to principal constituents. BSD: Back-Scatter Detector, FSD: Fore-Scatter Detector (Schwartz et al., 2010).* . . . . . . . . . . . . 28
2.6 *Trace of diffraction cones or Kikuchi lines on a phosphorous screen generated during interactions of an electron beam with a sample's atomic plane or diffraction plane (Schwartz et al., 2010).* . . . . . . 29
2.7 *Example of SEM-EDX energy spectra of olivine showing characteristic x-ray peaks of its chemical components obtained with the Oxford Instruments INCA software at 20 kV.* . . . . . . . . . . . . . . . . . 30
2.8 *Schema of an electron source. A high tension is applied onto a filament to generate electrons. A Whelnet cylinder focuses the electrons attracted by anodes (www.classle.net).* . . . . . . . . . . . . . . . . . . 32
2.9 *Imaging system of a TEM instrument with the relative position of the different components (objectives, apertures, and lenses). The vertical arrowheads represent different electron beam paths after interaction with a specimen. Only the double arrowheads form an interference pattern on the viewing screen (Egerton, 2005).* . . . . . . . . . . . . 34
2.10 *Schema representing the different electrons detectors (located at the base) of a TEM instrument: the direct electrons beam detector (BF, Bright Field) and transmitted electron detector for slightly deviated electrons (ADF, Annular Dark Field) and highly deviated electrons (HAADF, High-Angular Annular Dark Field) (www.microscopy.ethz.ch).* 35

2.11 *High resolution bright field image of olivine hosted clay minerals taken from Banfield et al. (1990) with olivine crystal orientation (or reciprocal crystal lattice, a$^*$ and c$^*$). The fully collapse state of the clay minerals (due to the absence of interlayer components) has created porosity that appears bright on the BF image.* . . . . . . . . . 36

2.12 *Schema presenting the relation between electron waves with a specific wave length $\lambda$ (whose traces are represented by oblique lines) and crystal lattice planes (horizontal lines) with regularly spaced atoms (dots on the horizontal lines) separated with a lattice spacing d which satisfies Bragg's conditions. The incident angle $\theta$ equals the reflected angle, while $\eta$ represent an integer (www.matter.org.uk).* . . . . . . 37

2.13 *Diffraction pattern and associated Bright Field (BF) and Dark Field (DF) image areas of a micro-crystalline ($ZrO_2$) thin sample. Each spot indicates the presence of a micro-crystal. A metal rod is used to block the direct beam to avoid overexposure and sample damages. Dark contrast on the BF image results from the crystal orientation almost parallel to the zone axis, while the bright contrast on the DF image arises because the diffracted beams partly pass the objective aperture (http://www.microscopy.ethz.ch).* . . . . . . . . . . . . . . 37

2.14 *Key diagram (a) showing the generation of diffraction patterns (DPs) from diffracted electrons on a screen detector and examples of DPs from a single crystal of unknown nature (b) and aggregate of nanocrystals of $MnZnO_3$ (c), http://cime.epfl.ch.* . . . . . . . . . . . . . 39

2.15 *Schema showing the relationship between crystal lattice planes (dot lines) with a lattice space d and the formation of a diffracted pattern satisfying Bragg's conditions (incident angle $\theta_B$ = reflected angle $\theta_B$). L represents a constant value called the camera length and R the distance between the “direct” beam (which does not undergo any deflection) and the diffracted beam. On a CCD detector, R can represent either the distance between two spots or the radius of a circle (Egerton, 2005).* . . . . . . . . . . . . . . . . . . . . . . . . . 40

2.16 *Example of typical electron energy loss spectrum of a thin specimen (here titanium carbide) recorded with a conventional 200 kV TEM. The first peak at 0 kV is called the zero-loss peak. It corresponds to transmitted electrons that have been elastically scattered via interaction with the atomic nuclei of the sample, spectrum taken from (Hofer et al., 2016).* . . . . . . . . . . . . . . . . . . . . . . . . 41

2.17 *Schema of the interior of a sample chamber of a FIB instrument with ion column, gas injection needles and detector relative to the sample stage (Giannuzzi and Stevie, 2004).* . . . . . . . . . . . . . . . . . . 42

2.18 *Schema representing the different constituent of a liquid metal ion source of a FIB instrument (liquid metal reservoir, solid substrate with a Taylor cone, and counter electrode) and the path followed by the liquid metal (along the solid substrate by capillary flow) during extraction of liquid metal ions (Orloff et al., 2003).* . . . . . . . . . 43

2.19 *SEM images during FIB sample preparation of an alteration vein within an olivine phenocryst. First, the area of interest is selected and covered by a layer of platinum (Pt). Second, the back and front trenches are milled around the area of interest. Finally, the lamellae is removed from the bulk sample (here the olivine grain) and mounted on a special FIB support prior to its thinning.* . . . . . . . . . . . . 45

3.1 *Energy-level diagram showing the energy states involved in Raman spectra. The electronic transitions accompanied with Rayleigh scattering (left) does not lead to gain or loss of energy unlike with Raman scattering (right), author unknown.* . . . . . . . . . . . . . . . . . . . 47

3.2 *Raman spectroscopy technique components, author unknown.* . . . . 48

3.3 *Raman spectra before and after baseline subtraction. Fluorescence emission and thermal background are unavoidable during sample analyses. They add themselves onto Raman spectrum (www.renishaw.com).* 49

3.4 *Configuration of an LA ICP-MS, unknown author.* . . . . . . . . . . 50

4.1 *BSE images of the nakhlites illustrating the dominance of augite. Augite comprise large cores and thin rims in NWA 5790, MIL 03346, and NWA 817. In Y 000749, Y 000593 and nakhla, augite display patchy and irregular rim zones whereas in Lafayette and NWA 998 they have no obvious rims. The nakhlites display a cumulate texture but the primary kinetic texture has been mechanically modified by sorting and compaction. Under the effect of compaction, augite grains in contact with each other have partly dissolved, a process called pressure-solution or grain coarsening (red arrows).* . . . . . . 56

4.2 *Ternary diagram with nomenclatures for the Ca-Mg-Fe clinopyroxene and Mg-Fe orthopyroxene and composition ranges of the various pyroxene present in the nakhlites. They include augite phenocrysts (core, rim, and overgrowth) and low-Ca pyroxene grains in the mesostasis. The different pyroxenes show a progressive evolution from core, rim to overgrowth/mesostasis illustrating a slow and protracted crystallization of pyroxene during rock solidification. The relatively constant Ca content in augite rim and small grains in the mesostasis in NWA 5790, MIL 03345 and NWA 817 probably reflects the absence of (co-crystallized) plagioclase in the rocks with a preferential incorporation of Ca into plagioclase.* . . . . . . . . . . 58

4.3 *Bivariate plots of major and minor elements v.s* $SiO_2$ *of augite phenocrysts from the different nakhlites. The augite phenocrysts have relatively homogeneous core (black square) but display strong variations in composition and zonation patterns along their thin rims within and between the meteorites. Despite their volumetric dominance, the cores of augite phenocrysts in all nakhlites analysed display very limited range of composition and no progressive compositional growth zoning in major elements suggesting that they experienced intense intra-crystalline diffusive re-equilibration during crystal growth.* . . 60

4.4 *BSE images of olivine grain texture in different nakhlites. Olivine in NWA 5790 and NWA 817 are euhedral, in Y 000749, Y 000593 and nakhla they partly enclose the neighbouring crystals whereas in Lafayette and NWA 998 they are anhedral. The perfect fitting of olivine and augite grains in Lafayette and NWA 998 suggests that both rocks experienced grain coarsening involving both mineral phases.* 62

4.5 *Bivariate plots of selected major and minor elements of olivine phenocrysts from the different nakhlites. The composition and zonation patterns of olivine phenocrysts vary between the rocks. To be noted: the composition of the large olivine phenocrysts in Y 000749 is distinct with a more evolved composition that further show little variation except in Na.* . . . . . . . . . . . . . . . . . . . . . . . . . 64

4.6 *EDS map of replacive low-Ca pyroxene in NWA 998. The low-Ca pyroxene overgrow onto olivine, plagioclase and to less extent augite. The low-Ca pyroxene sometimes contain lamellaes of augite and more rarely inter-growths of worm-like Ti-magnetite.* . . . . . . . . . . . 65

4.7 *BSE image of an unusual large orthopyroxene grain almost completely replacing an olivine phenocryst and overgrowing onto augite and plagioclase in Lafayette.* . . . . . . . . . . . . . . . . . . . . . . . . . 65

4.8 *X-ray maps of the mesostasis of NWA 5790, MIL 03346 and NWA 817. The three meteorites contain skeletal crystals of Ti-magnetite, olivine and augite but their proportion and size differ between the meteorites. Another characteristic of these meteorites is the apparent lack of plagioclase laths.* . . . . . . . . . . . . . . . . . . . . . . . 67

4.9 *X-ray maps of the mesostasis of both Yamato meteorites and Nakhla. Their main feature is the occurrence of radiating laths of plagioclase. Interstitial to the plagioclase occurs olivine, low-Ca pyroxene, pyrrhotite and magnetite. Rare apatite and blobs of silica also occur.* 68

4.10 *Mesostasis pocket in Y 000593 comprising laths of plagioclase, small grains of olivine and magnetite and large droplet-shaped crystals of cristobalite with its typical "cracked tile" texture. The absence of "voids" between cristobalite crystals suggests that they are a magmatic product and not shock-induced polymorphic transformation of quartz.* . . . . . . . . . . . . . . . . . . . . . . . . . . . . . . 69

4.11 *BSE images of the inter-cumulus mineral assemblage of Lafayette and NWA 998. Both meteorites are fully crystallized. Plagioclase (fdp) does not from lath as in the other nakhlites but anhedral grains. In lafayette, Ti-magnetite (mt) does not present the common ilmenite lamellae exsolution whereas olivine crystals show a continuous grain size from over 300 µm to 50 µm. Olivine in NWA 998 are only phenocryst a few hundreds of µm long.* . . . . . . . . . . . . . . . 70

4.12 *BSE images of the reactive melt present in NWA 998. The silica-rich melt was out of equilibrium with plagioclase and has partly dissolved it. The former grain boundary of the plagioclase lath can still be identified.* . . . . . . . . . . . . . . . . . . . . . . . . . . . . . 70

4.13 *Feldspar composition of Nakhla, Y 000593, Y 000749, and NWA 998. The wide range of feldspar composition of nakhla and NWA 998 represents crystal zoning.* . . . . . . . . . . . . . . . . . . . . . . 71

4.14 *Oxide ternary diagram (FeO-$Fe_2O_3$-$TiO_2$) showing the high temperature solid solution series ulvospinel-magnetite, ilmenite-hematite, and ferropseudobroobite-pseudobrookite, plotted on a mol per cent basis. The oxide compositions are plotted after $Fe^{3+}$ stoichiometric recalculation.* . . . . . . . . . . . . . . . . . . . . . . . . . . . . 72

4.15 *Poly-mineralic inclusions in olivine phenocrysts in NWA 817 (a) and Lafayette (b). The texture and mineralogy of the inclusions resemble those of the mesostasis. The inclusion in olivine from NWA 817 contain glass, sulfide (S) and skeletal low-Ca pyroxene, whereas Lafayette contain feldspar (fp), magnetite (mt) and sulfur.* . . . . . . . . . . . 73

4.16 *Large glassy inclusion in an augite phenocryst in Y 000593. The inclusion and its host have intensely exchanged elements to form a halo around the inclusion.* . . . . . . . . . . . . . . . . . . . . . . . 74

4.17 *Total Alkalis vs. Silica diagram for volcanic rocks (TAS; Le Maitre et al., 1989) showing the classification of the nakhlite meteorites bulk rock. MIL 03346 (Day et al., 2006), NWA 817 (Sautter et al., 2002), Y 000593 and 000749 (Imae et al., 2003), GV (Gomes and Kiel,1980), Nakhla (McCarthy et al., 1974), Lafayette (Boctor et al., 1976), NWA 998 (Treiman and Irving, 2008).* . . . . . . . . . . . . 76

4.18 *Bulk rock major and some minor elements composition of the different nakhlite meteorites. MIL 03346 (Day et al., 2006), NWA 817 (Sautter et al., 2002), Y 000593 and 000749 (Imae et al., 2003), GV (Gomes and Kiel,1980), Nakhla (McCarthy et al., 1974), Lafayette (Boctor et al., 1976), NWA 998 (Treiman and Irving, 2008).* . . . . . 76

4.19 *Mg/Si vs. Al/Si diagram of Martian meteorites, rocks and soils obtained at robotic landing sites and from orbiting spacecraft. The values for the Earth' s crust is given for comparison. Mg/Si vs. Al/Si are commonly used to differentiate Martian meteorites from terrestrial rocks. The Martian meteorites sampling the sub-surface of Mars is commonly depleted in alkali and Al relative to rocks and soils from Mars top surface (Fig. 1.4), McSween et al. (2009).* . . . . . . . . 77

4.20 *Bulk rock Mg/(Mg+Fe) vs. $Al_2O_3$ of the SNCs Martian meteorites and lunar and komatiitic Earth rocks. Martian meteorites are commonly enriched in Fe. Graph modified from Bridges and Warren (2006).* . . . . . . . . . . . . . . . . . . . . . . . . . . . . . . . . . 77

4.21 *Whole-rock REE abundances of different nakhlites (Treiman and Irving, 2008) and depleted mid-ocean ridge basalt (Earth d-MORB) for comparison. This rock type is believed to represent a rough approximation of the upper Earth's mantle (Workman and Stanley, 2005). REE abundances are normalized to CI chondrite (McDonough and Sun, 1995). Eu/Eu$^*$ represents an interpolated value of the size of the Eu anomalie. The La/Yb ratios provide an indication of the fractionation slope of the REEs.* . . . . . . . . . . . . . . . . . . . . . . 78

4.22 *REE abundances in augite phenocrysts normalized to CI chondrite (McDonough and Sun, 1995) from different nakhlite meteorites. NWA 5790 and NWA 998 do not have rims thick enough to be analysed using LA ICP-MS technique.* . . . . . . . . . . . . . . . . . . . . . . 80

4.23 *CI chondrite normalized (McDonough and Sun, 1995) trace element patterns (HFSE and LILE) from augite phenocrysts from different nakhlite meteorites. The lack of abundances for certain elements result from a concentration below the detection limits.* . . . . . . . . 81

4.24 *CI chondrite normalized (McDonough and Sun, 1995) REE (left) and HFSEs and LILEs (right) abundances in plagioclase and K-feldspar (pink) from Y 000593 and NWA 998. The absence of abundances for certain elements results from a concentration below the detection limits.* . . . . . . . . . . . . . . . . . . . . . . . . . . . . . . . . . 82

4.25 *REEs (left) and selected HFSEs and LILEs (right) abundances in orthopyroxene, the replacing product of olivine phenocryst and plagioclase, from three nakhlite meteorites (Y 000593, Nakhla, and NWA 998). The trace element abundances are normalized to CI chondrite (McDonough et al., 1995).* . . . . . . . . . . . . . . . . . . . . . . 84

4.26 *REE (left) and selected HFSE and LILE (right) abundances normalized to CI chondrite (McDonough and Sun, 1995) in glass (Nakhla and NWA 998) and poorly-crystallized mesostasis (NWA 817).* . . . 85

4.27 *Evolution of the composition of olivine phenocrysts core (c) and rim (r), and small olivine grain in the mesostasis (m) expressed as fayalitic percentage (% Fa) within the different nakhlites presented in their believed stratigraphic position (Mikouchi et al., 2012). The different core composition of olivine from Lafayette represent different grain populations (i.e. grain size).* . . . . . . . . . . . . . . . . . . . 88

4.28 *Polyphase inclusion in an augite phenocryst from MIL 03346. The inclusion has the same texture as the mesostasis. It contains an highly altered sulfide mineral (pink) transformed into Fe-oxide (purple), feldspar, Cl-amphibole, a silica phase and abundant apatite at the nm-scale (pinkish dots embedded in the glass.* . . . . . . . . . . 95

4.29 *Large poly-mineralic inclusion in an olivine phenocryst in NWA 998. The inclusion is composed from rim to core of pyroxene, magnetite, and plagioclase. The crystallization sequence reflects the cooling history. The inclusion was probably originally a melt droplet enclosed during olivine growth. Radiating fractures surrounding the inclusion probably result from volume increase during crystallization.* . . . . . 98

4.30 *Large poly-mineralic inclusions in olivine phenocrysts in Lafayette. The inclusions are composed of augite, Ti-magnetite, and feldspar with or without meniscus of glass. Augite crystals are commonly rimmed (right) or overgrown (left) with orthopyroxene (opx).* . . . . 99

4.31 *EDS map of NWA 998 with augite, olivine, plagioclase, apatite, and low-Ca pyroxene. The low-Ca pyroxenes partially replace olivine, plagioclase and augite but not apatite.* . . . . . . . . . . . . . . . . . 101

4.32 *EDS map of NWA 998 showing the distribution of the different mineral phases between cumulate augite and olivine: plagioclase with K-feldspar rims, apatite, magnetite, orthopyroxene, and remnants of poorly crystallized melt filling pore corners.* . . . . . . . . . . . . . . 103

4.33 *EDS maps of inter-cumulus material in NWA 998 with plagioclase (dark blue), K-feldspar(light blue), apatite, Fe-sulfide and "frozen" melt with orthopyroxene.* . . . . . . . . . . . . . . . . . . . . . . . 104

4.34 *EDS map of orthopyroxene that has overgrown onto plagioclase, olivine and augite in NWA 998. During the mineralogical transformation, magnetite and apatite have been enclosed and have remained unreactive.*105

4.35 *BSE images of the reactive textures of low-Ca pyroxenes (Px) replacing olivine (Ol), plagioclase feldspar (Fp) and augite (Au) in NWA 998. The crystallization of low-Ca pyroxene has partially erased the texture and structure of the rock.* . . . . . . . . . . . . . . . . . . . . 106

4.36 *EDS map of the various low-Ca pyroxene minerals found as a replacing product in NWA 998 and their relation with the early stable mineral assemblages. Interstitial plagioclase and magnetite are replaced by pigeonite hosting augite lamellae. "Pure" orthopyroxene occurs only as topographic replacement of olivine. Pigeonite and augite lamellae (within augite and pigeonite respectively) are parallel suggesting a same crystallographic orientation of the pyroxene hosts.* 107

4.37 *BSE image of different replacive low-Ca pyroxenes replacing olivine, augite and plagioclase in NWA 998. Vermicular magnetite represents oxidative exsolution of olivine that formed during olivine degradation.* 107

4.38 *Partition coefficient of the Rare Earth Elements (REEs) of various silicate minerals commonly found in basaltic rocks modified from Rollinson (1993). The graph illustrates the general incompatibility of REEs in silicate minerals and the greater incompatibility of the LREEs ($D < 1$) relative to the HREEs ($D > 1$).* . . . . . . . . . . 115

4.39 *Ionic radii vs. ionic charge for incompatible elements in common mafic minerals. High Field Strength elements (HFSEs) have a high ionic charge with $Z = 3$ to $6$. They are incompatible because of the difficulty in achieving charge balance with major element cations with generally $Z = 2$. Elements with relatively high ionic ratios (Large-Ion Lithophile Elements, LILEs) cannot substitute to major elements without structural distortion of the crystal which is energetically not favoured, unknown author.* . . . . . . . . . . . . . . . . . . . . . . 116

4.40 *Plots of log partition coefficient D of different incompatible ($D < 1$) and compatible ($D > 1$) elements of various charge and for different crystal sites M1 and M2 of clinopyroxene vs. ionic radii calculated from experiments, modified from Hill et al. (2000). The graphs is displayed only to show the relative and general compatibility/incompatibility of a broad range of elements in clinopyroxene without assuming that they represent absolute value of element partition coefficients for other magmatic system. Elements selected for analyses of augite phenocrysts in the nakhlites are surrounded in red for compatible elements, green for mildly incompatible elements and blue for highly incompatible elements.* . . . . . . . . . . . . . . . . . 118

4.41 *Ti vs. Zr and Ti/Ti* vs. Zr/Zr* in augite phenocrysts. The ratios represent a measure of the Ti and Zr depletion/enrichment relative to neighbouring elements on normalized incompatible element plots (Fig. 4.22). Such ratios are commonly used to quantify the strength of the positive or negative anomalies. Despite an increase of Ti with progressive crystallization, the strength of Ti anomalies decreases. Ti is less sensitive to fractional crystallization.* . . . . . . . . . . . . . 121

4.42 *Trace element abundances in augite phenocrysts from different nakhlites. Despite their similar major element compositions, the trace element compositions of the augite phenocrysts vary (in both abundance and extent of zonation) between the nakhlites.* . . . . . . . . . . . . . . . 123

4.43 *Selected trace elements in olivine phenocrysts and its high temperature oxidative replacement product (i.e laihunite, L) in Y 000593. Data from NWA 5790 represent measurements of the same large olivine grain.* . . . . . . . . . . . . . . . . . . . . . . . . . . . 125

4.44 *Binary diagram of Chromium (Cr) vs. Zirconium (Zr) and Nickel (Ni) in augite phenocrysts from different nakhlites. Chromium and Ni are compatible in augite, whereas Zr is incompatible. The arrows represent the magmatic evolution during fractional crystallization (FC) of Nakhla. A crystallization of the rocks through closed system FC should form overlapping trends.* . . . . . . . . . . . . . . 131

4.45 *Aluminium/Titanium (Al/Ti) vs. Magnesium number (Mg♯) in augite phenocryst core and rim (left) and core (right). Ratio of the augite incompatible elements are less sensible to pressure and temperature conditions than Al and Ti concentrations and thus are interesting to track variations in melt chemistry. Al/Ti ratios of augite can also serve to identify the relative timing magnetite and plagioclase crystallization.* . . . . . . . . . . . . . . . . . . . . . . . . . . . . 133

4.46 *Light rare earth element ratio (i.e. Lanthanum/Samarium, i.g. La/Sm) vs. augite incompatible (i.e. Barium, Zirconium and Strontium, i.g. Ba, Zr, Sr) and compatible element (i.e. Chromium, i.g. Cr).* . . . 134

4.47 *Zirconium/Hafnium (Zr/Hf) vs. Zr in augite phenocrysts. Both elements have similar substitution behaviour in clinopyroxene. The non-decoupling of element ratios between the nakhlites suggests that the meteorites are members of a genetically related suite of melts from a common parent magma.* . . . . . . . . . . . . . . . . . . . . . . 135

4.48 *Partition coefficient (D) of REEs and Sr for clinopyroxene/liquid (CPX/L) equilibria calculated for nakhla and Shergotitty (Shergotitte-group of the SNC Martian meteorites) from experiemntal study (Oe et al., 2001). The partition coefficients of NJ4 have been obtained from a melt with a major element composition that resembles that of Nakhla and so are believed to represent the most accurate coefficient partitions for the nakhlites. The coefficient partitions used in this study have been directly read from this graph (presented on Tab. 4.3).* 138

4.49 *Average augite REE abundances and estimate of the REE composition of the parent magmas from which they crystallized using the partition coefficient of Oe et al. (2001) and normalization factors of McDonough and Sun (1995). Bulk rock REE composition (dashed lines) are provided for comparison. The REE patterns of the magmas that crystallized augite (assuming equilibrium conditions) are parallel to the nakhlites' bulk rock suggesting closed-system crystallization.* . . 142

4.50 *Bulk rock composition of NWA 817 and NWA 998 measured by Treiman and Irving (2008) and calculated using average composition of the rock-forming minerals (this study) and their relative modal proportion in the rocks. Percentage of the different mineral phases are taken from (Treiman, 2005) with for NWA 817: 70 % augite, 10 % olivine and 20 % mesostasis; and for NWA 998: 68 % augite, 2 % orthopyroxene, 10 % olivine, 19 % mesostasis (assumed 100 % plagioclase) and 1 % glass. The rock compositions are normalized to CI chondrite using the normalization factors of McDonough and Sun (1995). The calculated and measured bulk rocks have relatively similar REE patterns suggesting an evolution of the rocks through fractional crystallization under closed-system condition. The high Eu anomalies in the calculated bulk rock composition of NWA 998 and high HREE abundances relative to the measured bulk rock reflect the assumption that the mesostasis is only composed of plagioclase whereas it contains also apatite a mineral that preferentially incorporates the LREEs relative to the HREEs.* . . . . . . . . . . . . . . . . . . . . . . . . . . . . 145

4.51 *Sketch modified from Imae et al. (2005) illustrating the two-stage crystallization history of the nakhlites (with the likely environments of crystallization of the main mineral phases) that served as a basis for the further investigation of the nakhlites geological history in the second part of this chapter. This included the petrological link of the individual rocks using trace element geochemistry. Based on trace element geochemistry of the various mineral phases of the nakhlites, the different rocks are not the product of a single lava flow but rather represent the solidified products of multiple magma pulses or bodies that were emplaced relatively contemporaneously.* . . . . . . . . . . 150

5.1 *Fundamental processes, effects and consequences of fluid-mineral interactions (Hochella and White, 1990).* . . . . . . . . . . . . . . . . 156

5.2 *Secondary minerals identified on Mars or in Martian meteorites and their respective general environmental conditions and style of formation, figure taken from Ming et al. (2007).* . . . . . . . . . . . . . . 160

5.3 *Schema illustrating the different reservoirs of volatiles on Mars and their interactions (http://photojournal.jpl.nasa.gov/jpeg/PIA16463.jpg).* 160

5.4 *Pictures of the nakhlite meteorite NWA 817. The rock displays reddish-brown rock staining unevenly distributed. Secondary minerals are strongly associated with olivine where they form veins and thin films cross-cutting and surrounding the olivine grains respectively. In the mesostasis they form patches of alteration.* . . . . . . . . . . . . . 162

5.5 *Crystallographic orientation of olivine grains (pole figures olivine forsterite 92) in NWA 817. The red, green and purple strips correspond respectively to the trace of the {100}, {010}, and {001} planes normal to the olivine grains. The veins are roughly parallel to the trace of the {001} planes.* . . . . . . . . . . . . . . . . . . . . . . . 164

5.6 *BSE images of the different alteration textures in olivine phenocrysts from the different nakhlites. Lafayette and NWA 817 have the largest veins with sawtooth margins, while Y 000593 and MIL 03346 are the only nakhlites with abundant channel-like alteration textures identified as laihunite (lai) by Noguchi et al. (2009).* . . . . . . . . . . . . 165

5.7 *BSE images of a rough surface of olivine from NWA 817 showing the presence of funnel-shape etch pits with a common orientation (a) and their likely growth by coalescence to form larger ones (b). Some of the etch pits are coated with clay minerals, possibly smectite, as suggest by the mineral crystallinity (c).* . . . . . . . . . . . . . . . . 167

5.8 *BSE images of a rough olivine grain from Nakhla showing the presence of a succession of coating layers that developed parallel to the grain surfaces. Below the thin films of alteration products, the olivine surface is heavily altered and show abundant denticulations intruding into the olivine grain. The coating layers display a dessication crack-like pattern. Underneath the cracks, olivine is more altered suggesting that the successive layers of alteration products have somewhat protected olivine from the fluids but were inefficient to prevent fluid access to the olivine surface.* . . . . . . . . . . . . . . . . . . . . . . 168

5.9 *BSE images of a rough olivine grain from Nakhla showing veins at different stages of evolution. On the left image, one of the vein is filled by secondary minerals displaying no obvious crystal faces. A second vein is marked by fine denticulations and etch pits spreading side-by-side and base-to-base. The poorly developed vein illustrates the early stage of vein formation that results from fluid ingress probably flowing an intra-crystalline plane defect and subsequent removal of selected elements from olivine. Image on the right shows the denticulated surface of olivine at the contact with a vein.* . . . . . . . . 169

5.10 *BSE image of the alteration products (ap) partially replacing skeletal olivine (ol) in the mesostasis of NWA 817.* . . . . . . . . . . . . . . 169

5.11 *BSE image of laihunite (the high temperature aqueous oxidative product of olivine) in the mesostasis of MIL 03346. In our sample of MIL 03346, all skeletal olivine grains have been transformed into laihunite.* 170

5.12 *EDS map of an altered olivine grain in the mesostasis of Y 000593. Some parts of the olivine grain are transformed into laihunite (the high temperature aqueous oxidative product of olivine). The "fresh" parts of olivine contain small veins of alteration products.* . . . . . . 171

5.13 *EDS maps of the olivine alteration products in NWA 817 comprising an Mg-rich product central to the veins, an Si-rich product making most of the veins and a marginal product rich in Fe and Mn.* . . . . 172

5.14 *BSE image of the fine inter-growth of alteration products along the margins of olivine veins in NWA 817.* . . . . . . . . . . . . . . . . . 173

5.15 *EDS maps of an unusually heavily altered olivine phenocryst next to a relatively unaltered one in the NWA 817 naklite. This probably reflect a very uneven fluid circulation throughout the rock.* . . . . . 174

5.16 *BSE image of an unusually large altered pyrrhotite in NWA 817. Pyrrhotite dissolution brought acidity which has enhanced glass alteration. The "darker' veins are terrestrial calcite.* . . . . . . . . . . 174

5.17 *Photomicrograph (reflective light) of skeletal Fe-oxide in NWA 817 and Raman spectra showing the progressive pseudomrphic replacement of magmatic magnetite by secondary goethite.* . . . . . . . . . 175

5.18 *BSE image of an olivine phenocryst from MIL 03346 with its characteristic alteration texture including laihunite along grain boundaries and intra-crystalline veins of secondary silicate. Pyrrhotite are also commonly altered and replaced by secondary silicate forming veins similar those in olivine and pseudomorphic replacements of secondary Fe-oxide (hematite). The magmatic magnetite grains appear largely unaltered.* . . . . . . . . . . . . . . . . . . . . . . . . . . . . . . . . 176

5.19 *EDS map of an olivine alteration veins comprising an Si-rich product and Fe-sulphate in MIL 03346. The sulfate cross-cuts the Si-rich product and can be traced through the mesostasis.* . . . . . . . . . . 177

5.20 *EDS map of a heavily altered area of MIL 03346. The aqueous fluids have partly dissolved the primary material and precipitated secondary minerals. For example, the sulfide grains have been completely re-crystallized into Fe-oxides. To be noted: at the contact with the aqueous fluids augite grains have been partly corroded and have lost through their altered rims their structural Fe and Mg (probably by solid-state diffusion).* . . . . . . . . . . . . . . . . . . . . . . . . 179

5.21 *BSE images of quartz and Fe-oxide filling impact-induced fractures in nakhlite MIL 03346.* . . . . . . . . . . . . . . . . . . . . . . . . 180

5.22 *BSE image of an alteration vein in Y 000749 with bands of Si-rich products with Fe-oxide (light grey strips), siderite, Fe-sulphate. Olivine alteration textures include empty etch pits and denticulation and filled curved channels.* . . . . . . . . . . . . . . . . . . . . . . 180

5.23 *EDS maps of the olivine-bounded alteration products in Y 000749. The alteration product central to the veins is strongly enriched in Si and Mg and is surrounded by siderite, a Fe-rich carbonate.* . . . . . 181

5.24 *EDS maps of olivine with laihunite (dirty patches) and alteration veins in Y 000593. The veins are zoned with an Si-Mg-rich product surrounded by an Si-Fe ±S-and P- (not shown) rich product. Alteration products enclose symplectite suggesting a formation through dissolution-precipitation, the symplectite being less soluble than the olivine.* . . . . . . . . . . . . . . . . . . . . . . . . . . . . . . . . . . 182

5.25 *High resolution bright field images of laihunite (dark strips) and alteration veins in an olivine phenocryst from Y 000593. The black diamond shaped grains within the laihunite are most probably goethite.* 183

5.26 *EDS maps of a heavily altered pyrrhotite grain replaced by Fe-sulphate and Mg-rich clay minerals (recognized by their crystallinity) in Y 000593.* . . . . . . . . . . . . . . . . . . . . . . . . . . . . . . . 184

5.27 *EDS maps of a completely altered area where once lays the mesostasis (identified thanks to the presence of remnants of plagioclase) containing salts and Mg-Si-rich fibrous phyllosilicates (clays) in Y 000593. Both silicate minerals displays the same bulk texture and mineralogy than those replacing the large pyrrhotite grain on Fig. 5.26.* . . . . . . 185

5.28 *BSE images of olivine dissolution textures (left) along a grain boundary and alteration vein (right) in Nakhla. Outside of these localized areas, olivine is unaltered.* . . . . . . . . . . . . . . . . . . . . . . . 186

5.29 *BSE images of nm-scale secondary minerals filling olivine veins from a non-polished sample of Nakhla.* . . . . . . . . . . . . . . . . . . . 186

5.30 *EDX montage map of a thin section of lafayette with localized alteration "rims" surrounding augite, olivine and orthopyroxene grains.* . . 187

5.31 *EDX map of a heavily altered area in lafayette with abundant clays replacing plagioclase, olivine, augite and orthopyroxene.* . . . . . . . . 188

5.32 *BSE image of the complex alteration products within olivine veins from Lafayette. Goethite has been identified using Raman Spectroscopy.* 189

5.33 *EDX map of well-organised smectite spreading perpendicular to the vein walls or forming rosette and siderite in Lafayette. To be noted: the preservation of the saw tooth shape and symmetry of the "double layer" of phyllosilicate.* . . . . . . . . . . . . . . . . . . . . . . . . . . 189

5.34 *BSE image of an olivine phenocryst from NWA 998. Olivine contains thin veins filled with a texture-less Si-rich alteration product and rare "patchy" Fe-Mn product along vein margins and transversal fractures cross-cutting the Si-rich product.* . . . . . . . . . . . . . . . . . . . . 190

5.35 *High resolution TEM bright field image of poorly crystallized and ill organized smectite from NWA 817. Bright field images are density contrast images, the lightest grey zones represent areas of low density.* 192

5.36 *High resolution TEM bright field images of "coarse" smectite from NWA 817 at different magnification. The coarse smectite spread between olivine vein walls (not shown on the image) and the fine poorly crystallized smectite making the olivine vein center.* . . . . . . . . . 194

5.37 *BSE image (left) and Ca $K_\alpha$ EDX map (right) of terrestrial calcite in NWA 817. Calcite contains fragments of olivine with its alteration products (white square). Textural relationships between calcite and olivine-bounded veins suggest that the veins are of Martian origin. Calcite fills post-landed fractures that cross-cut the meteorite.* . . . . 196

5.38 *BSE/STEM image of a FIB section of an olivine-bounded vein in NWA 817. EDS spot analyses reveal the presence of (Mn-bearing) calcite filling porosity created by the dissolution of the Martian clay minerals by terrestrial fluids. Ca and Mn are most probably terrestrial contaminants.* . . . . . . . . . . . . . . . . . . . . . . . . . . 197

5.39 *EDS map of impact-generated brecciated areas with their terrestrial alteration products, a mixture of clay minerals and P-S-Cl-rich salts in Y 000593 (left) and Fe-Mn-rich clay minerals in NWA 817 (right).* 198

5.40 *BSE images of terrestrial weathering products rich in ionic compounds (light grey shown by the white arrows) in the mesostasis (left) and olivine-bounded veins (right) in Y 000593. The ion-rich products in the mesostasis form bands along and intruding into the sheet of clay minerals. In the olivine veins, the ion-rich products follow fractures and cross-cut the Martian alteration assemblage.* . . . . . . 199

5.41 *Secondary mineral assemblage in Y 000593 with the material precursor of smectite (Si-rich) surrounded by Fe-sulphate. Fe-sulphate overgrow and cross-cut the proto-smectite suggesting that it crystallized last probably from a separate aqueous pulse.* . . . . . . . . . . . 204

5.42 *Schematic diagram illustrating the different stages of vein formation and mineralization in olivine phenocryst in Lafayette during multiple aqueous pulses. (1) Aqueous fluids probably entered into olivine grains following intra-crystalline fractures. (2) Fluid-rock interactions led to a partial dissolution of olivine and in situ deposition of insoluble component of olivine. (3) Further progressive dissolution of olivine and fluid maturity have led to the formation of well organized clay minerals that grew from, and perpendicular to, the Si-rich product. (4) Later infiltration of scarce $CO_2$-rich fluids in the rock resulted in the precipitation of carbonate in some of the veins between the clay minerals and olivine.* . . . . . . . . . . . . . . . . . . . . . 205

5.43 *Composition of olivine (phenocryst and mesostasis) and their respective clay mineral populations in NWA 817. Fine smectite are enriched in insoluble Si and Al reflecting a loss of metallic components to the fluids while coarse smectite are enriched in soluble Fe indicating a very restricted amount of fluids and a poor circulation of the solutions. Both smectite probably crystallized during distinct aqueous event and reflect the changes of aqueous conditions over time.* . . . 206

5.44 *Schema of olivine alteration veins showing the different mineral assemblage found in the individual nakhlites with their relative proportion and position in the veins. The nakhlites are presenting in their stratigaphic position according to the pettrographic model of Mikouchi et al. (2012), with NWA 817 sampling the top of the cumulate pile (red), Nakhla, Y 000749 and Y 000593 forming the interior of the igneous body (yellow) and Lafayette and NWA 998 the bottom (green).* 209

# LIST OF TABLES

1.1 *Geological timescale and chronology of Mars with its three main periods (Noachian, Hesperian and Amazonian) and characteristic geological processes and events. Table modified from Hartmann (2005).* 4

2.1 *List of standards used for quantitative analyses standardization with detection limits. Standardization of common major and minor elements in silicate minerals was performed using natural minerals. The lack of chemical composition for diopside and garnet has prevented calculation of detection limits for Ca, Si and Fe.* . . . . . . . . . . . . 31

3.1 *Operating conditions for the LA ICP-MS analyses.* . . . . . . . . . . . 52

4.1 *Table showing the trace elements selected for analyses of augite phenocrysts in individual nakhlites. The conservative elements represent elements that are either known to resist to sub-solidus diffusional reactions in clinopyroxene (Van Orman et al., 2002) or which are believed to still represent the original distribution in augite from the nakhlites (Wadhwa and Crozaz, 1995). The compatible, incompatible and conservative behaviour of a selection of elements (taken from Fig. 4.39) is provided for general understanding and comparison for the nakhlites augite.* . . . . . . . . . . . . . . . . . . . . . . . . . . . . 119

4.2 *Table summarizing the apparent behaviour of selected trace elements in augite during nakhlites crystallization. Compatible and mildly incompatible elements show complex zoning patterns reflecting both changes in element behaviour during augite growth and late sub-solidus re-equilibration.* . . . . . . . . . . . . . . . . . . . . . . . . . 131

4.3 *Estimated partition coefficients (i.e. D) calculated for Nakhla clinopyroxene of Oe et al. (2001) and average of REE abundances in ppm in augite cores in different nakhlites (measured in this work) with n the number of grains used to calculate the average.* . . . . . . . . . . 140

4.4 *Average of REE abundances in ppm in glass, feldspar and low-Ca pyroxene in NWA 817 and NWA 998, with n the number of analysed grains averaged.* . . . . . . . . . . . . . . . . . . . . . . . . . . . 144

4.5 *Approximate sequences of mineral crystallization in the quickly cooled nakhlites NWA 5790, NWA 817 and MIL 03346. Cristobalite* has only been found in MIL 03346.* . . . . . . . . . . . . . . . . . . . . . . 147

4.6 *Approximate sequences of mineral crystallization in the nakhlites Y 000749, Y 000593, Nakhla and Lafayette. Pyroxene*$^{**}$ *is used as a generic term for low-Ca pyroxene (including pigeonite and orthopyroxene). The last mineral to crystallize is orthopyroxene*$^{***}$*, it corresponds to a mineralogical re-equilibration from olivine-plagioclase. Its abundance in the nakhlites increases with the degree of crystallinity.* 148

4.7 *Approximate sequences of mineral crystallization in NWA 998. Pyroxene*$^{**}$ *is used as a generic term for low-Ca pyroxene (including pigeonite and orthopyroxene). The last formed orthopyroxene*$^{***}$ *corresponds to a mineralogical re-equilibration from the previously stable mineral assemblage olivine-plagioclase. It is abundant in NWA 998.* . . . . . . 149

# 1. INTRODUCTION TO MARS' SURFACE GEOLOGY DURING THE AMAZONIAN

## *1.1 Understanding of the Martian surface and its evolution*

Over the past decades, an extraordinary amount of new information about Mars' surface from Earth-based telescopes and Mars-based orbiting spacecraft and landers have been gathered and have enhanced our understanding of the geological evolution of the red planet. Mars exploration has revealed a complex planet shaped by a variety of geological and climatic processes similar to those on Earth (Mitchell and Wilson, 2003). Intense impact cratering, magmatic and liquid water activity have been amongst the most important geological processes responsible for the Martian surfaces we can see today. One of the most striking feature of Mars' surface is the presence of a global dichotomy whose origin still remains a mystery (Nimmo and Tanaka, 2005). The global dichotomy dividing the South from North hemisphere is marked by a sharp change in Mars crustal structure, elevation and age of geological units (Fig. 1.1). South of this boundary are the heavily cratered ancient terrains with a relatively high elevation (several kilometers above the Northern lowlands). The large impact basins present in the high plateaux include Hellas and Argyre. North to the dichotomy are the younger terrains of Mars with a general low elevation. They consist of vast sedimentary and volcanic plains but also comprise the Tharsis volcanic region and tectonic rift valleys including the 4000 km long Valles Marineris. Along the North-South dichotomy, a plethora of young erosional and depositional features of likely diverse origin (including volcanic, fluvial, lacustrine, glacial and eolian) can be found (Nimmo and Tanaka, 2005).

A major step in understanding the geological evolution of Mars is to define a Martian geological time-scale (Hartmann, 2005). Relative datation of planetary surfaces are commonly established using impact-crater isochrons based on size and density distributions of impact craters on undisturbed surfaces, while geologic periods are established based on the age range of representative rocks and main geological processes. Based on geomorphic textures, stratigraphic relationships and superposed impact crater populations, the geological history of Mars have been divided into three main periods with from oldest to youngest: Noachian (4.5 – 3.7 Ga), Hesperian (3.7 – 3.1 Ga) and Amazonian (3.1 Ga - now). Table 1.1 summarizes the main geological features and processes of Mars (including some young ones) and their relative datation. Data presented in the table provides a relative timescale and chronology for Martian evolution.

Despite the dominance of the Amazonian period over the Noachian and Hesperian, terrains of Amazoninan time are infrequent on the Martian surface (Fig. 1.2), and probably reflect the strong decrease in magmatic activity of Mars over this period (Hartmann, 2005). Detailed geological mapping associated to crater size fre-

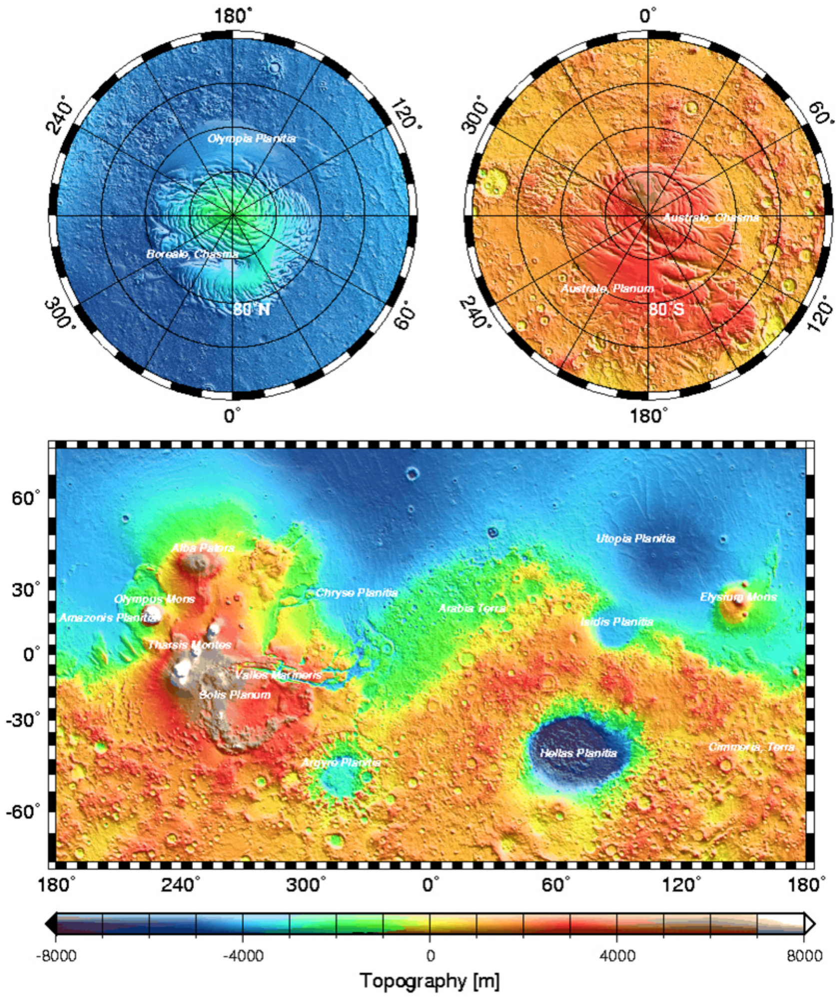

*Fig. 1.1: Global topographic map of Mars and major surface features labelled. Image from the MGS MOLA (Mars Global Surveyor Mars Orbiter Laser Altimeter Team, https://attic.gsfc.nasa.gov/mola/images.html). The ancient high plateaux of Mars forming the South hemisphere are much more heavily cratered than the plains forming the young Martian terrains.*

quency distribution have revealed that both volcanism and fluvial activity occurred mostly during the Noachian and Hesperian (4.5–3.7 Ga ago and 3.7–3.1 Ga ago, respectively) but have persisted during the Amazonian (3.1 Ga - now) until very recently (Carr and Head, 2010; Neukum et al., 2004; Hartmann, 2005). Although the large Martian volcanoes of the Tharsis region (the Olympus Mons, Ascraeus Mons, Arsia Mons, Albor Tholus and Hecates Tholus) and Elysium rise formed early, probably over 3 Ga ago, they display substantial evidence of episodic, quiescent volcanic activity during the Late Amazonian especially within their calderas and along their faulted flanks (Neukum et al., 2004; Chadwick et al., 2015). The youngest volcanic activity dated at only a few million years suggests that the volcanoes may even still be active today (Neukum et al., 2004; Hartmann, 2005).

Explosive Tharsis volcanism during the Late Noachian is believed to have released heat and volatiles from the mantle onto the surface with important implica-

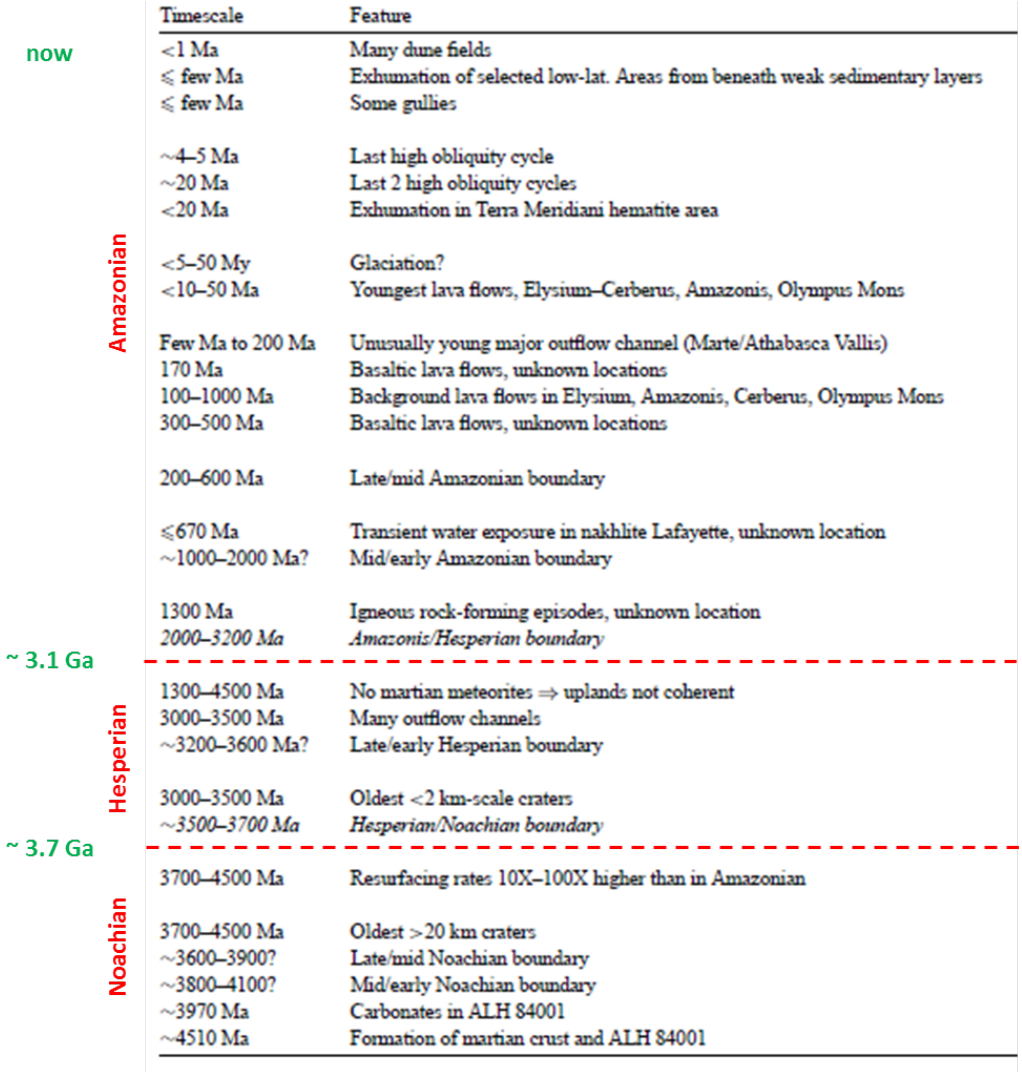

| Timescale | Feature |
|---|---|
| <1 Ma | Many dune fields |
| ⩽ few Ma | Exhumation of selected low-lat. Areas from beneath weak sedimentary layers |
| ⩽ few Ma | Some gullies |
| ~4–5 Ma | Last high obliquity cycle |
| ~20 Ma | Last 2 high obliquity cycles |
| <20 Ma | Exhumation in Terra Meridiani hematite area |
| <5–50 My | Glaciation? |
| <10–50 Ma | Youngest lava flows, Elysium–Cerberus, Amazonis, Olympus Mons |
| Few Ma to 200 Ma | Unusually young major outflow channel (Marte/Athabasca Vallis) |
| 170 Ma | Basaltic lava flows, unknown locations |
| 100–1000 Ma | Background lava flows in Elysium, Amazonis, Cerberus, Olympus Mons |
| 300–500 Ma | Basaltic lava flows, unknown locations |
| 200–600 Ma | Late/mid Amazonian boundary |
| ⩽670 Ma | Transient water exposure in nakhlite Lafayette, unknown location |
| ~1000–2000 Ma? | Mid/early Amazonian boundary |
| 1300 Ma | Igneous rock-forming episodes, unknown location |
| *2000–3200 Ma* | *Amazonis/Hesperian boundary* |
| 1300–4500 Ma | No martian meteorites ⇒ uplands not coherent |
| 3000–3500 Ma | Many outflow channels |
| ~3200–3600 Ma? | Late/early Hesperian boundary |
| 3000–3500 Ma | Oldest <2 km-scale craters |
| *~3500–3700 Ma* | *Hesperian/Noachian boundary* |
| 3700–4500 Ma | Resurfacing rates 10X–100X higher than in Amazonian |
| 3700–4500 Ma | Oldest >20 km craters |
| ~3600–3900? | Late/mid Noachian boundary |
| ~3800–4100? | Mid/early Noachian boundary |
| ~3970 Ma | Carbonates in ALH 84001 |
| ~4510 Ma | Formation of martian crust and ALH 84001 |

*Tab. 1.1: Geological timescale and chronology of Mars with its three main periods (Noachian, Hesperian and Amazonian) and characteristic geological processes and events. Table modified from Hartmann (2005).*

tions on the formation of the Early atmosphere and fluvial activity of Mars (Phillips et al., 2001). The old Noachian and Hesperian terrains exhibit geomorphological features suggesting abundant flowing water on Mars' surface which have required warmer and wetter conditions than those prevailing today (Baker et al., 1991). Some geomorphological evidence for fluvial activity can still be found in the Early to Middle Amazonian terrains but are largely lacking within the Late Amazonian terrains (Carr and Head, 2010). During the Amazonian period (making 60% of Mars geological history), fluvial activity has virtually ceased on the Martian surfaces. The superficial environments of Mars have rapidly evolved into a relatively dry arctic desert with physico-chemical conditions somewhat similar to those of the Antarctic Dry Valleys (Kargel and Strom, 1992).

The geomorphological features of the surface of the Red planet suggest that Mars experienced a drastic climate change over geological time scale. Today, Mars

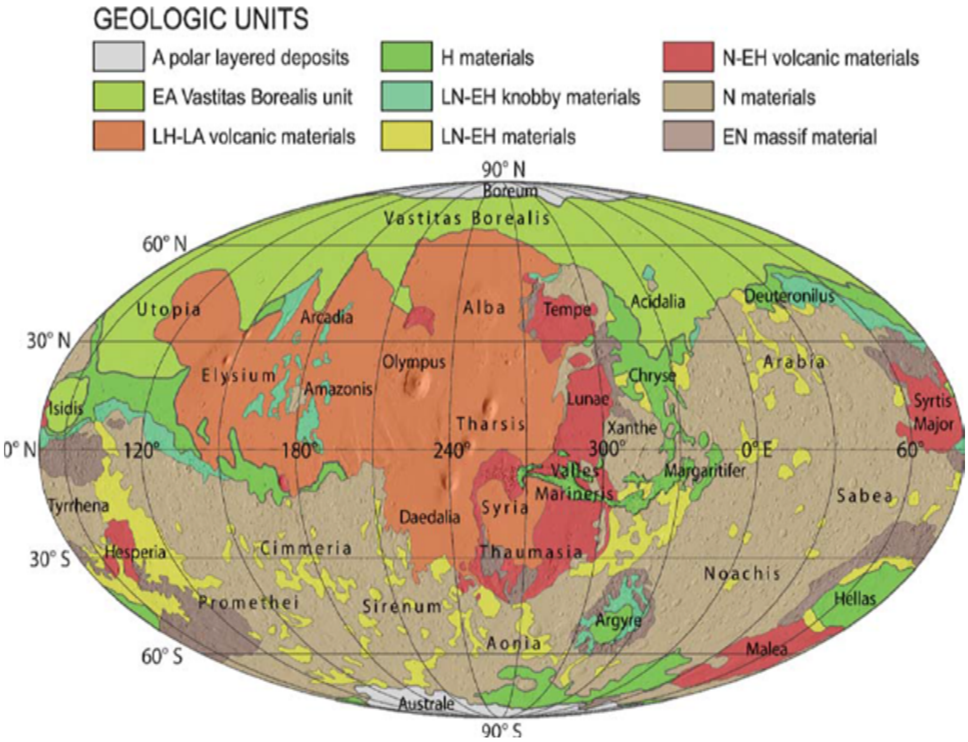

*Fig. 1.2: Global geological map of Mars with its principal geological units from the Early and Late (E and L) Noachian, Hesperian and Amazonian (N, H and A respectively). Map taken from Nimmo and Tanaka (2005).*

has a mean atmospheric pressure of 6.1 mbar (due to a $CO_2$ atmosphere) and mean temperatures ranging from 150 K at the poles to 215 K at low latitudes (Carr and Head, 2010). Such extreme conditions do not allow liquid water to be stable on the surface, while shallow ground ice water can only exist in the polar and circumpolar regions. Since the Early Amazonian, glacial activity (dry $CO_2$ ice) largely controls Mars' surface environments (Kargel and Strom, 1992). The most active processes occur in the polar regions where the atmospheric $CO_2$ seasonally cycles in and out of the dry polar caps (Tillman et al., 1993). The polar regions are mostly composed of dry ($CO_2$) ice but are known to contain $H_2O$ hidden at the base of the polar caps. Water in the form of ice has also been detected in the permafrost of the circumpolar regions of Mars and in minute clouds or haze in the lower Martian atmosphere (Pearl et al., 2001). Maps showing the current distribution of water (recalculated from H measurements) are provided on Fig 1.3. The polar regions are very sensitive to the extreme variations in the obliquity of the spin axis of Mars and orbit eccentricity (Laskar et al., 2004). When the obliquity of Mars is high, the poles receive more solar insulation. Temperatures and atmospheric pressures (due to the release of volatile compounds from the cryosphere into the atmosphere) rise allowing further $CO_2$ and $H_2O$ groundice to migrate towards the equatorial regions. The polar caps control the climate of Mars and the lateral redistribution of $CO_2$ and $H_2O$ and their variations in concentration between atmosphere and cryosphere over a wide range of time-scale from season to Ma (Kieffer and Titus, 2001; Laskar et al., 2004).

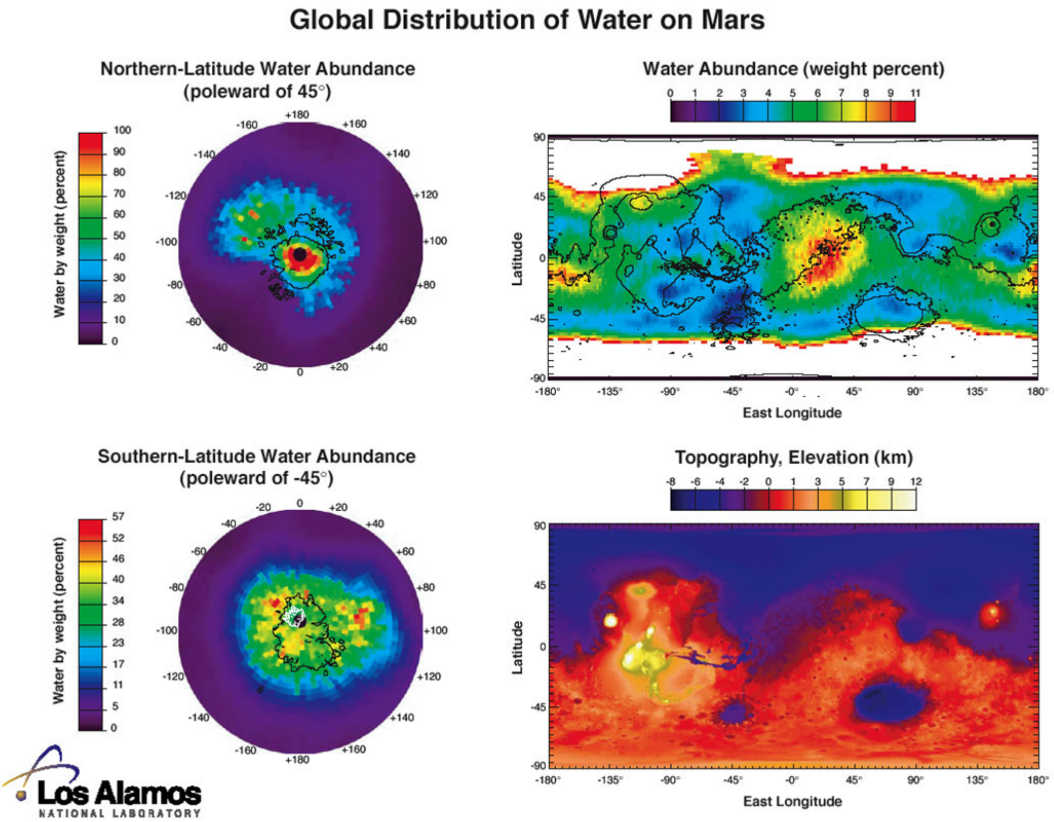

*Fig. 1.3: Estimates of the total amount of water stored near the Martian surface recalculated from hydrogen distribution identified by instruments aboard NASA's Mars Odyssey spacecraft. Water are mostly present in the circumpolar regions, below the dry ice polar caps and around the Tharsis bulge, http://www.spaceref.com/news/viewnews.html?id=740.*

Recent observations of Mars have revealed the likely gravity-driven accumulation of water, ice and erosion features associated with flowing water in the non-polar volcanic regions of the Red planet over the last tens of Ma (Neukum et al., 2004). Alternation of glacial and sporadic fluvial activity seems to have occurred over the Amazonian period and may still happen today (Hartmann, 2005). Currently, transient, and possibly non-equilibrium, hydrological activities (in the form of flowing brines?) are also regularly detected along the walls of impact craters and canyons in mid latitudes (Malin and Edgett, 2000; Gaidos, 2001). Despite the apparent dryness of Mars' topmost surfaces today, at least some water most probably in the form of ice, is still present locally and/or regionally within the Martian regolith and is sporadically activated. But how much water is currently stored in Mars crust and how does this water migrate through the crust? Has this water been in contact with the atmosphere of Mars? Are the different volatile reservoirs of Mars still interacting with each other? And what are the geological processes still in action today responsible for the sporadic and transient liquefaction and mobilization of this crustal water? Today, the sub-surface of Mars remains out of reach from Mars-based spacecraft and landers, and so the nature of Mars' recent hydrosphere and their possible interactions with the various volatile reservoirs of Mars remain unresolved.

Many secrets of Mars from magmatic to near-surface processes that are not accessible by landers and orbiters have been revealed by the Martian meteorites SNCs (acronym for Shergottite, Nakhlite, Chassignite) and the distinct and unique ALH84001 an ancient orthopyroxenite dated at $\backsim$ 4.089 Ga (Bridges and Warren, 2006; Bellucci et al., 2015) and the basaltic (impact) breccias North West Africa (NWA) 7034 including its numerous pairings whose lithological components formed contemporaneously $\backsim$ 4.44 Ga ago (Agee et al., 2013; Nyquist et al., 2016). Investigations of the Martian meteorites have divulged an early segregation into core, mantle and crust of the red planet, probably within the first million years after its accretion (Lee and Halliday, 1997), and the presence of a magnetic dynamo that disappeared early leaving the Martian atmosphere unprotected to solar wind (Weiss et al., 2002). The Martian meteorites are enriched in incompatible elements (Jones, 2003). The Martian crust, including the early one, represents a geochemically enriched reservoir of the planet (Nyquist et al., 2016). The numerically dominant Martian meteorites SNCs all have young crystallization ages ($\leqslant$ 1.3 Ga). They are fragments of Amazonian volcanic terrains, but their isotopic chemistry points toward old mantle sources with very primitive and possibly unchanged and intact composition, although chemically distinct and heterogeneous (Bridges and Warren, 2006). The mantle of Mars probably never experienced effective convective mixing (Lee and Halliday, 1997) but repeated partial melting events and melt extraction (Longhi, 1991).

The fundamental basaltic nature of Mars' crust has been further confirmed by the Martian meteorites. All meteorites are basaltic rocks or rocks derived from basaltic magmas (Bridges and Warren, 2006). Today, there is no evidence for the presence of highly differentiated rocks on Mars either from the Martian meteorites or Mars-based observations (Singer and McSween, 1970; McSween et al., 2009). Basaltic activity appears to be the dominant type of magmatic activity on Mars (Fig. 1.4). On Fig. 1.4, Tropospheric Emission Spectroscopy (TES) data suggest more evolved basaltic rocks (i.e. greater $SiO_2$ content) plotting in the field of basaltic andesite of the TAS diagram. However, McSween et al. (2009) interpreted the greater $SiO_2$ content of the rocks as resulting from interactions of the basaltic crust with water (i.e. weathering processes) and not from igneous processing including hydrous melting or fractionation.

The Martian meteorites are geological samples available for laboratory analyses (McSween, 1985). They can provide useful data about the basaltic magmatism of Mars that still remains poorly constrained. They include the physical and chemical properties of the magmas from which the SNCs derive, their rheology, density, viscosity and composition but also the eruption style and timing and the duration of the magmatic events. Furthermore, as fragments of young Amazonian sub-surface basaltic crust, the SNCs can offer a unique opportunity to understand the Martian lithosphere, atmosphere, and hydrosphere conditions and interactions during a very recent time. Most Martian meteorites including the nakhlites contain a suite of minerals indicating the presence of liquid water in Mars' sub-surface during the Amazonian (Bridges and Grady, 2001). Although they are present in very small quantities (Leshin and Vicenzi, 2006), the aqueous minerals represent a mineralog-

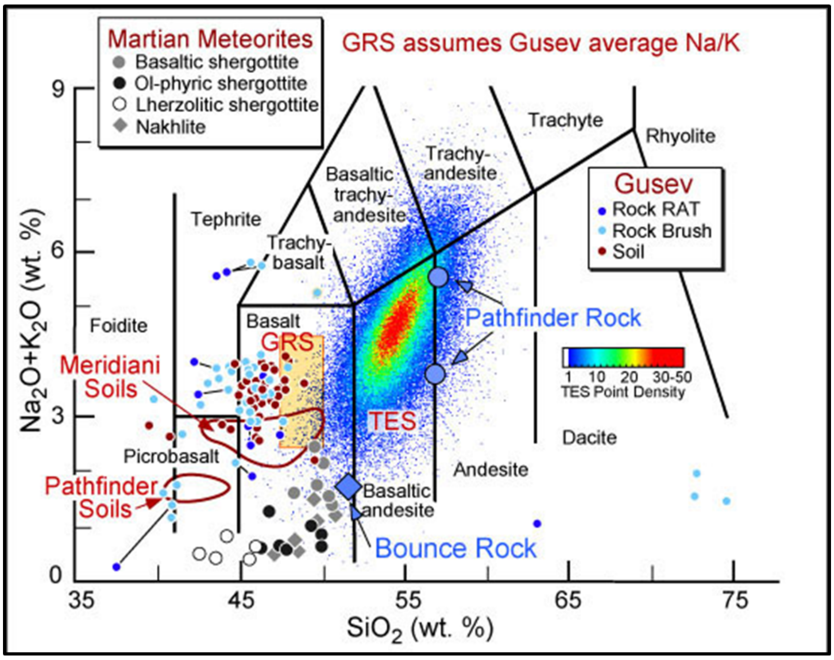

*Fig. 1.4: Total alkalis vs. silica diagram for Martian meteorites, analyses of soils and rocks at robotic landing sites, and chemical information from orbiting spacecraft (TES and GRS). All data cluster around the basalt field, showing the basaltic nature of the Martian crust (McSween et al., 2009).*

ical and chemical inventory of the near-surface water-rich environments of Mars including the environmental conditions and evolution over time. Based on crystallization and cosmic-ray exposition ages, the SNCs might represent at least seven distinct impact sites (Christen et al., 2005). Although limited, the pre-terrestrial alteration of all the SNCs suggests an expanded presence of restricted quantity of water within Mars' regolith. The meteorites can provide information on the nature of the ephemeral water-rich environments that existed in a recent past in the subsurface of Mars. Even if the SNCs are biased samples of Mars' crust (they only sample the Amazonian volcanic terrains), they can nevertheless serve as ground truth for in situ observations and future Mars exploration including the promising Mars' sample return mission.

## 1.2 The nakhlite meteorites

### 1.2.1 Young basaltic rocks from Mars

The nakhlites are achondrite meteorites ∽1.3 Ga old (Treiman, 2005). They are extra-terrestrial igneous rocks dominated by clinopyroxenes and minor olivine phenocrysts within a finely-grained matrix principally composed of Fe-Ti-oxides and plagioclase. Based on mineral texture and composition, the nakhlites are very similar to basaltic rocks from Earth (Friedman-Lentz et al., 1999). Chemical, isotopic, and chronological data provide evidence that the parental magma(s) of the nakhlites both erupted and solidified on Mars (Treiman, 2005). The nakhlites are fragments of young Amazonian igneous bodies, either lava(s) that flowed on the planet's surface or igneous intrusion(s) that crystallized within the shallow Martian crust (Treiman, 1987).

The liberation of rocks from Mars most likely implies impacts of meteorites, the only plausible process which could have generated sufficient energy to excavate and eject crystallized rocks from the surface of Mars (Head et al., 2002). At the time of their ejection, the nakhlites were probably located very near the planet's surface. Rocks excavated from deeper levels would not have reached the requisite velocity to exit Mars' thin atmosphere, while rocks at the top surface would not have survived the impact of the meteorite and would have been vaporized. Most nakhlites (except one) have similar cosmic-ray exposure age of $\backsim$ 11 Ma, which suggests a likely ejection into space by at least two distinct impacts of meteorite (Nyquist et al., 2001; Wieler et al., 2016). Presumably, the nakhlites are fragments of two different source craters including Martian bedrocks or source crater regions. As for any meteorite, the source regions of the nakhlites is unknown. However, by comparing their crystallization ages (1.3 Ga: Middle Amazonian) with relative age determination of the Martian surface by crater count chronology, the likely regions of origin include the volcanic provinces of Tharsis, Elysium or Syrtis major (Carr and Head, 2010).

### *1.2.2 Discovery of the nakhlite meteorites: Where, when, and how*

Today, nine non-paired nakhlites have been recognized. They include Nakhla, Lafayette, North West Africa (NWA) 817, the Miller Range (MIL) meteorites and Yamato (Y) meteorites, NWA 998, NWA 5790, Governador Valadares (GV), and NWA 10153 although their history of discovery is unclear for the majority. Nakhla, the eponym of the Martian meteorite group, was discovered in 1911 near Alexandria, Egypt (Prior, 1912). It represents a set of about 40 stones which fell onto the Earth as a meteorites shower. The Nakhla meteorites are the only nakhlite representative observed to fall to Earth to date. The 40 stones were directly collected, and so the Nakhla meteorites represent today potentially the least terrestrially altered of the nakhlites. North West Africa 817 (NWA 817) was found in the dry Moroccan Sahara by meteorites hunters in 2000 (Sautter et al., 2002). Measurements of noble gases produced by cosmic-ray exposure ($^3$He, $^{21}$Ne, $^{38}$Ar) have given an exposure age of about 9.7 ± 1.1 Ma (Marty et al., 2001). The fourth paired Miller Range (MIL 03346, MIL 090030, MIL 090032, and MIL 090136) specimens (Udry et al., 2012) were found in Antarctica in 2003-2004 by the NASA Mars Exploration Program ANSMET, three years after the discovery of the three paired Yamato (Y 000593, Y 000749, and Y 000802) specimens (Misawa et al., 2003); However, the Miller Range meteorites were found sufficiently far from the three Yamato meteorites to be recognized as a different representative of the nakhlites group. The Miller Range and Yamato specimens are not paired meteorites. Measurements of noble gases produced by cosmic-rays exposure ($^3$He, $^{21}$Ne, $^{38}$Ar) of the Miller Range meteorites have given an exposure age of about 9.5 ± 1.0 Ma (Murty et al., 2005).

The collection of the other nakhlites North West Africa 998 (NWA 998), North West Africa 5790 (NWA 5790) and its paired NWA 6814, Governador Valadares (GV), Lafayette and NWA 10153 is more uncertain. Lafayette was recognized as a meteorite in 1931 in Purdue University, Indiana, USA (Nininger, 1935). It was hypothetically observed to fall to Earth at an unknown location in Indiana during the 1920s. However, it has been kept for years in the University's Museum as a terrestrial striated rock. The fresh appearance of Lafayette argues for a very short residence time on the Earth exposed to atmospheric agents. However $^{14}$C and $^{10}$Be dating, giving a terrestrial residence time of about 2900 ± 1000 years, contradicts the Lafayette meteorite discovery history (Treiman, 2005). NWA 998 was found by nomads at an undisclosed location in eastern Morocco or Western Algeria in 2001. The meteorite, a single stone of 456 g, was then purchased from dealers at the Tucson Gem and Mineral Show in 2002. The $^{14}$C terrestrial age has been measured at 6000 ± 1000 years (Nishiizumi et al., 2004). The two paired specimens NWA 5790 and NWA 6814 were found in Mauritania. The cosmic-ray exposure age of NWA 5790 has been estimated at 7.3 Ma, which falls outside of the 9-13 Ma age cluster of other nakhlites (Wieler et al., 2016). The single specimen Governador Valadares (GV) was apparently found in the Brazilian city of the same name Governador Valadares, in the state of Minas Gerais in 1958 (Gomes and Keil, 1980). Its shining and well preserved appearance led to the assumption that it fell not a long time before its discovery (Burragato et al., 1975; Gomes and Keil, 1980). The last nakhlite discovered to date is NWA 10153 (Irving et al., 2015). It has been found as a single friable stone of 119 g lacking its shiny fusion crust in an unknown locality in the Saharan desert. The meteorite was purchased from a dealer in Erfoud (Morocco) in 2014. A Hf radiometric age for NWA 10153 of $\backsim$ 1.3 Ga suggests that the meteorite belongs to the nakhlite group of Martian meteorite (Irving et al., 2015).

### 1.2.3 Current understanding of the nakhlites's geological context and history

The nakhlite meteorites are geological samples available for laboratory investigations of Mars. However, as for any meteorite the geological context of the rocks is unknown, which drastically limits our interpretation and understanding of the geological history of Mars. Many investigations of the nakhlites have examined the mineralogy and petrography of the different meteorites to better understand their history and develop plausible petrogenetic models. However, the detailed magmatic processes responsible for their formation remain to date obscure.

All the nakhlites are olivine-bearing clinopyroxenites that crystallized $\backsim$ 1.3 Ga ago (Treiman, 2005). They are igneous rock derived from basaltic magmas that formed a young Martian bedrock of the Middle Amazonian time. The nakhlites have similar mineralogy and bulk chemical composition (Treiman, 2005). They all contain mm-sized euhedral to subhedral prisms of augite, the dominant mineral phase (Bunch and Reid, 1975; Berkley et al., 1980). The augite phenocrysts display large homogeneous cores and are normally zoned with thin rims enriched in Fe. Olivine are in the form of subhedral to euhedral grains. They are slightly larger than the augite phenocrysts and enriched in Fe relative to augite. Glassy, mono- and poly-mineralic inclusions are common in olivine phenocrysts but rarer in augite. The last-formed interstitial material contains plagioclase, K-felsdpar, olivine, augite, Ti-magnetite, Cl-apatite, and rare silica and pyrrhotite (Treiman, 2005). Modal abundances of the different mineral phases in the nakhlites range approximately from 68-81 % augite, 3-16 % olivine, and 8-21 % mesostasis (Treiman, 2005).

The texture of the nakhlites, an excess of augite embedded in a finely crystalline mesostase, suggests a two-stage crystallization history with an early formation of the homogeneous augite phenocrysts in a slowly cooled sub-surface magmatic environment prior to final extrusion/intrusion of the augite-bearing magma at or near the surface (Berkley et al., 1980; Imae et al., 2005). Post-emplacement accumulation of subcalcic augite within thick lava flow(s) or shallow sill(s) were an important process in the nakhlite formation, as it has formed the porphyritic texture and structure of the rocks. Sub-solidus diffusional re-equilibrium of the cumulus augite with the late inter-cumulus melt was also an important magmatic process as it has re-distributed chemical elements and modified the chemistry of the liquidus phases (Imae et al., 2005). It is largely believed that the nakhlites once at or near the surface cooled down at different rates. The various cooling rate experienced by the nakhlites in their final emplacement is thought to be responsible for the wide range of texture of the rocks' matrix and the degree to which the different rocks were affected by sub-solidus chemical re-equilibration. Variations in the petrographic and mineralogic properties of the nakhlites are believed to be the sole result of post-emplacement magmatic processes (Mikouchi et al., 2012).

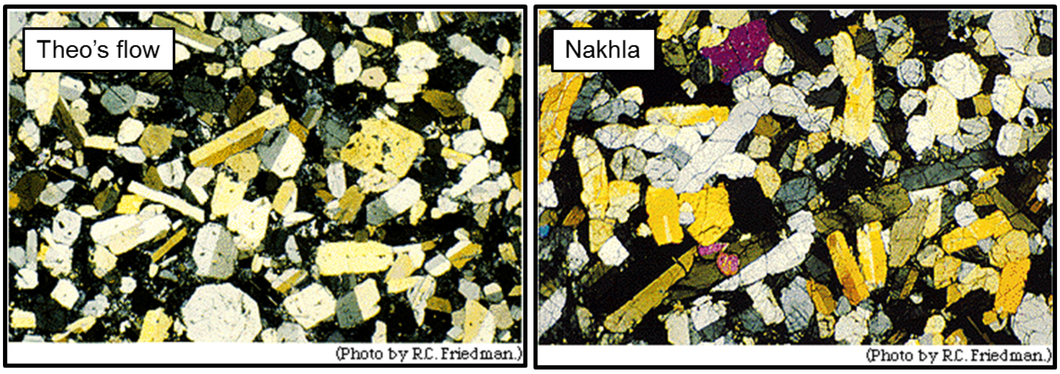

*Fig. 1.5: Photographs of a thin section of the Theo's Flow pyroxenite layer and Nakhla taken from Friedman-Lentz et al. (1999). The textural and mineralogical similarity between both rocks suggest that the nakhlites may have formed in a similar environment, a thick cumulate pile emplaced in a sub-surface environment.*

The mineralogy of the nakhlites, a predominance of augite and olivine phenocrysts with interstitial plagioclase and Fe-Ti oxides, is identical to the mineralogy of terrestrial basalt including pyroxenites from the Archean greenstone belts such as Theo's Flow, Ontario, Canada (Reid and Bunch, 1975; Berkley et al., 1980; Treiman, 1987; Friedman-Lentz et al., 1999). Theo's flow comprises a subsurface pyroxenite layer 60 m-thick with petrographic features astonishingly similar to the nakhlite meteorites (Fig. 1.5). This has led to the conclusion that the nakhlites formed in a similar magmatic environment, possibly from a single Martian basaltic intrusion/lava flow a few tens of meter-thick. A further argument for the cumulate pile model is the variations in petrographic and mineralogic properties which could reflect the structural and chemical variability (or depth profiling) of a shallow differentiated igneous body (Harvey and McSween, 1992; Mikouchi et al., 2012). Based on these property variations, Mikouchi et al. (2012) and Jambon et al. (2010) suggested a likely relative burial depth of the different meteorites (from top to bottom): NWA 5790 MIL 03346, NWA 817, Y 000593, Y 000749, Nakhla, GV, Lafayette, and NWA 998 (Fig. 1.6).

There is no petrological evidence that the nakhlites experienced any late-magmatic metasomatism or post-magmatic metamorphism (Berkley et al., 1980; Stoffler, 2000). However, most nakhlites contain traces of secondary minerals deposited from aqueous fluids (Reid and Bunch, 1975; Tomkinson et al., 2015). Petrographic and microstratigraphic relationships provide evidence that at least some precipitated on Mars (Gooding et al., 1991; Treiman, 1993). The alteration mineral assemblages in different nakhlites have been dated at ∽ 633 ± 23 Ma (Borg and Drake, 2005). The young age of the secondary minerals argues against an association of the aqueous fluids with the magmatic event that crystallized the nakhlites ∽ 1.3 Ga ago. Textural investigations of the assemblage of alteration minerals suggest that they most probably precipitated from aqueous fluids during low temperature secondary processing (Bridges and Grady, 2001; Velbel, 2012).

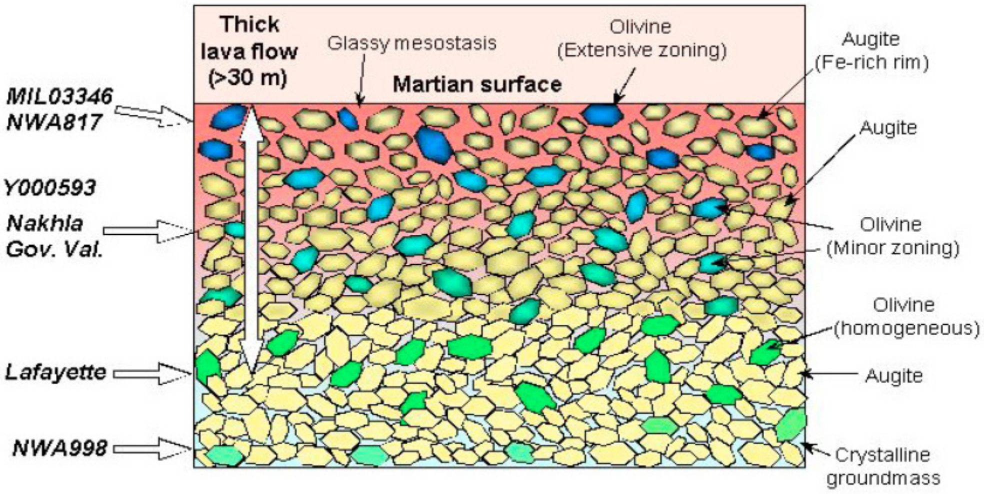

*Fig. 1.6: Cumulate pile model of Mikouchi et al. (2012) showing the relative stratigraphic position of the nakhlites based on proportion of olivine, augite and rock matrix and mineral zoning.*

The last important event in the nakhlites history was probably their ejection from Mars by impacts of meteorite a few Ma ago. The impact-launch event(s) only had few physical effects on the nakhlites including minor shock features such as micro-fractures, undulatory extinction of augite and olivine, and lamellar shock twins in augite (Berkley et al., 1980; Stoffler, 2000). However they probably had no effects on the chemistry of the rocks with the exception of shock-implantation of Martian atmospheric gases (Gilmour et al., 1999; Gilmour and Turner, 2001). The nakhlite meteorites landed on Earth relatively recently, a few thousand of years maximum, but have undeniably interacted with the terrestrial environments (Treiman, 2005). Although poorly documented, the nakhlites were subjected to terrestrial weathering processes and microbial activity (Treiman, 1993; Tomkinson et al., 2015).

## *1.3 Thesis context and outline*

### *1.3.1 Determination of science questions, aims and limitations*

The first aim of this project was to investigate, with as much details as possible, the petrography of a large set of nakhlite meteorites to test our current understanding the geological history and context of the rocks. These included the rocks petrogenesis, their composition, texture and mineralogy to better constrain the magmatic activity of Mars during the Middle Amazonian and deep and shallow magmatic processes at the origin of the rocks. As rocks formed in a sub-surface environment that experienced aqueous alteration, the nakhlites can further provide information about the superficial environmental conditions of Mars during the Late Amazonian with implications on the evolution of the hydrosphere, cryosphere and atmosphere of the planet. The elemental and mineralogical information of the water-rich system of Mars recorded in the secondary mineral assemblage of the nakhlites and their interpretations can provide important clues on the geological context under which aqueous environments existed in the Martian sub-surface in a recent past and on the possibility of Mars to have sustained crustal environments favourable to development of life. Therefore, the second part of this thesis aims at identifying and characterizing the mineralogy and chemistry of the secondary minerals deposited during aqueous fluids infiltration in the rocks.

#### *Refining the magmatic history and processes at the origin of the nakhlites*

The nakhlites have a similar mineralogy dominated by sub-calcic clinopyroxene, ferroan olivine and sodic plagioclase, and almost identical isotopic composition that distinguish them from other Martian meteorites (McSween, 2008). The nakhlites are most probably samples of a same volcanic complex fed by a unique mantle source region. Current models based on comparative petrology (Friedman-Lentz et al., 1999; Jambon et al., 2010; Mikouchi et al., 2012) suggest that the meteorites may have crystallized within a single sub-surface igneous body, while variations in volumetric abundances and composition of olivine, pyroxene and mesostasis between the meteorites is believed to reflect the internal structure of the thick differentiated cumulate pile; although the rocks may have formed from several related and similarly structured igneous bodies. Do the nakhlites really represent the final product of a "random" impulse of magma from the deep mantle that emplaced and differentiated as a single or multiple igneous bodies or are they the product of a magmatic center that was active for a longer period of time and erupted relatively contemporary repeated pulses of magma? Establishing the exact petrolgenetic link between the meteorites and identifying the possible number of magmas at the origin of the nakhlite suites remain a daunting task mostly because of the cumulate nature of the rocks and the various degree of sub-solidus re-equilibration processes that experienced olivine and pyroxene within and between the nakhlites. However, better understanding the true magmatic relationship of the nakhlites is critical for understanding of the young magmatic activity of Mars including relative timing and duration of magmatic events.

The first science questions being addressed by this project deals with the petrogenetic relationship between the meteorites including the identification of some compositional characteristics of the parent magma at the origin of the individual nakhlites and possible variations in the physico-chemical state of these magmas. To shed some light onto the magmatic activity of Mars during the middle Amazonian, the crystallization history of a large number of nakhlites have been re-examined and the composition of the different igneous minerals re-measured. Identifying distinctive mineral compositions could allow to discriminate between an evolution of the nakhlites suite through fractional crystallization-differentiation processes (single magma batch) supporting a genetic relationship (Mikouchi et al., 2012) or through mantle source processes (multiple batches) supporting a magmatic center volcanically active for a longer period of time.

A comparison of various mineral compositions and zonation patterns between the nakhlites outlines some clear differences that seem incompatible with a formation of the nakhlites from a large magma body experiencing intense fractional crystallization processes in the shallow magmatic environment, although care has to be taken because the small number of mineral grains analysed within and between the meteorites cannot represent the full range of mineral composition in each nakhlites. Other petrographic features (i.g. melt inclusion assemblages and composition and degree of chemical/mineralogical homogeneity of the feldspathic mesostasis, etc.) point also towards a crystallization of the individual nakhlites from multiple batches with each their own chemical properties and crystallization history. Nevertheless, variations in mineral chemistry can also result because of differences in the physical conditions (e.g. pressure, temperature, oxygen fugacity, etc.) in the magmatic environment. Hence, distinguishing between shallow magmatic processes and deep source-controlled variations (i.e. single *vs.* multiple partial melting events) requires to know the physical conditions and evolution under which the rocks crystallized. In particular, evaluation of the oxidation state and thermal history of the rocks is critical to interpret the chemistry of the liquidus phases; both remain today poorly constrained.

In order to gain new insights into the thermal history, crystallization conditions and general geological context of the nakhlites, I have thought about reconstructing the thermal history of one of the nakhlites (NWA 998) using the oxide silicate equilibria geothermometer QUILF (Quartz-Ilmenite-Fayalite and derivative) of Anderson et al. (1993), a program obtained from personal communication with one of the co-authors of the program. North West Africa (NWA) 998 is particularly well suited for such determination as it is fully crystallized and was subject to lengthy and slow crystallization such that various mineral phases have remained at subsolidus temperature for a sufficient length of time to experience intra-crystalline diffusion and exsolve more ordered mineral structure in the form of lamellae. For example, augite rims contain pigeonite lamellae while titanomagnetite display a tweed pattern of ilmenite exsolution. Furthermore, the rock has remained near solidus temperature after almost complete crystallization which has destabilized the initial stable mineral association and triggered a partial recrystallization (or mineralogical re-equilibration) of the rock. The three mineralogical transformations that occurred at specific stages of crystallization (from early crystallization of augite, to latter mesostasis solidification with oxide formation to finally recrystallization involving the last reactive melt along grain boundaries) provide a good opportunity to put some constraints about the thermal history of NWA 998 during crystallization.

Geothermometry relies upon the fact that minerals vary their compositions as a function of temperature, although there are other factors and assumptions to consider (such as oxygen fugacity, pressure, water activity, etc.). The method of measuring the temperature of mineral formation relying on chemical equilibrium between mineral pairs/assemblages depend on our capacity of measuring the chemical composition of the individual minerals. The principal difficulty with measuring chemical composition of the mineral of interest in NWA 998 is the size of the lamellaes. A possibility was to use a Transmission Electron Microscopy (TEM) combining both EDX and EELS methods (assuming the availability of standards). Even if no accurate and precise values would have been obtained, an idea about the right chemical composition could have been determined allowing a structural formula for the individual minerals to be established. Furthermore, a proper determination of structural formula for the individual minerals involved in the late mineralogical re-equilibration of the rock could also have served for determining (through mass balanced calculation) the chemical composition of the last reactive silicate melt. Unfortunately, the incapacity to get sufficient time on the TEM (only two days) has not allowed the measurement of the mineral of interests to be performed.

### *Understanding of a young Martian aquifer from the nakhlites secondary mineralogy*

In addition to providing information about the magmatic activity and the formation and properties of a young basaltic crust of Mars, the nakhlites with their secondary minerals that can only have formed from aqueous fluids give a unique opportunity to investigate the nature of a young water-rich environment of Mars. Understanding how and where aqueous environments existed in a recent past on Mars despite its apparent dryness and unfavourable physical conditions together with determining the nature and possible source reservoirs of the aqueous fluids remain today amongst the biggest scientific questions and major goal of Mars scientific exploration. Furthermore, determining the environmental conditions for aqueous alteration and geological context of the water-rich system of Mars are critical for assessing the extent and timing for possible life on Mars or at least possible environments favourable to the development of life as we know it (Des Marais et al., 2008).

The second science question being addressed by this thesis focuses on the nature, dynamic and geological history of the young Martian aquifer sampled by the nakhlites. A better characterization of the groundwater system on Mars could provide clues about how and where water (or traces of recent water activity) can be found in the young regolith of Mars, which is of fundamental importance for the future Mars sample return missions. It could also serve to predict how commonplace aqueous environments may have been on Mars and be useful for astrobiological models which depend on where, when, how and for how long water was present in Mars sub-surface. With this in mind, we have performed detailed textural, mineralogical and chemical investigations of the fluid-rock interactions in the hope of better understanding the groundwater system of the nakhlites, its chemistry and evolution in both space and time. The specific approach was to use evidence from the secondary mineralogy and chemistry to determine (1) how the aqueous fluids circulated into the nakhlite bedrock (i.e. through natural porosity, shocked fractures or by dissolution of the rock-forming mineral), (2) the relative life time of the aqueous solutions (i.e. single *vs.* multiple water pulses) in the nakhlites bedrock, (3) the origin of the solutes (i.e. brought into the bedrock with the fluids or derived from the nakhlites host rock), and (4) the structure and physoco-chemical properties of the groundwater system.

Aqueous alteration has modified the elemental and mineralogical composition of the nakhlites. A key requirement to understand aqueous alteration is the identification of mineral phases that precipitated from the aqueous fluids (Ming et al., 2007). The geological processes responsible for the deposition of secondary minerals in the nakhlites can be then compared to analogue processes on Earth where similar weathering products are formed and aqueous environments better understood. A variety of chemical and mineralogical indicators of aqueous alteration processes (including sulphate, siderite, halite, smectite, hematite/goethite and silica) have been identified, mostly as replacive products of olivine. They form bands with each their own texture and chemistry suggesting a deposition over discreet aqueous events. The extent of alteration and the nature of the mineral phases that precipitate depend on whether the rocks are altered in a closed or open system and the water-to-rock ratio (Ming et al., 2007). Preliminary results reveal that the altered materials in the nakhlites have a similar chemical composition than their host olivine (plus ionic compounds) suggesting an alteration from brines in closed aqueous system (except for the infiltration of aqueous fluids) and/or a low water-to-rock ratio incapable to transport solutes gained from in situ chemical reactions. The existence of phyllosilicates, carbonates, sulphates and halides in the nakhlites provides evidence for very different aqueous conditions during the late Amazonian, which may have a critical impact on the possibility of development of life on Mars.

The apparent decrease in volumetric abundance and distribution of carbonate, sulphate and halite minerals in the nakhlites suggest that they may represent the progressive crystallization path of the Martian solutions upon evaporation. However, not all meteorites contain the whole mineralogical assemblage while carbonate and sulphate have not been found inter-mixed together providing evidence for a sharp stratification of the aqueous solutions in the Martian sub-surface. Further detailed investigations of the distribution of carbonate and sulphate minerals are required to identify if they represent the solidified products of a same brine that evolved in space and time through continuous evaporative precipitation or various brines of different origin and geological history. A possibility would be to track the distribution of both mineral phases in the bulk rocks using computed tomography. Furthermore, determination of the true nature of the sulphate minerals in this study has not been established mostly because of the lack of time on the TEM. This undeniably need to be done especially since sulphate of terrestrial origin have also been clearly identified in the rocks (Hallis, 2013).

### *1.3.2 Sample set*

To complete this research project, a suite of seven different nakhlite meteorites (including two paired) have been assembled. They form probably the most comprehensible set of nakhlite meteorites ever assembled for a research project on the nakhlites. They include Lafayette (a thin section and separate grains of olivine and pyroxene), Nakhla (a series of grain mounts and separate grains), MIL 03346 (a

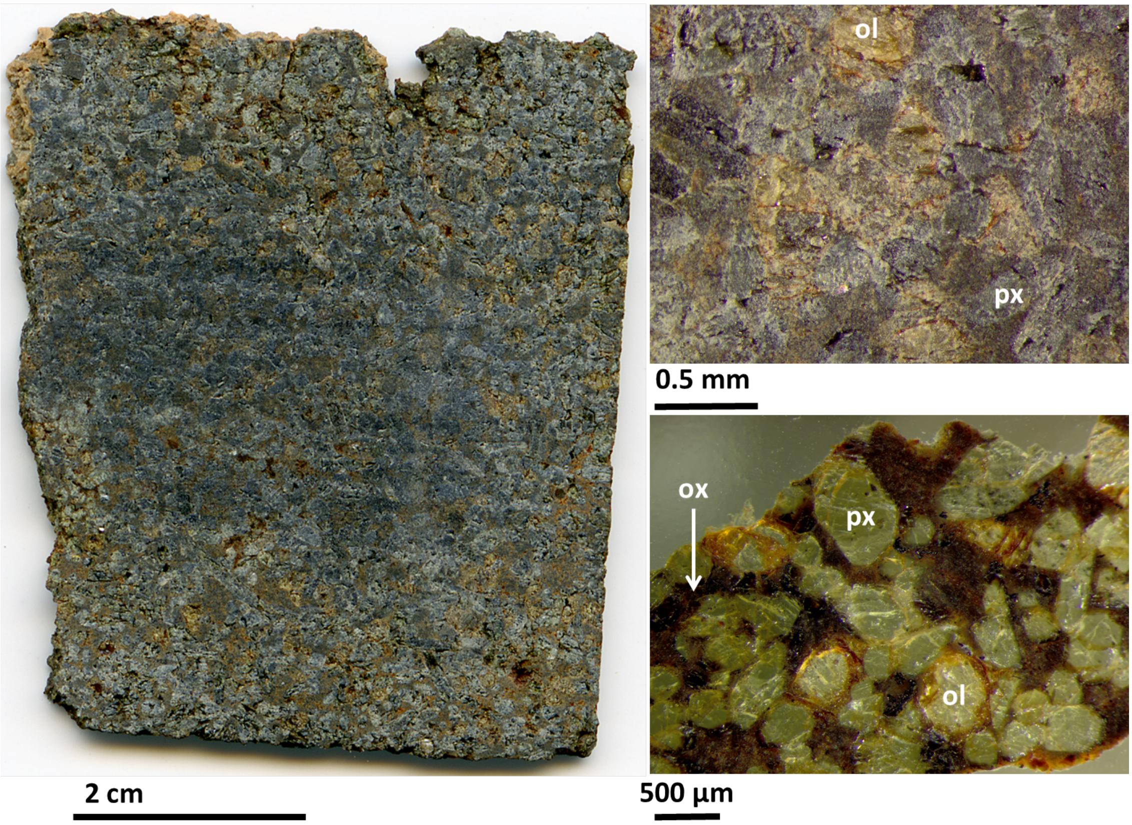

*Fig. 1.7: Photograph and photomicrograpgh of NWA 817 taken with a visible light microscope (reflective light). The brownish-yellowish product on the photograph are secondary minerals, easily recognisable with their natural porosity. Pyroxene (px) have a green color while olivine (ol) have a yellowish-greenish color due to alteration. The dark crystals in the mesostasis are Fe-oxides/sulfides.*

thin section and rock sample), Y 000749 and paired Y 000593 (several grain slices and rock sample), NWA 5790 (a large rock slice and rock sample), NWA 817 (a slice of rock sample) and NWA 998 (a rock sample). The meteorites have either been donated or are on loan, at the exception of NWA 817 and NWA 998 which have been purchased by Martin Lee from personal funds. Pictures of some of the material used in this study are provided on Fig. 1.7, 1.8, 1.9 and 1.10. In addition, BSE images of all the nakhlites analysed in this project are presented on Fig. 1.11 in their relative stratigraphic position in the cumulate pile model of Mikouchi et al. (2012).

### *1.3.3 Thesis outline*

This thesis initially describes the theory and methods used for the microanalysis of the set of nakhlite meteorites described above. The detailed petrographic investigation of the nakhlites were performed using electron microscopic techniques including a Scanning Electron Microscope (SEM) and a Transmission Electron Microscope (TEM) (chapter 2). The SEM is a method of choice to observe and characterize very fine texture and mineral properties. It has enabled us to obtain a variety of

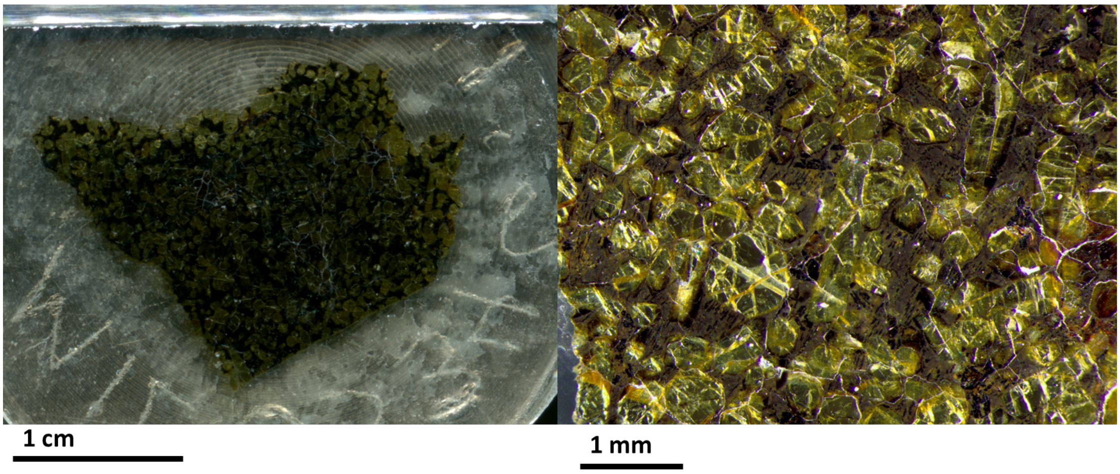

*Fig. 1.8: Photograph and photomicrograpgh of MIL 03346 taken with a visible light microscope (reflective light). The large green crystals are pyroxene while the dark crystals in the mesostasis are Fe-oxides/sulfides.*

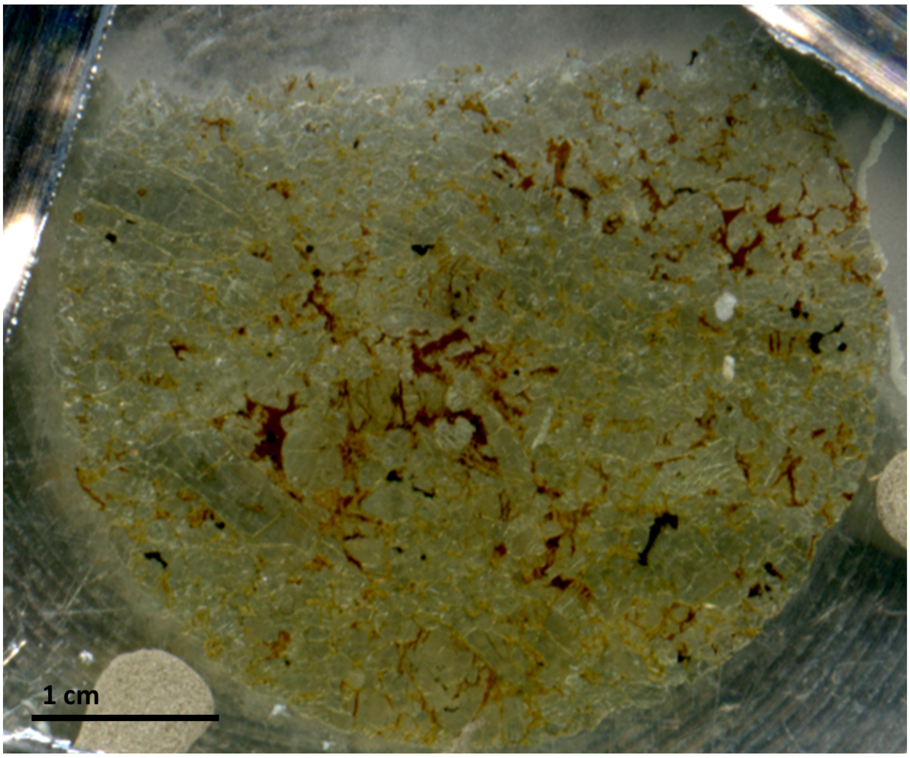

*Fig. 1.9: Photomicrograph of our thin section of lafayette. The green crystals are pyroxene and olivine. The brown product surrounding the crystals are alteration products while the dark grains are Fe-oxides/sulfides.*

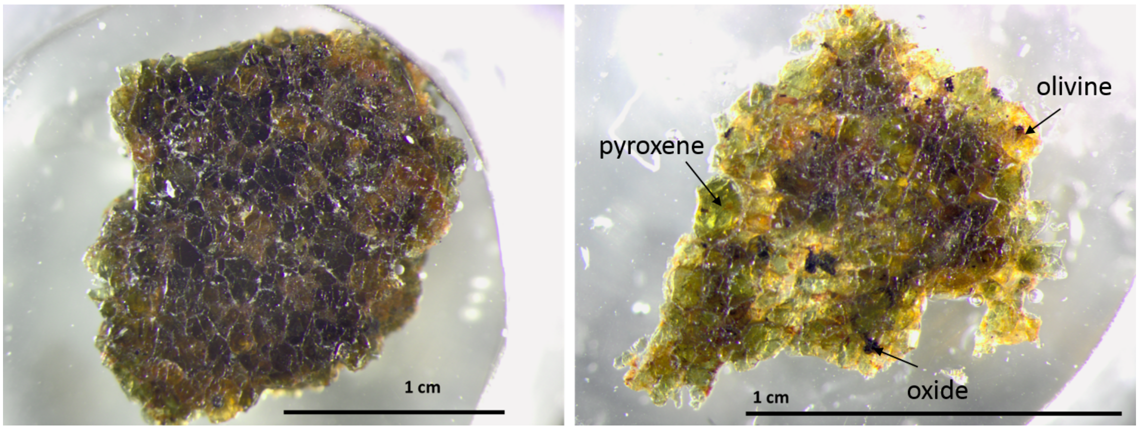

*Fig. 1.10: Photomicrograph of two polished rock mounts of NWA 998 taken with a visible light microscope (reflective light). The rock is fully crystallized. On the pictures, a distinction between pyroxene and olivine is difficult but olivine grains still appear slightly more brownish probably due to their alteration by aqueous fluids during secondary processing. The dark grains are Fe-oxides/sulfides. The brownish tint of the rock testifies of aqueous alteration.*

information about the different samples, including superficial micro-structure and topography, electron back-scattering diffraction (BSE) images, energy dispersal X-ray spectroscopy (EDS) spot component analyses and chemical maps of large sample areas. In addition to SEM studies, TEM investigations was performed to obtain information on both internal structure and chemistry of small areas of thin specimen at the nano-scale. They included the scarce and fine alteration products present in the nakhlites. No other technique can provide imaging of texture and internal structure, crystallographic information (electron Diffraction Pattern, DP), and chemical composition (EDS) simultaneously. Transmission Electron Microscope is a logical complement of the more established mineralogical instruments including the SEM.

Other laboratory techniques used in this thesis included Raman spectroscopy and Laser Ablation Inductively-Coupled Mass Spectrometry (LA ICP-MS) (chapter 3). Raman spectroscopy was used for mineralogical identification of the fine poorly crystallized alteration products. Raman spectroscopy analyses require little sample preparation and so, is a method of choice for the mineralogical identification of the fragile secondary minerals that may be easily contaminated or dissolved away during laboratory preparation. Finally, geochemical analyses of the different primary materials (including minerals and glass) forming the nakhlites were performed using a LA ICP-MS, a technique commonly used for in situ analyses of trace elements and stable isotopes. Measurements of trace element composition of the rock-forming minerals have served to identify chemical signatures of the parent melt composition and heterogeneity and deep and shallow magmatic processes at the origin of the nakhlites.

Finally, the data and interpretations of the detailed petrographic and geochemical investigation performed on the nakhlites including their primary composition, mineralogy and mineralogical properties are presented in chapter 4. Aqueous alteration of the nakhlites has led to specific changes in the elemental and mineralogical

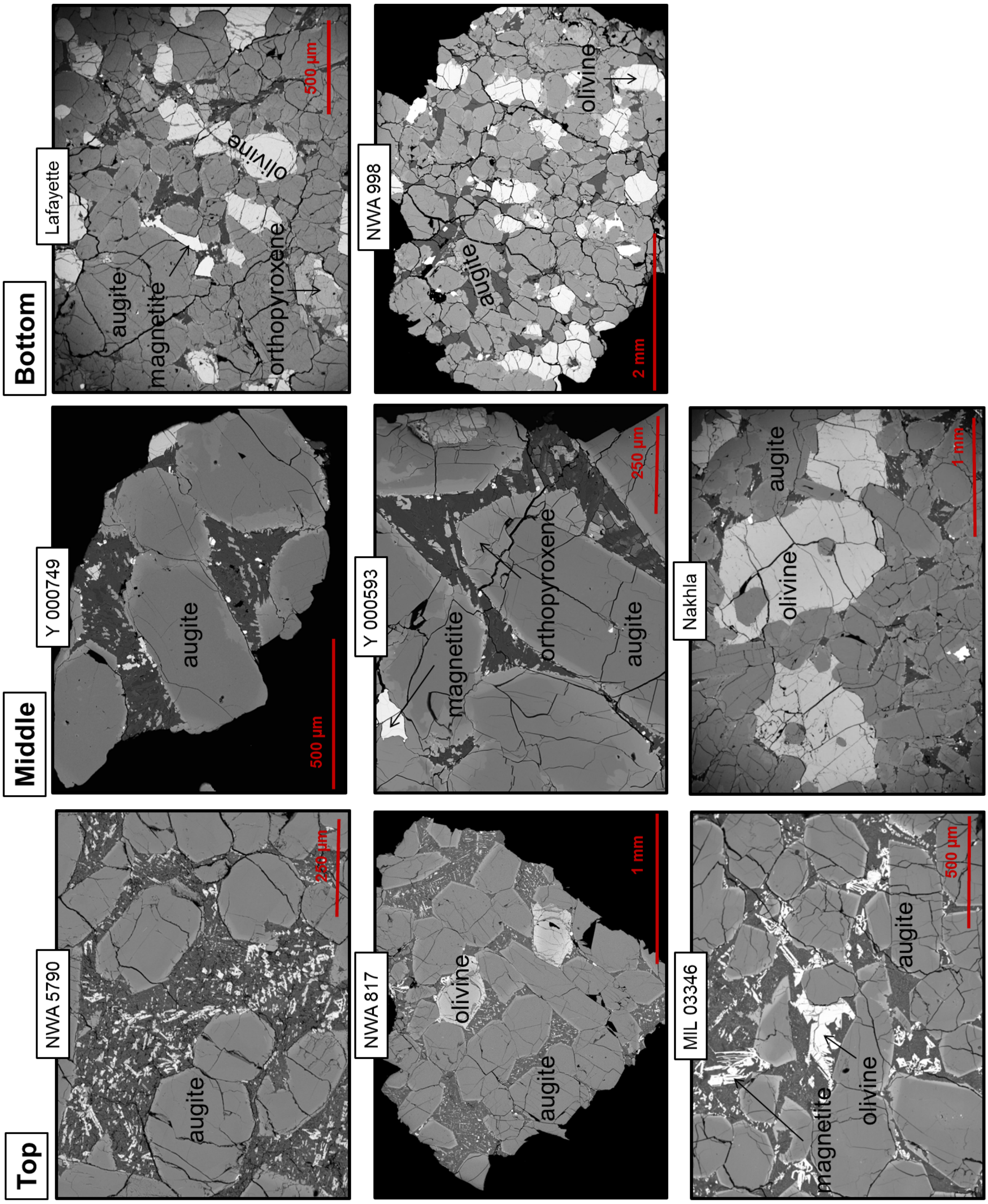

*Fig. 1.11: BSE images of the different nakhlites analysed in this study in their relative position in the cumulate pile model of Mikouchi et al. (2012).*

composition of the nakhlites that are keys for understanding the nature of an aqueous environment and conditions that existed in the Martian sub-surface in a recent past. The results and interpretations of the fluid-rock interactions that led to the deposition of the large variety of secondary minerals are presented in chapter 5. Finally, chapter 6 provides a summary of the most important findings of the nakhlites geological history from their formation to their late interaction with the Martian hydrosphere, and their implications about the general geological context of Mars during the Middle and Late Amazonian.

# 2. METHODOLOGY 1: THEORY AND APPLICATION OF ELECTRON MICROSCOPY

## *2.1 Introduction: Electron microscopy*

The most common microscopes are visible light microscopes. They use series of optical glass lenses to focus visible light reflecting off an object to produce a magnified image of this object. The power of magnification of a microscope is dependent on the wavelength of the illumination source. Objects smaller than the wavelength cannot physically interact with the waves and thus cannot be detected. Consequently, visible light microscopes cannot distinguish objects less than the wavelength of the incoming visible light, which is approximately 500 nm. To see features smaller than 500 nm, another illumination source (with shorter wavelengths) is required. In 1925, De Broglie was the first to discover the wave-like behaviour of the electrons, which have a shorter wavelength than the visible light. The first electron microscopes appeared not long afterwards and remain, to date, the most efficient tool for nano-scale characterization of material (Williams and Carter, 2009).

Two principal electron microscopes exist: the Scanning Electron Microscope (SEM) and the Transmission Electron Microscope (TEM). An SEM produces images by scanning a sample with a condensed electron beam at low energy. The electrons bounce off the surfaces of the sample, and are then detected by a sensor detector linked to a viewing screen. Therefore, SEM is a powerful technique to image the surface of a sample. Unlike SEM, TEM uses an electron beam with a sufficiently high energy to pass through the entire thickness of an ultra-thin slice of sample. During their journey, the high energy electrons are scattered by the atoms-forming material. The electrons once off the bottom surface hit a sensitive screen which produces an electron diffraction pattern representing a projection of the sample's internal atomic structure. Both electron microscopes are based on the principle of interaction between electrons and matter. However, the different microscopes have been set up to interact with a sample using the different properties of the electrons (i.e. wave and particle behaviour) and detect different signals released during electron-matter interactions. Electron microscopy is commonly used to obtain different information of the sample material such as its structure, topology, morphology, and chemical (i.e. elemental) composition. They are first choice techniques in the investigation of planetary materials because they have the advantage of being non destructive. In this chapter, the general theory about electron-matter interactions and their use in electron microscopy are described.

## 2.2 Electron-matter interactions and their application in Electron Microscopy

### 2.2.1 Introduction

Electron microscopy techniques are based on the interactions of electrons with matter. Without any interaction, no signals are generated and consequently, no sample properties can be measured. The different electron microscopy techniques have their own imaging and spectroscopic method to detect the various signals emitted during electron-matter interactions. Each signal is diagnostic of a specific physical property of a sample. However, to understand each technique, their limitation and the nature of the sample information that can be obtained, it is important to understand why and how electrons interact with matter, and what their relationships are.

### 2.2.2 The different electron-matter interactions

A bombardment of high energy electrons onto matter causes different (primary and secondary) physical processes affecting both the impinged electrons and material-forming atoms (Egerton, 2011). The primary effect is a scattering process of the incident electrons. In physic, scattering refers to the property of a particle, or subatomic particle, to be deviated from its trajectory as a result of a collision with another particle. Scattering can either be elastic or inelastic (Egerton, 2011). Elastic scattering occurs when incident electrons are highly deflected from their original trajectory by attraction of the positively charged, large mass of the atomic nuclei known as the Coulomb force. In this process, incident electrons conserve their velocity and kinetic energy. On the other hand, inelastic scattering occurs when incident electrons are slightly deviated from their original trajectory by interactions with the negatively charged, atomic electron cloud. During this process, incident electrons slow down and transfer one part of their kinetic energy to the orbital electrons of the matter-forming atoms. In order to reduce the gain in energy in the sample, different internal secondary processes occur: release of secondary electron, phonon excitation (i.e. heating), cathode-luminescence (i.e. visible light fluorescence), x-rays (i.e. characteristic radiation and continuum radiation also called Bremsstrahlung), plasmon (i.e. oscillation due to ejection of electrons), and auger electrons (i.e. ejection of electrons from the outer shell of electrons) (Fig. 2.1).

#### *Electron scattering: Surface sample imaging and elemental mapping*

Elastic and inelastic scattering results in the formation of back-scattered electrons and ejection of secondary electrons (i.e. electrons released from the sample surface). The proportion of electrons that are back-scattered, which means deflected through an angle greater than 90 degree, is strongly related to the atomic number (Z) of the target atom. An increase of the mass of the atomic target nuclei (i.e. Z) increases the strength of electron interactions with the atomic nuclei and thus the probability of high-angle deflection and high energy of spherical distribution of the incident electrons. Hence, heavy elements (with their high atomic number) more strongly back-scatter the incident electrons than light elements (with their low

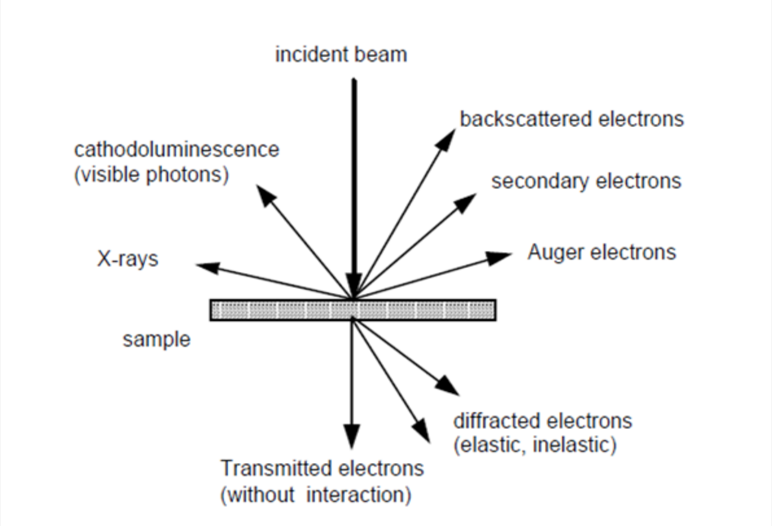

*Fig. 2.1: Signals generated during electron-matter interactions (unknown author). Primary processes include diffraction and backscattering of electrons from the electron beam while secondary processes comprise the generation of secondary and auger electrons, X-rays and cathodoluminescence.*

atomic number). Backscattered electrons are used in electron microscopy to image elemental variations of a sample surface. Contrary to back-scattered (incident) electrons, secondary electrons are electrons that originally belong to the sample. They are physically ejected from it by collision with high energy incident electrons (Fig. 2.2).

Because of their low energy, secondary electrons can only be released from the sample within the first nm of the surface sample, either by the colliding incident electrons or the escaping back-scattered electrons. Consequently, the number of secondary electron released is dependent on the surface of activation. At the contact with the electron beam, a certain number of secondary electrons are released. If the sample's surfaces are flat, then no variation in the number of secondary electrons escaped occurs. However, if the sample's surfaces present an angle relative to the electron beam, so the surface of activation will be larger below the electron beam, more secondary electrons will be released. This gives rise to secondary electron density contrast images that represent the sample topology (Fig. 2.3).

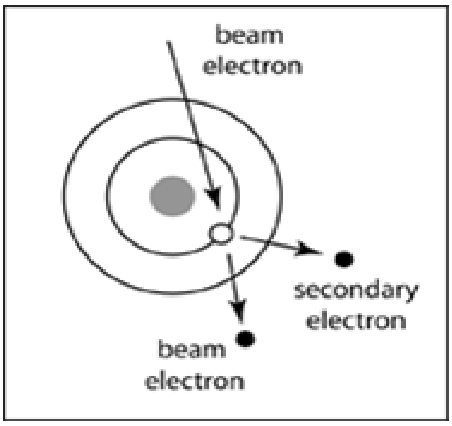

*Fig. 2.2: Physical interaction between an electron beam and the electron cloud of an atom. The electron from the electron cloud is ejected while the beam electron is deflected from its initial trajectory, (http://mcswiggen.com).*

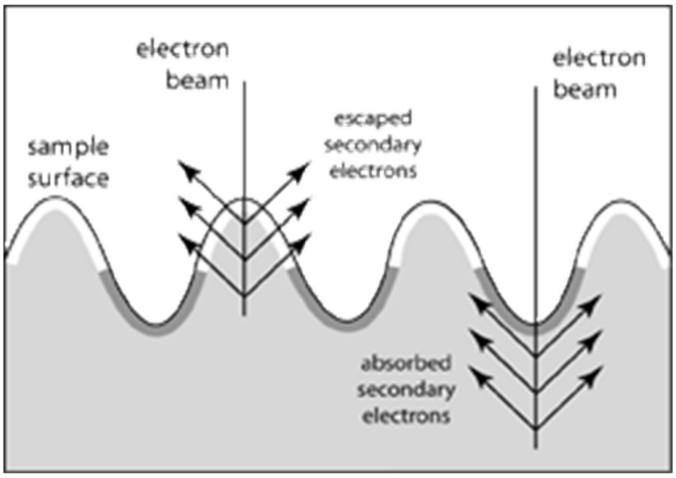

*Fig. 2.3: Effect of topography on the release of secondary electrons from the surface of a sample. Topographic highs appear brighter on virtual images because more secondary electrons are released (greater surface) which saturates the detector screen, whereas topographic lows appear darker because the secondary electrons are absorbed by the sample (http://mcswiggen.com).*

### *X-rays emission: elemental analyses*

The motion of high energy electrons through the strong electric field of an atom does not only deflect the incident electrons, but also produces the emission of both characteristic X-rays and continuous X-ray photons (i.e. Bremsstrahlung). Characteristic x-rays correspond to the energy released by electron shell transitions, when high energy incident electrons dislodge atomic electrons from inner electron shells, leaving a vacancy that is instantaneously replenished by an electron from an outer-shell. Atom ionisation by the loss of an inner-shell electron is the essential process responsible for the emission of characteristic X-ray photons. It requires an incident electron energy superior to the excitation energy needed for ionising the electron in the inner shell and varies approximately with $Z^2$. Hence, emitted X-ray photons have characteristic energy (with characteristic wavelength) for each atom, which makes the X-ray photons suitable for elemental analysis. On the other hand, Bremsstrahlung X-rays are emitted because of the decrease (or quantum jump) of the electron energy. The bremsstrahlung X-rays are undesirable as they may interfere and add themselves onto the spectrum of characteristic X-rays, which limits the detection of elements present in low concentration (Egerton, 2011).

### *Other secondary processes*

The energy released because of the high energy electron beam bombardment is not always expressed by the emission of X-ray photons, but sometimes is accompanied by the ejection of the other bound electron, called the Auger electron. The Auger effect tends to increase (at the expense of X-rays emission) with increasing Z. Certain non-metallic, semi-conductor samples emit photons with wavelength in the visible spectrum light by a phenomenon called Cathodo-Luminescence (CL). The photon emission corresponds to the dissipation of energy created by the ejection of an atomic electron (leaving a“hole”) from the valence band into the conduction band and a subsequent recombination of the ejected electron and the“hole”. In solid material, the valence band corresponds to the highest range of electron energies, the outer electron shell that is filled with electrons at absolute zero, while the conduction band corresponds to unfilled bands, where electrons are not binding with its atom but are free to move within the atomic lattice of a material. Both Auger electron and Cathodo-Luminescence are used in microscopy for surface sample imaging. All the secondary processes are commonly accompanied with gain and loss of energy of the target atom that are accommodated through phonon release that heat up the sample.

## 2.3 Scanning Electron Microscopy (SEM)

### 2.3.1 Introduction

Scanning Electron Microscopy (SEM) has especially been designed for sample surface imaging, although they are commonly coupled with an x-ray spectrometer for element imaging and analysis. Virtual images are created by scanning an electron beam over a sample and displaying the released signals, including backscattered or secondary electrons, onto an electron detector linked to a TV screen and computer monitor. Images can either be topographic (with a resolution better than 10 nm) or compositional (with a resolution better than 100 nm) according to the detector mode selected for imaging (Reed, 2005). The different detector modes have different applications. Acquisition of compositional images results from the detection of Back-Scattered Electrons (BSE), electrons that are deflected by elastic collision with atom nuclei at or close to the sample’s surface. The backscattered signal is a direct function of the mean atomic number Z of the sample’s target (Blundy and Cashman, 2009) (Reed, 2005). Therefore, the BSE mode (BSEM) is an excellent technique for mapping Z variation (i.e. elemental composition) at a sample’s surface, such as chemical zoning, although BSEM cannot differentiate minerals with similar or overlapping Z values. Topographic images are produced by the ejection of low energy Secondary Electrons (SE) from the K-shell of the specimen atoms from the surface.

### 2.3.2 SEM instrument

A conventional SEM consists (from top to bottom) of an electron gun generating and accelerating the electrons to 1-30 KV, a series of electromagnetic lenses and apertures to focus the electron beam, a sample chamber comprising a specimen holder and stage (operating in a vacuum system), and a signal detector and processing system (Fig. 2.4). An SEM is commonly coupled with an x-ray spectrometer, either an Energy Dispersive x-ray spectrometer (EDS) and/or a Wavelength Dispersive x-ray Spectrometer (WDS), which enables the user to obtain chemical spot analyses or maps.

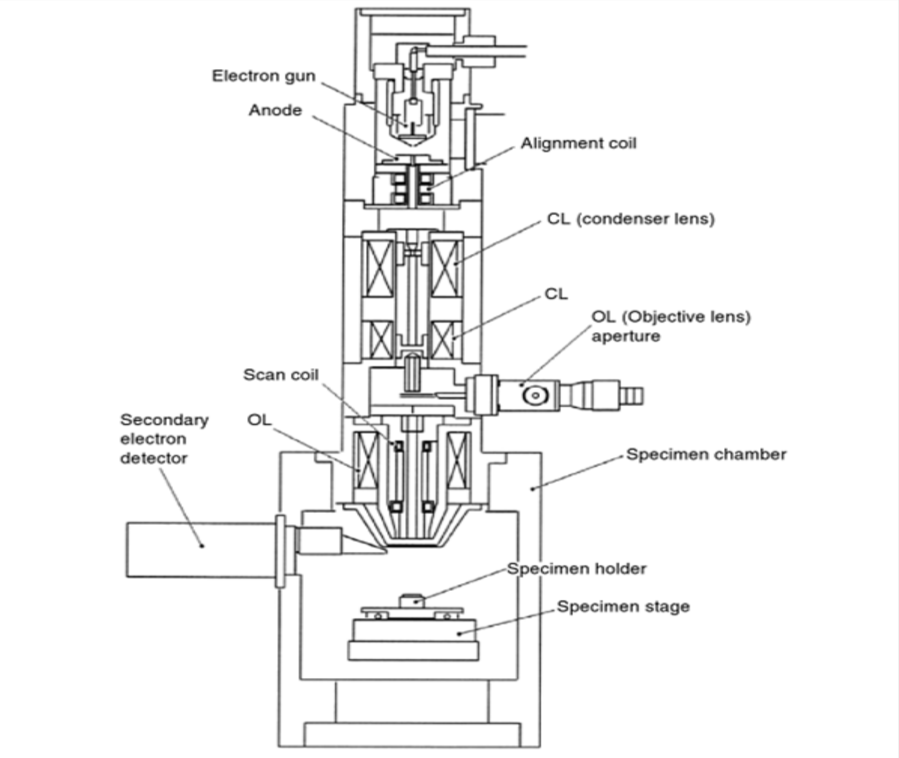

*Fig. 2.4: Schema of an SEM with its different components (unknown author).*

### 2.3.3 SEM sample requirement and preparation

SEM investigations do not require a particularly special sample preparation but only the use of a small amount of material (thin sections or blocks of material mounted in resin) properly polished to minimise secondary excitation processes and topographic effects. Sample roughness may prevent the signals from reaching the detectors or may release excessive signals from the top edges of topographic highs, which decrease the image quality. Samples composed of insulating material, such as most geologic materials, are subject to electrostatic charging once exposed to the high energy electron beam. The sample's surface gets negatively charged, which repulses the incident electrons, resulting in a poor image quality. To prevent a specimen charging, a thin coating (typically 10-20 nm) of metal (gold or chromium) or carbon can be applied on the sample surface. However, if the coating is undesirable, SEM investigations can also be performed at low-voltage (i.e. environmental mode). This reduces the charging of the specimen surface but increases the chromatic-aberration by enlarging the electron beam diameter (Egerton, 2011).

The SEM technique has many advantages, especially the minimal sample preparation (which limits the possibility of sample damage), and the ability to image a large area of a sample. However, the spatial resolution of an SEM is large relative to the atomic structure (with a volume of interaction of 5 $\mu$m$^3$), and thus limited for many mineralogical features such as chemical analyses of nm-scale exsolution lamellae or clay minerals.

### 2.3.4 Electron Backscattered Diffraction (EBSD)

Electron Back-scattered Diffraction (EBSD) is a technique associated with the SEM. It is commonly used to provide crystallographic orientation over large sample areas. EBSD uses the electrons that have been backscattered form the uppermost surface layer of a sample to generate diffraction patterns known as kikuchi patterns. To obtain EBSD data, a highly polished sample is tilted to an angle of 20 ° relative to the incident beam (Fig. 2.5). Because of the interactions with the crystal lattice of a sample, incident electrons are diffracted in different orientation. The presence at short distance from the sample of a phosphorous screen on a camera detector enables it to intersect the diffracted electrons and convert their colliding energy into light whose signal is transferred into a camera to generate a diffraction pattern (Fig. 2.6).

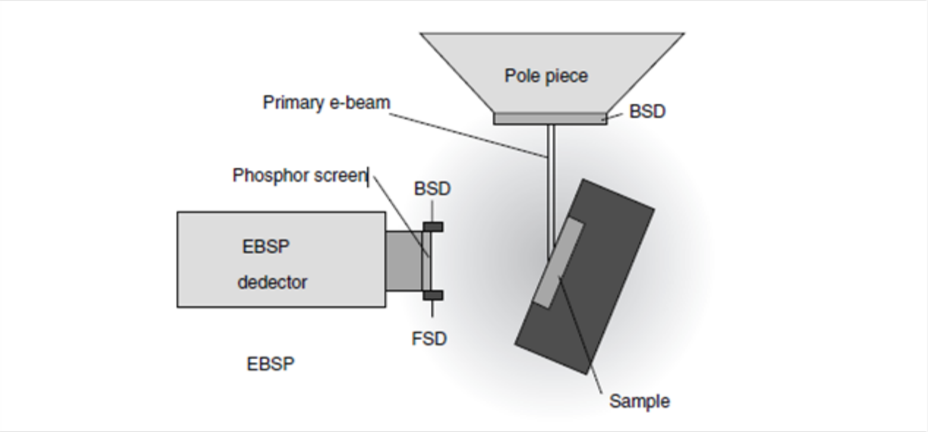

*Fig. 2.5: Schematic arrangement of a sample in an SEM for EBSD analyses relative to principal constituents. BSD: Back-Scatter Detector, FSD: Fore-Scatter Detector (Schwartz et al., 2010).*

The electron backscattered patterns or kikuchi lines (Fig. 2.6) depend on the lattice parameters, the crystal orientation, the wavelength of the incident electrons, and the distance sample-detector. Kikuchi bands are representations of different reflecting atomic planes of the crystal target, which taken together define the orientation of the crystal lattice. The width and intensity of the bands are functions of the atom spacing, while the angles between the bands represent the angles between the crystallographic planes (commonly known as $d$). Specific software using Hough transform then allows analysis of the diffraction patterns, and provided that the crystal phase is known, to determine the crystal orientation by comparing the measured inter-planar angles (or angles between the kikuchi bands) and inter-planar spacing (band widths); a process called crystallographic indexing (Kunze et al., 1993).

A great variety of analyses can be performed with EBSD technique, from grain size analysis to crystallographic orientation with different modes of micro-structural visualization. Analysis of grain size distribution is based on the fact that neighbouring crystals (of a same or different phase) have different crystallographic orientation. Grain boundaries are commonly determined from a difference in angle above 2-5 degree between two crystal neighbours, although high speed mapping may result in a higher limit of detection of angular difference. For more information see Maitland and Sitzman (2007) and Stojakovic (2012).

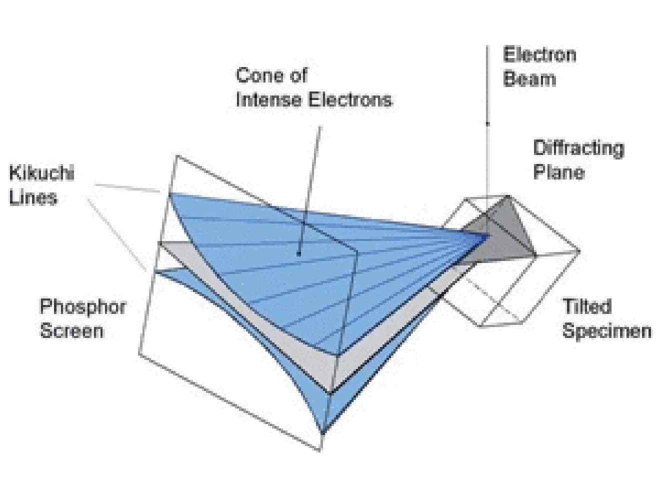

*Fig. 2.6: Trace of diffraction cones or Kikuchi lines on a phosphorous screen generated during interactions of an electron beam with a sample's atomic plane or diffraction plane (Schwartz et al., 2010).*

### 2.3.5 Qualitative and quantitative analyses using Energy Dispersive X-ray Spectroscopy

#### Qualitative analyses

Interaction of an electron beam with a sample produces different types of emissions including X-rays. These characteristic X-rays of the different chemical elements present in the sample can be detected and separated using an Energy Dispersive X-ray detector (EDS) and software to generate an energy spectrum (Fig. 2.7). At a given energy (usually ranging from 0 to 30 KeV), elements with Z higher than carbon can be identified if their peak intensities correspond to their transition lines present in the spectrum, unless they are trace elements (with concentration usually less than 1 wt%). The concentration dependence on the height of the peak intensities allows determination of the relative abundance of the main major elements constituting the material. EDS is commonly used to identify the rough chemical composition of a sample at a spot size of few microns and to create elemental mapping.

#### Quantitative analyses

From the X-ray spectrum, quantitative analysis can be calculated. This is feasible because the peak intensities of elements are proportional to their relative proportions in the sample. To obtain quantitative analysis, the unknown concentration of an element ($C_{\text{unknown}}$) within a sample is compared to the known concentration of the element within a standard ($C_{\text{standard}}$) such as

$$C_{\text{unknown}} \,/\, C_{\text{standard}} = I_{\text{unknown}} \,/\, I_{\text{standard}}$$

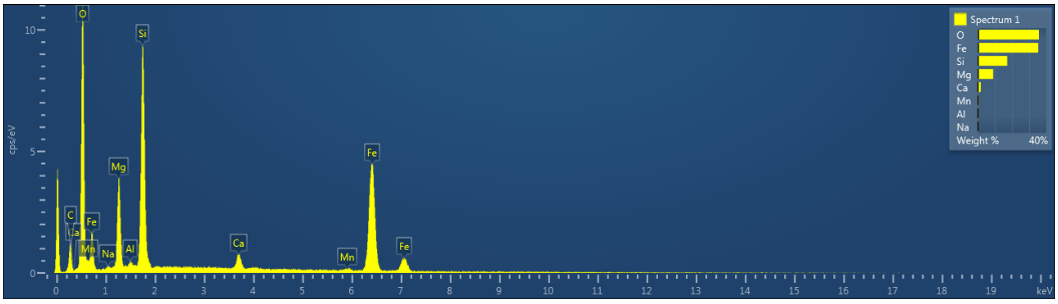

*Fig. 2.7: Example of SEM-EDX energy spectra of olivine showing characteristic x-ray peaks of its chemical components obtained with the Oxford Instruments INCA software at 20 kV.*

$$\Rightarrow C_{\text{unknown}} = C_{\text{standard}} * (I_{\text{unknown}} \,/\, I_{\text{standard}})$$

where $I$ is the measured X-ray intensity (corrected for background, peak overlap and dead time). The physical properties of the sample can also affect and modify the measured X-ray intensities. They include the atomic number (Z) of the sample, the absorption of X-rays related to the density and thickness of the sample, and secondary X-ray fluorescence. Different approaches exist to correct for these "matrix effect" such as the ZAF corrector factor. They are included in the data processing software.

### 2.3.6 SEM analyses of the nakhlites: Analytical procedure and standardization

Micro-analyses of the nakhlites were performed using a Carl Zeiss field-emission Sigma analytical Scanning Electron Microscopy (SEM) equipped with an Oxford energy dispersive microanalysis system in the School of Geographical and Earth Sciences at the University of Glasgow. Mineral compositions were determined in Energy Dispersive Spectral (EDS) mode using an accelerating potential of 20 KeV, a 1.97 nA beam current, 1 $\mu$m focussed beam size, peak counting time 60 s, and standard ZAZ correction procedures incorporated into INCA software. Natural standards were used for calibration and measured regularly to ensure data quality. Typically, detection limits were $\backsim$ 0.1 wt% for all elements except Ni (0.24 wt%). Table 2.1 shows the list of elements and respective minerals used for standardization and the detection limits of quantitative analyses.

## 2.4 Transmission Electron Microscopy (TEM)

Transmission Electron Microscopy (TEM) is a powerful analytical method for scientific investigations at the nano-scale capable of providing information about the morphology, composition and crystallography of samples (Hochella, 2002). It is a technique used for high resolution imaging and local chemical analysis. It has the ability to provide images of a sample at much higher magnification than the commonly used SEM. With the recognition that many physical and chemical properties of materials are different at the nano-scale than they are at larger scales, nano-scale investigations of geological materials have become important to better understand

| Elements | Minerals | Detection limits (wt%) |
|---|---|---|
| Na | Jadeite | 0.09 |
| Mg | Periclase | 0.07 |
| Al | Corundum | 0.07 |
| Si | Diopside | ? |
| P | Apatite | 0.10 |
| S | Pyrite | 0.10 |
| K | Orthoclase | 0.11 |
| Ca | Diopside | ? |
| Ti | Rutile | 0.16 |
| Cr | Chromite | 0.16 |
| Mn | Rhodonite | 0.15 |
| Fe | Garnet | ? |
| Ni | Ni-metal | 0.24 |

*Tab. 2.1: List of standards used for quantitative analyses standardization with detection limits. Standardization of common major and minor elements in silicate minerals was performed using natural minerals. The lack of chemical composition for diopside and garnet has prevented calculation of detection limits for Ca, Si and Fe.*

physical and chemical processes of a system of interest that may not be accessible from larger scale measurements (Hochella, 2002). The ability to combine various imaging, analytical, and diffraction techniques make the TEM a method of choice for analysing geological materials including polycrystalline materials, polyphase aggregates and polymorphic minerals. The different imaging techniques available with TEM can be used to illuminate specific areas in a sample to determine crystallographic orientation, spatial variations in atomic number (Z) and chemical composition. Electron diffraction patterns can provide information about the mineralogy and structural properties of samples, which together with chemical analyses can allow to uniquely identify and characterise geological materials.

### 2.4.1 TEM instrument

TEM is a microscopy technique which involves bombarding with an electron beam (accelerated at 100-300 KV) an ultra-thin sample such that impinged electrons pass through the sample without losing (significant) energy. Along their way through the specimen, incident electrons are diffracted by the atoms of the specimen and form (at the exit) an interference pattern that can be detected and visualized using a fluorescent screen (Williams and Carter, 2009). The phenomenon of diffraction occurs because of the wave behaviour of electrons, which gives them the ability to "bend" relative to their initial trajectory when at the proximity of charged particles. Hence, TEM relies on the wave-particle properties of electrons which are the essential mechanisms responsible for obtaining TEM data, including images, diffraction patterns (DPs) and spectroscopic data.

TEM offers different characterization techniques with a high spatial and analytical resolution, and as such is an important scientific technique to perform complete analyses of a material at atomic scale (Williams and Carter, 2009). The TEM instrument has been set up so as to obtain the best control possible on the electron beam that is responsible for the accuracy and efficiency of electron-sample interactions, and thus of the quality of emitted signals from which sample properties are measured. A TEM instrument consists of three sections (from top to bottom): an electron column, a specimen stage, and an imaging system (Egerton, 2005).

The column is composed of an electron emission source, a vacuum system where the electrons travel, and a series of electromagnetic lenses to manipulate and control the electron beam. The electron source, or“gun”, consists of a filament, a biasing circuit (voltage power supply), a wehlnelt cap (metal electrode), and an extraction anode (Fig. 2.8). The electron gun is an important part of a TEM, as it produces the electrons with the necessary properties essential for TEM investigations: brightness (current density), temporal and spatial coherency (how waves are“in step”), energy spread and size of the source (electron emitted from the same point of the source), and stability of the high voltage supply (Williams and Carter, 2009).

There are two different types of electron sources: a thermo-ionic source which produces electrons once heated and a field-emission source which produces electrons once an electrical potential gradient is created between it and an anode. The thermo-ionic sources may be a tungsten hairline filament or a lanthanum hexaboride single crystal, while field emitters consist of a tungsten needle. Both thermo-ionic and field electron emission emits electrons when a high voltage current is applied. The electron beam generated is then controlled and focused by electromagnetic coils (which recreate the effect of convex lenses) and apertures (thick annular metallic plates) to prevent the travel of electrons off axis (i.e. filtering) and decrease of the beam intensity (Williams and Carter, 2009).

The vacuum system is also an important part of a TEM as it enables air to be withdrawn inside the column causing a scattering effect of the electrons onto the gas molecules, and prevent a high voltage discharge by the electron beam on the specimen surface (Egerton, 2005). The vacuum system is comprised of different pumps that are used and work together. They contain valves that open and close in response to pressure changes. The first pump, which removes most of the air, is a mechanical rotary pump that contains internal vanes driven by an electric motor. The second pump is the diffusion pump; it is used for generating a high vacuum in the column. It consists of fluids heated up to their vapour phase which catch the unwanted gas molecules during their rise (i.e. act as carrier ligands) and trap them onto the pump floor or wall by a condensation process. Finally,

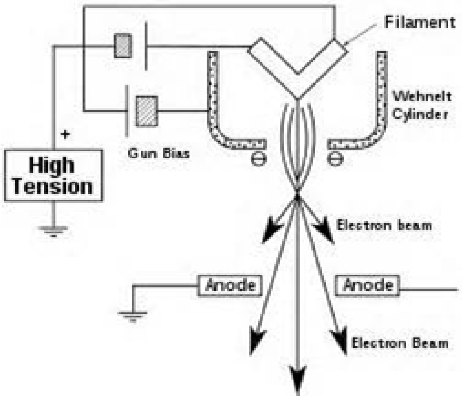

*Fig. 2.8: Schema of an electron source. A high tension is applied onto a filament to generate electrons. A Whelnet cylinder focuses the electrons attracted by anodes (www.classle.net).*

a turbo-molecular pump can also be supplemented to the diffusion pump. It consists of large electrodes that generate a potential difference of several kilovolts to attract (and keep) gas molecules in one of the electrodes (Egerton, 2005).

The specimen chamber includes airlocks to limit the increase of pressure in the microscope and a mechanism for sample stage motions in X, Y, and Z directions, but also a mechanism to rotate and tilt the specimen. The imaging system is located below the specimen chamber (Fig. 2.9). It is composed of a series of objective and condenser lenses, and apertures used to magnify the images of the specimen, and a viewing sensor screen that converts the impinged electrons into photons (i.e. visible light) by a fluorescence process. The spatial resolution of the images is strongly dependent on the quality of the lenses. The first lens is the objective lens which principally magnifies real images of a specimen. The second is the objective aperture or diaphragm (located at the back focal plane) followed by the selected-area aperture. Together, they enable us to select the passage of scattered electrons according to their angle of deflection. Electrons thereby rejected do not contribute to the final image. Finally, TEM contains several intermediate lenses (also called projector lenses) that enable us to control the magnification of the final image, and signals detectors to create virtual images (Egerton, 2005). Nowadays, the signal detectors are typically charge-coupled diode (CCD) sensors made of millions of silicon photo-diodes, which emit an electrical signal that is proportional to electrons intensity hitting the CCD (Egerton, 2005).

Many modern TEMs include a scanning mode (STEM) which uses a sharply converged electron beam (that may achieve almost 1 Å) to scan a sample and form electron density contrast images of the sample. STEM works like an SEM but, unlike this latter, it uses transmission detectors located below the sample to record signals from either the direct beam or diffracted electrons. Compared to the conventional TEM, STEM has the advantage to be both less aggressive for the sample as the beam is rastered (and not focused) onto the sample surface and less sensitive to sample thickness. Conventional TEMs are also commonly coupled with one or more spectrometers, especially Electron Energy-Loss Spectrometer (EELS) or Energy Dispersive X-rays Spectrometer (EDS).

### *2.4.2 TEM technique*

#### *Principle of Imaging and electron diffraction*

In the strict sense of the term, electron scattering refers to the particle behaviour of electrons. It is the essential process used to create virtual images in all electron microscopy including TEM. However, in addition to the use of the sub-atomic particle nature of the electron to generate virtual images, TEM technique also uses the wave nature of electrons to create diffraction patterns (DPs). Broadly, electron diffraction can be classified as a scattering process; however, it differs as it implies a bending effect of waves, and not a deviation of a particle trajectory, at the proximity of other particles. The TEM technique is set up to detect both properties of electrons (wave and particle) and display the resulting two dimensional data: images and diffraction patterns (Williams and Carter, 2009). Both virtual images and DPs are electron density contrast representation which occur because of variations in the extent of deflection angles. However, although electron scattering results in a

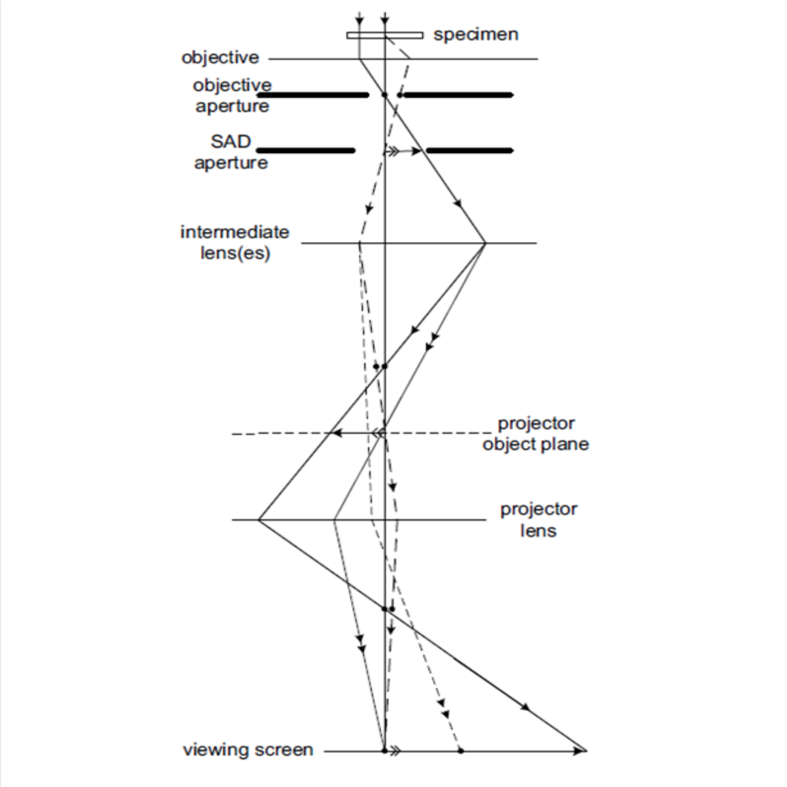

*Fig. 2.9: Imaging system of a TEM instrument with the relative position of the different components (objectives, apertures, and lenses). The vertical arrowheads represent different electron beam paths after interaction with a specimen. Only the double arrowheads form an interference pattern on the viewing screen (Egerton, 2005).*

wide range of electron deflection angles, only those which are not deflected far from their original path are collected during TEM investigations, primarily because of initial interest during the first construction of TEMs (Williams and Carter, 2009).

### *Principle of TEM imaging and different imaging mode*

To form an image of a sample, TEM uses elastically scattered electrons that pass through a sample and undergo only a small deviation (Fig. 2.10), unlike SEM that uses back-scattered and secondary electron for imaging. This makes the main difference between both TEM and SEM microscopes. The former enables us to obtain "in depth" images whereas the latter creates surface images of a sample. TEM imaging system can use either the direct beam and form "bright field" (BF) images or can use transmitted electrons with a semi-angle of $>$ 0.5-10 ° and form "dark Field" (DF) images. DF images are divided into two groups depending on their semi-angle: the annular dark field (ADF), also called low-angular annular dark field (LAADF), with semi-angle from 0.5 to 3 °, and high-angular annular dark field (HAADF) with semi-angle from 3 to 10 ° (Fig. 2.10). The selection of scattered electrons depending on their angular deflection is enabled thanks to objective apertures in the case of TEM or annular separate detectors using an

STEM.

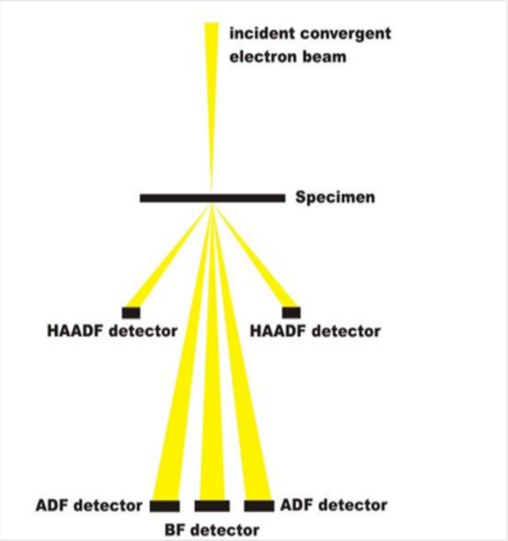

*Fig. 2.10: Schema representing the different electrons detectors (located at the base) of a TEM instrument: the direct electrons beam detector (BF, Bright Field) and transmitted electron detector for slightly deviated electrons (ADF, Annular Dark Field) and highly deviated electrons (HAADF, High-Angular Annular Dark Field) (www.microscopy.ethz.ch).*

### *Images contrast from atomic number (Z) and sample thickness*

The amplitude contrasts on BF and DF images are the result of variations in scattering angles, which themselves depend on the sample properties, especially the sample thickness and atomic numbers (Z) of the target material, generally referred to as mass-thickness images contrast (Egerton, 2005; Lee, 2010). Bright Field images (images formed using the direct beam) are especially sensitive of the sample thickness and atomic number. Increase in both thickness and atomic number increases the scattering angle of incident electrons and thus forms dark BF images. An example of thickness-dependence on BF images is given on Fig. 2.11 where interlayer porosity (due to the absence of interlayer components) of the clay minerals appear as bright strips. The electrons from the direct beam move through the mineral porosity and saturate the screen detector. The thickness dependence at very low semi-angle renders BF images is less useful for a geologist. However, the atomic number dependence at high semi-angle, together with its dominance over thickness (again at high semi-angle), provides a good opportunity to obtain Z-contrast images in the DF image mode. Because atoms scatter much more incident electrons than inter-atomic space, they form bright areas on DF images, which are even brighter for high atomic number.

### *Diffraction contrast imaging (Bragg diffraction)*

To create contrast on an image, the mass-thickness property of a sample is not the only parameter. Electron density contrast can also occur because of the crystalline

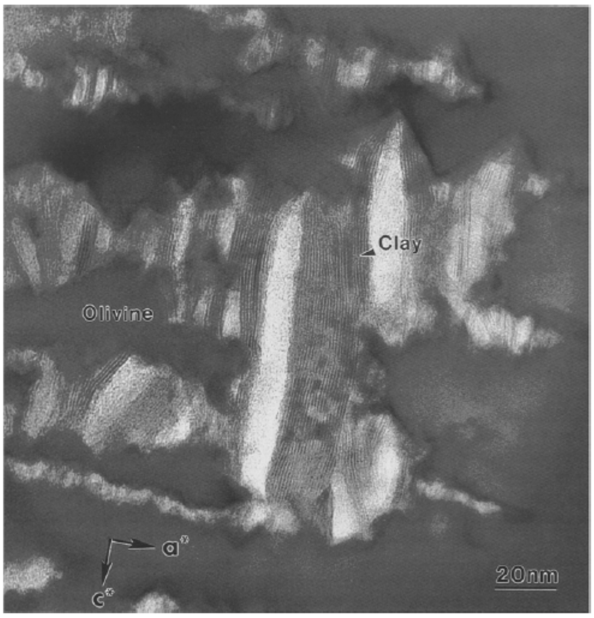

*Fig. 2.11: High resolution bright field image of olivine hosted clay minerals taken from Banfield et al. (1990) with olivine crystal orientation (or reciprocal crystal lattice, a* and c*). The fully collapse state of the clay minerals (due to the absence of interlayer components) has created porosity that appears bright on the BF image.*

state of a sample. Crystals are formed by a periodic arrangement of atoms regularly collocated in a lattice of rows and columns. In polycrystalline samples, crystals are generally randomly orientated and separated from each other by grain boundaries. Therefore, poly-crystalline materials, even with identical crystal composition and thickness, will potentially present contrast variation, which occurs because of their random spatial lattice orientation. Amongst these crystals, a certain number might have their lattice planes orientated so as to satisfy Bragg's reflection angle and thus, will be able to diffract the incident electrons (Fig. 2.12). To be Bragg-scattered, crystal lattice planes must be orientated at a small angle relative to the incident electron beam (generally less than 1 °), such that the angles of incidence and reflection are equal. This is defined by Bragg's Law

$$\eta \, \lambda = 2 \, d \, \sin \theta_{\mathrm{B}}$$

with $\lambda$ the wavelength, $d$ the atomic spacing between diffracting planes, $\theta_{\mathrm{B}}$ the Bragg angle, and $\eta$ an integer that represents the order of reflection. Hence, if the wavelength is known and the Bragg's angle measured or inferred, the $d$ spacing of the crystal can be calculated. Bragg diffraction occurs because electron waves that are diffracted from different lattice planes interfere with each other. Hence, Bragg diffraction generates a complex interference pattern with varying intensity that provides information of the crystal structure, such as the distance between the crystallographic planes $d$.

The different crystal orientations of a material are responsible for the contrast of spot size and intensity and size of DPs (Fig. 2.13). Crystals that are Bragg

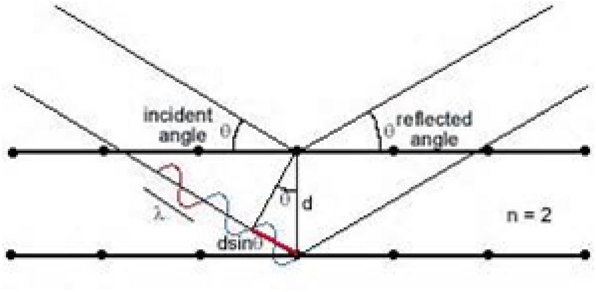

*Fig. 2.12: Schema presenting the relation between electron waves with a specific wave length λ (whose traces are represented by oblique lines) and crystal lattice planes (horizontal lines) with regularly spaced atoms (dots on the horizontal lines) separated with a lattice spacing d which satisfies Bragg's conditions. The incident angle θ equals the reflected angle, while η represent an integer (www.matter.org.uk).*

orientated strongly diffract the incident electrons, whereas a remoteness of a crystal orientation from Bragg conditions causes a decrease of the diffraction efficiency. In the BF imaging mode (using the direct beam), crystals that are Bragg orientated appear dark as they strongly diffract incident electrons which are then absorbed by the microscope apertures, whereas crystal grains which are not Bragg orientated appear bright as most of the incident electrons are not diffracted at high angles and blocked by the microscope apertures. In the case of DF images, only diffracted electrons are admitted (selected by annular detectors) and form bright regions (or spots called Bragg peaks). The variation in spot intensity and size reflect the diffraction efficiency on the lattice planes which in turn affect the angle remoteness from Bragg's angle.

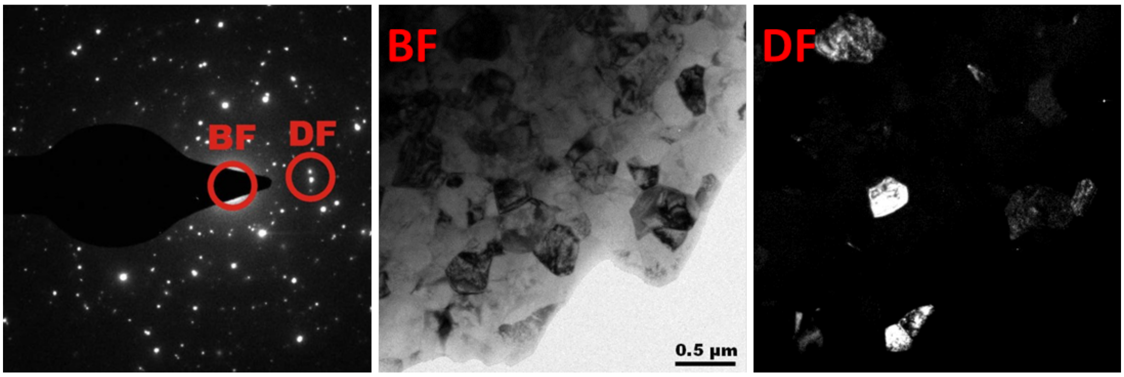

*Fig. 2.13: Diffraction pattern and associated Bright Field (BF) and Dark Field (DF) image areas of a micro-crystalline ($ZrO_2$) thin sample. Each spot indicates the presence of a micro-crystal. A metal rod is used to block the direct beam to avoid overexposure and sample damages. Dark contrast on the BF image results from the crystal orientation almost parallel to the zone axis, while the bright contrast on the DF image arises because the diffracted beams partly pass the objective aperture (http://www.microscopy.ethz.ch).*

### *Diffraction patterns*

To be effective, Bragg diffraction requires the orderly state of matter of crystallized material. The periodic structure of crystals functions as a diffraction grating medium that predictably splits and diffracts electrons. Hence, DPs correspond to a direct projection of the material internal structure and geometry. Examples of DPs are given on Fig. 2.14. Single crystals have a well ordered structure and electrons passing through will form DPs constituted of bright spots which enable us to determine directly the type of crystal structure, lattice parameter, and crystal orientation. If the material consists of aggregate of nano-crystals each with their own orientation, the electron beam passing through the polycrystalline material will interact with each single crystal and produce a DP that corresponds to the superposition of individual DP from each single crystal that the electron beam moves through. The resulting DPs will consist of several more or less well defined concentric rings, surrounding a bright central spot corresponding to the direct beam (Fig. 2.14, c). Each ring corresponds to electron scattering from atomic planes (satisfying Bragg's Law) of individual crystal grains with different orientation and *d* spacing. Amorphous materials present no atomic arrangements and in consequence are unable to provide Bragg reflection atomic planes essential for the obtaining of DPs. Images of amorphous phases only comprise a wide central spot (from the direct beam) and a thick, foggy single ring (from the randomly forward scattered electrons). Therefore, Bragg diffraction enables us not only to determine the internal structure, parameter, orientation and size of crystals but also to distinguish whether the material is amorphous or crystalline and potentially the presence of crystal defects.

### d *spacing calculation*

The radius (R) of a single diffraction ring is related to the camera length (L) and twice the Bragg's angle (2 $\theta_{\mathrm{B}}$), such that

$$\begin{gathered}\mathrm{R} = \mathrm{L}\tan 2\theta_{\mathrm{B}} \\ 2d\sin\theta_{\mathrm{B}} = \lambda \\ (1/d) = (\mathrm{R}/\mathrm{L}\lambda)\end{gathered}$$

From this equation and Bragg's equation, the *d* spacing of each ring can be calculated. Therefore, electron diffraction is a powerful technique which enables the determination of the atomic arrangement of crystals. The geometrical relationship between the radius of a diffraction ring, camera length and the Bragg's angle are illustrated on Fig. 2.15.

Diffraction contrast is not only the result of polycrystalline material but also arises because of atomic-scale defects within a single crystal such as dislocations or vacancies. Dislocations are line defect which force surrounding atoms to be bent to accommodate the structure. Along line dislocation electron scattering is high and most of the transmitted electrons are blocked by the microscope apertures, which results in the formation of dark regions in the DF images. Vacancies are a point defect, and they correspond to lacked atoms in the crystalline structure. The surrounding lattice planes are distorted to accommodate the "hole" in the crystal lattice. Generally point defects cannot be seen on TEM images, albeit the strain

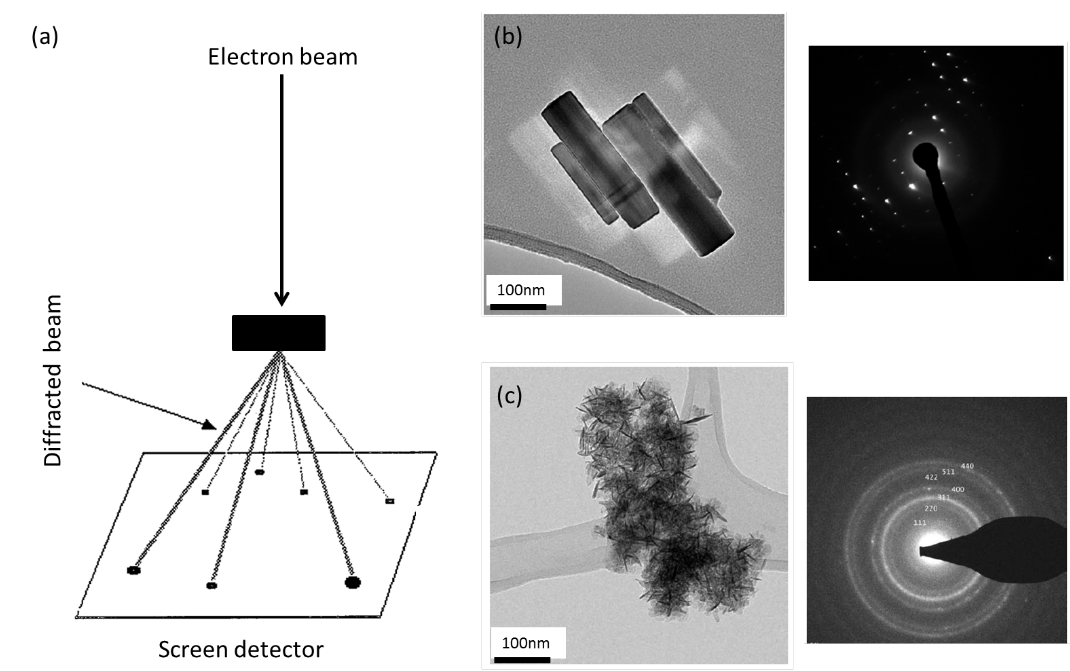

*Fig. 2.14: Key diagram (a) showing the generation of diffraction patterns (DPs) from diffracted electrons on a screen detector and examples of DPs from a single crystal of unknown nature (b) and aggregate of nano-crystals of MnZnO$_3$ (c), http://cime.epfl.ch.*

generated on the neighbourhood of a cluster or column of defect points can result in bright/dark diffraction contrast (Egerton, 2005).

### *Compositional analysis*

TEM has especially been set up for the detection of two different elastic signals (the direct beam and diffracted beam) to produce images of a specimen in a broad sense. However, much other information about the sample can be obtained from secondary processes related to inelastic scattering and are routinely used in other analytical electron microscopy (AEM) including TEM. The most common (and inevitable) secondary process related to inelastic scattering is the generation of X-rays. X-ray emission can be easily used to quickly obtain chemical (elemental) information of a sample. According to the Rutherford-Bohr model of the atoms, electrons orbit around a positively-charged nucleus in classical periods where only certain electron energies are allowed (and imposed by the quantum number n). The energy released by X-ray emission (characterized by the X-rays wavelength and intensity) is proportional to the orbital level from which the electron transfer occurred, but is also dependent on the nucleus size which imposes the strength of the atomic electron bounding. The TEM instrument generally contains an energy-dispersive X-ray detector (EDX) to collect the emitted X-rays, identify the elements and determine the concentration of the elements present (i.e. quantitative analyses). EDX can either be used in TEM or STEM mode, and enables us to obtain respectively spot analyses (although not statistical and biased by the operator) or element maps

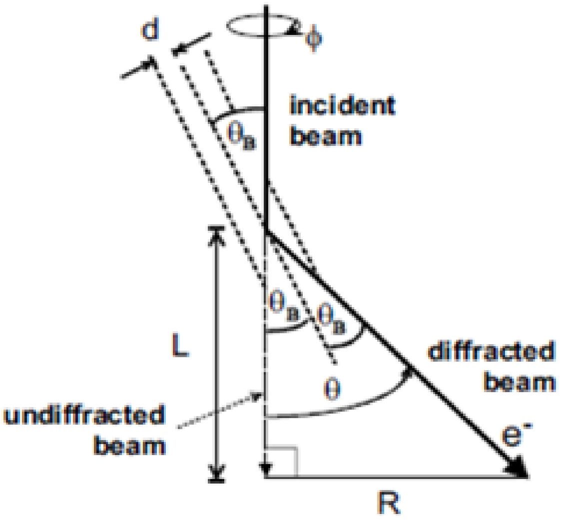

*Fig. 2.15: Schema showing the relationship between crystal lattice planes (dot lines) with a lattice space d and the formation of a diffracted pattern satisfying Bragg's conditions (incident angle $\theta_B$ = reflected angle $\theta_B$). L represents a constant value called the camera length and R the distance between the "direct" beam (which does not undergo any deflection) and the diffracted beam. On a CCD detector, R can represent either the distance between two spots or the radius of a circle (Egerton, 2005).*

(providing all relationships Egerton (2005)).

By definition, inelastic scattering process implies a loss of electron energy that can be measured via an electron energy-loss spectrometry (EELS). Electron Energy-Loss Spectrometry enables us to analyse energy changes of an initially known mono-energetic electron beam after having interacted with a specimen. It relies on the fact that electrons, when inelastically scattered, transfer a certain amount of their kinetic energy to the atoms, which in response, become excited, vibrate, possibly eject an electron and emit a specific signal (phonon, plasmon...). The emission of a particular signal (at the expense of another one) is characteristic of the amount of energy gained by the atom that is roughly equal to the incoming electrons energy loss. The quantity of electron energy loss and its distribution strongly vary with the domain of interaction within the target atom (either the outer or inner atomic electron shells) and thus are theoretically dependent on (the size) of the element (with a characteristic number of electrons and atomic number). Consequently, it can be stated that the signals emitted by the sample are directly linked to (and translate) the quantity of electron energy loss, whereas the dependence of the loss of electron energy (roughly equal to the atomic electron-nucleus binding energy) onto the atomic number enables us to identify the elements present in the target. An example of EELS spectrum is given on Fig. 2.16. Electron Energy-Loss Spectrometry is especially well suited for the detection of light elements although it has the capacity of detecting and analysing all elements of the periodic table (Egerton, 2011).

The intensity of energy loss is also dependent on the volume of interaction

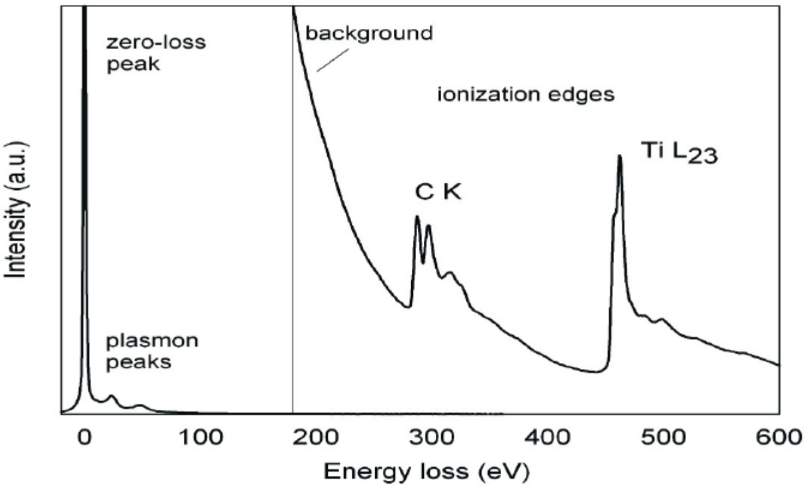

*Fig. 2.16: Example of typical electron energy loss spectrum of a thin specimen (here titanium carbide) recorded with a conventional 200 kV TEM. The first peak at 0 kV is called the zero-loss peak. It corresponds to transmitted electrons that have been elastically scattered via interaction with the atomic nuclei of the sample, spectrum taken from (Hofer et al., 2016).*

between the electron beam and specimen as well as the specimen thickness. Hence, EELS does not only offer the possibility to identify the elements present in the target specimen, but also enables us to obtain the elemental composition of a specimen. Furthermore, because the signals are directly released by excited atoms causing both an ionization of the atoms and a vibration state of the molecules, information on bonding and valence state of the elements can be obtained. And finally, because of the sole atomic dependence of EELS analyses, all the different elemental information of a specimen can be obtained whatever their nature: amorphous or crystalline.

### 2.4.3 Specimen preparation for TEM investigations

TEM is a very powerful technique to obtain internal structural data at atomic scale. However, because data depend on the efficiency of electrons to be elastically transmitted through the specimen, samples have to be prepared so as to be “electron transparent” or sufficiently thin such that the incoming electrons do not lose energy along the way. Hence, TEM imposes the use of an ultra-thin specimen, which means a specimen thickness strictly less than 100 nm, depending on the specimen component and acceleration voltage of the electron microscope that will be used during analyses. There are different techniques to prepare (polish) specimens for TEM investigations such as electro-polishing, Argon ion milling, chemical etching, ultra-microtomy, or focused ion beam (Williams and Carter, 2009). For this work a Focused Ion Beam (FIB) technique was used, and so only this technique will be described here. The Focused Ion Beam technique is already known as an efficient technique for TEM specimen preparation but although it very easily damages samples, it is recognized as an efficient technique for the conservation of very fine features of the samples such as bulk textures of nm-scale clay minerals (Heaney et al., 2001; Lee et al., 2003).

### *Focused Ion Beam (FIB) technique and limitations*

The principle of the FIB technique is bombarding a specimen with a beam of accelerated heavy atoms so as to eject atomic material from the specimen's surface until it becomes sufficiently thin for TEM analysis. During the ions bombardment, certain impinged ions will only be back-scattered from the surface sample and deposited afterwards onto the target surface whereas others will physically (and aggressively) interact with the sample causing a sputtering process. The ion collision will then cause a momentum transfer from the impinged ions into the target atoms. Consequently, the incident ions lose energy and are very probably physically trapped (or implanted) in the crystal lattice; while the atoms and molecules from the target gain sufficiently energy to be ejected from the specimen surface. The implantation of ions in the target sample often causes radiation damage and an amorphization of the material because of the depth penetration of incident ions breaking the sample atomic bonds (Giannuzzi and Stevie, 2004). The FIB technique is particularly aggressive for fragile material, such as clay minerals, which can in addition undergo chemical and structural (*d* spacing) changes and desiccation (Lee, 2010).

### *FIB instrument*

A FIB commonly comprises a vacuum system, an ion column (including a liquid metal ion source with an emission source from the tip of the tungsten needle typically in the range of 2-5 nm), a sample stage that can be displaced in three directions (X, Y, and Z) but also that can be tilted and rotated, detectors, and a gas delivery system controlled and run by a computer (Fig. 2.17). A FIB instrument commonly contains two different detectors: one to collect secondary electrons and the other for secondary ions collection. The use of gas ejection during the process of sample thinning can be helpful to control the exact site of metal deposition and the etching process. Modern FIB instruments are often coupled with an SEM, albeit the association with a TEM or other analytical instruments is possible (Giannuzzi and Stevie, 2004).

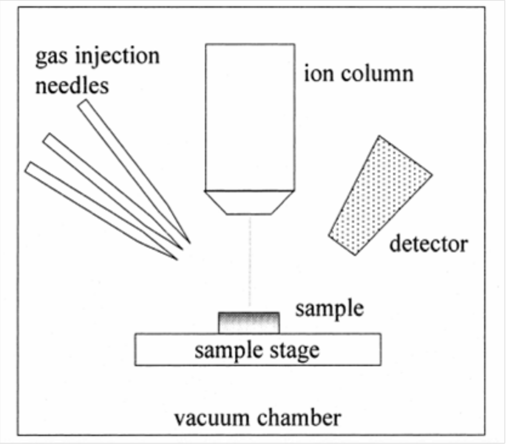

*Fig. 2.17: Schema of the interior of a sample chamber of a FIB instrument with ion column, gas injection needles and detector relative to the sample stage (Giannuzzi and Stevie, 2004).*

A FIB instrument works similarly to an SEM, although certain differences exist. In particular, FIB uses a beam of ions and not electrons. The ions come from a liquid metal ions source (LMIS), most commonly composed of $Ga^+$. Metallic $Ga^+$ is electro-hydro dynamic, which means that once heated it tends to produce ions rather than droplets resulting in the formation of charged droplets (Orloff et al., 2003). To produce ions, a reservoir filled with metallic $Ga^+$ is heated above the metal melting point. Once liquefied, the charged droplets flow along a tungsten needle up to its tip (called Taylor cone) by a capillary process, where $Ga^+$ ions can be extracted, or evaporated, if an electric field is applied (Fig. 2.18). The replacement of $Ga^+$ extracted ions occurs via a continuous flowing of liquid metal (Orloff et al., 2002). In the ion column, as with an SEM, ion beams are accelerated and then focused and aligned onto the surface sample by using electrostatic lenses, while the beam spot size and beam deflection are controlled by microscope apertures, enabling control at a nm-scale of the primary ion beam onto the target sample.

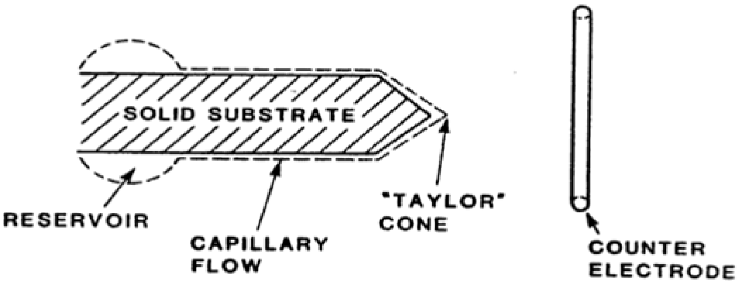

*Fig. 2.18: Schema representing the different constituent of a liquid metal ion source of a FIB instrument (liquid metal reservoir, solid substrate with a Taylor cone, and counter electrode) and the path followed by the liquid metal (along the solid substrate by capillary flow) during extraction of liquid metal ions (Orloff et al., 2003).*

### *FIB specimen preparation*

FIB specimen preparation can be effectuated from different types of material: thin sections of rocks, powdered material in epoxy, metals, alloys, glass and others (Williams and Carter, 2009). Albeit the shape and nature of the sample is not restrictive, its surface roughness is decisive to precisely locate the sputtering site and requires to be less than 1 $\mu$m. Commonly, a TEM foil is approximately 15-20 $\mu$m $*$ 10 $\mu$m $*$ 0.15 $\mu$m, whereas the final specimen thickness can be as thin as 80 nm.

To prepare a specimen, the first step involves working the region of interest by milling a cross on each side, and then by deposing a thin layer of about 1-2 $\mu$m of platinum or tungsten onto the sample where the foil will be cut. The milling begins with the cutting of pairs of trenches, one in the front and one in the back of the Pt-strip (Fig. 2.19). The milling then continues with the sputtering of the sample on both sides until the final thickness is achieved. The Pt-strip is finally cut and the foil lifted out with a glass fibre possessing a sharp tip to be deposited on a FIB special support.

### *FIB/TEM procedure conditions*

TEM investigations in this research project were required for textural characterization of the poorly crystallized secondary mineral assemblages present in the nakhlites. A dual column FIB-SEM instrument available in the School of Physics and Astronomy at the University of Glasgow was used for the preparation of ultra-thin specimen of various alteration products selected for more detailed examination. In the School of Physics and Astronomy at the University of Glasgow, the FIB-SEM instrument is equipped with a sidewinder ion column, an omniprobe 100 micro-manipulator (extraction devise), a platinum and tungsten deposition facilities, and an Oxford Instruments INCA Energy Dispersive X-ray analyser. It has allowed in situ sectioning of various µm-sized areas of interest and a rapid and precise removal of the sections. Prior to FIB sectioning using a $Ga^+$ ion beam, selected areas were capped with a 15 * 4 µm Pt layer of approximately 150 nm thickness. The capping layer has served to protect the sample from the ion beam during the milling and ion deposition processes. A $Ga^+$ ion beam operated at 20 kV was used for milling of an approximately 150 nm thick wafers of olivine-hosted secondary assemblage in an attempt to help preserve the fine clay minerals. Wafers were approximately of 15 µm length and 4.5 µm large. They were then extracted and attached to an Omniprobe copper grid. Final polishing to remove surface damage and obtain ultra thin specimen for optimal electron transparency were performed using a low acceleration voltage (2 kV).

A FEI Tecnai T20 TEM instrument available in the School of Physics and Astronomy at the University of Glasgow was used for textural analyses of the extracted specimen of secondary mineral assemblage. The TEM instrument was operated at low acceleration voltage (200 kV) using a $LaB_6$ filament electron source to minimized sample damage during analyses. Bright Field (BF) images, High Resolution TEM (HRTEM) and Selected Area Electron Diffraction (SAED) analyses were performed on the various TEM specimens. Due to contortion and irregularities of fringes of the clay minerals, $d$-spacing measurements were made from the HRTEM BF images using a histogram intensity profile tool with the Gatan Image Filter (GIF 2000) micrograph camera software. Diffraction patterns were obtained using a SIS Megaview III CCD Camera.

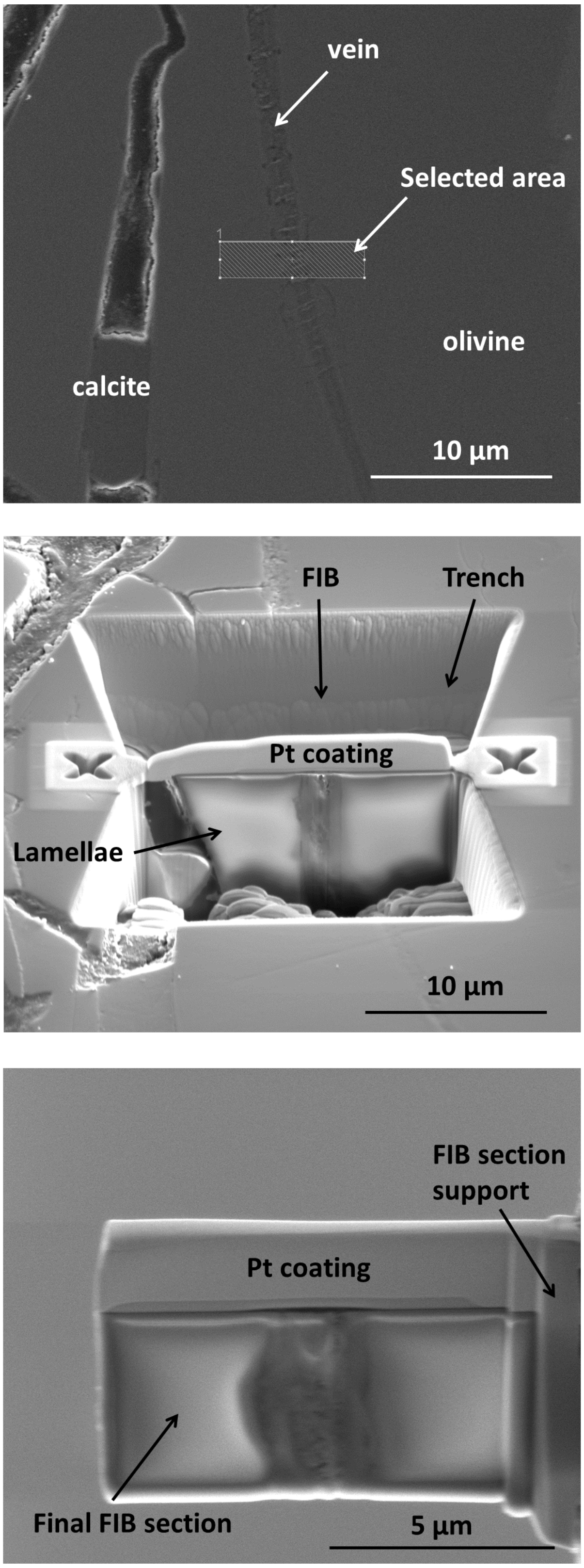

*Fig. 2.19: SEM images during FIB sample preparation of an alteration vein within an olivine phenocryst. First, the area of interest is selected and covered by a layer of platinum (Pt). Second, the back and front trenches are milled around the area of interest. Finally, the lamellae is removed from the bulk sample (here the olivine grain) and mounted on a special FIB support prior to its thinning.*

# 3. METHODOLOGY 2: RAMAN SPECTROSCOPY AND MASS SPECTROMETRY

## *3.1 Raman spectroscopy*

### *3.1.1 Introduction to Raman spectroscopy*

Raman spectroscopy is an analytical technique that measures the vibrational frequencies of molecular bonds of a material. It uses electromagnetic radiation emanating from a sample when illuminated with a monochromatic (with similar wavelength) visible light laser beam. The monochromatic light interacts with a molecule's electron cloud in the system (Fig. 3.1). When passing through a molecule, the electric field of the incident light perturbs and distorts the molecule's electron cloud. The molecule undergoes electronic transitions (or a shift of energy) to a higher energy state (i.e. virtual state) that is released with different energy. The difference in energy is equal to the vibrational transition $\Delta$E of the molecule. The virtual energy level represents an excited state and not a "natural" quantum mechanical state of the molecule.

Upon interactions with matter, most of the incident photons elastically scatter. The scattered photons have the same energy (frequency and wavelength) as the incident photons. There is no exchange in energy with the molecule and color of the light, a phenomenon called Rayleigh scattering. However, a tiny part of the light ($<$0.001%) exchanges energy with the material which then vibrates. The photons undergo inelastic scattering known as Raman scattering. Because of the exchange in energy, the visible light is scattered by the excitation with a slightly different colour. The energy of the photon laser can be either shifted up or down whether the molecule releases energy to the photon (i.e. anti-Stokes Raman scattering) or absorbs energy of the photon (i.e. Stokes Raman scattering). The energy difference between the absorbed and emitted photon is independent of the initial energy of the photon. It corresponds to the amount of energy required to excite a molecule to a higher vibrational mode. Shifts in photon energy are then diagnostic of the molecule species.

An intrinsic difficulty with Raman Spectroscopy arises because of the very small fraction of light that is Raman scattered, especially relative to Rayleigh scattering. Hence, an important part of Raman spectroscopy relies on the efficiency of separating the weak inelastically scattered light from the intense Rayleigh scattered laser light. This is done by filtering out the laser beam using either a notch filter, edge pass filter, or a band pass filter.

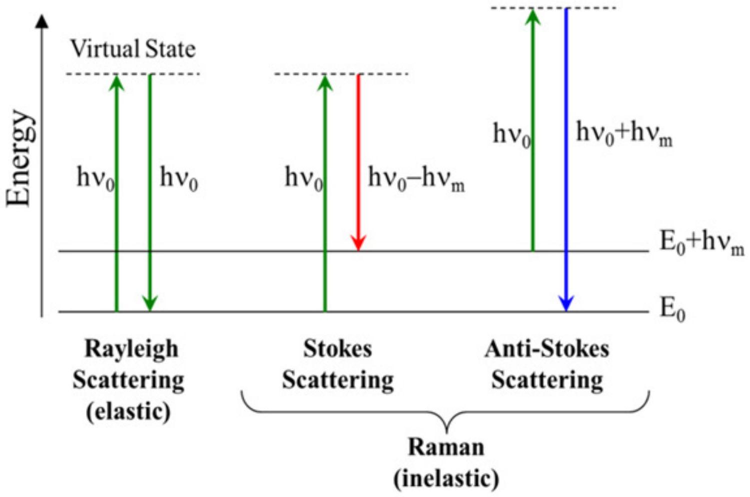

*Fig. 3.1: Energy-level diagram showing the energy states involved in Raman spectra. The electronic transitions accompanied with Rayleigh scattering (left) does not lead to gain or loss of energy unlike with Raman scattering (right), author unknown.*

### *3.1.2 Raman spectroscopy instrument and technique*

Raman spectroscopy is a microscopic technique using monochromatic visible light (Fig. 3.2). The Raman instrument generally consists of a monochromatic light source, a microscope to collect the scattered light, filters to separate the Raman spectra to the Rayleigh spectra, a device for splitting the Raman scattered light into spectra (diffraction grating), a light-sensitive device for detecting the light (usually a CCD camera), and a computer to control the instrument and analyse the data.

Raman shifts are commonly expressed as wave numbers:

$$\Delta\omega\ (\mathrm{cm}^{-1}) = (\frac{1}{\lambda_0(nm)} - \frac{1}{\lambda_1(nm)}) * \frac{10^7(nm)}{1(cm)}$$

with $\Delta\omega$ the Raman shift, $\lambda_0$ the excitation wavelength, and $\lambda_1$ the Raman spectrum wavelength. Raman spectra commonly represent the Raman shift (in cm$^{-1}$) *vs* counts/intensity (arbitrary units), or how much energy is exchanged between the incident light and sample at a certain wavelength.

Because during analyses, samples emit various degrees of fluorescence and thermal background (noisy signals), spectra were manually corrected for the sloping background through baseline subtraction using the cubic spline (or polynomial) interpolation. Polynomial interpolations are commonly used to approximate complicated Raman spectra by selecting the apparent lower “counts” at the base of the Raman spectra. Figure 3.3 shows a Raman spectra before and after baseline subtraction.

### *3.1.3 Raman spectroscopy application and configuration for sample analyses*

The instrument used in this study was the Renishaw inVia confoncal Raman microscope equipped with WiRE 3.4 software in the School of Geographical and Earth

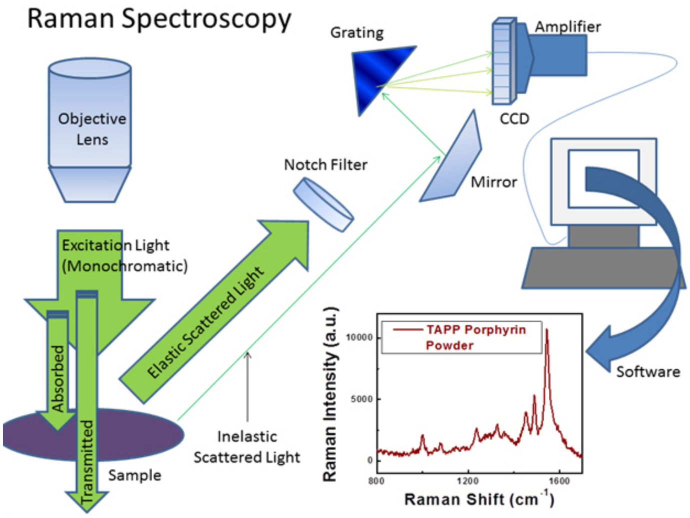

*Fig. 3.2: Raman spectroscopy technique components, author unknown.*

Sciences at the University of Glasgow. Analyses were performed with a 514 nm excitation laser, 20X long working distance objective, a grating at 2400 l/mm with a static grading scan type. Selected spectral acquisition parameters included an exposure time of 1s and a laser power at 50% to avoid damage of the sample.

Raman spectroscopy allows molecular and mineralogical identification of a sample without much sample preparation. It is a non-destructive method which enables to perform analyses with a high spatial resolution ($<1\ \mu$m). By definition, a mineral is characterized by a chemistry and crystalline structure. Because Raman spectroscopy measures the vibrational state of molecules, it can provide information on the chemistry, chemical bonding and molecular structure including the identification of polymorph and the stress that has been applied onto the sample of interest. It further allows the analysis of poly-phase melt compositions and mineral inclusions that are otherwise difficult to analyse. Raman spectroscopy is a rapid and reliable technique that has been used in this thesis mostly to identify the finely-grained minerals within the mesostasis including the presence of poly-morphs, which can provide important information about the environment of rock formation. Unfortunately, because the alteration products contain water, they do not survive long enough under the visible light beam to be properly analysed.

## 3.2 Laser Ablation Inductively-Coupled Mass Spectrometry (LA ICP-MS)

### 3.2.1 LA ICP-MS technique and instrument

Inductively-Coupled Mass Spectrometry (ICP-MS) is a relatively new technique used for elemental determination. It is a technique of choice for many geochemical analyses thanks to its very low detection limits and good accuracy and precision (Liu et al., 2013). It can be used for a wide range of trace elements and stable isotope analyses (Potts, 1990). Inductively-Coupled Plasma Mass Spectrometry has advantages over many other elemental analysis techniques. For example, it

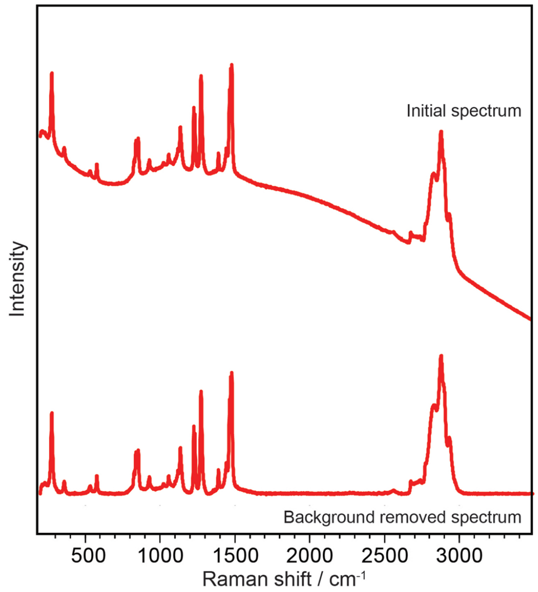

*Fig. 3.3: Raman spectra before and after baseline subtraction. Fluorescence emission and thermal background are unavoidable during sample analyses. They add themselves onto Raman spectrum (www.renishaw.com).*

can analyse materials with both simple and complex matrices with a minimum of matrix interferences (Jochum et al., 2007). This results from the high temperature of the ICP source. It is also an extremely rapid technique that can measure a wide range of elements simultaneously.

An ICP-MS combines two techniques, a high-temperature Inductively-Coupled Plasma and a Mass Spectrometer (Thomas, 2013). It can be associated with a Laser Ablation (i.e. LA) system to analyse in-situ material (Fig. 3.4). The ICP is a “flame” technique. It uses Ar and a radio frequency coil to generate a torch. The radio frequency field causes Ar atoms to enter into collision, ionize by ejection of an electron ($Ar \rightarrow Ar^+ + e^-$) and form a high-temperature plasma with a temperature ranging from 6000 to 10,000 K. The Ar torch is used to convert the atoms of a sample into gaseous atoms and finally ions toward the end of the torch. The sample transported in the ICP plasma can only be a fine aerosol. The generation of an aerosol from a sample results first from either aspiring a solution or vaporizing a solid sample using a pulsed laser (i.e. Laser Ablation system). The sample's particles are then introduced into the ICP by a pneumatic nebulizer which uses mechanical forces of a gas flow to dissociate elements and generate the aerosol.

Analyte ions (i.e. aerosol) are forced into the Mass Spectrometer thanks to a mechanical pump. Once the ions enter the Mass Spectrometer, they are focused by electrostatic lenses into the system and separated according to their mass-to-charge ratio before being detected by the Mass Spectrometer on an electron multiplier (Jackson, 2008). The most common type of Mass Spectrometer is the quadrupole mass filter which uses four rods with alternating voltages applied to opposite pairs of rod. These voltages form an electrostatic filter that only allows ions of a single mass-to-charge ratio to enter the rods. Once they leave the quadrupole mass analyser, ions are attracted to the high negative charge of the conic electron multiplier device.

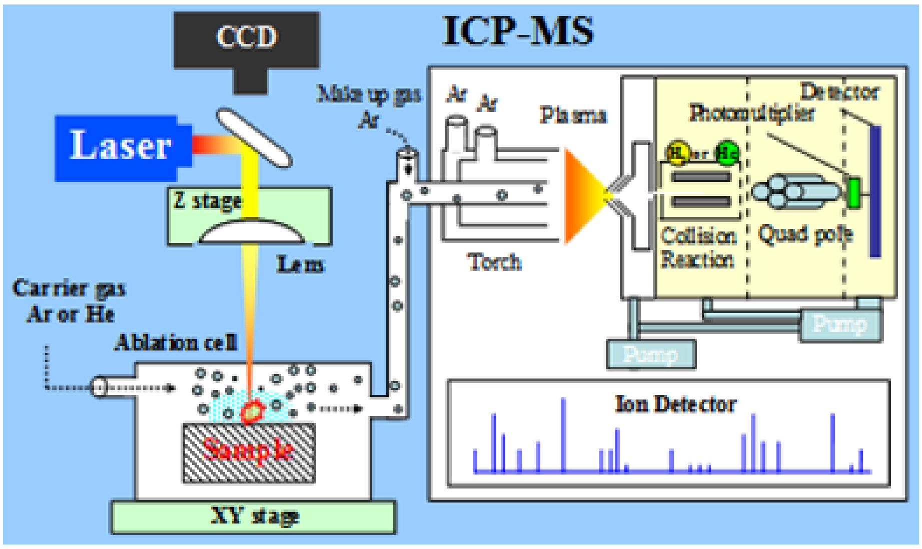

*Fig. 3.4: Configuration of an LA ICP-MS, unknown author.*

The collision of the ions onto the electron multiplier device generates secondary electrons. The electron multiplier cone has a potential gradient from entrance to exit which enables electrons to flow though the cone. Each time electrons hit the cone wall, more electrons are generated creating pulses of many millions of electrons that are then detected by a very fast pre-amplifier and digital discriminator and counting device (Jackson, 2008).

### *3.2.2 LA ICP-MS limitations and quantitative analyses*

Laser Ablation Inductively Coupled Plasma Mass Spectrometry technique also has some weaknesses (Jackson, 2008). For example, ions formed with an ICP are positive, hence elements that tend to form negative ions are not easily measured via ICP-MS. Furthermore, it is not completely interference-free, it may form background polyatomic ions and suffers of major loss of elements in the ICP (not all ions reach the Mass Spectrometer). Finally, it is a relatively "unsteady" technique that requires frequent recalibration especially when working with geological materials (Jackson, 2008). This arises because of their inhomogeneous chemical, physical and optical properties. Geological samples respond differently during ablation processes which results in various amounts of material being ablated (i.e. ablation pit size and form), transported and inserted into the ICP. Ablation properties may also change during the ablation process: a phenomenon commonly known as "ablation yield". Data correction and calibration using the LA ICP-MS technique require both external calibration using a solid reference standard plus internal standardization (Jackson, 2008). External calibration is commonly used for investigations of sample compositions while internal standardization, generally using a major element whose concentration has been measured using an independent technique (i.e. electron microscopy), is used to correct for ablation yield between sample and reference material.

Calculation of element concentrations in a sample using LA ICP-MS is based on the count rate for the element of interest and signal normalized sensitivity corrected for element fractionation (weight of sample ablated/transported/ionized and background noise) such as

$$C_{X_s} = \frac{R_{X_s}}{S}$$

with $C_{X_s}$ the concentration of the element X in the sample s, $R_{X_s}$ the count rate of the element X in the sample s, and S the calibration standard (Longerich, 1996).

### *3.2.3 Analytical procedure and operating conditions*

Laser Ablation Inductively Coupled Plasma Mass Spectrometer analyses in this thesis were carried out on a low noise collision cell Thermo XSERIES 2 instrument equipped with a laser ablation of solid samples device using a New Wave solid state UP-193 Nd:YAG laser system in the Department of Earth Sciences at Durham University. A laser spot of 50 $\mu$m and a pulse repetition rate of 5 Hz were used for all spot analyses. Detailed operating conditions for the laser and the ICP-MS instrument are listed in Table 3.1. Each analysis included an approximately 20 s background acquisition (i.e. gas blank) followed by 50 s data acquisition from the sample. Every 10 spot analyses, two analyses of NIST 612 and NIST 610 followed by four analyses of BHVO-2G and BCR-2G and then again two analyses of NIST 612 and NIST 610 were performed in order to correct the time-dependent drift of sensitivity and mass discrimination. All analyses were acquired using time resolved software.

To conduct quantitative analysis by LA ICP-MS, the relative element sensitivity for each element was usually calibrated using both external calibration and internal standardization. The external quantitative calibration was performed using the well known NIST 612 and NIST 610 standard materials (mafic glasses with low REE concentration) and tested using two basaltic glass references (BHVO-2G and BCR-2G). The NIST synthetic glasses SRM 612 and SRM 610 have the advantage that the concentrations of all trace elements are similar and high enough (50 ppm and 500 ppm, respectively) for a precise primary calibration (Jochum et al., 2005). On the other hand, the reference glasses BHVO-2G and BCR-2G have chemical compositions of natural rocks (Jochum et al., 2005) and are homogeneous at the $\mu$m to mm scale with respect to major elements (RSD $<$ 1–2 %) and most trace elements (RSD = 1–4 %) (Jochum et al., 2005). Furthermore, trace element data obtained from the reference glasses BHVO-2G and BCR-2G have previously shown a good agreement when analysed with different laboratory techniques with an uncertainty ranging from 1 to 5 % (Jochum et al., 2005). Consequently, BHVO-2G and BCR-2G represent appropriate reference materials for external calibration of the Martian basaltic materials analysed in this thesis.

Long-term sensitivity drift during ICP-MS analysis is a well known problem. Sensitivity of LA ICP-MS is not only affected by the ICP-MS instrument, but also by sample position within the cell, laser focusing and variation in ablation efficiency between minerals and glasses. The contribution of sample position, laser focusing and ablation efficiency to the time-drift is generally corrected by normalizing to a major element (e.g. Si, Ca or Al) because high concentrations of any given element

| **ICP-MS conditions** | |
|---|---|
| RF power | 1350 W |
| Plasma gas | 14 L $\text{min}^{-1}$ Ar |
| Auxiliary gas | 0.9 L $\text{min}^{-1}$ Ar |
| Make-up gas | 0.8 L $\text{min}^{-1}$ Ar |
| Detector | Dual (pulse and analog counting) |
| Dwell time/mass | 6 ms |
| **Laser parameters** | |
| Wavelength | 193 nm |
| Energy density | 14 J $\text{cm}^{-2}$ |
| Carrier gas | Ar |
| Ablation style | Single spot |
| Ablation spot size | 50 $\mu$m |
| Repetition rate | 5 Hz |
| Laser pulse | 300 burst |

*Tab. 3.1: Operating conditions for the LA ICP-MS analyses.*

can be measured more precisely than low concentrations. Consequently, reference values of high concentrations are generally more accurate than low concentrations. In this study, each analysis was normalized to the concentration of Ca (and so, is the internal standard element) using the stoichiometrically calculated oxide CaO wt% obtained from electron microscope quantitative analyses. Calcium is known as a reliable elemental internal standard because it is present at sufficiently high level in most geological samples and synthetic glasses (Jackson, 2008). Finally, data reduction was carried out using the GLITTER software.

# 4. BASALTIC PETROGENESIS OF THE NAKHLITES

## *4.1 Introduction*

The nakhlites are fragments of a young Martian basaltic crust, $\sim$ 1.3 Ga old, that have been excavated and ejected into space following a meteorite impact $\sim$ 11 Ma ago (Nyquist et al., 2001), although one nakhlite falls out of the nakhlites' ejection age cluster with a Cosmic Ray Exposition (CRE) age dated at $\sim$ 7.3 Ma (Wieler et al., 2016). The similar ejection age of the nakhlites presupposes that these meteorites (but one?) sample the same launch site, which is consistent with their identical approximate crystallization age and the probably limited volcanic activity of Mars during the Middle Amazonian (Christen et al., 2005). The nakhlites are all medium-grained pyroxenite likely formed by fractional crystallization of basaltic magma(s) and subsequent accumulation of the early formed augite phenocrysts at the bottom of a magma chamber (Imae et al., 2005). Petrographic features of the nakhlites indicate a final crystallization of the rocks in a superficial crustal environment (either lava flow(s) or shallow intrusion(s)) (Friedman-Lentz et al., 1999; Day et al., 2006; Richter et al., 2016). The importance of the nakhlites lies in the information they can provide about the deep and subsurface magmatic processes that resulted in their formation, which should give further insights into the young basaltic magmatism of Mars and the formation of a Martian crust during the Amazonian.

Decades of investigations have revealed information on the geological history of the nakhlites (Treiman, 2005). The nakhlites represent distinct meteorite falls but they are thought to originate from a common parent magma because they exhibit a narrow range of bulk compositions, textures and isotopic compositions including crystallization and cosmic ray exposure ages (Treiman, 2005). Yet, their petrogenetic relationships remain uncertain. Many characteristics of the nakhlites can be explained by a stratigraphic sampling of a single cumulate-rich igneous body (Friedman-Lentz et al., 1999; Mikouchi et al., 2012); although the nakhlites may also originate from multiple similarly structured igneous bodies that were emplaced nearly simultaneously. The nakhlites formed from basaltic magma(s) but the composition of the magma(s) is unknown. As the nakhlites are cumulate rocks, their bulk chemistry is not representative of the composition of their parent magma(s). Hence, the composition of the magma(s) at the origin of the nakhlites has to be inferred indirectly which intrinsically bears uncertainties. Estimations of the nakhlite parent magma composition obtained using different approaches have given similar compositions suggesting a co-genetic (if not genetic) link (Treiman, 2005). However, they fail to explain many of the petrological characteristics of the meteorites indicating that the calculated magma composition may not be representative of the real parent magma(s) of the nakhlites and/or that certain important magmatic processes during magma solidification are beyond our current reach. Consequently, the genetic link of the nakhlite meteorites may not be true (Treiman, 2005).

The nakhlites are differentiated basaltic rocks (Friedman-Lentz et al., 1999). Their parent magma(s) formed by partial melting of the mantle but they have experienced mechanical processes that have modified their "primitive" composition (Imae et al., 2005; Day et al., 2006). The nakhlites formation began with the crystallization of large augite phenocrysts which presupposes the existence of slowly cooled subsurface magmatic reservoir(s). The excess of augite in all nakhlites and their preferential alignment are diagnostic of cumulate processes (Bunch and Reid, 1975; Berkley et al., 1980; Day et al., 2006), the gravitational settling of crystals from a single batch of magma experiencing fractional crystallization. The principle behind fractional crystallization is that as crystallization proceeds the composition of the magma evolves accordingly because it "loses" elements that enter into the solid phases while gravitational settling physically separate the crystal cargo from its parent melt. Therefore, information about the composition of the magma and its physico-chemical evolution during fractional crystallization are not completely lost but have been recorded in the chemical composition of the successive crystallizing phases. The mineralogy and chemistry of the liquidus phases can inform us about the intensive magmatic variables (i.e. variables that do not depend on the size of the system: composition, crystallinity, pressure, temperature, oxygen fugacity, etc.) at the time the specific mineral phases precipitated, assuming the order of crystallization and the number of mineral phases that potentially co-precipitated is known. The texture and mineralogy of cumulate rocks are diagnostic of the physico-chemical conditions under which the rocks formed.

Intrinsic difficulties commonly associated with long-lived magmas as the origin of porphyritic rocks are chemical homogenization of minerals and melt upon cooling and crystal separation with possible "gravitational loss" of one or more mineral phases in the basaltic plumbing system. Further constraints with cumulate processes are the effects of trapped liquid migration through the cumulate pile and removal of intermediate melts. In the nakhlites, cumulus augite and inter-cumulus materials including olivine are out of chemical equilibrium (Harvey and McSween, 1992; Treiman, 1990). They represent the solid products of a melt at two distinct stages of evolution. Furthermore, cumulus augite contain undoubted evidence of sub-solidus exchange with the late inter-cumulus melt (Wadhwa and Crozaz, 1995; Richter et al., 2016). As such augite phenocrysts represent only an incomplete relic of the most primitive melt. The nakhlites do not display clear evidence of the intermediate stages either except some cryptic chemical reactions that cannot be identified from the late reactions. Parts of the crystallization history of the nakhlites have therefore been lost.

Despite the obscure fractionation path taken by their parent magma(s), the nakhlites must have preserved in their various mineral phases at least some chemical signatures of the primary magma(s) and its complex evolution history en route to and onto the surface. These chemical signatures may be one of the keys to identify the petrogenetic link between the meteorites. The objectives of this chapter are to better identify the geochemical characteristics of the early parent magma(s) and determine the relative time-integrated crystallization-differentiation processes of the nakhlites. The specific scientific approaches used in this study are first to establish from the texture and mineralogy of the rocks the crystallization path of the nakhlites (including determining the possible co-precipitation of different mineral phases), with a potential focus on identifying any textural and mineralogical variations between the rocks. The second step concentrates on the specific composition and micro-distribution of key elements within and between mineral phases. By comparing them with our understanding of their specific behaviour during magmatic activity, we aim to better constrain the magmatic environment and hopefully distinguish between mantle source and crystallization-differentiation processes.

## 4.2 The nakhlites petrography: Mineral texture, chemistry and characteristics

The nakhlites are olivine-bearing clinopyroxenites with interstitial feldspar, Fe-Ti-oxides, Fe-sulfide and silica (Treiman, 2005). Augite porphyrocrysts and minor olivine dominate the texture and structure of the rocks. The nakhlites have similar mineralogy and texture but still display variations in mineralogical and petrographical properties. The most obvious differences between the rocks are the sharpness of mineral zoning of augite and olivine and the degree of crystallinity and grain size of the rocks' matrix (Treiman, 2005). These variations are believed to reflect the thermal structure and history of the thick cumulate igneous body upon crystallization (Mikouchi et al., 2012). The nakhlites which sample the top of the cumulate pile (NWA 5790, NWA 817 and MIL 03346) have augite and olivine porphyrocrysts strongly zoned and a poorly-crystallized rock matrix. The rocks that sample the core of the igneous body (Y 000593, Y 000749 and Nakhla) have their olivine and augite populations mildly zoned and a rock matrix fully crystallized. The nakhlites from the bottom of the cumulate pile (Lafayette and NWA 998) are fully crystallized with coarse grains and augite and olivine phenocrysts displaying no obvious chemical zoning.

### 4.2.1 Augite

Augite is the most abundant mineral phase in all nakhlite meteorites (Fig. 4.1). The augite occurs mainly as phenocrysts in the form of euhedral to subhedral prisms in most nakhlites except in Lafayette and NWA 998 where phenocrysts are subhedral to anhedral (Fig. 4.1). In all nakhlites, the augite phenocrysts form the texture and structure of the rocks. When in contact with each other, the augite phenocrysts closely fit together (Fig. 4.1). The primary kinetic texture has slightly been mechanically modified by sorting and compaction. Sometimes, augite phenocrysts are partially or completely enclosed by olivine phenocrysts (Fig. 4.1) and more rarely by large Ti-magnetite suggesting that augite crystallized first. Rare nm-size grains of Fe-Ti-oxide and Fe-sulfide can be found within the augite rims. The augite rims most probably represent late-stage igneous crystallization and not post-solidification diffusional re-equilibration with late fractionated melts, although partial chemical re-equilibration have also been an important processes in the final chemical composition of the augite.

The augite phenocrysts have large homogeneous cores dominating the phenocrysts (Fig. 4.1). They do not display obvious oscillatory zoning. However,

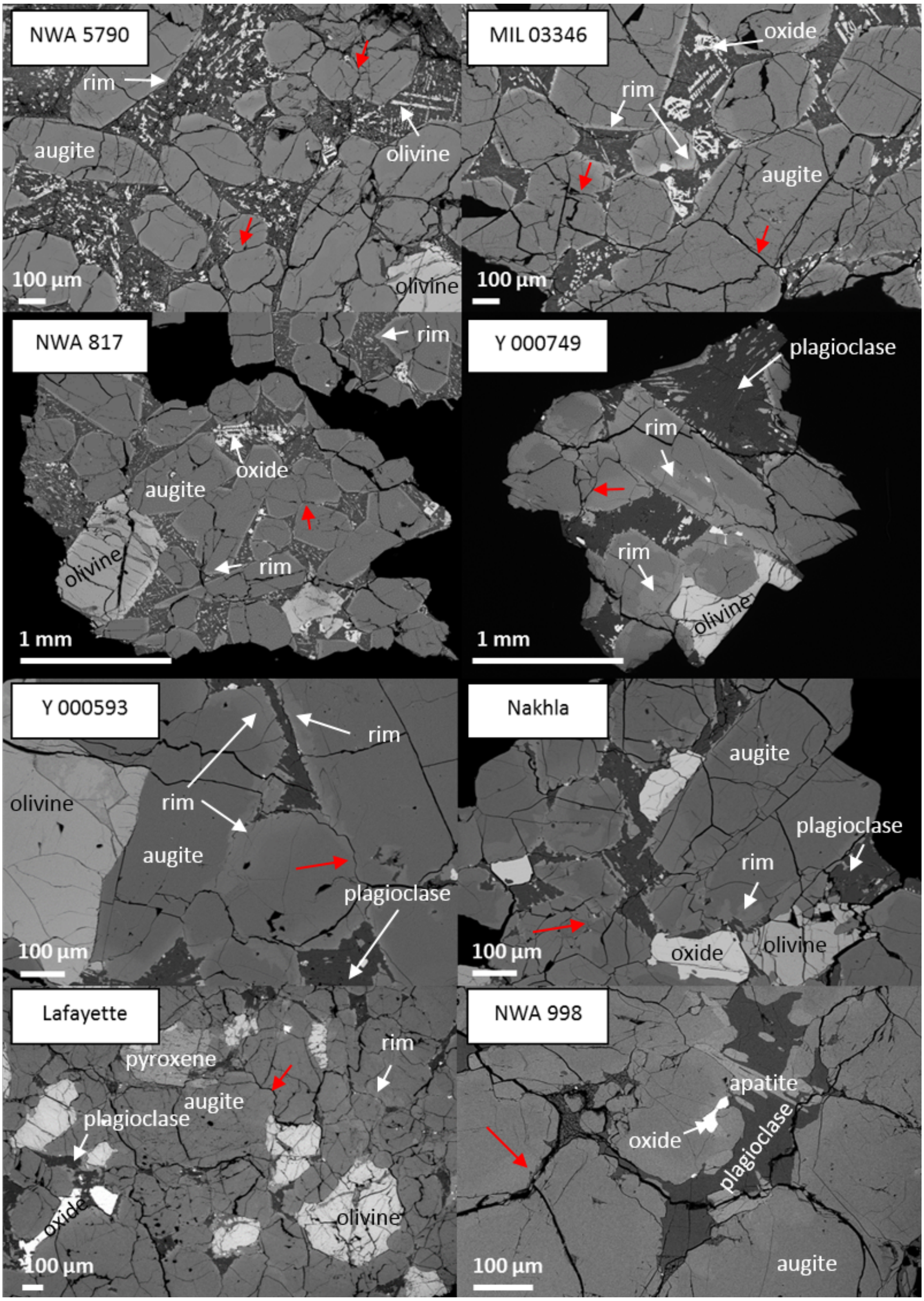

*Fig. 4.1: BSE images of the nakhlites illustrating the dominance of augite. Augite comprise large cores and thin rims in NWA 5790, MIL 03346, and NWA 817. In Y 000749, Y 000593 and nakhla, augite display patchy and irregular rim zones whereas in Lafayette and NWA 998 they have no obvious rims. The nakhlites display a cumulate texture but the primary kinetic texture has been mechanically modified by sorting and compaction. Under the effect of compaction, augite grains in contact with each other have partly dissolved, a process called pressure-solution or grain coarsening (red arrows).*

augite phenocrysts commonly display straight or patchy rims whose composition and thickness vary between the rocks. Except in NWA 998, the rims are easily identifiable on Back Scattered Electron (BSE) images by their light grey colours (Fig. 4.1). Some nakhlites contain also irregular low-Ca pyroxene overgrowths with a similar composition than the low-Ca pyroxene grains present in the rocks' matrix.

The large homogeneous cores of augite phenocrysts correspond to sub-calcic augite (Fig. 4.2). The chemical composition of the large augite core is nearly identical in all nakhlite meteorites. The augite phenocryst rims are normally zoned with ferroan composition. The Fe enrichment occurs also as thin irregular zones following intra-crystalline hairline fractures, which may have acted as diffusion pathways for the late Fe-rich melt and chemical re-equilibration processes. The nakhlite meteorites commonly contain small low-Ca pyroxene grains in the mesostasis. Together with augite phenocrysts, they form a continuous chemical evolution that sometimes overlaps or displays a compositional gap marked by a sharp change in Fe and/or Ca content (Fig. 4.2). The evolved chemical composition (Fe-rich) of augite overgrowths and mesostasis low-Ca pyroxenes suggests a crystallization from a differentiated residual melt.

### *Augite in NWA 5790, NWA 817 and MIL 03346 (top of the cumulate pile)*

The cores composition of augite in NWA 5790, NWA 817 and MIL 03346 is similar but the rims display variations in zonation patterns and chemistry (Fig. 4.2). In the three nakhlites, the augite rims are very thin but are chemically distinct relative to the core (Fig. 4.1, 4.2). The boundaries between core and rims are sharp, straight and parallel to the grain surfaces. There is no textural evidence suggesting that the augite cores partially dissolved prior to rim precipitation (i.e. resorbed grain surfaces), unlike in NWA 998. In NWA 5790, augite rims are almost non-existent ($\ll 1$ $\mu$m) and are difficult to analyse separately. Augite rims in MIL 03346 and NWA 5790 display a unique chemical zonation pattern within the nakhlite family, a progressive decrease of Ca with increasing Fe content followed by an increase of both elements.

NWA 817 is a unique nakhlite with respect to augite composition as its augite phenocrysts do not present any obvious decrease or enrichment in Ca from augite core to rim despite a gradual increase in Fe content. Another unique characteristic of NWA 817 is the composition of its small augite grains present in its mesostasis, which forms a progressive chemical composition with augite phenocrysts. The relatively constant Ca content in augite phenocrysts and late-formed augite grains in the mesostasis may record a progressive crystallization of the two augite populations in the absence of large-scale crystallization of plagioclase, although augite phenocryst rims in MIL 03346 present a decrease in Ca and no obvious plagioclase crystals embedded in the mesostasis such as NWA 817.

### *Augite in Y 000749, Y 000593 and Nakhla (core of the cumulate pile)*

In Y 000749, Y 000593 and Nakhla, augite phenocrysts show a complex history with a formation of large and homogeneous core and latter precipitation of very irregular and thick rims and abundant"patchy" zonation either in between or during rim crystallization. The patchy zoning probably represents partial post-solidification

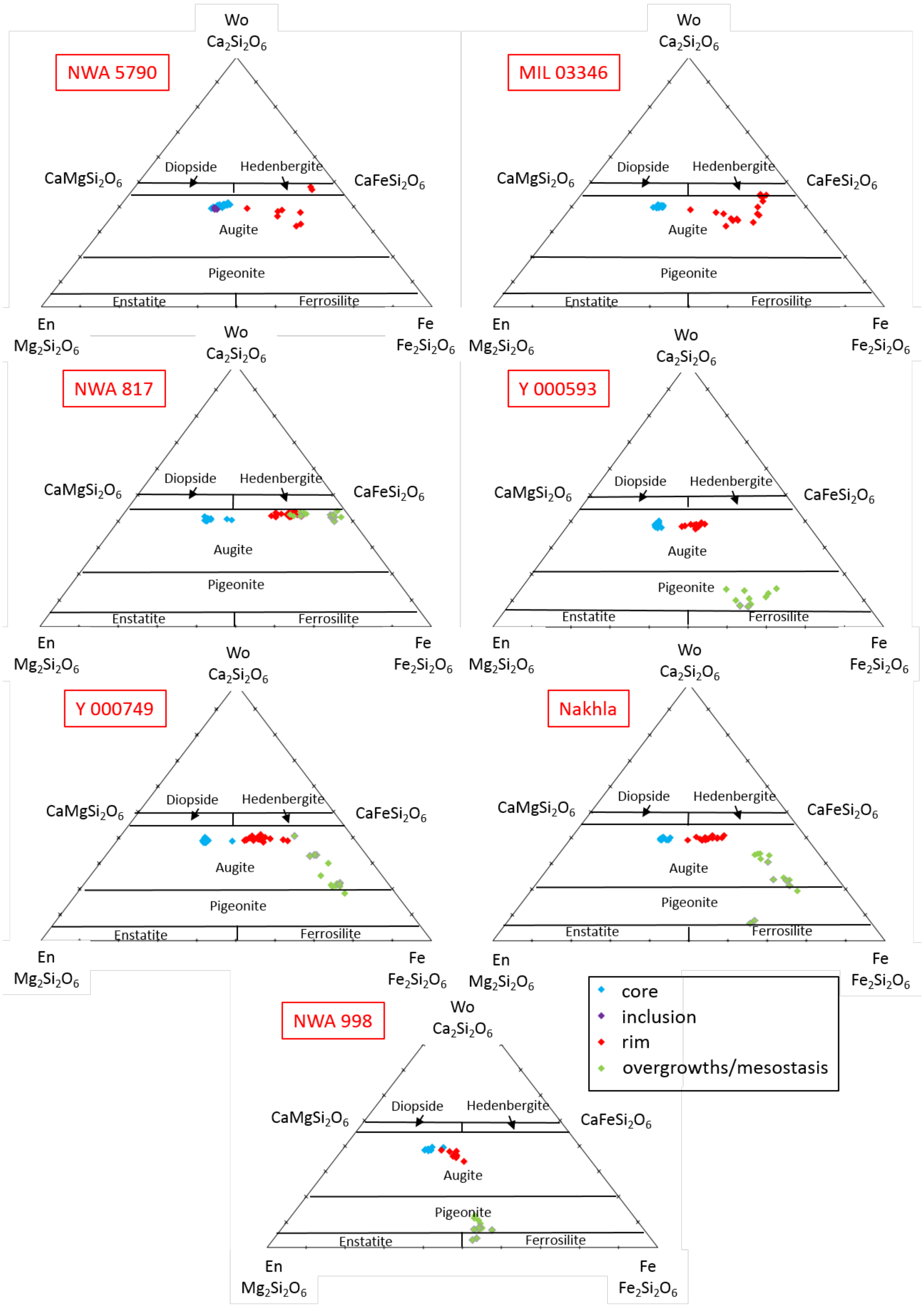

*Fig. 4.2: Ternary diagram with nomenclatures for the Ca-Mg-Fe clinopyroxene and Mg-Fe orthopyroxene and composition ranges of the various pyroxene present in the nakhlites. They include augite phenocrysts (core, rim, and overgrowth) and low-Ca pyroxene grains in the mesostasis. The different pyroxenes show a progressive evolution from core, rim to overgrowth/mesostasis illustrating a slow and protracted crystallization of pyroxene during rock solidification. The relatively constant Ca content in augite rim and small grains in the mesostasis in NWA 5790, MIL 03345 and NWA 817 probably reflects the absence of (co-crystallized) plagioclase in the rocks with a preferential incorporation of Ca into plagioclase.*

diffusional re-equilibration (Fig. 4.1). The rims are normally zoned with a ferroan composition commonly associated with a decrease of Ca content either progressive in the case of the Y 000749, or sharp in the case of Nakhla and Y 000593 (Fig. 4.2). Furthermore, at the contact with the mesostasis, augite rims display abundant low-Ca pyroxene overgrowths that crystallized onto augite phenocrysts during late magmatic processes (post-emplacement) after rim formation. The low-Ca pyroxene overgrowths display a similar size and chemical composition than the low-Ca pyroxene grains present in the rocks' mesostasis.

### *Augite in NWA 998 (bottom of the cumulate pile)*

Unlike the previous nakhlites, augite phenocrysts in NWA 998 do not display obvious zonation pattern on BSE images. The augite grain boundaries are irregular and smooth (Fig. 4.1). They could reflect partial dissolution processes. Rim zonation in augite phenocrysts in NWA 998 may be either non-existent or resorbed, although augite phenocrysts display some compositional change along some of their rims as underlined the very slight decrease of Ca and increase of Fe (Fig. 4.2). Small low-pyroxene grains are abundant in the rock matrix and display the strongest Ca depletion and smaller Fe enrichments relative to all nakhlites (Fig. 4.2). This could be explained by a Ca and Fe uptake by the abundant and large plagioclase and oxide respectively (i.e. competitive growth).

### *Minor element in augite*

The augite phenocrysts within the different nakhlites have very similar major element patterns and abundances, especially in Mg (Fig. 4.2). Patterns and abundances of Fe and Ca are also very similar within the augite phenocryst cores but display abundance variations within the rims from one nakhlite to another (Fig. 4.3). Crystallization of the augite phenocryst rims corresponds to a change in the availability of Fe and Ca within the melt phase possibly due to melt differentiation associated or not with the crystallization of new mineral phase(s) rich in one of these components such as plagioclase (competitive uptake of Ca and not Fe). However, the minor element abundances in the augite phenocrysts vary significantly, even within a single nakhlite, especially their Na content. The augite cores display mild oscillatory zoning patterns, especially with their Al and Ti content (Fig. 4.3). Oscillatory zoning commonly occurs during crystallization. The preservation of primary oscillatory zoning implies that augite cores did not chemically re-equilibrate (at least regarding these elements) with the melt post-crystallization. The cores of the augite phenocrysts have preserved parts of their original elemental composition and distribution.

### *4.2.2 Olivine*

Olivine phenocrysts are much less abundant than augite but the crystals tend to be slightly larger. The proportion of olivine (in vol %) varies from one nakhlite to another, from MIL 03346 (2.9 +/- 1.7 %), to GV (8.9 +/- 3.1 %), NWA 998 (10 %), Nakhla (10.8 +/- 4.7 %), Y 000593 (12.2 %), NWA 817 (12.5 %), and finally Lafayette (16.7 +/- 5.7 %) (Treiman, 2005). Olivine is a dense mineral phase

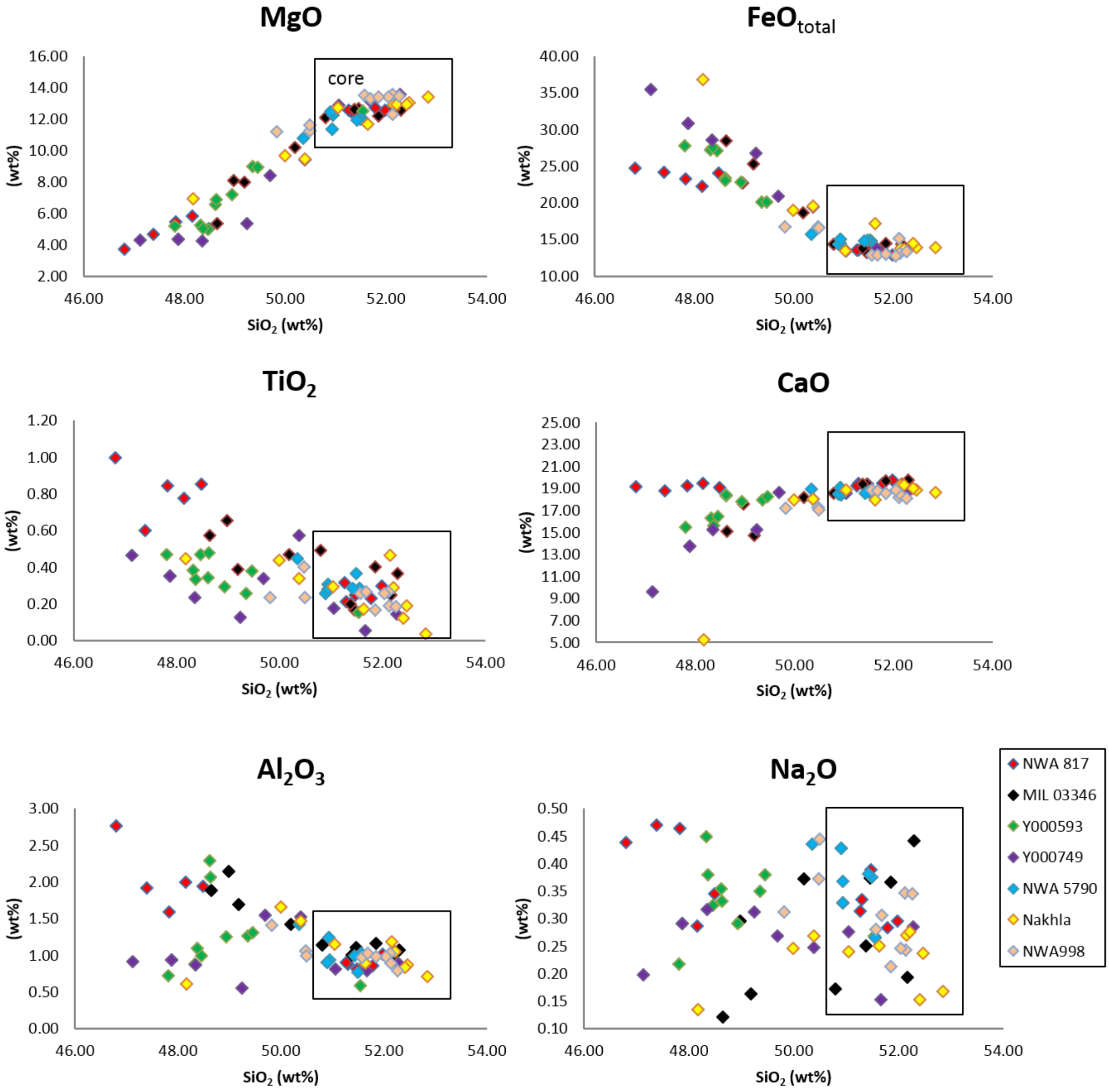

*Fig. 4.3: Bivariate plots of major and minor elements v.s $SiO_2$ of augite phenocrysts from the different nakhlites. The augite phenocrysts have relatively homogeneous core (black square) but display strong variations in composition and zonation patterns along their thin rims within and between the meteorites. Despite their volumetric dominance, the cores of augite phenocrysts in all nakhlites analysed display very limited range of composition and no progressive compositional growth zoning in major elements suggesting that they experienced intense intra-crystalline diffusive re-equilibration during crystal growth.*

composed of metallic ions, Mg and Fe. It naturally tends to accumulate at the base of cumulate piles. The apparent proportion of olivine in the different nakhlites does not vary with the stratigraphy (Fig. 4.4), although olivine phenocrysts are both heavier and larger than augite phenocrysts. Small olivine grains are common in the mesostasis of all the nakhlites except in the nakhlite from the lowest part of the presumed cumulate pile (i.e. NWA 998) (Fig. 4.8, 4.9 and 4.11). Olivine phenocrysts comprise large cores of constant composition within a given nakhlite but display variations between the different nakhlites (Fig. 4.5). The Mg abundance does not show the overlapping pattern of the augite phenocrysts

### *Olivine in NWA 5790, NWA 817 and MIL 03346 (top of the cumulate pile)*

Olivine phenocrysts are in the form of euhedral to subhedral grains in NWA 5790, NWA 817 and MIL 03346 (Fig. 4.4). They are either larger or similar in size than augite phenocrysts in NWA 5790 and NWA 817 respectively; but smaller than the largest augite phenocrysts in MIL 03346. The olivine phenocrysts display very thin but sharp rims in NWA 5790 whereas in NWA 817, olivine rims are large. In MIL 03346, olivine phenocrysts are largely altered and transformed into laihunite (a non-stoichiometric oxidative product of olivine) and so possible rim zones cannot be identified.

In NWA 5790, olivine contains augite inclusions and intrude into augite phenocrysts. As such, it is likely that olivine crystallized after augite. The small size of the completely enclosed augite suggests that olivine began to crystallize only slightly after the augite (before they could have reached their full phenocryst size), while the larger size of the olivine relative to augite suggests that they grew quicker or have continued to grow after augite crystallization stopped.

### *Olivine in Y 000593, Y 000749 and Nakhla (core of the cumulate pile)*

Olivine phenocrysts are in the form of subhedral to anhedral in Y 000593, Y 000749 and Nakhla (Fig. 4.4). They are either larger or relatively similar in size than augite phenocrysts. The olivine phenocrysts commonly poikilitically (either partly or completely) enclose augite phenocrysts. The small size of the augite inclusions and their absence of rims on augite inclusions further suggests that olivine began to crystallize slightly after the augite at least before they could have reached their full phenocryst size and before the melt was differentiated. The larger size of the olivine relative to augite and the intrusive growth of olivine phenocrysts along augite phenocrysts and plagioclase laths (Fig. 4.4) suggest that they have grown quicker and have continued to grow after augite crystallization stopped and together with plagioclase crystallization. Most nakhlites show normal zoning with rims enriched in Fe. However, their zoning patterns are smoother and more difficult to identify on BSE images than those of augite phenocryst (Fig. 4.4). The olivine phenocrysts composition (Fe content) and patterns (zoning trend) contrast both with those of the augite phenocrysts.

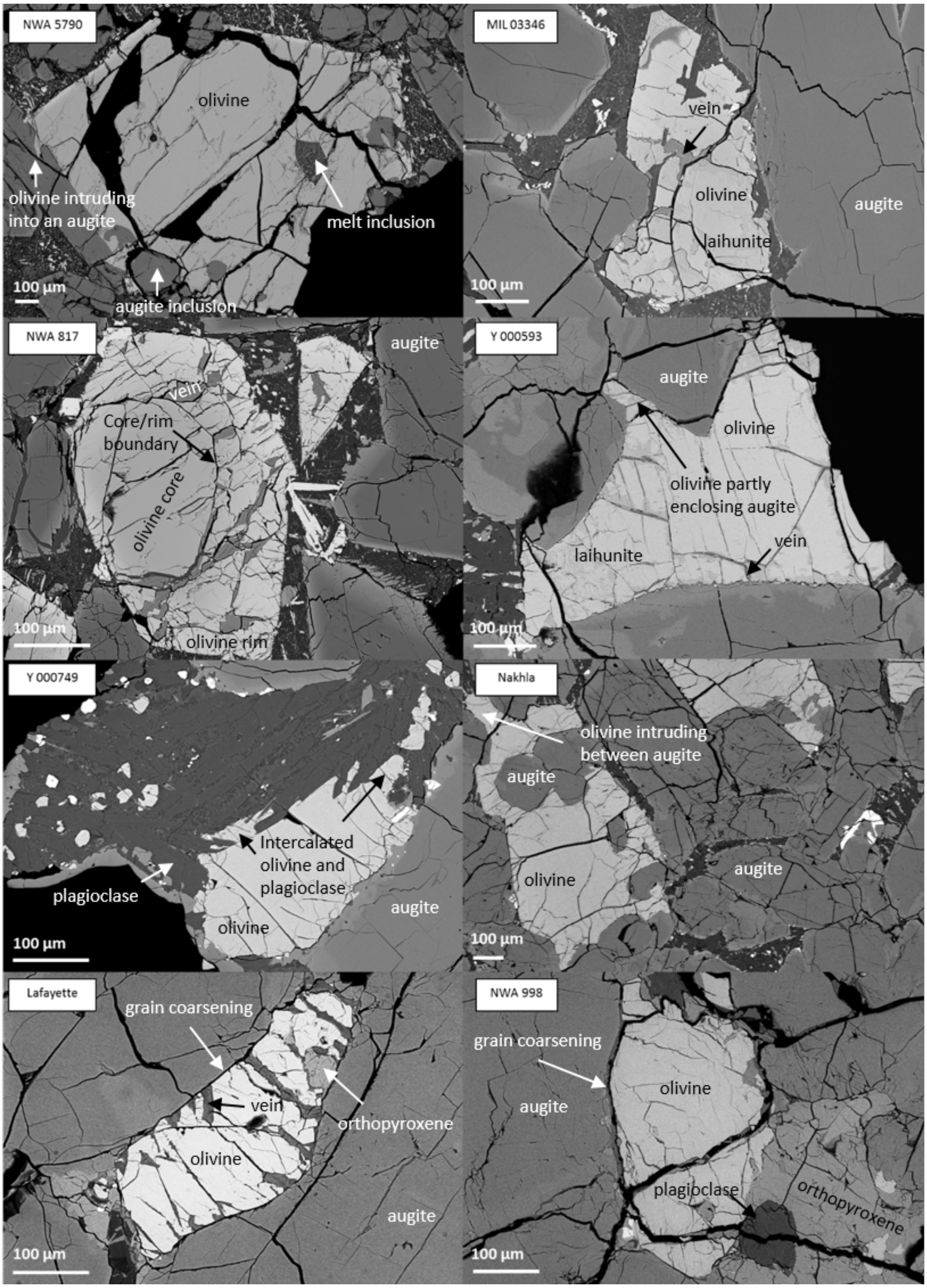

*Fig. 4.4: BSE images of olivine grain texture in different nakhlites. Olivine in NWA 5790 and NWA 817 are euhedral, in Y 000749, Y 000593 and nakhla they partly enclose the neighbouring crystals whereas in Lafayette and NWA 998 they are anhedral. The perfect fitting of olivine and augite grains in Lafayette and NWA 998 suggests that both rocks experienced grain coarsening involving both mineral phases.*

#### *Olivine in NWA 998 and Lafayette (bottom of the cumulate pile)*

Olivine phenocrysts in NWA 998 and Lafayette are anhedral. The olivine grain boundaries display evidences for mechanical grain coarsening that likely happenned during rocks compaction. Bothe Lafayette and NWA 998 are the only nakhlite with olivine phenocrysts lacking obvious rim zoning.

#### *Minor element in olivine phenocrysts*

Commonly, olivine phenocrysts in all nakhlites are enriched in Fe, especially if compared to augite phenocryst composition, and do not display obvious oscillatory zoning (i.e. magmatic) in minor elements except within the phenocryst cores. Therefore, one can conclude that either olivine did not crystallize in equilibrium with the augite or that olivine underwent post-crystallization diffusion re-equilibration (Treiman, 2005). Both the absence of oscillatory zoning in minor elements within the large olivine rims and the occurrence of augite inclusions favour the hypothesis of incomplete post crystallization diffusion processes.

### *4.2.3 Low-Ca pyroxene*

The large augite phenocrysts are commonly rimmed and overgrown by low-Ca pyroxene, with the exception of the nakhlites NWA 5790, NWA 817 and MIL 03346 (Fig. 4.3). Small crystals of pigeonite are also commonplace within the Yamato meteorites and Nakhla mesostasis unlike NWA 817 and MIL 03346 which contain acicular skeletal pyroxene enriched in Ca (relative to the other nakhlites mesostasis), most probably augite. The nakhlites Nakhla, Lafayette and NWA 998 also contain “pure” orthopyroxene mineral (with Ca $\leqslant$ 5 wt %) whose texture and micro-stratigraphic relationships suggest both a formation during late-stage magmatic processes. The low-Ca pyroxenes display three different textures/settings: (1) patchy replacements of olivine and augite, (2) exsolution lamellae within augite rims, and (3) large euhedral prismatic grains (only found in NWA 998). The low-Ca pyroxenes represent post-cumulus minerals that grew at the expense of early minerals (olivine, augite and plagioclase feldspar). Their crystallization provides evidence of a change in the late or post magmatic physico-chemical conditions, which will be discussed later on.

The meteorite NWA 998 is the unique orthopyroxene-bearing nakhlite (Treiman and Irving, 2008). It contains the greatest abundance of low-Ca pyroxene whose lath-shaped crystals are as large as the augite phenocrysts (Fig. 4.6). Both orthopyroxene and pigeonite are present but the distinction between both is sometimes not completely clear because they tend to form a continuum of chemical composition rather than two distinct chemical compositions. The low-Ca pyroxenes occur either as euhedra (lath-shaped) of orthopyroxene, as replacement products of both augite and olivine phenocrysts, or small grains (augite overgrowths) abutting feldspar. “Pure” orthopyroxene (with Ca $\leqslant$ 5 wt %) occurs only as a topographic replacing product of olivine. It sometimes contains inter-growths of vermicular Ti-magnetite (Fig. 4.6). Remnants of olivine, plagioclase and apatite can also be found within the large orthopyroxene.

The pigeonite and orthopyroxene grains are chemically homogeneous with no

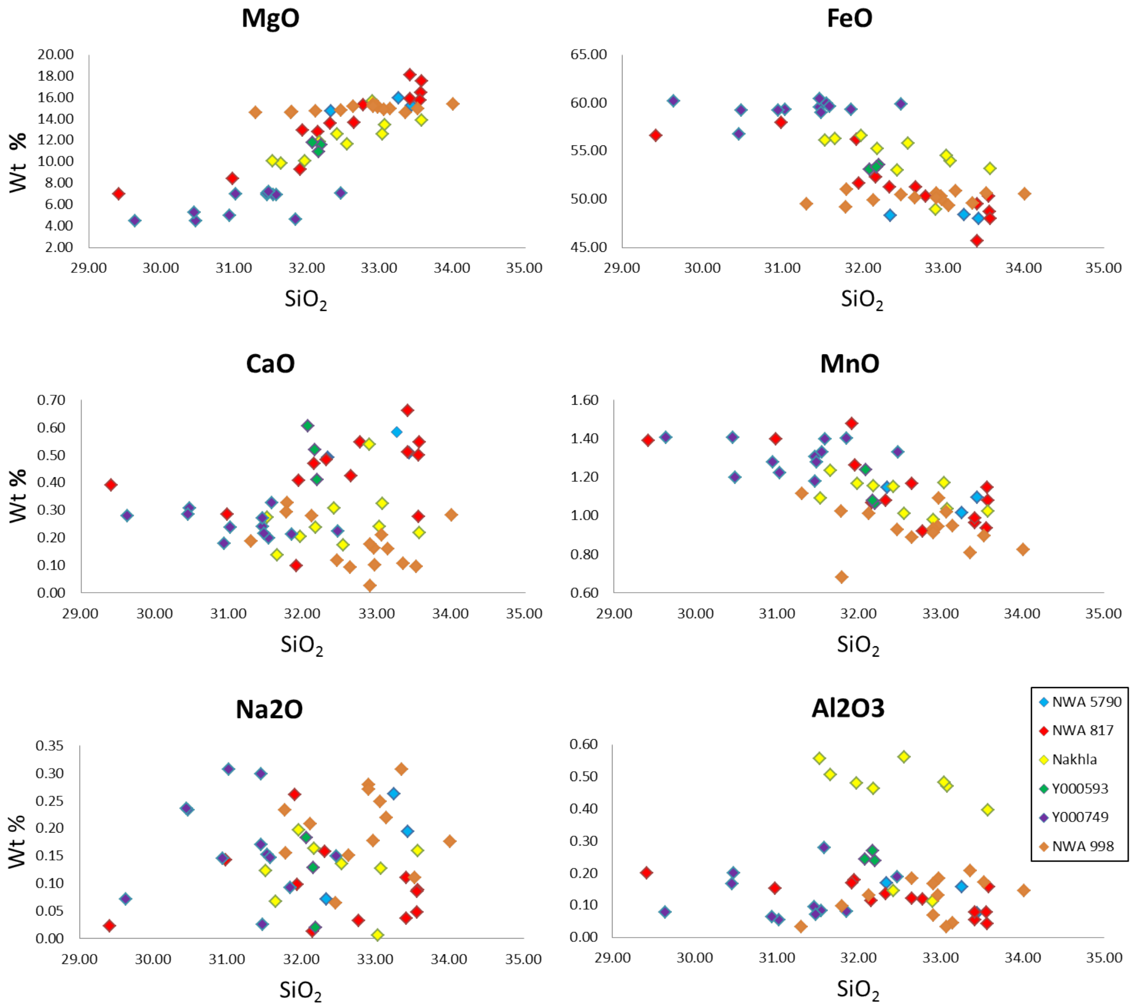

*Fig. 4.5: Bivariate plots of selected major and minor elements of olivine phenocrysts from the different nakhlites. The composition and zonation patterns of olivine phenocrysts vary between the rocks. To be noted: the composition of the large olivine phenocrysts in Y 000749 is distinct with a more evolved composition that further show little variation except in Na.*

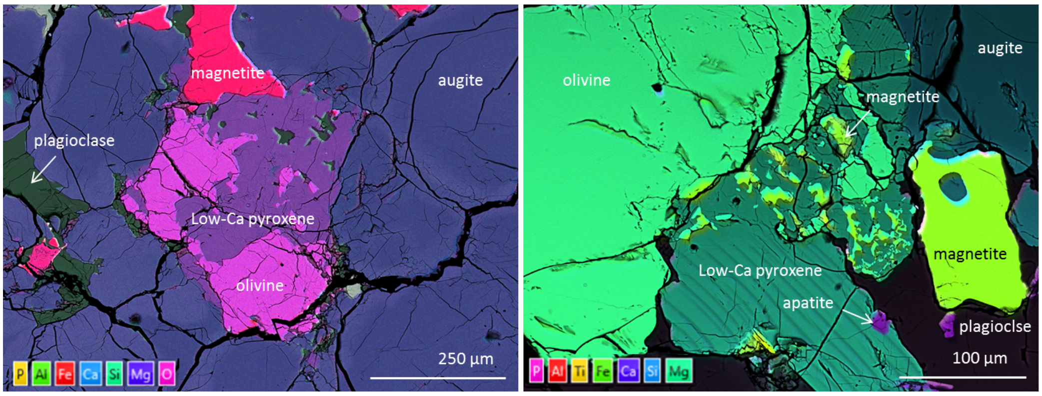

*Fig. 4.6: EDS map of replacive low-Ca pyroxene in NWA 998. The low-Ca pyroxene overgrow onto olivine, plagioclase and to less extent augite. The low-Ca pyroxene sometimes contain lamellaes of augite and more rarely inter-growths of worm-like Ti-magnetite.*

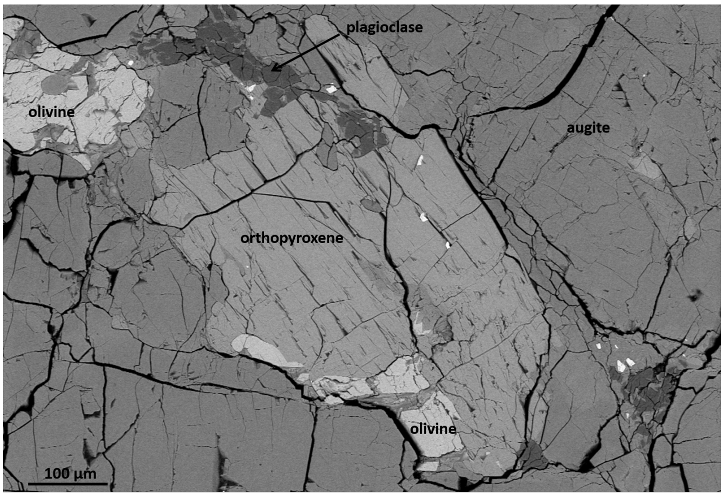

*Fig. 4.7: BSE image of an unusual large orthopyroxene grain almost completely replacing an olivine phenocryst and overgrowing onto augite and plagioclase in Lafayette.*

zoning (Fig. 4.6). They are more magnesian and ferroan than the replaced augite but less than the replaced olivine. However, they contain more Mn than both phenocryst phases suggesting an external origin of Mn. Large orthopyroxenes partially replacing olivine, plagioclase and augite phenocrysts are also present in Lafayette (Fig. 4.7). In our Lafayette sample, Ti-magnetite inter-growths have never been found associated with the orthopyroxene replacing olivine. Nakhla and the Yamato meteorites also contain patchy, few $\mu$m-size lath-shaped low-Ca pyroxene within the augite rims. However in the Yamato meteorites, they have never been found associated with olivine.

### 4.2.4 Mesostasis

Between augite and olivine phenocrysts is an inter-cumulus mesostasis, a finely crystallized groundmass composed of a poly-mineralic assemblage. The abundance of the mesostasis varies within and between the nakhlites. When in contact with the mesostasis, augite and olivine phenocrysts display rinds of more ferroan composition. Zoned rims are largely absent when the phenocrysts are in contrast with each other which provides evidence that both augite and olivine phenocrysts have reacted with and/or continue to grow from the late post-cumulus fractionated melts. Based on the mesostasis texture, the nakhlite meteorites can be divided into three groups, with each group related to its presumed position within the cumulate pile model. The first one forms the rapidly cooled (quenched) top of the cumulate pile (NWA 5790, NWA 817 and MIL 03346), the second forms the slowly cooled interior of the igneous body (Y 000593, Y 000749, Nakhla and GV), and the last one the base of the fully crystallized cumulate pile (Lafayette and NWA 998).

### *Mesostasis texture and mineralogy: NWA 5790, NWA 817 and MIL 03346*

NWA 5790, NWA 817 and MIL 03346 contain abundant mesostasis relative to the other nakhlites. The mesostasis in the three meteorites is poorly crystallized and displays skeletal and cruciform Fe-Ti oxide, augite and olivine crystals (Fig. 4.8). The "spinifex" texture with high surface area to volume ratio of olivine, augite and Fe-Ti oxide are indicative of rapid cooling and non-equilibrium crystallization (Lofgren, 1983). The proportion of the three different mineral phases and their size vary between the three meteorites. The skeletal grains in NWA 5790 are dominated by fayalitic olivine although they have similar crystal size and shape to Ti-magnetite; they are difficult to distinguish from each other on BSE images. NWA 5790 does not contain much skeletal augite grains in its mesostasis. In NWA 817, skeletal Fe-Ti oxides are significantly larger than olivine and augite, whereas in MIL 03346 magnetite grains are much larger while augite numerically dominate over olivine grains. The three meteorites contains much less augite grains in their mesostasis than the other nakhlites and lack low-Ca pyroxene. In our samples, only NWA 817 seems to contain rare, very thin plagioclase laths. Plagioclase have never been found in MIL 03346 (Day et al., 2006) but have already been detected in NWA 5790 (Jambon et al., 2010). They seem to be lacking in our samples.

Many other mineral phases have been detected in NWA 5790, NWA 817 and MIL 03346. They include discreet sprays of needle-shaped apatite and unevenly distributed droplet-shaped silica and Fe-sulfides identified respectively as cristobalite and pyrrhotite (with possibly either pyrite or marcassite) using Raman spectroscopy. The texture of the cristobalite (i.e. drop-shaped) suggests that it possibility represents late silica immiscible melt. Except tiny sprays of apatite, no crystallized silica or Fe-sulfides have been identified in our NWA 5790 sample although both amorphous Si-rich and Fe-rich products have been identified by McCubbin et al. (2013). Only NWA 817 contains apatite rich in Cl (chlorapatite) whereas the two other nakhlites contain most probably fluor-apatite (by deduction from the general lack of hydrous molecules in the nakhlites (McCubbin et al., 2013) and Cl in NWA 5790).

### *Mesostasis texture and mineralogy: Y 000749, Y 000593 and Nakhla*

In the Yamato meteorites and Nakhla, the mesostasis is largely crystallized and does not display a "spinifex" texture as seen in the NWA 5790, NWA 817 and MIL

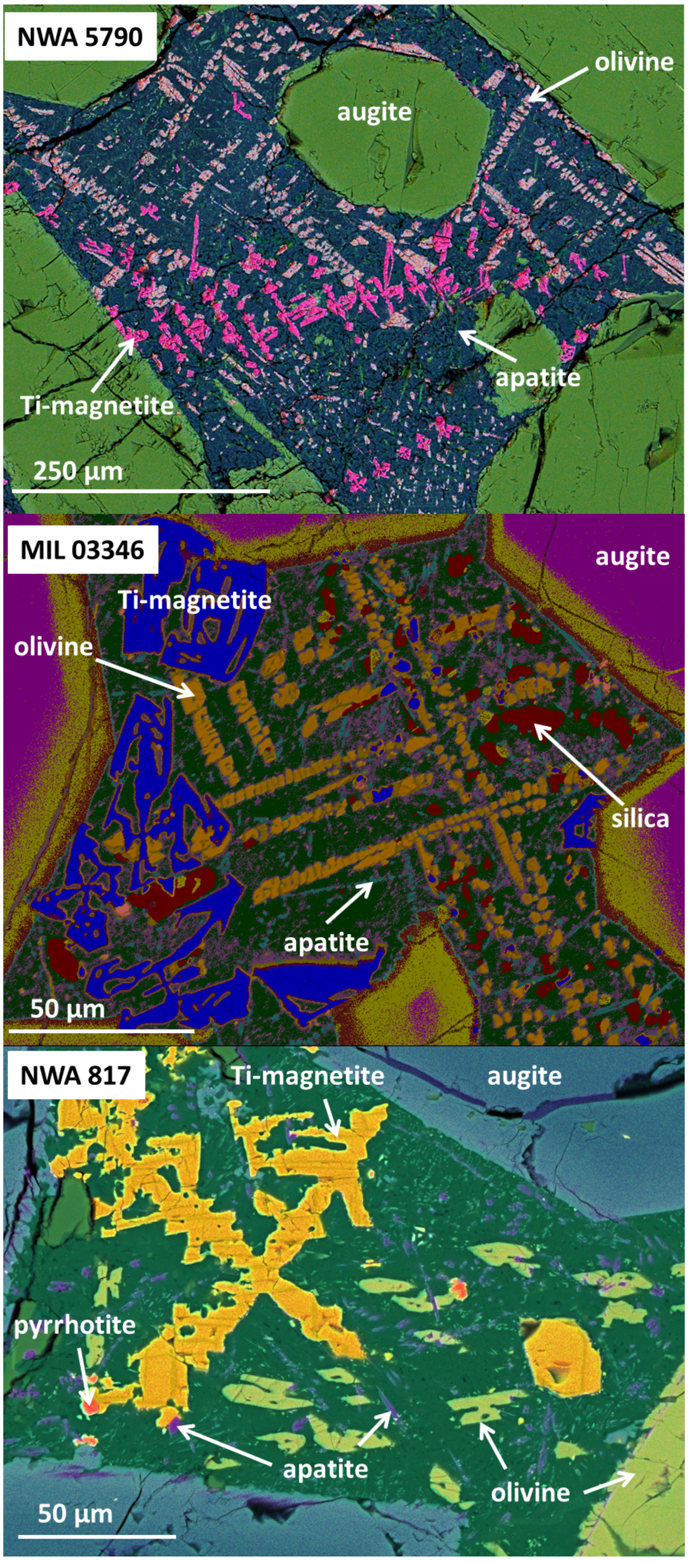

*Fig. 4.8: X-ray maps of the mesostasis of NWA 5790, MIL 03346 and NWA 817. The three meteorites contain skeletal crystals of Ti-magnetite, olivine and augite but their proportion and size differ between the meteorites. Another characteristic of these meteorites is the apparent lack of plagioclase laths.*

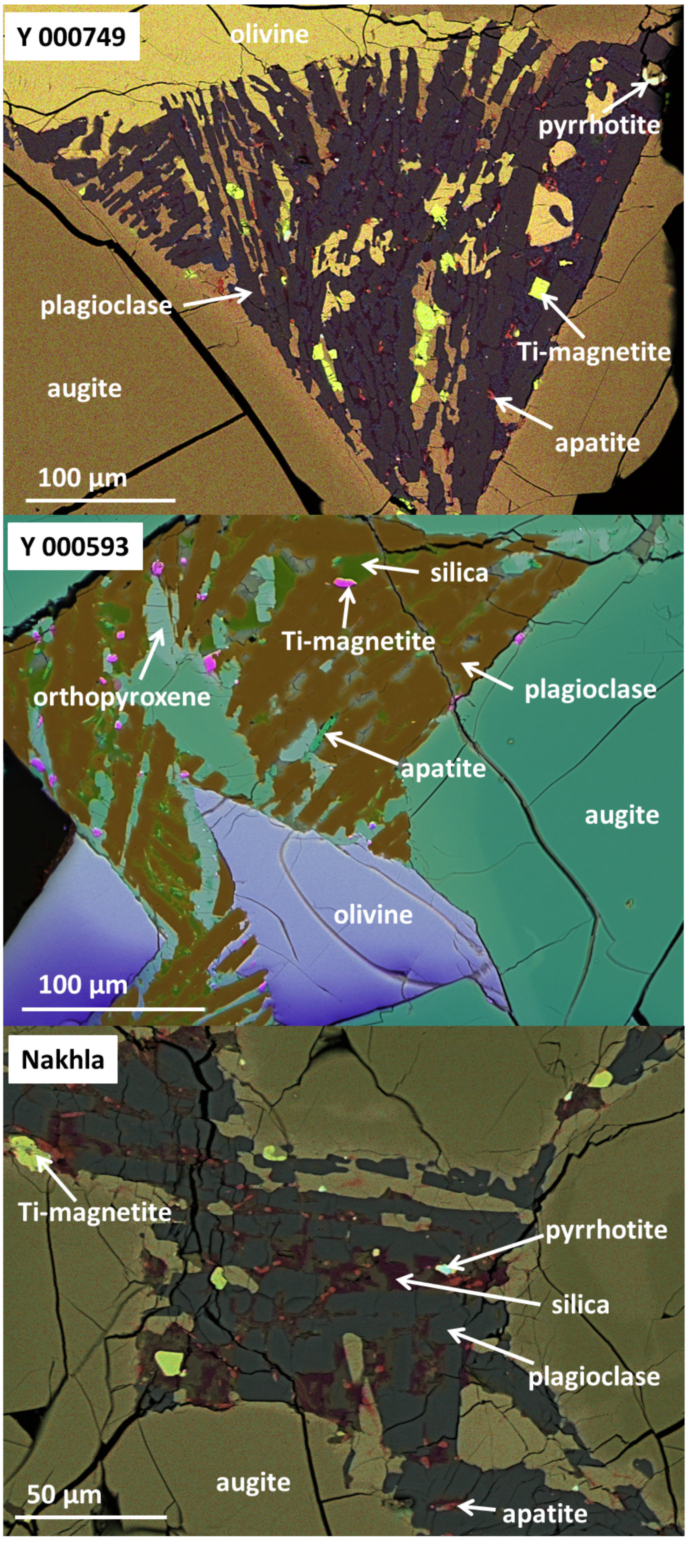

*Fig. 4.9: X-ray maps of the mesostasis of both Yamato meteorites and Nakhla. Their main feature is the occurrence of radiating laths of plagioclase. Interstitial to the plagioclase occurs olivine, low-Ca pyroxene, pyrrhotite and magnetite. Rare apatite and blobs of silica also occur.*

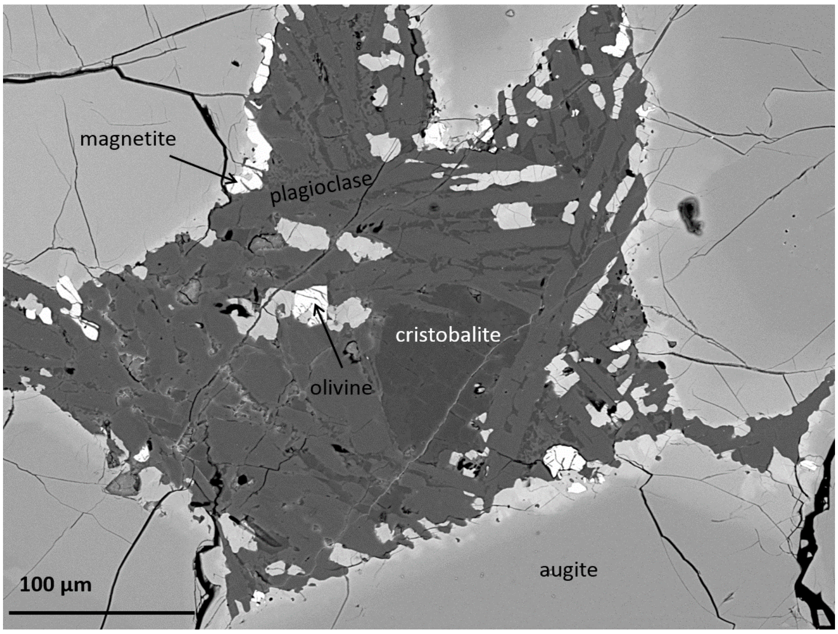

*Fig. 4.10: Mesostasis pocket in Y 000593 comprising laths of plagioclase, small grains of olivine and magnetite and large droplet-shaped crystals of cristobalite with its typical "cracked tile" texture. The absence of "voids" between cristobalite crystals suggests that they are a magmatic product and not shock-induced polymorphic transformation of quartz.*

03346 nakhlite meteorites (Fig. 4.9). The mesostasis within the Yamato and nakhla meteorites are composed of abundant radiating laths of plagioclase (dominating the mesostasis) and subhedra to anhedra Fe-Ti-oxides, low-Ca pyroxene, and olivine present amongst the plagioclase. Needle-shaped Cl-apatite and droplet-shaped Fe-sulfide mineral and silica identified respectively as pyrrhotite and cristobalite (Fig. 4.10) using Raman spectroscopy are also present. The main difference between the Yamato meteorites and Nakhla is the proportion of the mesostasis which tends to be smaller in Nakhla at least in our samples.

### *Mesostasis texture and mineralogy:Lafayette and NWA 998*

Lafayette and NWA 998 do not present a mesostasis as describes above. They are fully crystallized with compact subhedral to anhedral plagioclase, large Fe-Ti oxide grains, Fe-sulfide and Cl-rich apatite filling inter-cumulus space between augite and olivine phenocrysts (Fig. 4.11). The main difference between both meteorites is the size of the interstitial crystals especially plagioclase and apatite which are much larger in NWA 998. Both meteorites seem to lack the droplet-shaped silica (cristobalite) common in the other nakhlites. Nevertheless, NWA 998 contains remnants of silica-rich melt along plagioclase grain boundaries and pore corners. The silica melt was out of equilibrium with the mineral assemblage forming the rock matrix and has intensively reacted with previously formed minerals as indicate the mineral texture at the contact with the melt (Fig. 4.12).

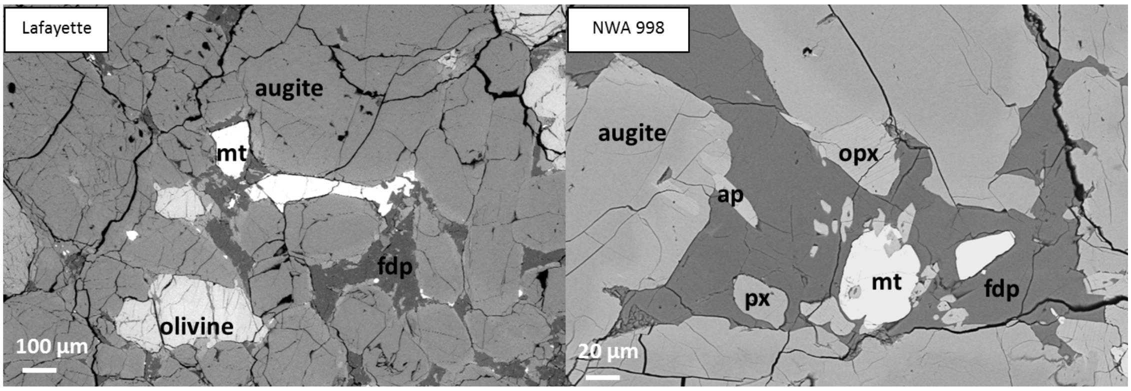

*Fig. 4.11: BSE images of the inter-cumulus mineral assemblage of Lafayette and NWA 998. Both meteorites are fully crystallized. Plagioclase (fdp) does not from lath as in the other nakhlites but anhedral grains. In lafayette, Ti-magnetite (mt) does not present the common ilmenite lamellae exsolution whereas olivine crystals show a continuous grain size from over 300 µm to 50 µm. Olivine in NWA 998 are only phenocryst a few hundreds of µm long.*

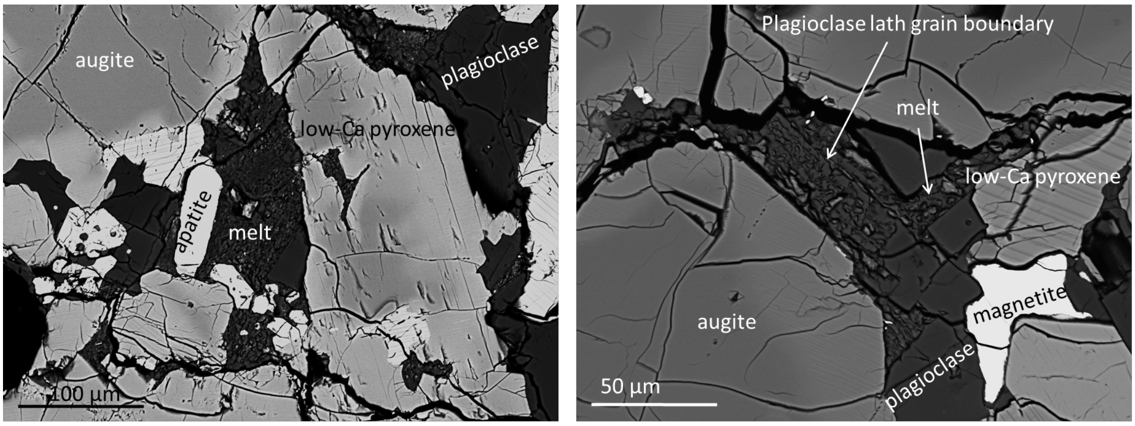

*Fig. 4.12: BSE images of the reactive melt present in NWA 998. The silica-rich melt was out of equilibrium with plagioclase and has partly dissolved it. The former grain boundary of the plagioclase lath can still be identified.*

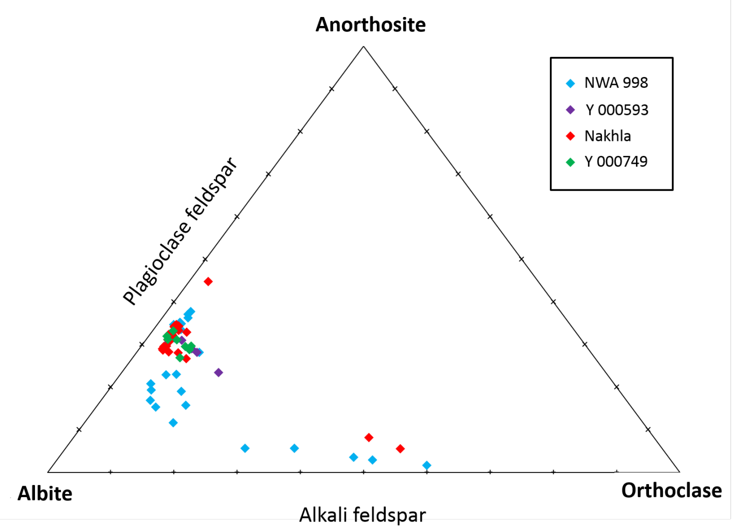

*Fig. 4.13: Feldspar composition of Nakhla, Y 000593, Y 000749, and NWA 998. The wide range of feldspar composition of nakhla and NWA 998 represents crystal zoning.*

### *Feldspar*

The nakhlites have two distinct feldspar populations: plagioclase and alkali feldspar (Fig. 4.13). The most evolved composition (alkali feldspar) is only found at grain boundaries where it represents fine normal crystal zoning. This compositional zoning is mostly present within NWA 998 and Nakhla. It may also occur in the Yamato meteorites but is too small to be clearly identified and quantitatively analysed using electron microscopy. Both mineral phases are apparently largely lacking in the nakhlite meteorites NWA 5790, NWA 817, and MIL 03346.

Feldspar in all the most coarsely crystallized nakhlites is largely dominated by plagioclase feldspar. The composition of the feldspar core between the different nakhlites is very similar ($\sim$ $An_{30\text{-}40}$). However, the major element compositions of feldspar rims within NWA 998 (and Nakhla) show a continuous, gradual decrease of $X_{\mathrm{An}}$ at the crystal margins. Major element diffusion in plagioclase is slow (Grove et al., 1984). Hence, a decrease in $X_{\mathrm{An}}$ of the plagioclase is more likely to reflect a progressive feldspar crystallization from a differentiating melt. The chemical zoning of feldspar shows a weak correlation to stratigraphic height within the cumulate pile. The presence of K-rich feldspars increases downward is the cumulate pile. They are mostly present in the lowermost sample NWA 998 and to less extent in Nakhla.

### *Fe-Ti oxides*

Fe-Ti oxides are common in all the nakhlite meteorites. They occur as large anhedral grain between olivine and augite phenocrysts in Lafayette and NWA 998 and small anhedral grain intercalated between plagioclase laths in the Yamato meteorites and Nakhla. In MIL 03346, NWA 817 and NWA 5790, they occur as large skeletal crystal. In all meteorites, except Lafayette and NWA 998, Fe-Ti oxides are (sometimes) partially enclosed within augite phenocryst rims suggesting that they

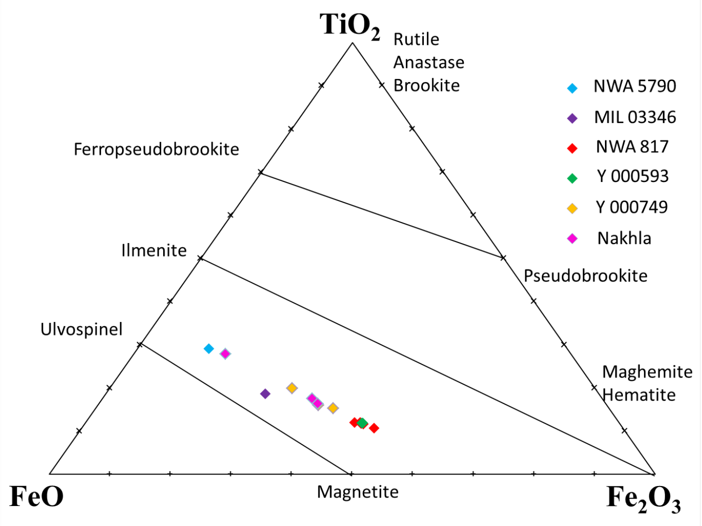

*Fig. 4.14: Oxide ternary diagram (FeO-$Fe_2O_3$-$TiO_2$) showing the high temperature solid solution series ulvospinel-magnetite, ilmenite-hematite, and ferropseudobroobite-pseudobrookite, plotted on a mol per cent basis. The oxide compositions are plotted after $Fe^{3+}$ stoichiometric recalculation.*

crystallized before or during the augite rims and that the augite rims probably represent crystal overgrowth and not late magmatic diffusional re-equilibration. The Fe-Ti oxides within all the nakhlites (Lafayette?) display a tweed pattern composed of Ti-rich exsolution lamellae, most probably ilmenite.

Iron-bearing oxides typically contain appreciable quantities of Fe in its oxidative state (i.e. $Fe^{3+}$) (Droop, 1987). Unfortunately, quantitative analyses using electron microscopy cannot detect the two oxidation states of Fe separately. If such a method is used, the $Fe^{2+}/Fe^{3+}$ ratio of the oxide has to be indirectly estimated. Re-calculation can be done because in order to maintain an electro-statical neutrality in the mineral, the negative charges brought by O (the only anion present in oxide) have to be balanced by positive charges brought by the cations. However, the charge balance method implies some assumptions: (1) that there is no vacant cation, (2) that Fe is the only element with variable valency, and (3) that there has been no goethite pseudomorphic transformation ($H^+$ that cannot be analysed using electron microscopy). The stoichiometric re-calculation does not reflect the real composition of the oxides, and contains uncertainties that are important to keep in mind during interpretation.

Figure 4.14 shows the oxide composition of the different nakhlites after $Fe^{3+}$ stoichiometric recalculation. Fe-Ti oxides in all the nakhlites belong to the ulvospinel-magnetite solid solution. However, they contain very fine oxidation-driven exsolution lamellae enriched in Ti, most probably ilmenite. Using electron microscopy, separate analyses of Ti-magnetite and ilmenite are not feasible, hence the data plotted on Fig. 4.14 correspond to a mixture of both mineral phases after recalculation of $Fe_2O_3$ and FeO proportion using charge balance and stoichiometry.

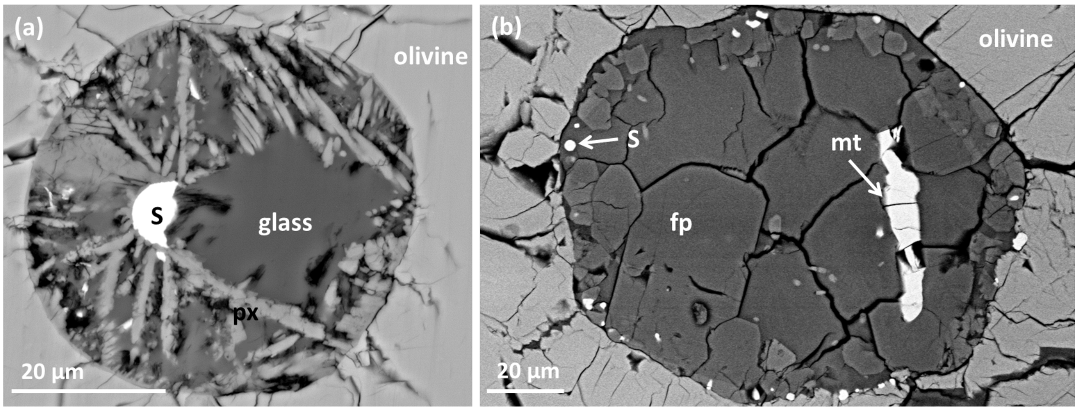

*Fig. 4.15: Poly-mineralic inclusions in olivine phenocrysts in NWA 817 (a) and Lafayette (b). The texture and mineralogy of the inclusions resemble those of the mesostasis. The inclusion in olivine from NWA 817 contain glass, sulfide (S) and skeletal low-Ca pyroxene, whereas Lafayette contain feldspar (fp), magnetite (mt) and sulfur.*

### 4.2.5 Magmatic inclusions

Augite and olivine phenocrysts contain inclusions which may provide important information to help understand the petrogenesis of the nakhlites. Large Ti-magnetite grains do also contain small inclusions but are much rarer. The inclusions are either mono-mineralic or poly-mineralic. Both may be very large, typically greater than 100 $\mu$m, although all other smaller size of inclusions occur. Olivine commonly bear both types of inclusions, whereas augite and large Ti-magnetite contain mostly mono-mineralic inclusions.

Mono-mineralic inclusions in olivine correspond to augite. They are subhedral and have the same composition as the core of the augite phenocrysts. They correspond to the early crystallized subcalcic augite entrapped during olivine growth. The poly-mineralic inclusions in olivine phenocrysts typically have a spherical or ellipsoidal shape and display a complex mineralogical assemblage. Both the mineralogical composition and texture of the inclusions are very similar to those of the mesostasis. In all the nakhlites, the poly-mineralic inclusions within olivine phenocrysts contain variable proportions of pyroxene, magnetite, feldspar and rare and tiny apatite and sulfide droplets with or without glass (Fig. 4.15). The only difference between the nakhlites is the texture of the poly-mineralic inclusions, especially the crystal size, shape and spatial distribution. The larger crystal grains within poly-mineralic inclusions occur in NWA 998. Rarely, poly-mineralic inclusions contain spherical void spaces which could be vesicles, “fossilized” gas bubble that formed because of vapour phase segregation during crystallization.

Large inclusions in augite phenocrysts are much less common. They are smaller than in olivine (rarely exceed few tens of $\mu$m), are almost exclusively mono-mineralic (except in MIL 03346) and only occur close to the rim. Mono-mineralic inclusions can either be glass or tiny Fe-oxide or sulfide droplet-shaped crystals trapped within the augite rims along grain boundaries. Glassy inclusions within augite phenocrysts have a very heterogeneous chemical composition within a single inclusion, as expected from amorphous product. From BSE images, it is clear that the inclusions and their augite host have intensely exchanged with the crystal host to form reaction rims surrounding the inclusions (Fig. 4.16). The glassy inclusions are commonly rich in Si, Al and to less extent Na and are depleted in all other elements. They contain more Na than K. The reaction rims around the glassy inclusions have roughly similar chemical composition to the augite rims. The tiny inclusions of oxide and sulfide grains are too small ($\ll 1\ \mu$m) to be analysed but seem to be mostly composed of Fe and devoid of Ti.

The presence of poly-mineralic inclusions in augite phenocrysts seems to be restricted to MIL 03346. They occur both central to the phenocrysts and along rims. The largest ones are tens of $\mu$m large and the smallest ones only a few $\mu$m. They all have a glassy matrix of similar chemical composition but display an increasing number of different mineral phases with increasing inclusion size. Commonly, the poly-mineralic inclusions contain a mesostasis-like texture and mineralogy. The inclusions have a poorly crystallized groundmass and commonly display relatively large Fe-Ti-oxide or Fe-sulfide grains. Tiny apatite grains are also very common within the glassy matrix but are difficult to recognize because of their small size. In our sample, no fayalitic olivine or pyroxene have been detected in the mineral assemblage of the melt inclusions. However, a Cl-rich mineral phase is common in most melt inclusions. It correspond to chloro-amphibole, a mineral phase recognised by Sautter et al. (2006). The main differences between poly-mineral phase inclusions and mesostasis is the presence of Cl-amphibole and feldspar in the largest (few tens of $\mu$m large) inclusions and the absence of fayalitic olivine. The inclusions have probably undergone a slower cooling rate than the mesostasis which could have allowed feldspar to precipitate. The presence of Fe oxide and sulfide demonstrate that the magma was almost saturated relative to these phases at the time of entrapment. The presence of traces of Cl has also been detected in the glassy matrix of a poly-mineralic inclusion in olivine of NWA 817.

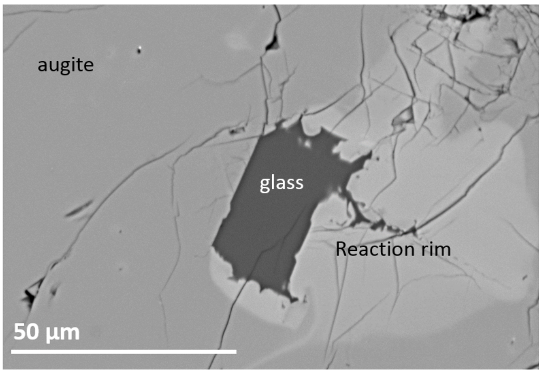

*Fig. 4.16: Large glassy inclusion in an augite phenocryst in Y 000593. The inclusion and its host have intensely exchanged elements to form a halo around the inclusion.*

Large Ti-magnetite grains rarely display small glass inclusions. A small augite inclusion has also been found in a compact Ti-magnetite in NWA 998. The augite inclusion has a mineral composition ($En_{34.1}Fs_{30.9}Wo_{35.0}$) roughly similar to the rims of the augite phenocrysts. Hence, the titanomagnetie probably crystallized post-emplacement after crystallization of augite rims.

## 4.3 Bulk chemical composition

### 4.3.1 Major element composition

The nakhlite meteorites are all basaltic rocks (Fig. 4.17). They are all largely depleted in alkali elements. Plotted on a Total Alkalis *vs.* Silica (TAS) diagram for volcanic rocks, the nakhlite meteorites show a differentiation trend toward more andesitic compositions, with NWA 817 being the most evolved meteorite. The increase in $SiO_2$ correlates positively with an increase in $Na_2O$ and $K_2O$. The differentiation trend does not follow the stratigraphic position of the different nakhlites within the presumed cumulate pile model of Mikouchi et al. (2012), but as the nakhlites' bulk rocks are not representative of their parent magma (because they are cumulate rocks) this cannot be an argument against the cumulate pile model. The nakhlites have very similar whole rock chemical composition of major and minor elements (Fig. 4.18), which is consistent with their identical mineralogy and relatively similar modal abundance. They are very poor in alkali (Fig. 4.17) and Al (Fig. 4.18) relative to Martian rocks and soils analysed at robotic landing sites and from orbiting spacecraft but also relative to common crustal basaltic rocks from the Earth (Fig. 4.19 and 1.4), a chemical feature shared by all Martian meteorites analysed so far ((McSween et al., 2009)). The depletion in Al is believed to reflect an early depletion of the mantle source regions through repeated partial melt events (Longhi, 1991; McSween et al., 2009). Bulk rock composition of the nakhlite meteorites are enriched in Fe relative to Earth basaltic rocks (Fig. 4.20, Bridges and Warren (2006)), which may reflect the general greatest FeO content of the primitive mantle of Mars compared to the Earth' mantle estimated by geophysical data (Bertka and Fei, 1998). The constant lower bulk rock Mg $\sharp$ between the basaltic Martian meteorites and analogous terrestrial mafic–ultramafic igneous rocks (and moon rocks) further indicates the likely more ferroan composition of the mantle of Mars (Bridges and Warren, 2006).

### 4.3.2 Trace element composition

#### Whole rock

The first common feature of the nakhlites' bulk rock geochemistry is their enrichment in trace elements relative to chondrite, with elemental abundances $\gg 1$ (Fig. 4.21). All the nakhlites are enriched in LREEs relative to HREEs. They present parallel whole rock REE abundance patterns but with distinct concentration increasing from NWA 998 to Nakhla, Lafayette, Y 000593, MIL 03346 and finally NWA 817 (Fig. 4.21). The fractionation of the LREEs relative to HREEs is similar in all nakhlites as underlined by their respective La/Yb ratio (Fig. 4.21). Only NWA 817 shows a slightly more fractionated REE pattern but this reflects the relative high La content relative to other nakhlites including MIL 03346.

As incompatible elements, the REEs (especially the LREEs) remain preferentially in the melt phase during crystallization. Thus, the mesostasis probably records the greatest abundance in REEs. The different abundance patterns between the nakhlites could reflect the difference in mesostasis proportion within the different meteorites, whether they sample the same igneous body or not. The overlapping REE abundances of MIL 03346 and NWA 817 may reflect a cessation of

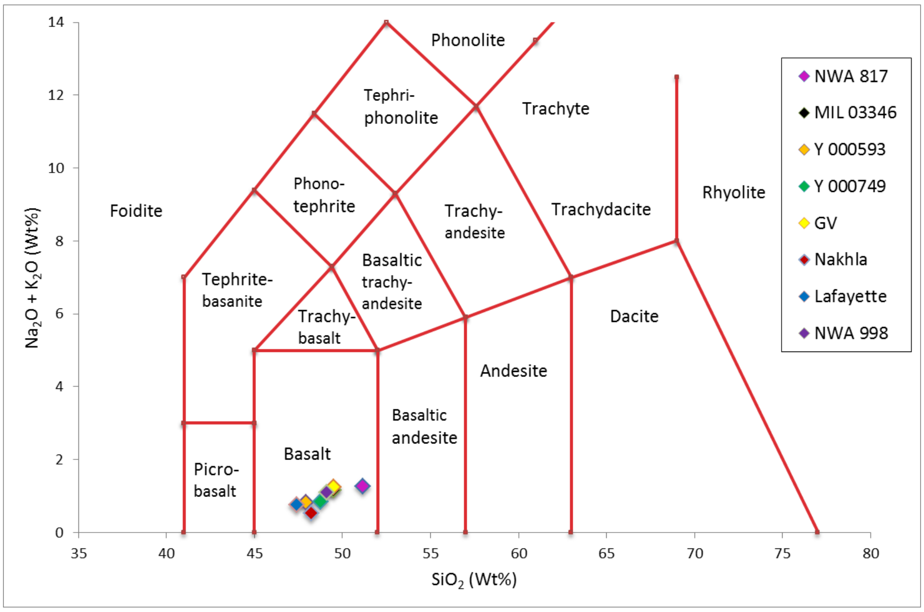

Fig. 4.17: *Total Alkalis vs. Silica diagram for volcanic rocks (TAS; Le Maitre et al., 1989) showing the classification of the nakhlite meteorites bulk rock. MIL 03346 (Day et al., 2006), NWA 817 (Sautter et al., 2002), Y 000593 and 000749 (Imae et al., 2003), GV (Gomes and Kiel,1980), Nakhla (McCarthy et al., 1974), Lafayette (Boctor et al., 1976), NWA 998 (Treiman and Irving, 2008).*

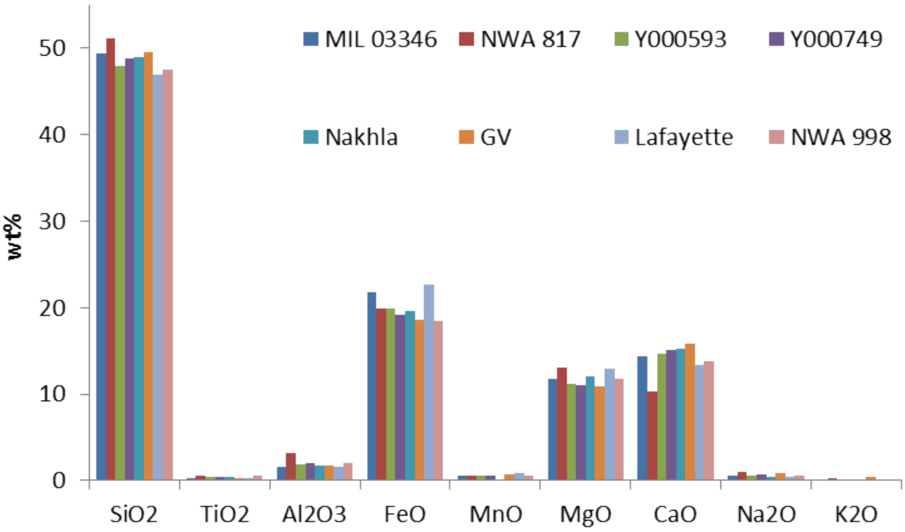

Fig. 4.18: *Bulk rock major and some minor elements composition of the different nakhlite meteorites. MIL 03346 (Day et al., 2006), NWA 817 (Sautter et al., 2002), Y 000593 and 000749 (Imae et al., 2003), GV (Gomes and Kiel,1980), Nakhla (McCarthy et al., 1974), Lafayette (Boctor et al., 1976), NWA 998 (Treiman and Irving, 2008).*

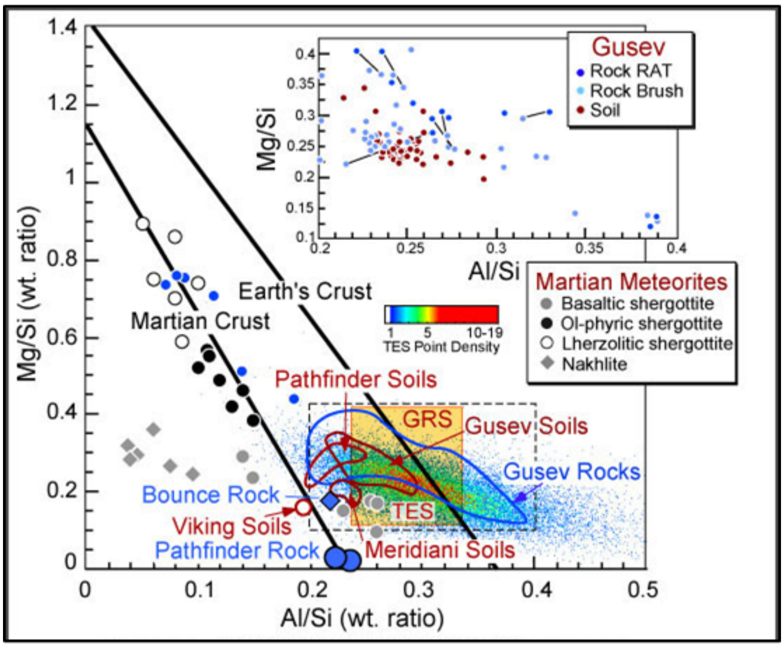

*Fig. 4.19: Mg/Si vs. Al/Si diagram of Martian meteorites, rocks and soils obtained at robotic landing sites and from orbiting spacecraft. The values for the Earth' s crust is given for comparison. Mg/Si vs. Al/Si are commonly used to differentiate Martian meteorites from terrestrial rocks. The Martian meteorites sampling the sub-surface of Mars is commonly depleted in alkali and Al relative to rocks and soils from Mars top surface (Fig. 1.4), McSween et al. (2009).*

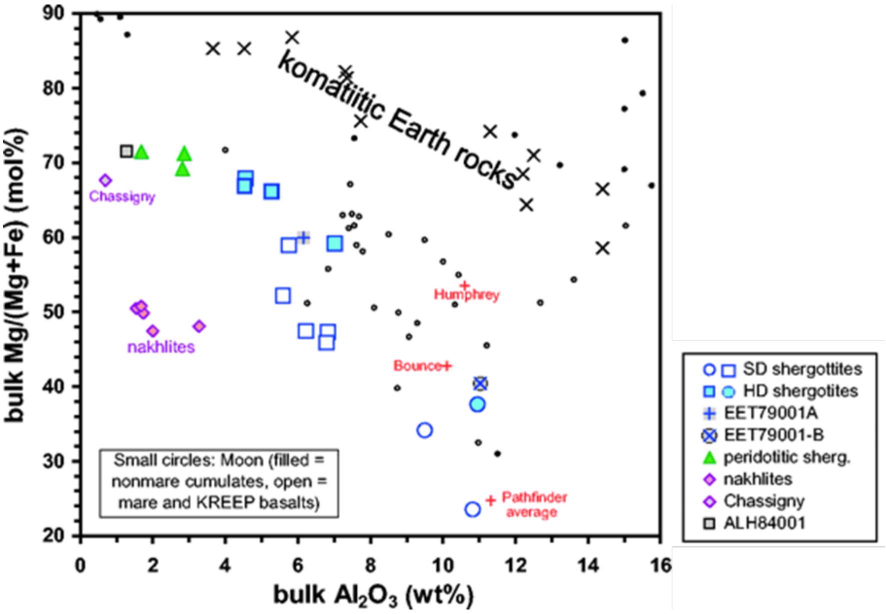

*Fig. 4.20: Bulk rock Mg/(Mg+Fe) vs. $Al_2O_3$ of the SNCs Martian meteorites and lunar and komatiitic Earth rocks. Martian meteorites are commonly enriched in Fe. Graph modified from Bridges and Warren (2006).*

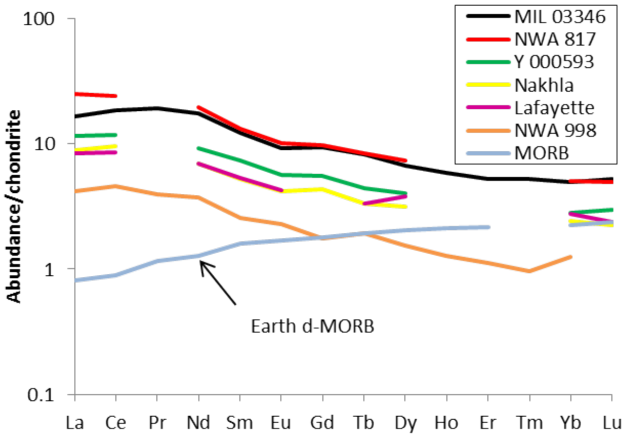

| | Eu/Eu* | La/Yb |
|---|---|---|
| MIL 03346 | 0.85 | 4.863 |
| NWA 817 | 0.883 | 7.222 |
| Y 000593 | 0.884 | 6.039 |
| Nakhla | 0.876 | 5.384 |
| Lafayette | | 4.494 |
| NWA 998 | 1.067 | 5 |

*Fig. 4.21: Whole-rock REE abundances of different nakhlites (Treiman and Irving, 2008) and depleted mid-ocean ridge basalt (Earth d-MORB) for comparison. This rock type is believed to represent a rough approximation of the upper Earth's mantle (Workman and Stanley, 2005). REE abundances are normalized to CI chondrite (McDonough and Sun, 1995). Eu/Eu$^*$ represents an interpolated value of the size of the Eu anomalie. The La/Yb ratios provide an indication of the fractionation slope of the REEs.*

fractional crystallization, which is consistent with their glassy, crystal-poor mesostasis and the absence of plagioclase. If the varying REE abundances represent the different modal proportions between the nakhlites then both NWA 817 and MIL 03346 should have the highest enrichment in LREES (highest La/Yb ratio) while Lafayette should be the most depleted meteorite as it contains the greatest proportion of olivine and that olivine is a mineral phase commonly depleted in REEs (Foley et al., 2013).

All nakhlites have slight negative Eu anomalies with the exception of NWA 998 which has a slight positive Eu anomaly (Fig. 4.21). The Eu anomalies are commonly expressed as

$$\mathrm{Eu} / \mathrm{Eu}^* = \mathrm{Eu} / (1/2\ (\mathrm{Sm} + \mathrm{Gd}))$$

which represents a measure of the size (or strength) of the Eu anomalies relative to other element abundances. The Eu anomalies in the nakhlites may result from feldspar crystallization and settling out from the melt. NWA 998 has the largest feldspar plagioclase population which could explain its slight positive Eu anomaly (substitution of $\mathrm{Ca}^{2+}$ by $\mathrm{Eu}^{2+}$), whereas the other nakhlites with their slight negative Eu anomalies could reflect an early gravitational loss of Eu-bearing feldspar plagioclase (into NWA 998?). However, the positive Eu anomaly in NWA 998 could also reflect more reducing conditions experienced by this meteorite during crystallization. None of the nakhlites seem to display a Ce anomaly, either positive or negative, that commonly results from terrestrial weathering (Crozaz et al., 2003), although it is difficult to clearly identify it with the absence of a value of Pr for most nakhlites.

The REEs are commonly mobilized, fractionated, and precipitated during aqueous alteration (Crozaz et al., 2003). In general the REE abundances, especially the LREE, increase with the degree of aqueous alteration. The poor overall degree of aqueous alteration of the nakhlites should not and apparently did not significantly affect the whole rock REE composition and pattern. The best example is probably Lafayette which is the most altered nakhlite meteorite. Its REE patterns and abundance almost perfectly overlap with Nakhla a much less aqueously altered meteorite. The REE patterns of the different nakhlites most probably reflect the mantle processes that generated the basic magmas and their crystallization histories.

### *Augite*

The REE abundances and patterns in augite phenocrysts vary between the nakhlite meteorites but also within a single nakhlite (Fig. 4.22). Surprisingly, none of the augite from the nakhlite meteorites have the typical HREE enrichment characteristics of the high-Ca pyroxenes (White, 2013), but are rather slightly enriched in LREEs. Within all the nakhlites, the REE patterns of the augite phenocrysts present an upward trend from La to either Nd (NWA 5790, NWA 817, Y 000749, and NWA 998) or Sm (Y 000593 and nakhla), and a downward trend from Sm to Lu. Most of of the augite patterns have very slight negative Eu anomalies or no anomalies at all. Rims of augite phenocrysts have slight positive Eu anomalies suggesting a co-precipitation with plagioclase.

The REE patterns (chondrite CI normalized, McDonough and Sun (1995)) from augite phenocrysts irrespective of the nakhlite meteorites have similar shape. However, the abundances of each elements within a single augite consistently vary by a factor of few units, the absolute abundances of REE increasing from core to rim with no disruption in the general patterns. Both NWA 5790 and NWA 998 have rim zones too thin (NWA 5790) or difficult to identify (NWA 998) to be analysed using the LA ICP-MS technique. The core of augite phenocrysts in both Y 000749 and Nakhla have the lowest REE abundances with more or less chondritic value for the light and middle REEs (except a clear depletion in La).

Multi-element diagrams normalized to CI chondrite (McDonough and Sun, 1995) show the abundances of LILEs and HFSEs of augite phenocrysts from different nakhlites (Fig. 4.23). All spider diagrams show a slight enrichment of the HFSEs relative to chondrite values, especially within augite from the nakhlites NWA 5790 and NWA 817, or roughly chondritic values. All patterns display sharp negative anomalies in Zr, and positive anomalies in Ti. The positive and negative anomalies within all the nakhlittes are similarly developed. All nakhlites display an increasing trace elements content toward the rims (with increasing degree of melt fractionation) with a decrease of the Zr negative anomalies but less obvious changes in the positive Ti anomalies. With the exception of two patterns from the augite rims in NWA 817, the LILEs Rb and Ba are depleted relative to CI chondrite composition ($<1$ on the log scale). In all nakhlites cumulus augites, Th is the most depleted element. Thorium is largely below detection limits in most analyses.

The nakhlites Nakhla, Y 000593 and Y 000749 have all their augite rims depleted in Sr unlike NWA 817 which displays strong Sr and Ba enrichments in certain augite phenocrysts including the augite rim. The high Ba and Sr abundances may record incorporation of crustal material. Thorium and to less extent Nb seem to have been the most incompatible elements in augite phenocrysts within all nakhlites.

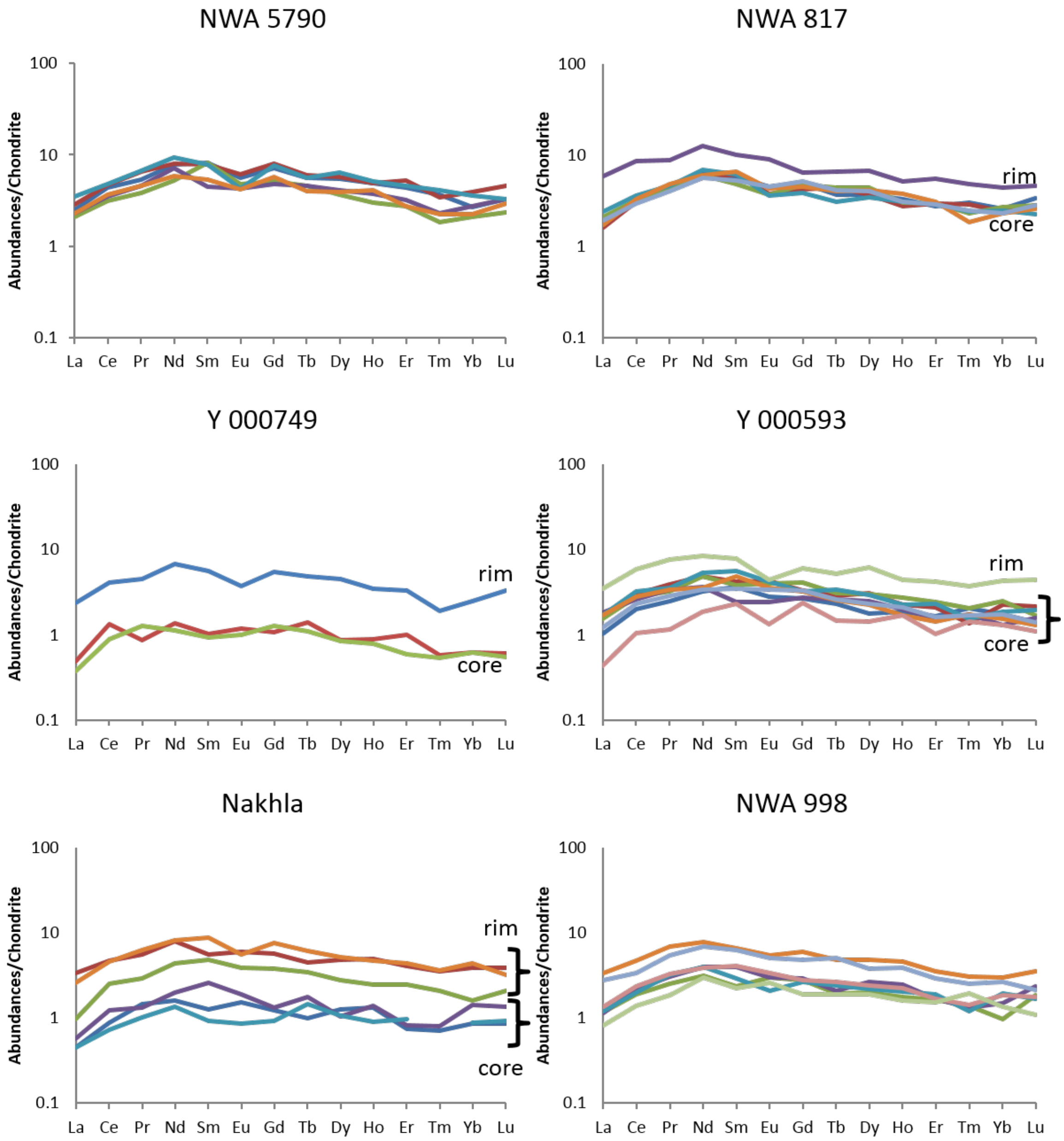

*Fig. 4.22: REE abundances in augite phenocrysts normalized to CI chondrite (McDonough and Sun, 1995) from different nakhlite meteorites. NWA 5790 and NWA 998 do not have rims thick enough to be analysed using LA ICP-MS technique.*

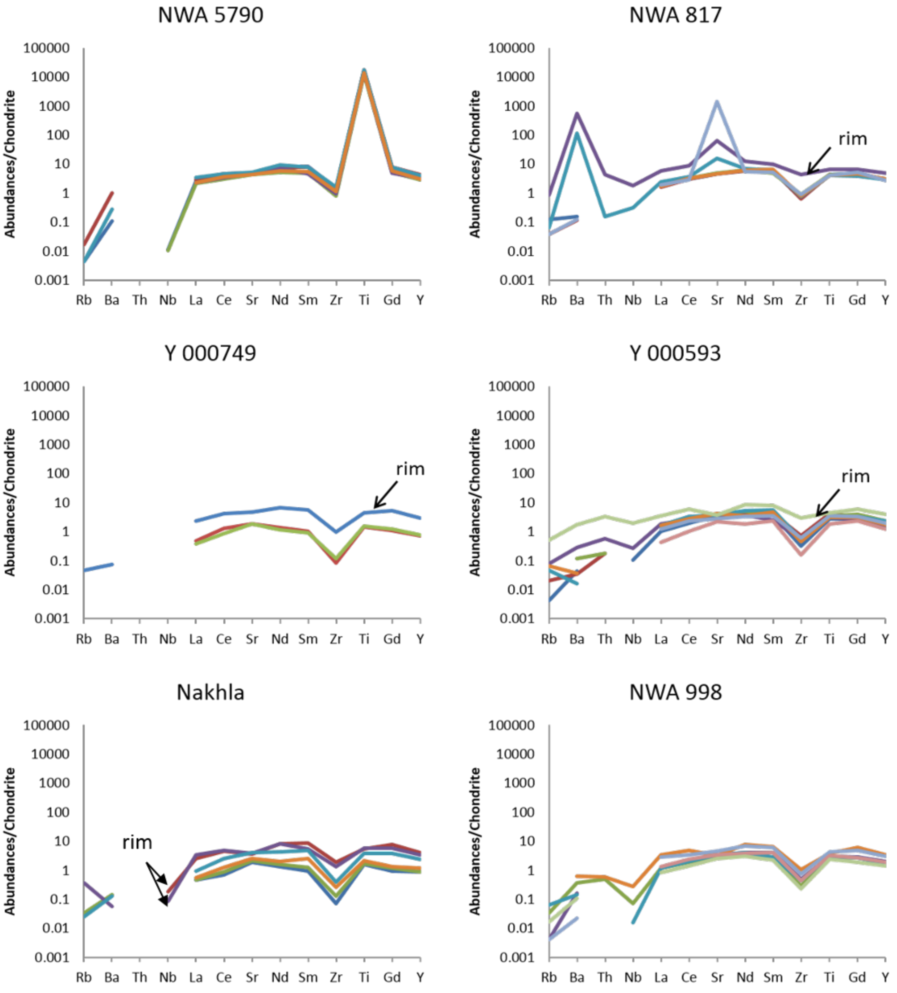

*Fig. 4.23: CI chondrite normalized (McDonough and Sun, 1995) trace element patterns (HFSE and LILE) from augite phenocrysts from different nakhlite meteorites. The lack of abundances for certain elements result from a concentration below the detection limits.*

Despite these similarities, the nakhlites NWA 5790 and NWA 817 have distinct multi-element patterns. Augite phenocrysts within both nakhlites are more enriched in incompatible elements relative to the other nakhlites. In addition, like for the REE patterns, nakhlite NWA 5790 have multi-element patterns which do not display abundance variation from one augite to another.

### *Plagioclase*

Only Y 000593 and NWA 998 contain plagioclase crystals large enough to be analysed using LA ICP-MS technique. REE abundances within the feldspar populations (plagioclase and K-feldspar) from Y 000593 and NWA 998 have roughly similar REE patterns but less marked similarity in their LILEs and HFSEs patterns (Fig. 4.24). The feldspars from both meteorites show an enrichment in REE abundances from the earliest formed plagioclase (core) to the K-feldspar (rim). All REE patterns show a strong fractionation with an enrichment in LREEs (up to almost 100 times

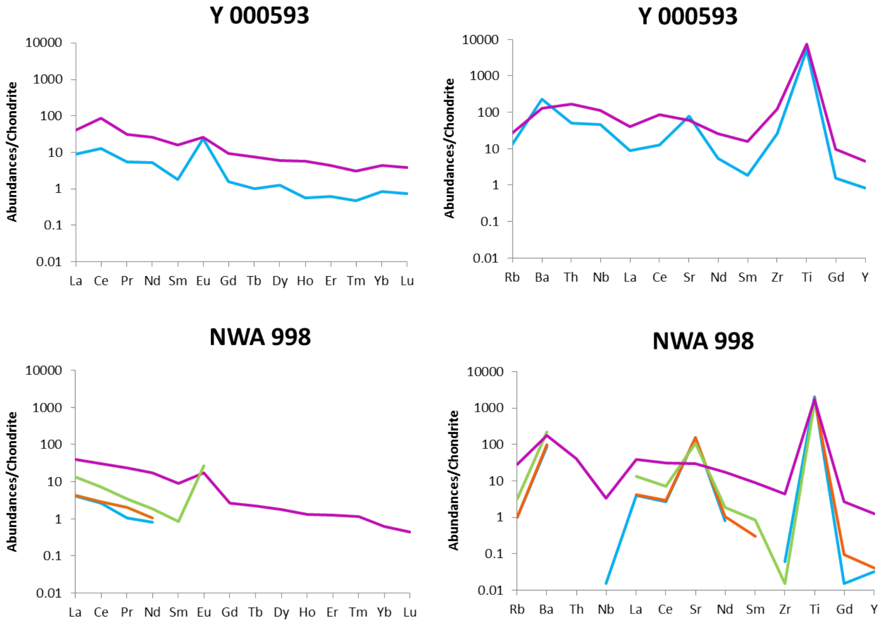

*Fig. 4.24: CI chondrite normalized (McDonough and Sun, 1995) REE (left) and HFSEs and LILEs (right) abundances in plagioclase and K-feldspar (pink) from Y 000593 and NWA 998. The absence of abundances for certain elements results from a concentration below the detection limits.*

the chondritic abundances for the K-feldspar) to approximately chondritic value for the HREEs. However, the REE abundances in both feldspar populations (i.e. plagioclase and K-feldspar) are more enriched and less fractionated in Y 000593 than in NWA 998. Plagioclase have strong positive Eu anomalies, showing a substitution of Ca by Eu.

The HFSEs and LILEs are relatively enriched in feldspar in both Y 000593 and NWA 998, although much greater in the former with abundances always $\gg 1$ (Fig. 4.24). Like for the REEs, HFSEs and LILEs in the K-feldspar are enriched relative to the plagioclase. Both meteorites have their plagioclase and K-feldspar strongly enriched in Ti (like augite). However, the feldspars in Y 000593 do not display the Zr negative anomalies like its augite population and NWA 998. Both nakhlites display a marked Sr enrichment in their plagioclase but not K-feldspar, which reflects a Ca-Sr substitution in the plagioclase. The highest Sr abundances in the plagioclase relative to Eu in both Y 000593 and NWA 8998 may reflect a preferential incorporation of Sr over Eu in the Ca site. The inter-cumulus melt that crystallized plagioclase in Y 000593 was therefore more enriched and fractionated than that which crystallized NWA 998.

### *Low-Ca pyroxene*

Rare Earth Elements and selected HFSEs and LILEs CI chondrite-normalized (McDonough and Sun, 1995) of low-Ca pyroxene (the replacing product of olivine and plagioclase) in the nakhlites Y 000593, Nakhla and NWA 998 are presented in Fig. 4.25. The REE abundances and patterns strongly differ between the nakhlites. In

Y 000593, the REE patterns are flat and just a few units above the CI chondrite values. Low-Ca pyroxene in Nakhla are strongly enriched in REEs, especially in the LREEs, and fractionated; a very unique REE pattern. The low-Ca pyroxene in NWA 998 are in general depleted in LREEs relative to the HREEs although the LREE abundances strongly vary between the different low-Ca pyroxene grains. Europium anomalies are either positive or negative in Y 000593 and NWA 998. The only REE pattern of low-Ca pyroxene in Nakhla has a negative Eu anomaly, however the occurrence of positive anomalies in the low-Ca pyroxene within the meteorite cannot be excluded.

High Field Siderophile Elements and LILEs of the nakhlites Y 000593, Nakhla, and NWA 998 display few similarities (Fig. 4.25). They are strongly enriched in Ti, Ba, and Th, and have negatives anomalies in Nb and Zr. The low-Ca pyroxene in Nakhla is the most enriched in HFSEs and LILEs with abundances a few units above the CI chondrite except for Rb and Nb. Nakhla and some low-Ca pyroxene in NWA 998 have Sr negative anomalies, whereas Y 000593 has either no or positive Sr anomalies. The low Sr abundance in the low-Ca pyroxene suggest that plagioclase was probably not an important mineral phase in the development of the low-Ca pyroxene. Trace elements are very depleted in olivine and most of them below detection limits using LA ICP-MS, hence the general high abundances of the trace elements imply the involvement of another material rich in incompatible trace elements.

### *Glass*

Trace elements in primary glass within the meteorite NWA 817, Nakhla and NWA 998 have been analysed (Fig. 4.26). The glass analysed in NWA 817 corresponds to the very finely crystallized mesostasis and not a glass sensu stricto (i.e. amorphous material). It contains abundant sprays of tiny apatite grains (a mineral carrier of REEs) that cannot have been avoided during the analyses. However, the similarity in patterns and abundances within both analyses from this meteorite suggests a relatively homogeneous mesostasis composition, including apatite content and distribution. The REE abundances in the glass are much greater than in the whole rocks. The glass within the meteorite Nakhla is the most fractionated with a strong enrichment in LREEs, as shown in the REE abundances of its low-Ca pyroxene. Both NWA 817 and NWA 998 have parallel REE patterns with NWA 817 more enriched in REEs than NWA 998. The REEs patterns of both nakhlites are parallel to that of their respective whole rock unlike Nakhla whose glass REE pattern is much more strongly fractionated.

The HFSEs and LILEs of the glass and glassy mesostasis have very similar patterns to the low-Ca pyroxene, a strong Ti peak, an enrichment of Ba or Th and a depletion in Nb and Zr (Fig. 4.25, 4.26). Despite similar patterns, abundances of trace elements in the glass are in general greater than in the low-Ca pyroxene, with the exception of Nb and Zr in Nakhla that are more strongly depleted in the glass than in the low-Ca pyroxene.

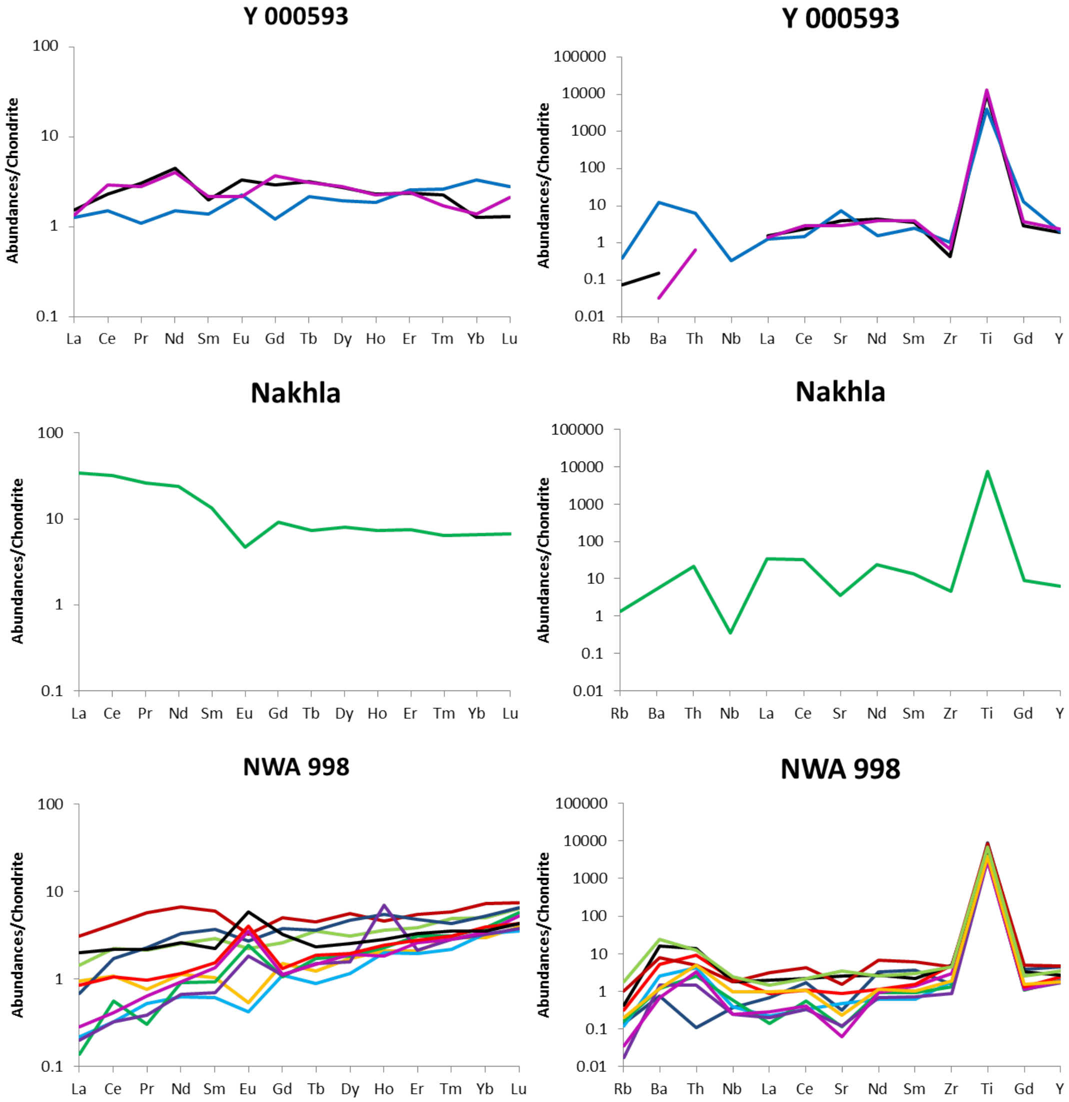

*Fig. 4.25: REEs (left) and selected HFSEs and LILEs (right) abundances in orthopyroxene, the replacing product of olivine phenocryst and plagioclase, from three nakhlite meteorites (Y 000593, Nakhla, and NWA 998). The trace element abundances are normalized to CI chondrite (McDonough et al., 1995).*

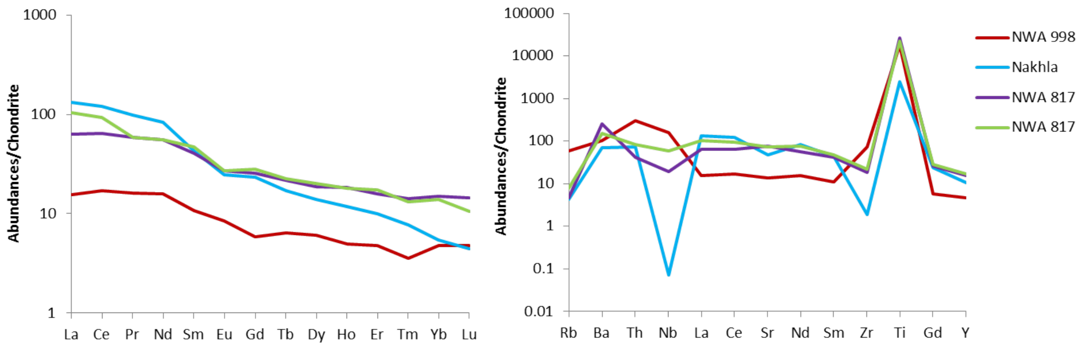

*Fig. 4.26: REE (left) and selected HFSE and LILE (right) abundances normalized to CI chondrite (McDonough and Sun, 1995) in glass (Nakhla and NWA 998) and poorly-crystallized mesostasis (NWA 817).*

## 4.4 Fractional crystallization-driven magmatic differentiation

### 4.4.1 The nakhlites are complex basaltic rocks

The nakhlite meteorites are most likely fragments of a young sub-surface Martian basaltic crust (Treiman et al., 1993). The best arguments in favour of an igneous origin are probably their mineralogy (pyroxene, olivine, plagioclase and Fe-Ti-oxides), mineral chemistry and texture (large cumulus crystals in a fine-grained groundmass), and bulk rock composition (TAS diagram), which are similar to terrestrial basaltic rocks. The nakhlites crystallized from basaltic magma(s) (Treiman et al., 1993), that formed by partial melting of the mantle. Their whole-rock composition is enriched in REEs, especially the most incompatible LREEs, although the fractionation of the REEs is very small (Fig. 4.21). Such REE patterns are characteristic on Earth of a low degree of partial melting; a characteristic shared amongst the nakhlites. Small degrees of partial melting have also been inferred to explain the large fractionation of the calculated time-integrated $^{147}$Sm/$^{144}$Nd ratios of the nakhlite source region and the $^{147}$Sm/$^{144}$Nd ratio of Nakhla (Shih et al., 2010; Treiman, 2005).

Because the nakhlites are cumulate rocks, their bulk chemical compositions do not represent the parental basaltic magma composition (Treiman, 2005). The nakhlites are differentiated basaltic rock. Their bulk chemical compositions and mineralogy result from complex and continuous magmatic differentiation and segregation processes whose nature, duration and chronology are difficult to constrain (Treiman, 2005). However, clues about the fractionation processes of the parent basaltic magma(s) have still been recorded in the crystallization sequence and chemical composition of the respective solid phases.

### 4.4.2 Fractional crystallization

#### Fractionation of phenocrysts

The mineralogy of the nakhlite meteorites and mineral chemistry are consistent with a formation of the meteorites by fractional crystallization of basaltic magma(s)

(Treiman et al., 1993; Treiman, 2005). The chemical composition of augite phenocrysts (the first-crystallized mineral phase, i.e. liquidus phase) reflects mineral-basalt element partitioning. The large cores are magnesian and rim zones are progressively enriched in incompatible elements (i.e. Na, Ti, Al) and depleted in compatible elements (i.e. Cr), an expected pattern in crystals that grew from a continuously fractionating (i.e. crystallizing) magma in a closed system (Fig. 4.3). However, the constancy of major element abundances (i.e. Mg, Fe, and Ca) throughout the large phenocryst cores (Fig. 4.3) most probably reflects a early crystallization in an open system possibly during the (slow) rise of the magma(s) where melt differentiation is unlikely, although a early crystallization within large hypabyssal igneous body(ies) with continuous diffusional re-equilibration can also be considered.

The excess of augite phenocrysts within the nakhlites and their preferential alignment likely shows cumulate processes post emplacement with augite grains settling out from the basaltic magma(s) (Bunch and Reid, 1975; Friedman-Lentz et al., 1999; Day et al., 2006). The apparent lack of rims at augite-augite boundaries (and not at rim-mesostasis boundaries, Fig. 4.1) suggests rim crystallization from inter-granular fractionated melts post-emplacement and cumulus processes. The preservation of oscillatory/growth zoning (or rapid change in composition during crystal formation) of minor elements (Fig. 4.3) and the absence of obvious patchy zoning within the large augite core of NWA 5790, MIL 03346, and NWA 817 (Fig. 4.1) indicates little or no post-cumulus diffusional modification unlike the other nakhlites. The significant enrichment in Ca, Ti, Al and Na in augite rims in NWA 817 (Fig. 4.3) indicate a sudden increase in crystal growth rate, while the sharpness of the core-rim boundaries, constant rim thickness and preservation of the crystal shape (Fig. 4.1) suggest no hiatus between the core and rim formation. This feature is probably shared with NWA 5790 and MIL 03346.

The crystallization history of the olivine grains is less obvious. It is not clear if they represent a pre- or post-cumulate mineral phase. The large crystal size (sometimes larger than augite) and euhedral to subhedral shape of certain olivine grains may suggest a pre-cumulate crystallization as for augite (Fig. 4.4). However, olivine phenocrysts commonly poikilitically, either partially or completely, enclose large augite grains. The augite inclusions do sometimes occur central to the olivine phenocrysts and have the same composition as the augite phenocrysts core. The textural relationships suggest that olivine most probably began to crystallize slightly after augite. Large olivine grains, especially within Y 000593, fill space available between augite phenocrysts (Fig. 4.4) suggesting that olivine have grown faster than augite and/or have continued to grow after cessation of augite crystallization. However, the olivine texture does not give irrefutable evidence regarding the pre- or post-emplacement environment of the early olivine core crystallization.

The chemical composition of igneous minerals reflects the melt composition at the time the minerals crystallized with likely post-solidification chemical exchanges with the fractionated melt (Simkin and Smith, 1970). Olivine phenocrysts in NWA 817 and Nakhla display two different zoning patterns of major and minor elements, one central to the grains and one throughout the rim thickness. The fine-scale chemical variations within the olivine cores may represent a relic of the original fractionation (i.e. oscillatory zoning) that commonly develops during crystal growth, whereas sharp changes in elemental abundances and distribution patterns within the rims may reflect solid-melt re-equilibration exchanges (Fig. 4.5). Variations in rim thickness between the nakhlites and their apparent lack of fine-scale oscillatory zoning provide evidence that solid-liquid re-equilibration processes have indeed occurred. If the different zoning patterns of the olivine cores do represent original fractionation then complete post-growth re-equilibrium with the melt has not been reached and olivine cores may still represent their original composition. The olivine phenocrysts in Nakhla and NWA 817 have cores relatively poor in Mg which suggests that olivine may have begun to crystallize from a fractionated melt (and so after the large augite cores), which is consistent with the olivine texture in the nakhlites.

Olivine phenocrysts in Y 000749 are all (and the most) depleted in Mg and enriched in Fe (Fig. 4.5). They display relatively constant concentration of the major and minor elements except for their Na abundances. They have probably completely re-equilibrated with the late evolved melt. Olivine phenocrysts in NWA 998 and NWA 5790 do not display obvious elemental fine or large-scale zoning (Fig. 4.5). They may either have completely re-equilibrated with a less evolved late melt or not at all.

Solid-liquid diffusional re-equilibration during late-stage magmatic processes is both temperature and time dependent (Simkin and Smith, 1970). Olivine crystals within the quickly chilled margin of an igneous body retain a more primitive composition than olivine in the slowly cooled interior. With this in mind, progressively wider rim zones in olivine grains are expected in the slowest cooled igneous bodies (Simkin and Smith, 1970). Based on chemical variations of the olivine, the Yamato meteorites (Y 000749 and Y 000593) appear to have been the most re-equilibrated nakhlites. Their olivine phenocrysts are largely depleted in Mg and enriched in Fe, especially if compared to the other nakhlites (Fig. 4.27), and do not display obvious normal or oscillatory zoning. The Yamato meteorites could have undergone the slowest cooling rate of the nakhlites which could have given time for the olivine to completely re-equilibrate with the melt. Nonetheless, the olivine within the Yamato meteorites could also have crystallized relatively late during the crystallization history from a more differentiated melt which is consistent with their poikilitic texture. The chemical compositions of the olivine phenocrysts from the Yamato meteorites are consistent with crystallization from a chemically fractionated, slowly cooled interior of an igneous body. The most primitive olivine composition is displayed by the olivine core in NWA 817. However, olivine phenocrysts within NWA 817 also display the widest chemical variation. Olivine composition within NWA 817 is consistent with crystallization from a differentiating melt and relatively fast cooling to avoid extensive (i.e. in depth) sub-solidus chemical re-equilibration.

In their study, Simkin and Smith (1970) demonstrated a pressure dependence of the amount of Ca an olivine can incorporate in its structure during its crystallization. Olivines crystallizing in a high pressure environment (i.e. plutonic environment) are commonly more depleted in Ca than olivines crystallizing in a shallow magmatic environment. With this in mind, one can say that NWA 998 with its low Ca content in olivine crystallized in the deepest environment which is consistent with its unique gabbroic texture; whereas NWA 817, Y 000593 and NWA 5790 crystallized in a stratigraphically higher environment, and Nakhla and

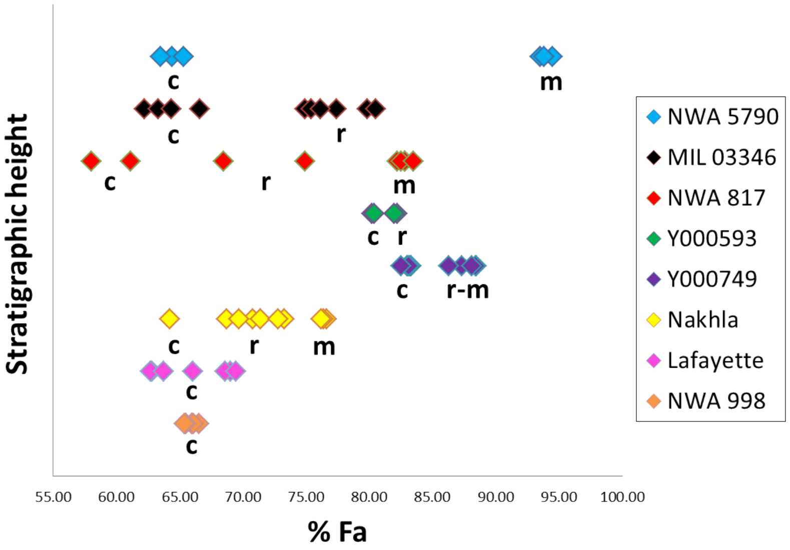

*Fig. 4.27: Evolution of the composition of olivine phenocrysts core (c) and rim (r), and small olivine grain in the mesostasis (m) expressed as fayalitic percentage (% Fa) within the different nakhlites presented in their believed stratigraphic position (Mikouchi et al., 2012). The different core composition of olivine from Lafayette represent different grain populations (i.e. grain size).*

Y 000749 intermediate. Calcium abundance within the olivine phenocrysts and the degree of post-crystallization re-equilibration with the melt are both consistent with a crystallization of the different nakhlites under different physical and chemical conditions within the parental igneous body(ies).

Commonly, cumulate piles show variations in the distribution of olivine phenocrysts because of the physical mechanisms (crystal settling and flow accumulation) operating during the differentiation processes of the igneous bodies. Such variations are relatively predictable and show a decrease of olivine abundances upward in cumulate piles. The distribution of olivine phenocrysts in the nakhlites is erratic. In our samples, Lafayette and NWA 817 are the main olivine-bearing nakhlites, although they sample the lower and upper parts of the postulated cumulate pile, respectively. In both meteorites, olivine populations form relatively well distributed clusters of subhedral grains (a feature only found in these two meteorites) although olivine phenocrysts from NWA 817 are somewhat larger, an unexpected feature. Olivine grains from MIL 03346 (whose thermal history is similar to NWA 817) display rare, sparse and skeletal olivine grains. Its olivine grains are also larger than the two former meteorites. The skeletal texture of large olivine grains in MIL 03346 (a unique characteristic of this nakhlite) is inconsistent with contemporaneous crystallization in the same shallow magmatic system as the (subhedral) olivine phenocrysts of the other nakhlites. The poikilitic texture of olivine in the Yamato meteorites with olivine filling spaces between augite phenocryts also suggests a post-cumulus crystallization of olivine. The distribution and composition of olivine in the nakhlites cannot be explained by a physical sorting by size and weight during igneous emplacement but by kinetic effects associated with contrasting physical conditions in the final magmatic environment.

Large Ti-magnetite most probably crystallized early. They rarely contain small augite inclusions whose composition is similar to the augite phenocryst cores. They are also partially enclosed within augite phenocryst rims. Hence, like the olivine phenocysts, they probably crystallized slightly after the onset of augite crystallization but before and/or during the formation of augite rims. The skeletal texture of the Ti-magnetite grains of NWA 817 and MIL 03346 is typical of non-equilibrium crystallization in quickly cooled rocks. Consequently, it is more probable that the oxides crystallized post-emplacement despite their crystal size of a few tens of $\mu$m long.

Augite, olivine, and Ti-magnetite represent the early stages of magma crystallization pre- and post-emplacement. Based on textural relationships and major and minor element composition of the three different mineral phases, it is very probable that augite cores crystallized first from the most primitive magma followed by the crystallization of augite rims and both olivine and Ti-magnetite. The latter two probably crystallized in-situ more or less contemporaneously from a progressively differentiating basaltic melt in the final (sub-)surface environment. Variations in element composition and distribution patterns in olivine and olivines texture between the nakhlites probably reflect different kinetic effects.

### *The role of trapped melt and post-cumulus processes*

Accumulation of phenocrysts within an igneous body commonly leads to the development of a crystal framework with pockets of melt filling inter-cumulus spaces. At the time of crystal accumulation, both crystals and “trapped” melts are in chemical equilibrium (Hardie and Eugster, 1970). However, as further crystallization of the crystal mush layer proceeds, the physico-chemical conditions of the inter-cumulate melt evolve and may strongly diverge relative to the bulk magma or the magma at the time of entrapment, giving rise to different crystallization paths of the inter-cumulus melt throughout cumulate piles (Holness et al., 2011). The compositional evolution of the inter-granular melt is dependent on the interconnectivity between the inter-granular melt pockets and the magma pool above the cumulate layer. If melt communication is maintained, crystallization of the interstitial melts produce relatively unzoned overgrowth on cumulate phases with possibly slightly fractionated mineral phases but no evolved mineral phases. However, if communication is lost, the interstitial melts progressively fractionate, continuously crystallizing more evolved mineral phases. During fractional crystallization, trapped melts become more and more in disequilibrium with the surrounding cumulate crystals and may react with the latter, changing the chemical composition of both solid and trapped melt (Holness et al., 2011). Mechanical compaction of the cumulate pile may also affect the chemical evolution of the trapped evolved melts by reducing the crystal mush permeability, squeezing melt out of the cumulate layer, and mixing melts (with possibly different degrees of evolution) that come from different part of the igneous body. The different cooling rates of the different layers within a cumulate igneous body is also an important factor as it controls diffusion processes including the degree of solid-melt chemical re-equilibrium (Holness et al., 2011). Cumulate processes can result in the development of strongly stratified igneous bodies.

The nakhlite meteorites all contain an inter-cumulus mesostasis. The mesostasis represents the solidified product of the post-cumulus differentiated basaltic melts. As such, it may provide information about the igneous conditions and processes within the shallow Martian crust. The nakhlite meteorites have very similar mineralogy and chemical compositions especially those of the large augite cores. However, they present subtle textural and chemical variations which reflect contrasting physico-chemical conditions during post-emplacement solidification. The most obvious difference is the texture of the mesostasis which is glassy-poorly crystallized in NWA 817, NWA 5790 and MIL 03346, finely crystallized in the Yamato meteorites and Nakhla, and completely crystallized in Lafayette and NWA 998. The meteorites mesostasis texture can be directly related to different cooling rates undergone by the different meteorites; the more crystallized, the more slowly cooled.

At the contact with the mesostasis, augite and olivine cumulus phases within all the nakhlites commonly display ferroan rims, overgrowths and diffusive re-equilibration zonation evidencing: (1) a chemical disequilibrium between the cumulate phases and the late inter-cumulus melts; and (2) a certain degree of differentiation of the interstitial melt through, most probably, fractional crystallization. Like the mesostasis texture, the thickness of olivine phenocryst zoning reflects the different cooling rates experienced by the different nakhlites. Olivine phenocrysts from NWA 817 have thick and strongly zoned rims but may have preserved primary composition within their core suggesting crystallization from a fractionating melt with not enough time for "in depth" post-crystallization exchanges. The meteorites Y 000593, Y 000749, and possibly NWA 998 (absence of an obvious zoning pattern) have olivine phenocrysts that have intensely or completely re-equilibrated with the melt showing a slower cooling rate. Olivine phenocrysts in Y 000593, Nakhla, Lafayette and NWA 998 have been locally replaced by orthopyroxene late in the rock solidification history suggesting that the last inter-cumulus melts were probably still at rough sub-solidus temperatures.

In most nakhlites, the mesostasis contains abundant lath-shaped plagioclase feldspars. They commonly radiate from the augite phenocrysts and are intercalated with low-Ca pyroxene overgrowths onto augite phenocrysts. The spatial distribution, size and shape (euhedral to subedral) of the plagioclases suggest that they crystallized post-emplacement from relatively un-crystallized residual melts to have sufficient space in order to form well-shaped crystals. The plagioclases are poor in Fe and Ti and do not display any obvious zonation relative to these elements. Titanium content within plagioclase has been shown to reflect the crystallization path of residual melts, especially the onset of Fe-Ti-oxide crystallization (Humphreys, 2009). The chemical composition of the plagioclase suggests crystallization most probably occurred after olivine and titanomagnetite but contemporaneous with the pyroxene overgrowths on augite phenocrysts. The absence of Ca depletion within augite rims in NWA 817 could be related to the apparent lack of obvious plagioclase crystals within the meteorite; Ca preferentially partitioning into plagioclase.

The plagioclase feldspars do not display compositional changes between the nakhlites; the "early" residual melts followed a similar crystallization path. Only NWA 998, and to less of an extent Nakhla, contain rare alkali feldspar mostly as very thin zoning along plagioclase grain boundaries and as poorly crystallized material within pore corners, where the last inter-cumulus melts resided before complete rock solidification. The presence of thick rim zones in plagiocale within NWA 998 suggests a high degree of evolution of the interstitial melt possibly associated with a very poor communication of the last melts with the rest of the igneous body.

Within pore corners, the poorly crystallized melt with an alkali feldspathic composition has a rough-bubbly texture that may reflect either a poor crystallization due to a drop of temperature (i.e. quenched effect) during the very last igneous stage or a post-magmatic partial melting event (as Treiman and Irving (2008) already suggested). The partial melting could have been associated or not with a partial released of semi volatile elements such as K and Na that could account for the bubbly texture. Possible explanations for the increase in temperature could be either magmatic with the emplacement of a new igneous body in the vicinity (through heat diffusion) or post meteorite impact due to the release of energy through heat.

A droplet-shaped silica mineral also occurs in all nakhlites except NWA 5790, NWA 998 and Lafayette. When in contact with other mineral phases such as plagioclase or Fe-oxide, the silica interfaces are straight. The silica shape is controlled by the adjacent materials. Its singular texture suggests that the silica is a residual melt that possibly results from Si-rich melt segregation. The silica mineral corresponds to the high temperature silica polymorph cristobalite (identified using Raman spectroscopy). The lack of textural features indicating a decrease in volume (from $\alpha$-quartz 22.688 cm$^3$/mol to $\alpha$-cristobalite 25.925 cm$^3$/mol, Smyth and Bish (1989)) of the silica phase argues for a magmatic origin of the latter and not a metamorphic (impact-induced) polymorphic transformation of quartz.

The mesostasis petrogensis provides evidences of high chemical evolution of the interstitial melt. But does the mesostasis in each nakhlite represent a closed or open magmatic system? A relatively closed system fractionation of the interstitial melt is inferred from the sharp cumulate mineral zonation and late solid-melt diffusional re-equilibration exchanges. The occurrence of highly evolved mineral phases such as alkali feldspar and silica provide further evidence of extensive fractional crystallization up to possibly the generation of silica melt immiscibility. However, the chemistry of the plagioclase from the different nakhlites (when present) is particularly constant and unzoned. Hence, it is possible that at least a small inter-pore chemical diffusion leading to a relatively homogeneous melt composition has occurred in the very early stage of mesostasis solidification. Yet, the limited abundance of K-feldspar (in pore spaces) and apparent lack of silica (cristobalite) in NWA 998 and Lafayette may reflect an almost complete “loss” of the last highly fractionated melt in both rocks (except in pore corners). The residual melt removal was probably concurrent with mesostasis crystallization, possibly because of the progressively increasing crystal load leading to compaction and reduction of crystal mush permeability during mesostasis crystallization. It is possible that the maximum rock compaction occurred after the crystallization of laths of plagioclase to give them time and space to crystallized as euhedral, chemically homogeneous crystals.

If we assume that the nakhlites crystallized form the same magma pool and that at the time of augite accumulation, cumulate crystals and trapped melts are in chemical equilibrium then crystallization of sealed inter-cumulus melt pockets of the different nakhlites should result in the formation of relatively similar mineral phases albeit with different modal proportion depending on the size of the melt pockets. The mesostasis in the nakhlites NWA 998 and Lafayette lacks small augite and olivine grains that seem to have crystallized after plagioclase feldspar in the other nakhlites based on their occurrence along plagioclase laths (interstices). However, it is possible that they have been removed with the squeezed melt during the process of compaction. Both meteorites also contain orthopyroxene that are lacking in the other meteorites, except in Y 000593 and Nakhla.

Apatite is an ubiquitous mineral phase in all the nakhlites, however it displays interesting variations in grain texture and spatial distribution. The glassy mesostasis of NWA 817, NWA 5790, MIL 03346 and to less an extent Nakhla contains sprays of tiny apatite grains that are thoroughly distributed within and between inter-cumulus mesostasis pockets. The large and even distribution of apatite indicates that the melt was homogeneously saturated relative to apatite ($P_2O_5$) in the parental magma(s). The Yamato meteorites also contain abundant sprays of tiny apatite grains but also $\mu$m- large euhedral to subedral grains of apatite. In NWA 998, apatite grains are euhedral to subedral and few tens of $\mu$m-long. They occur mostly as clusters confined in certain inter-cumulus areas. The occurrence of clusters of apatite and their erratic distribution within the rock indicate that the residual melt was chemically inhomogeneous (at least relative to $P_2O_5$) in the most coarsely crystallized rock, which provides further evidence of a lack of melt communication between the different melt pockets.

The nakhlites' mesostasis differs from one another in some respects in their post-cumulus products. Their most obvious differences include their texture and degree of chemical reactions between the phenocryst phases and the inter-cumulus melts. Both igneous features reflect different thermal histories experienced by the nakhlites. Another difference is the variation in accessory mineral distribution and proportion, including K-feldspar and apatite. Both mineral phases commonly crystallized late from highly fractionated melt once saturation in the incompatible elements K and P, in basaltic melt, is achieved. The P and K contents of basaltic magmas are not affected by chemical re-equilibration with the cumulate phases (i.e. olivine and augite). As such, both K-feldspar and apatite are important mineral phases for tracing the distribution and degree of evolution of fractionated residual melts. The different texture and erratic distribution of both mineral phases reflect divergent chemical evolution of the late inter-cumulus melts with heterogeneous melts occurring in the most slowly cooled cumulate layers. During the crystallization of the mesostasis, the cumulate body(ies) underwent a progressive decrease of melt mobility which has led to the divergent degree of evolution of the last residual melts before their mobilization by rock compaction, the more coarsely crystallized Lafayette and NWA 998 being the most affected. The variations in both texture and mineral composition of the mesostasis amongst the nakhlite meteorites provide evidence of a structured parental igneous body(ies) with contrasting physico-chemical conditions and little to no communication throughout the cumulate body(ies) prior to complete rock solidification.

## 4.5 Magmatic inclusions: A key for better understanding early magma composition

As igneous rock derived from basaltic magma, the nakhlites are important sources of information about mantle and magmatic processes on Mars. However, the initial chemical composition of the nakhlites parent magma(s) and the fractionation paths which have led to the final composition of the nakhlites remain to date uncertain (Treiman, 2005). Determining the nakhlites' parent magma composition is not straightforward because the nakhlites are cumulate rocks and their bulk composition do not represent the parental magma composition. The presence of melt inclusions (droplets of magma trapped in crystal defects during its growth) may therefore potentially offer a great opportunity to access the magmatic composition including volatile elements at the time of crystal host crystallization (i.e. melt entrapment, Kent (2008)). Nevertheless, special care has to be taken when dealing with magmatic melt inclusions as (1) they may represent the compositional boundary layer at crystal/melt interface (this problem may arise especially when dealing with small inclusions and/or fast growing phenocrysts) and (2) during and after entrapment they chemically react (i.e. exchange) with the host crystal, an unavoidable process at magmatic temperatures (Kent, 2008).

The nakhlites present different types of inclusions: mono-mineralic and poly-mineralic. Mono-mineralic are either crystal inclusions or glass inclusions, whereas poly-mineralic inclusions display complex textures (from fully crystallyzed to vitrophyre) and mineral assemblage with or without glass. However, two questions arise: (1) do the magmatic inclusions really represent entrapments of melt droplets or embayements of a (partly crystallized) mesostasis; and (2) have they been completely isolated from the external inter-cumulus melt? The first question requires detailed petrographic study while the second is more difficult to assess from 2D thin sections. The presence of volatile elements in the melt inclusions from crystal that crystallized in a deep environment demonstrates that the inclusions were sealed during crystal growth.

### 4.5.1 Mono-phase inclusions in augite, olivine and magnetite

Glassy inclusions are common in augite phenocrysts in all nakhlites, although they are also present in large (and not skeletal) Ti-magnetite. However, they are absent in olivine phenocrysts. Glass inclusions are evenly distributed throughout the augite phenocrysts and display very irregular shapes and various size up to a few tens of $\mu$m-large, although they are most commonly a few $\mu$m-large. They generally form clusters in the pyroxene cores and sometimes contain droplet-shaped Ti-magnetite grains ($< 1$ $\mu$m). In augite phenocrysts, glass-bearing inclusions have intensively chemically exchanged with the mineral host as evidenced by reaction rims at the inclusion-mineral host contact (Fig. 4.16). Hence, they have not preserved their original composition. The inclusions are chemically heterogeneous within a single inclusion as expected from amorphous products. In both Ti-magnetite and augite, their compositions are always largely dominated by Si ($\geq 65$ wt%) although they also contain Al (especially in Ti-magnetite-hosting inclusions) but almost no K and Na. The occurrence of glass inclusions is difficult to understand and has been the subject of controversy about the basaltic nature of the nakhlites (Varela et al., 2001, 2003). The composition of glass inclusions is roughly similar to feldspar (although more depleted in alkali elements) or feldspathic glass found in the mesostasis. The presence of "anomalous" glassy inclusions reflects most probably entrapments of melt droplets as no such igneous material has been found in the mesostasis final product (Fig. 4.16). No "pure" glass has been found in the rock's matrix including in the glassy mesostasis of certain nakhlites that always contain crystal seeds. Glass inclusions may represent the "depleted" melt layer at the crystal boundary which could explain the absence of at least crystal seeds although their relatively large size of a few tens of $\mu$m disfavour this hypothesis. They may also represent feldspar crystal amorphized by the impact of meteorite (maskelynite?). This hypothesis is unlikely as maskelynite or shock-induced crystal amorphization have not been found in any nakhlites' mesostasis.

It is impossible to know if the chemical exchange between the melt inclusions and their crystal host resulted after the melt entrapment or as a result of heat release through induction by the impact-launching event. However, it should be noted that the reaction rims are chemically similar to the augite rims. As such, they most probably represent a differentiated melt trapped during the crystal growth that has actively exchanged prior to complete solidification. The glass inclusions occur generally within the large homogeneous phenocryst cores. They provide evidence that the magma from which augite phenocrysts crystallized was already fractionated and that the large augite core composition did not record the early melt differentiation, but rather reflect the physical conditions under which augite crystallized.

The non primitive nature of the nakhlites' parent magma(s) has already been suggested by Treiman (2005), based on comparison between the Mg values of the inferred parent magma of the nakhlites and those of the augite and olivine phenocrysts. Furthermore, the glass inclusions are depleted in K relative to Na, a chemical feature shared with the glassy mesostasis. The depletion in K relative to Na probably reflects a characteristic of the composition of the nakhlites' parent magma(s) and does not result from complex magma differentiation processes. Olivine phenocrysts in all nakhlites commonly contain sparse subhedral augite inclusions with a chemical composition similar to the cores of augite phenocrysts. Augite inclusions represent crystal entrapments during olivine growth. Both augite and olivine crystallized from the same parental magma while augite crystallized first.

### 4.5.2 *Poly-phase inclusions in augite and olivine*

Poly-mineralic inclusions are present in olivine in all nakhlites but absent in augite with the exception of MIL 03346. The origin of the poly-mineralic inclusions is puzzling as they are very similar in texture and mineralogy to the mesostasis suggesting that they may represent mesostasis embayment and not melt entrapment (Fig. 4.15, 4.29). However, the small size of the minerals in inclusions, their different crystal shape and their spatial orientation (crystallization from the inclusion walls toward the center) and distribution (from high temperature mineral along inclusion walls to lower temperature mineral feldspar or glass central to the inclusion) suggest that the magmatic inclusions are magma droplets trapped during crystal growth. The magmatic inclusions probably solidified later once sealed from the magma pool. Another argument for post-entrapment crystallization are the radiating fractures surrounding the inclusions that probably result from an increase in volume during melt solidification (Fig. 4.29). The melt inclusions often occur central to the phenocrysts. Hence, they most probably represent the early melt from which the phenocrysts crystallized.

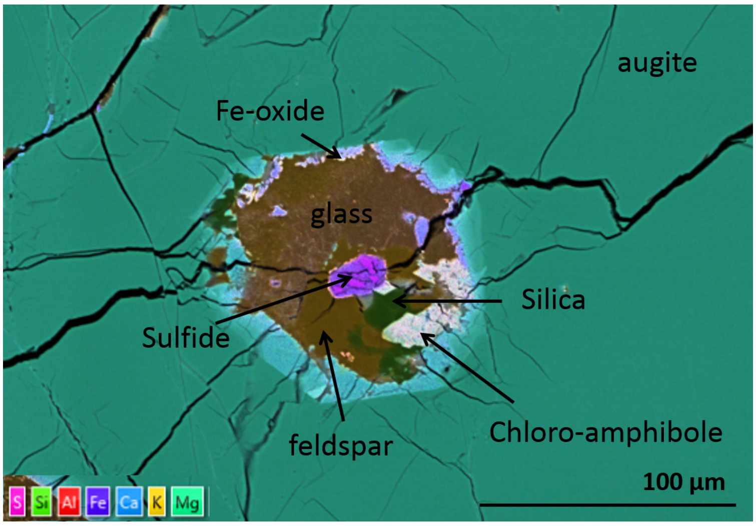

*Fig. 4.28: Polyphase inclusion in an augite phenocryst from MIL 03346. The inclusion has the same texture as the mesostasis. It contains an highly altered sulfide mineral (pink) transformed into Fe-oxide (purple), feldspar, Cl-amphibole, a silica phase and abundant apatite at the nm-scale (pinkish dots embedded in the glass.*

### *Volatile-bearing inclusions in MIL 03346: Evidences for Cl-rich magmatic fluids*

Poly-mineral inclusions are rare within augite phenocrysts in the nakhlite meteorites. They are much more frequent in olivine phenocrysts. However, augite-hosted poly-mineralic inclusions are common in the nakhlite MIL 03346. The augite-hosted poly-mineralic inclusions in MIL 03346 present a surprising mineralogy different from the mesostasis as they contain feldspar and Cl-amphibole identified by Sautter et al. (2006) but no fayalitic olivine (Fig. 4.28). The occurrence of feldspar in the inclusions and not in the mesostasis probably reflects the lower cooling rate in the inclusions than in the mesostasis where the slow crystallization rate has enabled feldspar saturation within the melt to be reached before complete melt solidification. It is most probable that feldspar would have crystallized within the MIL 03346 mesostasis if the cooling rate had been slow enough. The poly-mineralic inclusions contain a silica phase and widespread apatite embedded in glass but with no preferential alignment as in MIL 03346 mesostasis (Fig. 4.28). The glassy matrix of the poly-mineralic inclusions is depleted in K relative to Na, a chemical feature shared with the rock mesostasis. The unique mineralogy of the multi-phase inclusions in MIL 03346 indicates that the melt inclusions crystallized once sealed.

The occurrence of Cl-amphibole in the inclusions is surprising as no amphibole has ever been found in any of the nakhlites except in certain augite inclusions in MIL 03346 (Sautter et al., 2006). Cl-amphibole is known to precipitate as a result of hydrothermal or metasomatic activity and not as a primary magmatic product (Mazdab, 2003). Hence, the presence of Cl-amphibole most probably demonstrates the existence of high temperature chlorine-rich fluids in the magmatic environment. The occurrence of hydrothermal or metasomatic fluids in all of the largest (tens of $\mu$m large) augite-hosted inclusions suggests that augite phenocrysts began to crystallize in a deep environment where pressure was high enough to prevent gas phase separation (from fluid or melt) and its subsequent lost from the igneous body. The precipitation of Cl-rich amphibole within melt inclusions suggests that the inclusions have been sealed quickly from the rest of the melt in the deep magmatic environment to prevent Cl exsolution and removal as apparently occurred in the mesostasis; the solubility of Cl in $H_2O$-under-saturated magmas being strongly pressure-dependent and having only a weak temperature-dependence (Webster, 1997). The origin of the Cl-rich fluid is difficult to determine. It can either result from hydrosaline fluid separation from the parent melt or from an external hydrothermal fluid which has co-existed with the melt at the time of melt entrapment.

The different mineralogy between poly-mineralic inclusions and mesostasis (presence of feldspar and Cl-amphibole and absence of fayalitic olivine in the inclusions) suggests that the magmatic inclusions represent droplets of melt trapped during crystal growth and not mesostasis embayments. The different mineralogy between melt inclusions and mesostasis are possibly the result of a different line of descent experienced by the melt inclusion because of contrasting physico-chemical conditions including oxygen fugacity (i.e. $fO_2$), cooling rate and pressure (due to the absence of volatile degassing). The position of the melt inclusion central to augite phenocrysts attests to an early melt entrapment from a largely uncrystallized magma. At such an early magmatic stage, occurring most probably deep in the crust and at high temperature and pressure, the co-existence of magma with external hydrothermal fluids is less likely. If correct, the Cl content provides evidence for juvenile Cl-rich fluid separation processes from the supercritical parental fluid during cooling and crystallization. The generation of hydrosaline liquid fluids and not vapour fluids (apparent absence of vesicles from the 2D thin section) in melt inclusions suggests that augite began to crystallize at depth where pressure was sufficient to suppress gas exsolution.

Despite the undeniable presence of Cl in the magmatic system, apatite grains (identified thanks to their P and Ca content) in the melt inclusions and mesostasis seem to lack Cl (no Cl X-ray has been detected during EDS mapping) contrary to inter-cumulus apatite common in all other nakhlites. The closed-system fractionation of melt droplets within the inclusions has led to the preferential partitioning of Cl into the earliest crystallized amphibole (that crystallized from the inclusion walls inward) relative to the melt phase and latter crystallized apatite (within the glassy melt central to the melt inclusions). In magmatic environments, apatite forms a solid solution from its three end-members Cl, F and OH. Its Cl-F-OH composition reflect the Cl, F and OH concentration in the melt at the time of apatite saturation. Therefore, apatite composition reflects changes in Cl-F-OH melt/fluid composition. The abundance of F and Cl relative to OH within apatite (measured by McCubbin et al. (2013)) shows that the parental magmas of the nakhlite meteorites were rich in the former and largely depleted in the latter.

Cl-amphibole is present in all tens of $\mu$m large inclusions showing that the size of the melt inclusion had some effect on the precipitation of amphibole, probably that only the $\mu$m large inclusions were large enough to contain sufficient volatile to crystallize amphibole. The Cl-depletion of the apatite can result from its preferential incorporation into the earliest crystallized amphibole. A further argument for a very early incorporation of Cl in minerals is the Cl content of amphibole that continuously decreases inward to be apparently absent in amphibole central to the inclusions. Amphibole in melt inclusions are strongly zoned. The Cl-rich fluid that precipitated amphibole was segregated from the melt and constrained along the melt wall. The apparent lack of Cl in apatite from the mesostasis as common in most nakhlites but also the lack of Cl-amphibole possibly reflect a magmatic degassing prior to mesostasis solidification, which is consistent with an early crystallization of augite at depth prior to final emplacement in a sub-surface environment and mesostasis (and apatite) solidification. MIL 03346 was probably emplaced in a shallower environment than the other nakhlites. The lack of Cl in apatite may be compensated by a higher content of F and/or OH. F is difficult to identified using qualitative EDS (Energy Dispersive Spectroscopy) because the characteristic K$\alpha$ x-ray energy of F overlap with the characteristic L$\alpha$ x-ray energy of Mn, an element present in traces in apatite. However, the presence of significant OH in apatite grains in the different nakhlites has not been detected in previous studies, although OH commonly degassed largely after Cl (at lower pressure) in subterranean magmatic environments (McCubbin et al., 2013).

The composition of the inclusion in MIL 03346 may represent the composition of the undegassed parent magma or at least its more primitive composition. The large presence of Cl shows that the parent magma was relatively enriched and homogeneous in Cl at least early in the crystallization history. Chlorine has never been found in the silica-rich glass of the mesostasis which probably reflects the high insolubility of Cl in more silica-rich melt and thus its loss during early magmatic processes. In the mesostasis, Cl has probably been exsolved prior to extensive intercumulus melt crystallization (i.e. differentiation) while in the melt inclusions it has been incorporated in early formed amphibole. Chlorine was probably the dominant volatile element in the nakhlites' parent magma(s). Unfortunately, MIL 03346 does not contain much olivine and those present in our sample lack inclusions. Hence, comparison of the composition of parental magmas and environment from which olivine and augite crystallized, as inferred from melt inclusions, are not possible.

#### *Inclusions in olivine grain from NWA 998 and Lafayette: Evidences for early differentiated melt*

Poly-mineral inclusions for mineralogical study within olivine phenocrysts are rare with the nakhlite meteorites because, despite the large size of the inclusions (up to hundreds of $\mu$m-large), individual crystals are too small for electron microscopy. The inclusions commonly have a vitrophyric texture with poorly developed crystals. However, olivine phenocrysts in our NWA 998 and Lafayette samples sometimes contain poly-mineralic inclusions with individual crystal size large enough for mineralogical study (Fig. 4.29).

The olivine inclusion in NWA 998 contains pyroxenes that have crystallized directly on the inclusion wall, with magnetite and feldspar filling the center of the inclusion. Poly-mineral inclusions in NWA 998 display a mineralogical concentric zoning with a mineralogy similar to that of the rock matrix. Compared to the augite phenocrysts, the pyroxenes within the inclusions are depleted in Ca and enriched in Fe. The feldspar-bearing inclusions are slightly depleted in incompatible elements Na and Al and compatible Ca relative to their counterparts in the mesostasis. The relative depletion in Ca in the feldspar from the inclusion reflects the low Ca content

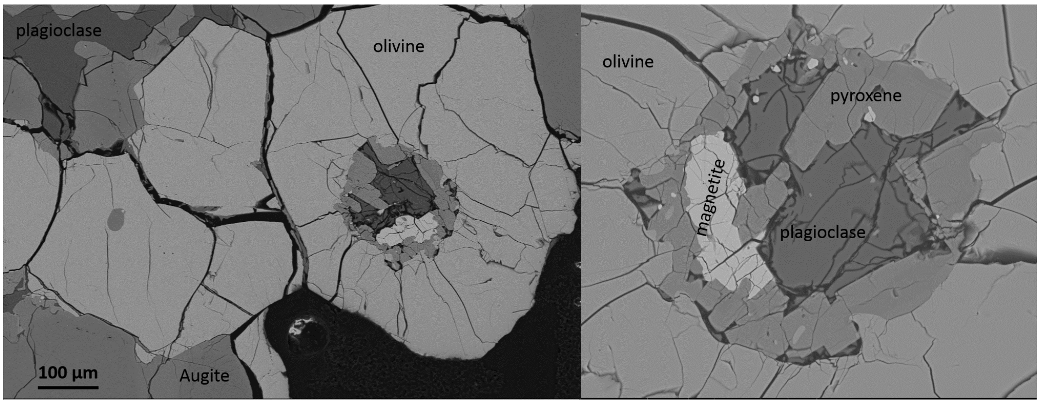

*Fig. 4.29: Large poly-mineralic inclusion in an olivine phenocryst in NWA 998. The inclusion is composed from rim to core of pyroxene, magnetite, and plagioclase. The crystallization sequence reflects the cooling history. The inclusion was probably originally a melt droplet enclosed during olivine growth. Radiating fractures surrounding the inclusion probably result from volume increase during crystallization.*

of the melt (fractionated melt) from which olivine crystallized and the incorporation of the poor amount of Ca in the trapped melt in the low-Ca pyroxene prior to feldspar precipitation. The chemical variation between minerals from the olivine inclusion and inter-cumulus matrix shows that olivine crystallized from a relatively evolved melt after augite crystallization while fractional crystallization was active. The apparent absence of apatite and rare Fe-sulfide within the inclusion suggests that the parent melt of olivine was not homogeneously saturated relative to $P_2O_5$ and $SO_x$, contrary to olivine from MIL 03346. This characteristic is consistent with petrographic observations of the rock matrix.

Olivine phenocrysts in Lafayette contain large poly-mineralic inclusions with small crystals of augite and Ti-magnetite embedded in poorly crystallized feldspar crystals, with or without a meniscus of quenched silicate liquid (Fig. 4.30). The composition of augite crystals are again similar to that of augite phenocrysts including their zonation. The augite rim zones (identifiable by their lighter grey colors in the BSE image (Fig. 4.30 right) in the inclusions correspond to orthopyroxenes (<5 wt% Ca) as the rims of augite phenocrysts. The inclusions are most probably melt inclusions that solidified once sealed rather than embayments of poorly crystallized mesostasis, because the mesostasis of Lafayette has a coarse grained texture with no glassy product. However, it is still possible that the small augite crystals have been incorporated in the melt inclusions together with the melt (co-trapped) but not the orthopyroxenes overgrowth (Fig. 4.30, left) and reactive rims (Fig. 4.30, right) intruding into or at the contact with the feldspar. They may have formed later, possibly after complete melt entrapment during near or sub-solidus reactions (Fig. 4.30, left). The poorly crystallized feldspar in olivine-hosted inclusions has the same composition as the cores of the feldspar in the rock matrix.

The formation of orthopyroxene in both inclusions in Lafayette probably results from reactions between augite grains (co-entrapped with the melt?) and the evolved late melt rich in $SiO_2$. The development of orthopyroxene overgrowth rather than

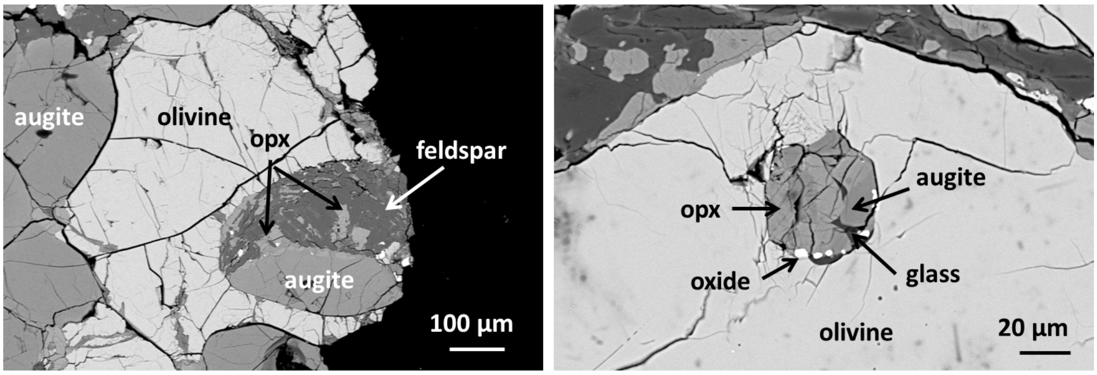

*Fig. 4.30: Large poly-mineralic inclusions in olivine phenocrysts in Lafayette. The inclusions are composed of augite, Ti-magnetite, and feldspar with or without meniscus of glass. Augite crystals are commonly rimmed (right) or overgrown (left) with orthopyroxene (opx).*

reactive rims may reflect the quantity of $SiO_2$ from the melt and thus reflect the size of the inclusion. In the absence of entrapped augite grains in olivine-hosted inclusions as in NWA 998, orthopyroxene directly crystallized at the contact with olivine. Melt inclusions and intercumulus melt experienced a similar fractionation path. There is no mineralogical or chemical evidence that the rock crystallized its phenocryst phases and matrix in different magmatic environments as in MIL 03346, which in the latter case could account for the different mineralogy between inclusion and matrix.

### 4.5.3 Origin of compositional variations of melt inclusions

From petrographic observations of the magmatic inclusions, certain information about the petrogenesis of the nakhlites and the parent magma composition can be inferred. As already recognized, the igneous history began with the crystallization of augite, now preserved as mineral inclusions in olivine. Augite probably crystallized from a relatively evolved and non-primitive melt. This is suggested by the numerous Si-rich (fractionated) glass inclusions and the zoned halos surrounding the melt inclusions indicating intense post-entrapment diffusional equilibration with the trapped melt from which augite crystallized. The crystallization of augite occurred from more evolved melts than suspected by their large and homogeneous cores. The post-entrapment diffusive halos may reflect a slow cooling magmatic environment and crystallization rate.

As augite crystallization proceeded, the physico-chemical conditions of the magmatic environments changed and olivine crystallized from a similar but more differentiated and differentiating melt. This led to the contrasting chemical composition between olivine and augite although it is undeniable that sub-solidus re-equilibration has further increased the chemical disequilibrium between both mineral phases. During olivine growth, pockets of melt were entrapped and began to crystallize once sealed (crystallization from the wall inwards). The liquid line of descent of the melt inclusions was similar to the melt within the rocks matrix in the fully crystallized Lafayette and NWA 998. Both meteorites most probably did not experience a drastic change in physico-chemical conditions during their whole crystallization history associated with a change in magmatic environment. The inclusions in both meteorites did not contain phosphate minerals but only rare sulfide (both sparingly distributed in the rocks' matrix) suggesting that their composing elements were not homogeneously distributed in the magmas that crystallized augite and olivine, a mineralogical pattern shared with the rocks matrix.

The pervasive presence of Cl-amphibole in large augite inclusions in MIL 03346 provide evidence for the existence of hydrosaline fluids in the deep magmatic environment. The similarity in texture and mineralogy (including the even and widespread distribution of apatite) between the melt inclusions and intercumulus melts suggest that augite and mesostasis crystallized from the same homogeneous magma but in different environments. The apparent absence of Cl in the rock mesostasis suggests a final crystallization of the rock in a shallow environment after intensive Cl degassing.

Within a single nakhlite, all magmatic inclusions (of similar size) in phenocrysts have relatively similar texture, mineralogy and mineral paragenesis as their rock matrix, except some variations with MIL 03346 that can be explained by different physical conditions experienced by this meteorite during its crystallization. This suggests a homogeneous melt composition at the time of phenocryst crystallization within a single nakhlite. However, the difference in texture, mineral composition and modal proportion of the magmatic inclusions in phenocryst phases from one nakhlite to another reflects crystallization of both mineral phases from deep magmatic environments under different physico-chemical conditions. The magmatic inclusions (except glass-bearing inclusions) from each studied nakhlite are very similar to the mesostasis texture and mineralogy suggesting preservation of these chemical characteristics (except Cl) during the whole crystallization history. The nakhlites represent different melt compositions that co-existed in the shallow magmatic system of Mars. The separate nakhlites have remained largely unmixed or contaminated during their final emplacement.

## 4.6 Crystallization of reactive low-Ca pyroxenes during late stage magmatic processes

NWA 998 is a unique nakhlite as it has the texture and mineralogy of a typical terrestrial gabbro (Treiman, 2005). It is fully crystallized with augite and olivine forming a framework for an interstitial mineral assemblage comprised of abundant plagioclase and K-feldspar, titanomagnetite, apatite and rare Fe-sulfide (Treiman and Irving, 2008). The interstitial plagioclases display very rarely crystallographic faces. They are not a cumulus mineral phase but more probably formed in-situ filling available space between the cumulate phases. Another unique feature of NWA 998 is the presence of low-Ca pyroxenes in textural disequilibrium with the other minerals (Fig. 4.31). The low-Ca pyroxenes occur mostly as replacing products of olivine, plagioclase and augite. The distribution of low-Ca pyroxene appears to be strongly controlled by the presence of olivine, and more specifically by the contact between olivine and plagioclase (Fig. 4.31). Olivine-plagioclase reactions are common in terrestrial gabbro and result from changing physico-chemical conditions either during late-stage magmatic processes or metamorphism (De Haas et al.,

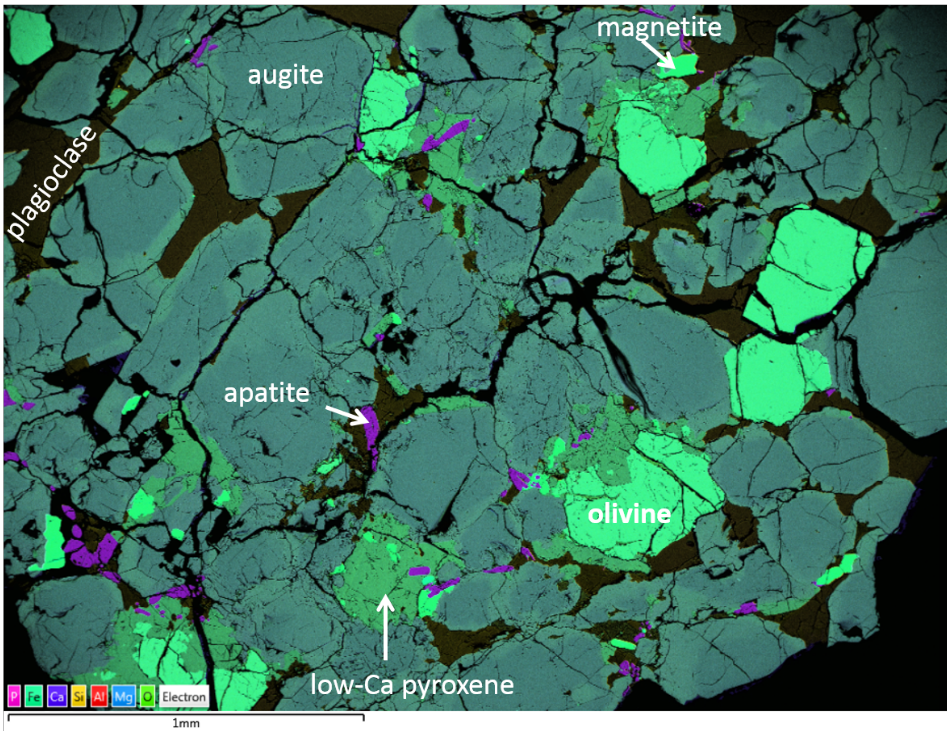

*Fig. 4.31: EDS map of NWA 998 with augite, olivine, plagioclase, apatite, and low-Ca pyroxene. The low-Ca pyroxenes partially replace olivine, plagioclase and augite but not apatite.*

2002).

### 4.6.1 A complex magmatic history from basaltic to silicic magma composition

NWA 998 rock began to form with the accumulation of augite and olivine to form a crystal mush with inter-granular pockets of melt. At the time of crystal accumulation, the interstitial melt was probably in chemical equilibrium with the augite phenocrysts. However, the rock and mineral texture and mineralogy of the inter-cumulus material suggest a complex post-cumulus magmatic history with a progressive evolution of the interstitial melt out of equilibrium with the crystal mush. Decoding the chemical evolution path of the inter-granular melt is not straightforward as many processes may drive the evolution of the late melts, such as the permeability of the crystal mush and connectivity of the inter-granular melts and their possibility of chemical exchange with the magma pool outside of the cumulate layer or with cumulate phases, or again the redistribution/flowing of late melts throughout the cumulate pile during compaction, a process called filter-pressing (Humphreys, 2009). However, a record of post-cumulus chemical melt evolution during rock solidification may have been preserved within the inter-cumulus mineral assemblage, texture and compositional zoning.

The pyroxene phenocrysts correspond to sub-calcite augite. They are composed of a large core of nearly constant composition but display distinct, sometimes patchy, rim zones of more ferroan composition. The chemical composition of the augite phenocrysts reflect those of the bulk magma from which they have crystallized, with more or less post-cumulate overgrowth crystallization and chemical re-equilibration with the melt. The pyroxenes display abundant exsolution of lamellae which indicates the slow cooling history of the rock (Poldervaart and Hess, 1951). Olivine phenocrysts are unzoned and correspond to approximately $Fa_{65}$. The absence of either normal or oscillatory zoning suggests intra-crystalline chemical re-equilibration during the slow crystal growth. The chemical composition of the phenocrysts provides evidence of intense melt differentiation through fractional crystallization prior to cumulate processes.

Interstitial melt pockets have crystallized an evolved mineral phase assemblage comprised of large magnetite grains rich in Ti, plagioclase and K-feldspar, and rare and disseminated Fe-sulfide and Cl-apatite. The crystallization of evolved inter-cumulus mineral phases provides evidence of a limited exchange of the interstitial melts with the bulk magma outside of the cumulate layer. In our sample, titanomagnetite does not present obvious ilmenite exsolution tweed pattern typical of most nakhlite meteorites, although it displays rare incomplete exsolution lamellae and patchy zones of ilmenite (Treiman and Irving, 2008). The interstitial plagioclase are normally zoned with compositions ranging roughly from $An_{40\text{-}20}$ within the large core to $An_{<5}$ along grain boundaries. The chemical zoning of the feldspar is underlined by a decrease of Mg and Ca and an increase in K, Na and Si rimward, which is consistent with a crystallization from a differentiating melt. The very low content of incompatible Ti and lack of normal Ti zoning within the feldspar suggests that they crystallized after titanomagnetite as recognized above in the different nakhlites. The feldspar compositional zoning is very irregular (patchy) within a single grain and from one inter-cumulate pocket to another (Fig 4.32, 4.33 (b)). Post-crystallization re-equilibration of plagioclase has proven to be too slow to occur before complete basaltic rock solidification (Humphreys, 2009). Hence, it is possible that the patchy zoning of plagioclase feldspar results from partial resorption by late reactive melts before crystallization of K-feldspar onto plagioclase. If correct, this could provide evidence for the presence of a highly reactive silicate melt that has circulated through the cumulate layer. The compositional variation of the feldspar from one inter-cumulus pocket to another show an uneven melt composition and circulation prior to feldspar crystallization and limited exchange between the inter-cumulate melt pockets.

Euhedral to subedral apatite grains are commonly enclosed within the K-feldspar rims (Fig. 4.32). The $P_2O_5$ content of basaltic rocks is generally low, as apatite crystallizes late in the crystallization sequence, once $P_2O_5$ saturation within the residual melt is reached. The occurrence of apatite associated with the late crystallized K-feldspar shows progressive fractional crystallization processes from partially trapped interstitial melt and the existence of the last residual melts with a high degree of evolution. Apatite grains are unevenly distributed throughout the NWA 998 rock and tend to be concentrated (i.e. clustered) in a few inter-cumulus areas. The sporadic distribution of apatite suggests that the inter-cumulus melt was unevenly saturated in $P_2O_5$ (i.e. non equilibrium melt distribution) or has resulted because of different degrees of fractional crystallization within the different inter-cumulus melt pockets which could reflect an uneven rock permeability.

NWA 998 seems to lack a “pure” silica crystal phase such as cristobalite common in most nakhlites. However, it contains rare igneous material with a feldspathic-

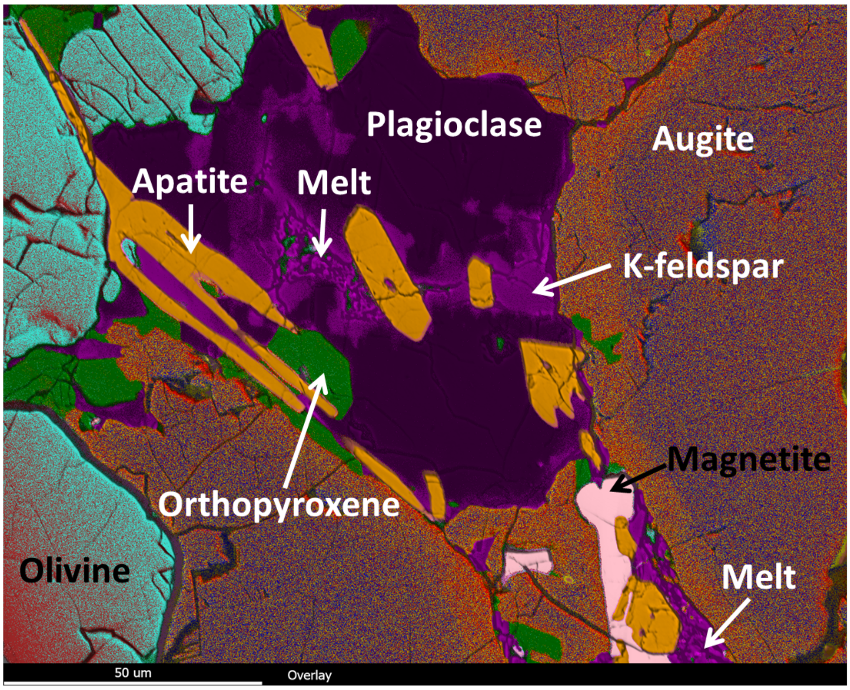

*Fig. 4.32: EDS map of NWA 998 showing the distribution of the different mineral phases between cumulate augite and olivine: plagioclase with K-feldspar rims, apatite, magnetite, orthopyroxene, and remnants of poorly crystallized melt filling pore corners.*

silicic composition present in some pore corners ("melt" in Fig. 4.32, 4.33). The igneous material has a rough, bubbly texture and contains a few crystal "seeds", too small to be properly identified, although some of them may be low-Ca pyroxene. Both the texture and distribution of the alkali silica rich material suggest that it represents the last remnants of "frozen" magma. The "frozen" melt was out of equilibrium with the augite and plagioclase primocrysts as suggested by the resorption textures at the melt-solid interfaces. Proper and reliable quantitative analysis of the "frozen" magma is not possible because of its amorphous, bubbly nature; however it seems to have a more evolved chemical composition than the adjacent k-feldspar. Relative to K-feldspar, it is enriched in Si and K, displays no enrichment or depletion in Al, and is depleted in Na.

The chemical composition of the interstitial minerals shows an inter-granular melt differentiation toward alkali and silica-rich composition (i.e. Bowen type). Late post-cumulus olivine re-equilibration and crystallization of magnetite and Fe-rich pyroxene overgrowths onto augite have controlled (i.e. buffered) the Fe content of the inter-granular melt. The very low modal proportion of evolved "frozen" melt (mostly filling small pore corners) suggests that late interstitial melts have been largely expelled from the cumulate layer before complete rock solidification, possibly because of compaction (i.e. filter pressing). Expulsion of melt upward in the cumulate pile may have put into contact melts with different degrees of chemical evolution and redistributed these melts throughout the cumulate pile. This could explain the chemical disequilibrium between the last crystallized feldspar and interstitial "frozen" melts in NWA 998. It also implies that the last inter-cumulus

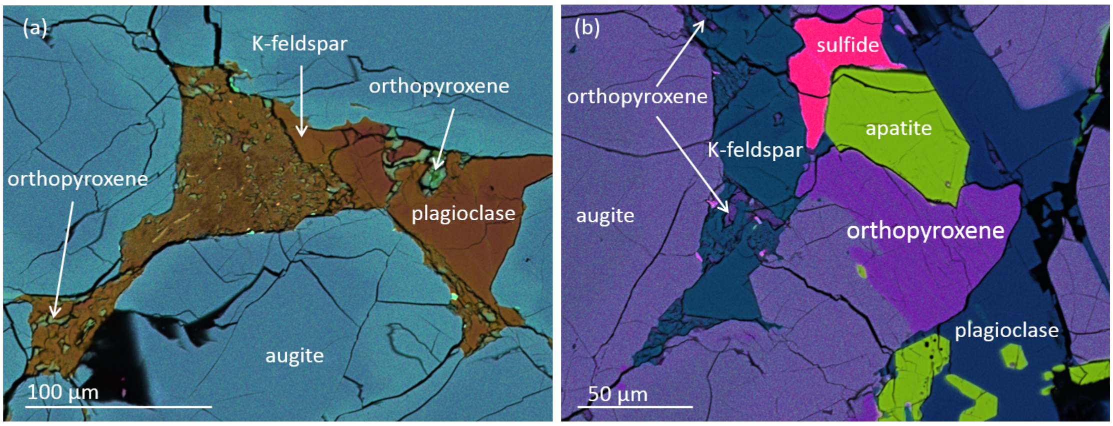

*Fig. 4.33: EDS maps of inter-cumulus material in NWA 998 with plagioclase (dark blue), K-feldspar(light blue), apatite, Fe-sulfide and "frozen" melt with orthopyroxene.*

melts were progressively more evolved downward in the cumulate pile which could result from the decrease in crystal mush permeability and fractional crystallization processes in relatively closed systems. The apparent absence of symplectite exsolution of magnetite and augite in olivine suggests a rock solidification under more reducing conditions than for the other nakhlites.

### *4.6.2 Petrographic observations of reactive low-Ca pyroxenes*

The distribution of low-Ca pyroxenes is clearly associated with, but not restricted to, that of olivine (Fig. 4.31, 4.34, 4.35). Low-Ca pyroxene form either well-shaped laths or uneven masses of different size locally erasing the primary texture and structure of the rock (Fig. 4.35). Remnants of early-crystallized olivine and plagioclase, and inclusions of (apparently unreacted) apatite grains are commonplace within the low-Ca pyroxenes suggesting that the low-Ca pyroxenes grew at the expense of both olivine and plagioclase. At first glance, the low-Ca pyroxenes correspond to orthopyroxene although in details, the mineral phase composition appears to be more complex. In addition to "pure" orthopyroxene, pigeonite-hosted augite lamellae (recognized by Treiman and Irving (2008)) and augite-hosted pigeonite lamellae are present. "Pure" orthopyroxene contains rare inter-growths of vermicular oxy-symplectite exsolution of titanomagnetite. The different low-Ca pyroxene assemblages represent the last crystallized mineral phases out of equilibrium with the rest of the rock. This also implies that the rock completely crystallized at high sub-solidus temperature.

Low-Ca pyroxenes display different textures and compositions suggesting a complex replacement history with a certain degree of petrographic control (Fig. 4.36). The only low-Ca pyroxene replacing topographically olivine corresponds to "pure" orthopyroxene (CaO $< 5$wt%). It is surrounded by pigeonite-hosting augite lamellae (of variable thickness between the different pyroxene grains) replacing topographycally plagioclase. The boundaries between orthopyroxene and pigeonite-augite are smooth and irregular and do not display obvious crystal grain boundaries (Fig. 4.36). Pigeonite-hosted augite lamellae occur either as replacing products of plagioclase or form protrusions on augite phenocrysts. Pigeonite-hosted augite lamellae

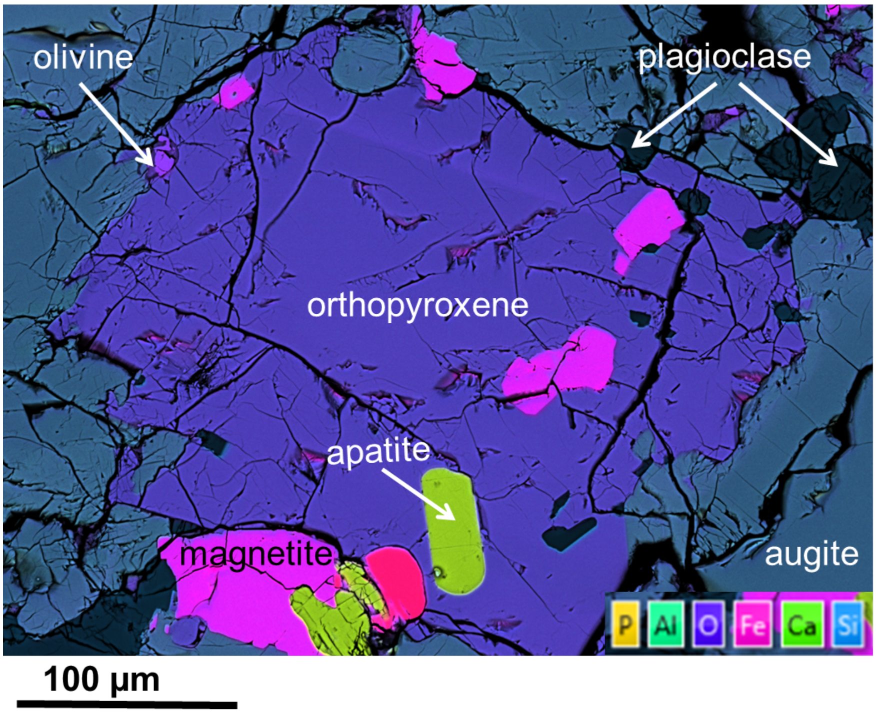

*Fig. 4.34: EDS map of orthopyroxene that has overgrown onto plagioclase, olivine and augite in NWA 998. During the mineralogical transformation, magnetite and apatite have been enclosed and have remained unreactive.*

are also present as small grains replacing plagioclase feldspar and seem to have no apparent link with olivine. On Fig. 4.36, the pigeonite-hosted augites are separated by thin remnants of unconsumed feldspar. Another late-stage pyroxene associated with disequilibrium texture are pigeonite lamellae which have exsolved from the augite phenocryst rims at the contact with pigeonite-augite protrusions. Exsolution of pigeonite and augite commonly occurs parallel to (001) in augites and pigeonite respectively because cation diffusion is easier along the silica tetrahedra (Poldervaart and Hess, 1951). On Fig. 4.36, the augite and pigeonite lamellae from pigeonite and augite crystal hosts respectively are parallel to each other indicating the same crystallographic orientation of both crystal hosts.

The presence of pyroxene exsolution in basaltic rocks is indicative of plutonic environments where magmas remain at a temperature high enough and for sufficient time to experience active and very slow intra-crystalline diffusion (Poldervaart and Hess, 1951). Basaltic magmas with identical chemical compositions and mineralogy that rapidly cool in a sub-surface environment cannot provide sufficient time at sub-solidus temperature for their clinopyroxene population to form more ordered structures (i.e. exsolution lammellae) by intra-crystalline ionic diffusion.

The "pure" orthopyroxene contains rare vermicular oxy-symplectite exsolution of titanomagnetite (Fig. 4.37). They occur only as topographic replacement products of olivine. The cross-cutting relationship of "pure" orthopyroxene with pigeonite-hosted augite lamellae suggests that they precipitated last replacing the latter. The exsolution of vermicular titanomagnetite seems to be the result of olivine oxidation during replacement where titanomagnetite directly exsolved from the olivine before

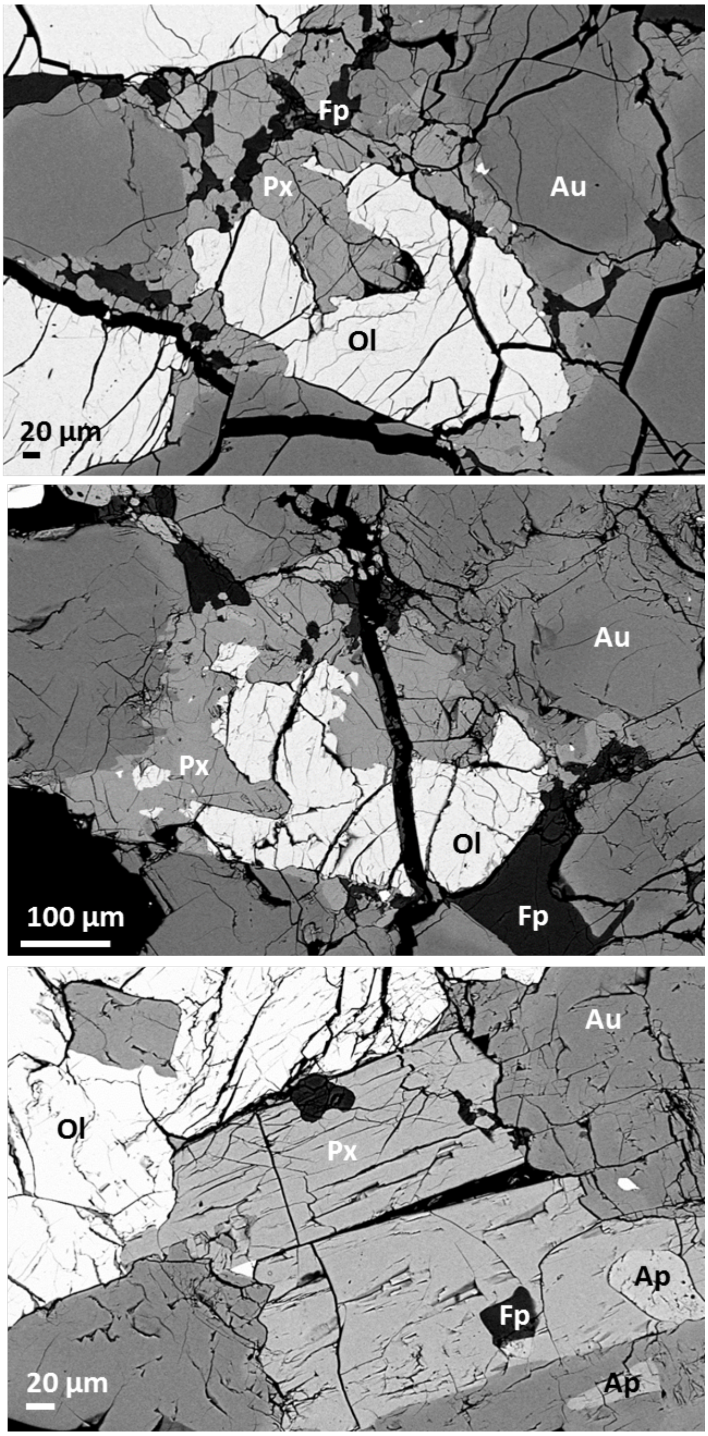

Fig. 4.35: *BSE images of the reactive textures of low-Ca pyroxenes (Px) replacing olivine (Ol), plagioclase feldspar (Fp) and augite (Au) in NWA 998. The crystallization of low-Ca pyroxene has partially erased the texture and structure of the rock.*

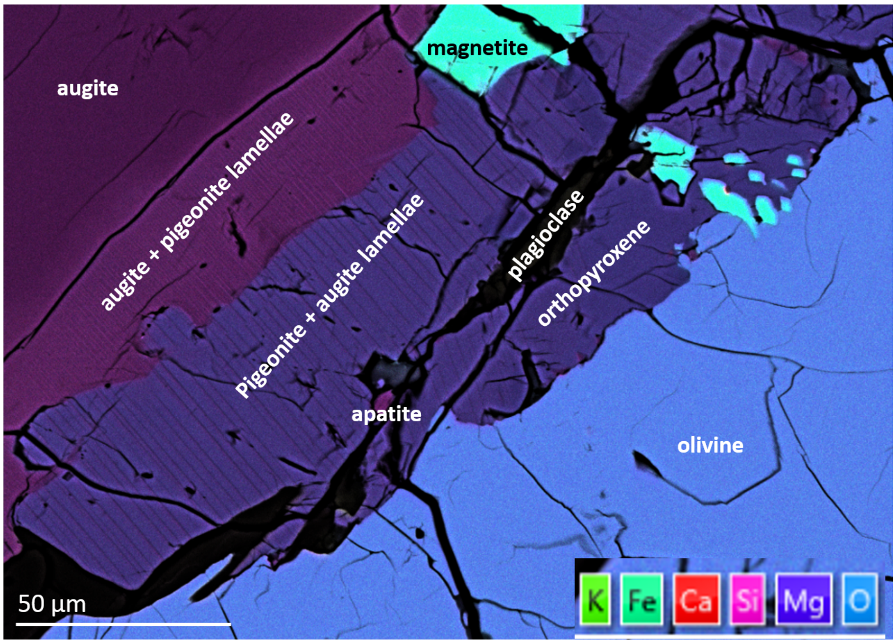

Fig. 4.36: *EDS map of the various low-Ca pyroxene minerals found as a replacing product in NWA 998 and their relation with the early stable mineral assemblages. Interstitial plagioclase and magnetite are replaced by pigeonite hosting augite lamellae. "Pure" orthopyroxene occurs only as topographic replacement of olivine. Pigeonite and augite lamellae (within augite and pigeonite respectively) are parallel suggesting a same crystallographic orientation of the pyroxene hosts.*

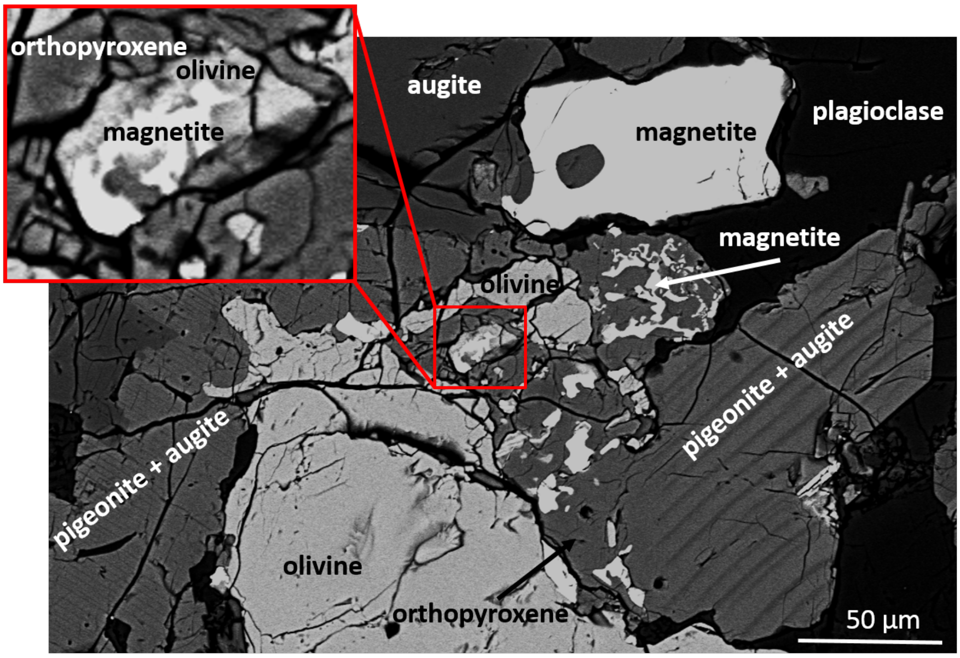

Fig. 4.37: *BSE image of different replacive low-Ca pyroxenes replacing olivine, augite and plagioclase in NWA 998. Vermicular magnetite represents oxidative exsolution of olivine that formed during olivine degradation.*

a complete degradation of the olivine into orthopyroxene. This suggests a progressive increase of the oxygen fugacity during the mineralogical re-equilibration processes.

### 4.6.3 Low-Ca pyroxenes: Mineralogical re-equilibration from what?

Petrographic observations provide evidence that low-Ca pyroxenes developed along olivine-plagioclase grain boundaries and have progressively intruded into olivine, plagioclase and adjacent augite. Remnants of unconsumed olivine and plagioclase and “inclusions” of apatite are commonplace within 100 $\mu$m long lath-shaped low-Ca pyroxenes (Fig. 4.35). The crystallization of low-Ca pyroxene has locally erased the primary texture and structure of the rock (Fig. 4.31). Their reactive textures reflect a return of mineralogical equilibrium to early stable mineral associations.

The low-Ca pyroxene crystals display compositional variations according to their petrological settings (Fig. 4.36). The pyroxene topographically replacing olivine corresponds to orthopyroxene with rare magnetite, while the pyroxene replacing plagioclase is pigeonite-hosted augite lamellae. Roughly, the chemical compositions (i.e. Ca content) of the low-Ca pyroxenes reflect those of the reactants they replace (either olivine or plagioclase). The occurrence of inclusions of chemically homogeneous plagioclase within orthopyroxene, with a composition similar to the core of the interstitial plagioclase, and compositional variation of the low-Ca pyroxene with petrographic settings argue against a replacement reaction involving partial melting of olivine, plagioclase and augite and re-crystallization of low-Ca pyroxene from this “second generation” of melt. The reactants and their daughter products appear to be in optical continuity and form crystallographically coherent replacements.

The formation of low-Ca pyroxene probably began with the development of small grains-forming discontinuous layers with a raspberry-like texture between olivine and plagioclase grain boundaries (Fig. 4.35). Further growth of the low-Ca pyroxene grains probably involved annealing and chemical and crystallographic re-arrangement of the small grains to form large stable and chemically homogeneous orthopyroxene grains with remnants of unconsumed olivine, plagioclase and apatite grains (Fig. 4.35). In our samples, there is no evidence of early-formed orthopyroxene (i.e. primocryst) as suggested by Treiman and Irving (2008).

The crystallization of low-Ca pyroxene resulted from mineralogical instability between the formerly juxtaposed olivine and plagioclase feldspar grains. The absence of low-Ca pyroxenes along olivine-augite contacts argues against reactions only occurring between the early-formed olivine and residual silicate melts. Olivine-plagioclase seems to have been a weak mineral association within the rock, although the further growth of low-Ca pyroxene has involved degradation of augite. The olivine-plagioclase instability may have been caused by changes in temperature or oxygen fugacity (i.e. solid-state transformation) or because of the presence of a thin film of reactive silicate melt between olivine-plagioclase grain boundaries. The residual melts in NWA 998 show an enrichment trend towards more silica and alkali rich compositions, as underlined by the occurrence of both K-feldspar and “frozen” alkali-silica-rich melt filling corner pores (Fig. 4.32, 4.33). The“frozen” melt and rarely K-feldspar display tiny crystals of most probably low-Ca pyroxene. Although the occurrence of reactive silicate melt droplets may have have been an important agent in the processes of mineralogical transformation especially to trigger the reactions, petrographic observations suggest that solid-state (sub-solidus) reactions have been the main mechanism for the further development of large low-Ca pyroxene within the reactive zones (Fig. 4.35).

Sub-solidus reactions require diffusional (solid-state) re-arrangement of elements to form new mineral phases. In NWA 998, diffusion of elements occurred between adjacent olivine and plagioclase. It has involved the partial consumption of both mineral phases to form a variety of pyroxenes and rare oxide. If we neglect elemental gain or loss and systematic formation of spinel, a general (qualitative) mineralogical reaction could be:

$$\text{olivine} + \text{plagioclase} = \text{orthopyroxene} + \text{clinopyroxene} + \text{spinel}$$

The elemental interdependencies between reactants (olivine or plagioclase) and products (low-Ca pyroxene) show a replacement process with some degree of internal control consistent with solid-state re-arrangements. The topographic degradation of olivine into “pure” orthopyroxene and magnetite can happen without addition or removal of material. For example, an increase in oxygen fugacity during the late-stage magmatic processes could have triggered the mineralogical transformation through oxidation reaction:

$$3\ (\mathrm{Mg, Fe})_2\ \mathrm{SiO_4} + 0.5\ \mathrm{O_2} = 3\ (\mathrm{Mg, Fe})\ \mathrm{SiO_3} + \mathrm{Fe_3O_4}$$

However, an increase in $SiO_2$ activity during late-stage magmatic processes could also have triggered the mineralogical transformation from the peritectic liquidus relationship olivine + quartz = orthopyroxene as common in terrestrial basaltic rock:

$$(\mathrm{Mg, Fe})_2\mathrm{SiO_4} + \mathrm{SiO_2} = 2\ (\mathrm{Mg, Fe})\ \mathrm{SiO_3}$$

In this reaction, there is no need for an increase of oxygen fugacity or formation of “secondary” magnetite, which seems mineralogically more consistent with our petrographic observations.

The formation of magnetite requires the presence of Fe in its two different valence states ($Fe^{2+}$ and $Fe^{3+}$). Hence, if the oxygen fugacity is low, magnetite does not form or only in the very latest stage of the reaction when the pyroxene incompatible $Fe^{3+}$ content becomes sufficiently high to allow magnetite precipitation. In NWA 998, reactive product magnetite is rare and appears to be associated with late orthopyroxene precipitation as suggested by the texture and micro-stratigraphic relationships of different reactive products (Fig. 4.37). Consequently, it is unlikely that the mineralogical transformation has been triggered by an increase of oxygen fugacity such as, for example, during oxygen degassing.

The transformation of plagioclase into pigeonite with augite lamellae does not result in a good chemical balance as Mg and Fe have to be added (by diffusion processes from the adjacent olivine and/or orthopyroxene ?) while Al, K and Na have to be removed. A transfer of metallic cations of Mg and Fe from the degrading olivine into the adjacent pigeonite could explain the increase in $SiO_2$ required for orthopyroxene precipitation from olivine and the apparent almost systematic lack of magnetite co-precipitation (which acts as a sink for metallic ions) within the orthopyroxene. The mineral reactants olivine and plagioclase have not fully retained their chemical composition during the mineralogical transformations. Some elements such as metallic ions may have been exchanged between the different low-Ca pyroxenes during or after their formation, while others have been lost to the system. In our NWA 998 sample, there is no evidence of “secondary” K-Na-Al-bearing mineral phase which implies that these elements have been removed from the rock (as a melt or gas phase or through inter-crystal diffusion ?).

The large low-Ca pyroxene masses correspond to “pure” and homogeneous orthopyroxene. They spread across olivine, plagioclase and sometime augite boundaries but do not display the chemical variations in their major elements according to their petrographic settings any more. The small low-Ca pyroxene grains have probably annealed at the contact with each other during or after their dovetailing to form the large masses. If true, this further provides evidence for active sub-solidus chemical diffusion and a very slow cooling rate. The reactant mineral olivine and large orthopyroxene daughter product are unzoned and chemically constant throughout the crystals in major elements. The chemical composition of the reactant plagioclase is more difficult to constrain as it slightly varies between the different inter-cumulus pockets, especially the extent and pattern of zoning (patchy zoning is common). However, at first glance, an isochemical reaction (in major elements) appears to be relatively unlikely as components from the plagioclase feldspar such as Ca, K, Na and Al have to be almost completely removed from the system.

Further evidence for the existence of a third component is the high trace element composition of the orthopyroxene, including REEs, that cannot be explained by recrystallization from the olivine and plagioclase solely (Fig. 4.25) but by the presence of a highly differentiated melt intrinsically rich in REE. The development of low-Ca pyroxene at the expense of olivine most probably resulted from olivine-orthopyroxene peritectic reaction. However, the chemical implication of the residual melts seems to have been restricted to the input of $SiO_2$ and incompatible trace elements, with no other chemical components seemingly provided by the last melt. The budget of trace elements varies between the orthopyroxenes suggesting different proportion of olivine, plagioclase and melt involved in the reactions. NWA 998 lacks crystals of cristobalite or traces of Si-rich (Na-K-poor) melt imiscibility in its matrix that preferentially develop along plagioclase grains in some of the other nakhlites. Unlike quartz, cristobalite has a very open crystal structure that can easily accommodate foreign cations including the REEs (Deer et al., 1992). The silica-rich melts that reacted with olivine-plagioclase in NWA 998 may have a similar chemical condition to the ones that crystallized cristobalite in some other nakhlites. In NWA 998, mineralogical re-equilibration over cristobalite crystallization may have been favoured because of the deeper environment (higher pressure and temperature, and slower cooling rate) of crystallization of NWA 998.

The presence of reactive melts is evident from the resorption textures on plagioclase and augite (resorptive rims). The chemical disequilibrium between the last residual melts and plagioclase and K-feldspar and augite could be explained by a continuous process of melt expulsion by compaction. Uneven melt circulation through the cumulate pile could also explain the compositional variation between the melt pockets, for example the erratic distribution of clusters of apatite grains and compositional variation of the feldspar from one inter-cumulus pocket to another (Fig. 4.33 (b)). It is highly probable that during the late magmatic processes, the cumulate layer has been modified by the movements of reactive inter-cumulus magmas (and possibly gas ?) which may have destabilized the primocrysts. The mineralogical re-equilibration has probably been triggered by an increase in silica activity during the very late-stage of igneous activity. The texture and morphology of the silica melt together with the late-stage crystallized minerals attest to the occurrence of a late silica-rich magma within the Martian crust. The absence of traces of melt at the contact with olivine, plagioclase and orthopyroxene suggests that it may have been the limiting factor in the development of orthopyroxene, while pigeonite exsolution in the orthopyroxene suggests that the rock has remained at sub-solidus temperature long after complete solidification.

## *4.7 Constraint on the nakhlites magmatic history using trace elements*

### *4.7.1 Trace element geochemistry*

#### *Definition*

By definition a trace element is an element present in a rock, or mineral, in a concentration inferior to 0.1% (White, 2013). Trace elements sometimes form mineral species in their own but most commonly they substitute to major elements in crystals' structure. They are not expressed as wt% oxide but as ppm or ppb (part per million and part per billion, respectively). Despite their small concentration and their passive behaviour, they are important elements because they are more numerous and in general more sensitive to magmatic processes and physico-chemical conditions during magmatic processes than the major elements (Karner et al., 2006). As a result, primary silicate minerals in basaltic rocks display (proportionally) greater variations in concentration even at the ppm-scale (White, 2013). Moreover, each chemical element has specific chemical properties. Hence, variations in abundance of any given element bear a unique geochemical information about the origin and evolution of magmas. The trace element composition of primary minerals contain geochemical and geological information that are not available from compositional variations of major elements (White, 2013).

Trace element geochemistry is an important tool in understanding the origin and subsequent magmatic evolutionary processes of igneous rocks (Karner et al., 2006). Although each chemical element has unique chemical properties, certain trace elements have similar geochemical behaviours which serve as a basis to group them (White, 2013). Each group displays subtle but important trends that reflect their slightly differing degree of substitution in mineral structures. The groups of trace elements commonly used in igneous petrology include the alkali and alkaline Earth, transition elements, High Field Strength Elements (HFSEs), and the lanthanide series also called Rare Earth Elements (REEs).

The alkali (Li, Cs, Na, K, Rb) and alkaline Earth (Be, Mg, Ca, Sr, Ba, Ra) are reactive metallic elements that lose their outer electron(s) to forms $1^+$ and $2^+$ ion with non-metals, respectively (White, 2013). Their bonding to other elements is ionic. Ionic bonds have the particularity to be easily broken by water molecules because of the polarity of the water molecules. Hence, the alkali and alkaline Earth elements are soluble and mobile in aqueous solutions either in high temperature (metamorphic or hydrothermal) or low temperature (weathering) environments. The behaviour of the alkali and alkaline Earth elements during igneous processes is governed by their ionic charge but also by their large ionic radius. For example the Large-Ion-Lithophile elements (LILEs) including K, Ba, Sr, Cs, Rb cannot enter into the crystal lattice of common early-formed minerals in basaltic rocks without causing lattice distortion (White, 2013). As such, they preferentially concentrate into the melt phase either during partial melting of the mantle or magma crystallization.

The first series transition elements (Sc, Ti, V, Cr, Mn, Fe, Co, Ni, Cu, and Zn) share a number of chemical properties (White, 2013). Their d-shell is not completely filled with electrons and exist in two or more different valence states which influences the geochemical behaviour of the different elements. Their bonding is either ionic (with oxides) or covalent (with metals). They are in general less soluble than the alkali and alkaline Earth elements although their solubility remains dependent on their valance state and the presence of ligands within the aqueous fluids. During magmatic processes, the first series transition metals are generally either moderately incompatible (Ti, Cu, Zn) or compatible (Cr, Ni, Co) although their relative degree of compatibility remains controlled by the mineral composition. In addition, variations in oxygen fugacity conditions in the mantle source regions and during crystallization lead to changes in the valance state of the first series transition elements which consequently impact their degree of incorporation in mineral structures (White, 2013).

The High Field Strength Elements (HFSEs) consist of Zr, Hf, Nb, and Ta (White, 2013). They have small ionic radius and high cationic charge. As a result they are strongly bond to more than one anions in the crystal lattice (i.e. cross-bond). Thorium and U are sometimes associated with the HFSEs because of their high valance state, +4 for Th and either +4 or +6 for U. Thorium and U are amongst the most incompatible elements (White, 2013). The HFSEs have a high electric field strength; their charge is too great to substitute in to major elements such that their insertion in a crystal lattice requires (charge-balanced) coupled substitutions which are energetically less favourable. In general, Zr and Hf are less incompatible than Nb and Ta and much less than Th and U. During partial melting, they are preferentially partitioned into the magma and migrate towards the surface with the melt. They are enriched in the lithosphere. Multiple episodes of partial melting fractionate and deplete Th and U relative to Zr and Hf. Because of their high charge, the HFSEs are insoluble and immobile during metamorphism and weathering (White, 2013). They are considered “conservative” elements.

The Rare Earth Elements (REEs) belong to the third series transition elements (White, 2013). They include La, Ce, Pr, Nd, Sm, Eu, Gd, Tb, Dy, Ho, Er, Tm, Yb, and Lu. They have similar ionic size. The element Y is commonly included in the REE group because it has a similar ionic size to the REEs, especially Ho (White, 2013). The REEs with the lowest atomic number (La to Pm) are commonly called Light Rare Earth Elements (LREE) while those with higher atomic number (Er to Lu) are known as the heavy Rare Earth Elements (HREE). The REEs are incompatible elements that have geochemically coherent behaviour during magmatic processes and are immune to moderate fractional crystallization. Rare Earth Element ratios are not modified during early crystallization of basaltic magmas. The REEs have a relatively high charge and large ionic size which are difficult to accommodate in most mineral structures by substitution of major or minor elements (White, 2013). However, because their ionic radius progressively decreases with increasing atomic number, their degree of incompatibility decreases from the LREEs to the HREEs. Consequently, geological processes (such as partial melting and crystallization) fractionate the REEs relative to each other. For instance, small degrees of partial melting release preferentially into the melt the most incompatible elements (i.e. the LREEs). Conversely, elements that are the most excluded from crystals during magma crystallization (especially the LREEs because of their large radii) remain in the melt phase. Commonly, rocks formed by fractional crystallization display near parallel REE patterns.

All the REEs form stable trivalent ions which gives them similar chemical and physical properties. However, two REEs also exist in other oxidation state than 3+: $Eu^{2+}$ and $Ce^{4+}$. Their change of oxidation state results in an increase and decrease of their ionic size, respectively. This leads to differences in how these ions can partition versus the other REEs. For example, in an oxidizing magma, Eu in its trivalent form is incompatible whereas in a reducing magma Eu in its divalent form is compatible and substitutes for Ca in minerals especially plagioclase. Crystallization of plagioclase from basaltic magmas commonly show strong Eu positive anomalies. Hence, crystallization of stable plagioclase and accumulation of plagioclase crystals before complete rock solidification induces an enrichment of Eu ($Eu^{2+}$) in the whole-rock relative to the other REEs in the cumulate layer while the rest of the igneous rock will then be depleted in Eu relative to the other REEs. The relative timing of plagioclase crystallization in the crystallization sequence can also be determined thanks to the Eu anomalies as minerals formed after plagioclase will display negative Eu anomalies. The REEs are poorly soluble in the weathering environment and immobile during metamorphism.

### *Application to the nakhlites*

Pivotal questions that still stand out for understanding the nakhlites petrogenesis are the composition of the parental magmas (including the number of magmas at the origin of the nakhlites), their evolution path (in closed or open systems) and differentiation processes during crystallization. The first difficulty in identifying the parent magma composition(s) is that as the nakhlites are cumulate rocks, their bulk composition do not represent the composition of their parent magma(s) (Berkley et al., 1980; Papike, 1996). Hence, the "original" composition of the parental magma(s) has to be indirectly determined. A method commonly used involves mineral/basalt partitioning of trace elements (Longhi and Pan, 1989; Papike, 1996). But then a second issue arises because all rocks have experienced disequilibrium conditions during late-stage magmatic processes that have led to active sub-solidus diffusional re-equilibration with the inter-cumulus melt (Harvey and McSween, 1992). The chemical elements have been partially redistributed between the early solid products and late melts such as the final chemical compositions of the primary minerals including their zoning do not completely represent their original compositions (i.e. liquidus chemistry), as common with cumulate rocks (Papike, 1996).

Despite these undeniable issues, the nature and composition of the parent magma(s) can still be addressed using trace and minor elements in the different mineral phases

(Wadhwa and Crozaz, 1995; Cherniak and Liang, 2007). Trace and minor elements are very sensitive to most magmatic processes and conditions, in general more than major elements, and distribute themselves in the different magmatic products accordingly during crystallization (Blundy and Wood, 2003; White, 2013). Their distribution in specific mineral phases provide fingerprints of magmatic conditions and processes at the time of crystallization of the specific minerals (Papike, 1996). Critically, certain trace elements are known to be “conservative” during most secondary processes, either magmatic or metamorphic; they do not significantly diffuse out of minerals post solidification (Papike, 1996; Van Orman et al., 2002). Their preservation in minerals results mostly from their high charge (strong bonding) which prevents them from diffusing quickly enough to be completely re-equilibrated during the lifetime of magmas (Van Orman et al., 2002). Amongst the elements that diffuse slowly in clinopyroxene are the REEs, Th and U (Van Orman et al., 2002). The behaviour of trace and minor elements during nakhlite crystallization were no exception; in augite phenocrysts a series of trace elements retained their extensive original igneous zonation (Wadhwa and Crozaz, 1995). The nakhlites have therefore preserved partial chemical signatures of the parent magma(s) from which they crystallized.

Preservation of trace element distribution in minerals can provide clues about the rocks petrogenesis but also about their history as a group that major elements are unable to provide (Papike, 1996; Cherniak and Liang, 2007). For example, partial melting of the mantle always produces a basaltic magma with a homogeneous composition, whatever the source region or depth (White, 2013). On the large-scale, major element composition of the mantle is likely to be largely uniform much like their partial melts. The formation of basaltic magmas with different major element compositions are mostly the result of magmatic processes that occur in the shallow crustal environment: stagnation of the primary basaltic magmas in magma chambers and fractional crystallization processes, magma mixing and/or crustal assimilation (Bowen, 1928). In contrast, trace element composition of the mantle is heterogeneous (White, 2013). The diversity of trace element chemistry of primitive basaltic magmas is the result of deep mantle processes and conditions including the mineralogy (if mineral-carrier of trace elements are present) and chemical composition of the source region (intrinsic heterogeneity) and the depth and degree of partial melting.

Furthermore, unlike the major elements, trace elements are passive, they have only a weak influence on crystal structure and chemistry but they have coherent behaviour in the magmatic system (Blundy and Wood, 2003). At equilibrium, they partition themselves in solid and melt proportionally to their concentration; during crystallization trace elements generally obey Henry’s Law (White, 2013) although at very low concentration it is not always the case (Watson, 1985). If Henry’s Law behaviour is obeyed, the distribution of trace elements in solid and liquid can be modelled using the Nernst partition coefficient also known as distribution coefficient D, which represents the ratio of concentration (C) of a given element in a mixture of two immiscible phases such as solid (s) and liquid (l), as

$$D^{s\text{-}l} = C^{s} / C^{l}$$

This simple relationship allows us to indirectly determine the trace element

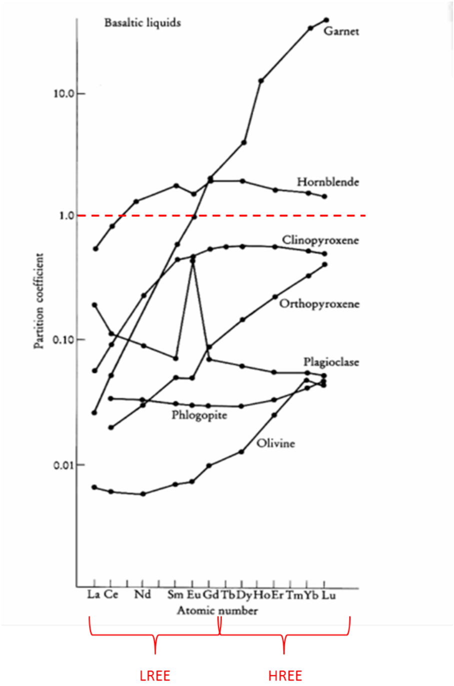

*Fig. 4.38: Partition coefficient of the Rare Earth Elements (REEs) of various silicate minerals commonly found in basaltic rocks modified from Rollinson (1993). The graph illustrates the general incompatibility of REEs in silicate minerals and the greater incompatibility of the LREEs (D < 1) relative to the HREEs (D > 1).*

abundances of parent magmas from which specific minerals have crystallized, assuming equilibrium conditions. During crystallization at defined pressure and temperature, the partition coefficients of trace elements in crystal is proportional to their concentration in the melt (Blundy and Wood, 2003). The graph on Fig. 4.38 shows the melt/mineral partition coefficient of the REEs in some silicate minerals commonly found in basaltic rocks. It highlights the general incompatibility of the REEs in most mineral phases (D < 1) and general greater incompatibility of the LREEs relative to HREEs.

Partial melting commonly generates only a small amount of melt in localized mantle areas such as the mantle source region remains dominated by the solid phase (White, 2013). Trace elements with an affinity for the solid phase (compatible elements with D > 1) are not very useful in defining the nature of partial melting and mantle source because they largely remain in the mantle solid phases. In contrast, trace and minor elements with strong affinity for the liquid phase (incompatible elements with $D \ll 1$) are very powerful in identifying the extent and history of partial melting of mantle sources (Van Orman et al., 2002). The behaviour (compatible *vs.* incompatible) of major, minor and trace elements is of fundamental importance in understanding the wide ranges of magmatic processes (White, 2013). Compatible elements are the best indicators of fractional crystallization processes and liquid line of descent of magmas while incompatible trace elements are best suited to model partial melting processes, partial melting history and mantle geochemistry (Blundy and Wood, 2003; White, 2013).

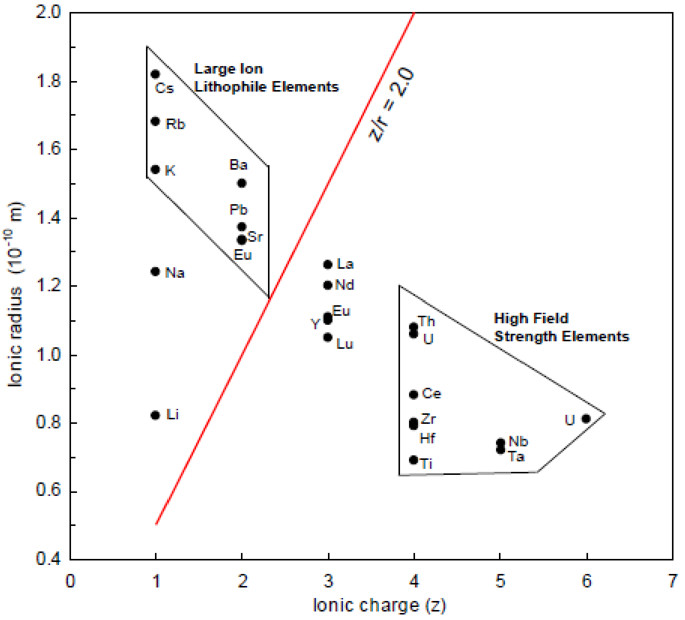

*Fig. 4.39: Ionic radii vs. ionic charge for incompatible elements in common mafic minerals. High Field Strength elements (HFSEs) have a high ionic charge with Z = 3 to 6. They are incompatible because of the difficulty in achieving charge balance with major element cations with generally Z = 2. Elements with relatively high ionic ratios (Large-Ion Lithophile Elements, LILEs) cannot substitute to major elements without structural distortion of the crystal which is energetically not favoured, unknown author.*

The partitioning of trace elements between crystal and their parent melts and the trace element content of basaltic rocks can provide information on the origin and evolution of the parental magma from which the rocks formed (**?**Van Orman et al., 2002; Cherniak and Liang, 2007). Therefore, understanding the behaviour of trace elements and experimentally determining crystal-liquid partition coefficients for the different crystalline phases is of great importance to reconstruct the magmatic history of igneous rocks (Hill et al., 2000). However, defining accurate partition coefficients are not straightforward because the specific degree of compatibility or incompatibility of trace elements in a given mineral varies with the temperature, pressure and composition of the mineral/magma system and the fundamental properties of the elements of interest (Lundstrom et al., 1998; Hill et al., 2000; White, 2013). Consequently, the absolute value of the partition coefficients D of a given element cannot be accurately predicted but some generalization can still be made. Figure 4.39 lists some of the incompatible elements commonly found in mafic minerals. Their incompatibility in minerals, including in clinopyroxene, are due to their high cationic charge or radius that are difficult to accommodate in crystal structure and thus, they do not substitute easily to major elements with common cation charge of $2^+$ (White, 2013). However, some elements (including the minor and trace elements of common silicate minerals) have relatively similar ionic charge and radius and so have similar affinity in crystal site and can substitute relatively easily for each other (for example Ta and Nb, Fig. 4.39).

Given the importance of trace element partitioning in geochemical modelling of magmatic system, it is often easiest to assume that the partition coefficient D of any given element is a constant, independent of composition, pressure and temperature of the magmatic system (Hill et al., 2000). Figure 4.40 shows calculated partition coefficients of a broad range of elements according to their ionic radius and crystal site of incorporation into clinopyroxene (Fig. taken from Hill et al. (2000)). The figure is only shown to provide a general idea on the compatible and incompatible behaviour of different elements in clinopyroxene during mineral crystallization. The elements squared represent the elements selected for analyses of augite phenocryst in the nakhlites with in red the augite compatible elements, in green the mildly incompatible elements and in blue highly incompatible elements. This is given as a general trend of specific element behaviour in clinopyroxene/melt system without absolute knowledge of specific partition coefficient values for the unique magmatic environment of interest. Variations within and between the trace elements selected for further analyses of the nakhlites augite phenocrysts are highly likely because of the difference in pressure, temperature and composition of the Martian basaltic system (Lundstrom et al., 1998; Hill et al., 2000). Of great importance for the variations in trace element compositions and abundances in clinopyroxene is the Al and Na content of the mineral-melt system (Lundstrom et al., 1998; Hill et al., 2000), that is significantly lower in the Martian meteorites relative to common terrestrial basaltic rocks (Fig. 4.17, 4.18 and 4.18). The list of trace elements selected for further analyses of augite from the nakhlites' magmatic suites are summarized in Tab. 4.1.

Another issue that may affect the final trace element composition and abundance in augite phenocrysts in the nakhlites is the intense sub-solidus diffusional re-equilibration experienced by the augite phenocrysts in contact with trapped intercumulus melt during late magmatic processes (Harvey and McSween, 1992). Subsolidus re-equilibration of major elements in augite along their rims is obvious from the patchy and irregular rim zones displayed by the augite grains. However, elements are known to diffuse at different rate within a single or between different mineral phases (Longhi and Pan, 1989; Cherniak and Liang, 2007), which led to a fractionation of elements, a process called diffusive fractionation (Van Orman et al., 2002). The late partial re-equilibration of some of major elements in augite does not automatically reflect a general chemical re-equilibration (Papike, 1996). A previous study of trace element composition of trace element budgets in augite from the nakhlites has demonstrated that a series of trace elements still reflect the original composition (Wadhwa and Crozaz, 1995). They included the REEs and other trace and minor elements, such as Y, Zr, Sr, Ti, and Al. Little work has been done on diffusive fractionation processes of mineral/basaltic melt system, and thus it is difficult to give a broad picture of element fractionation in specific minerals by diffusive processes (Van Orman et al., 2002). Nevertheless, it has been demonstrated that the REEs, Th and U diffuse too slowly in clinopyroxene to be re-equilibrated over the life time of magma. Van Orman et al. (2002) suggested that the slow diffusion rate of these elements in clinopyroxene is due to their high charge and so reflect their strong bonding into the clinopyroxene crystal structure. Consequently, it can be assumed that all elements with high ionic charge are unlikely to diffuse during sub-solidus re-equilibration reactions and may still represent their original

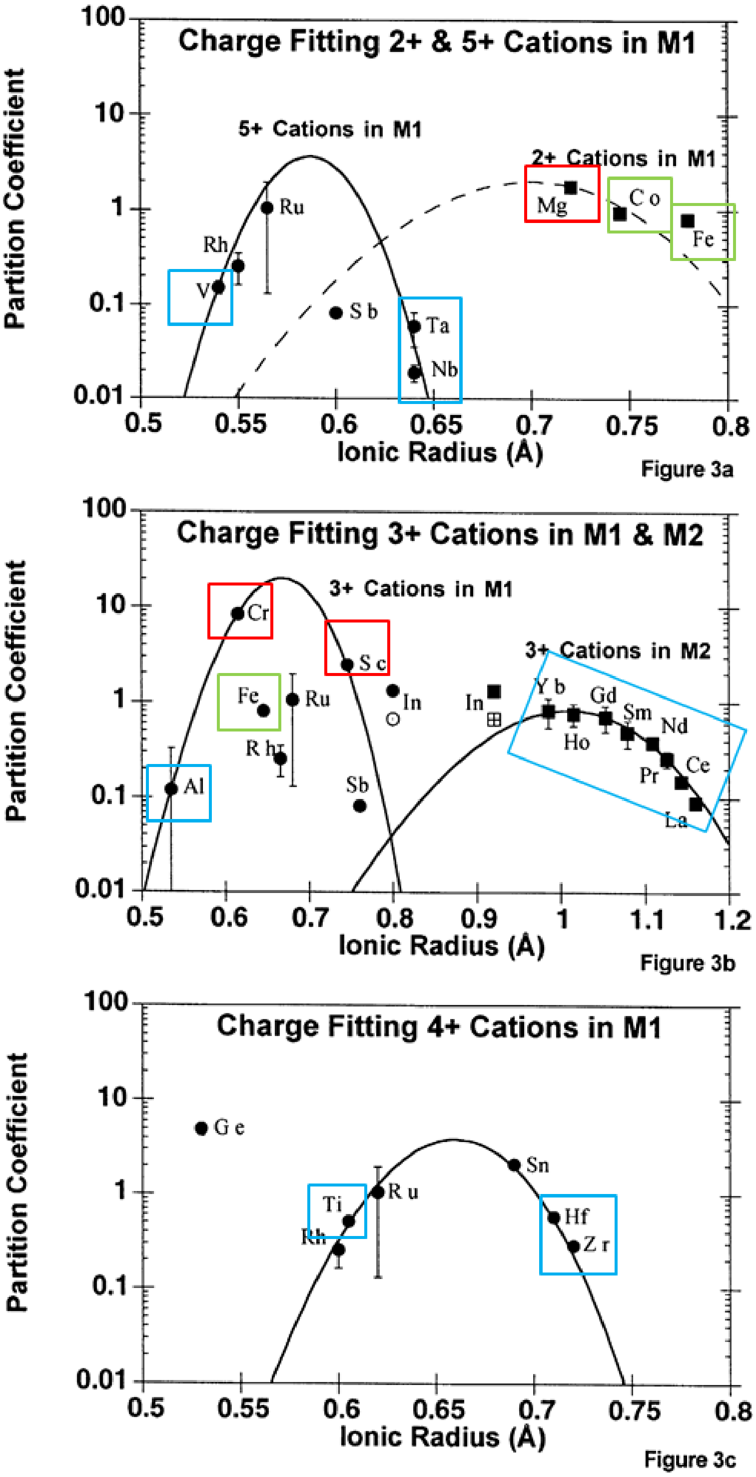

Fig. 4.40: *Plots of log partition coefficient D of different incompatible ($D < 1$) and compatible ($D > 1$) elements of various charge and for different crystal sites M1 and M2 of clinopyroxene vs. ionic radii calculated from experiments, modified from Hill et al. (2000). The graphs is displayed only to show the relative and general compatibility/incompatibility of a broad range of elements in clinopyroxene without assuming that they represent absolute value of element partition coefficients for other magmatic system. Elements selected for analyses of augite phenocrysts in the nakhlites are surrounded in red for compatible elements, green for mildly incompatible elements and blue for highly incompatible elements.*

| | |
|---|---|
| Compatible | Mg, Cr, Sc |
| Mildly incompatible | Fe, Co |
| Strongly incompatible | Ti, V, Ta, Nb, Y, Sr, REEs, Zr, Ba, Th, Rb, Hf, Al |
| Conservative | REEs, Zr, Th, Hf, Al, Ti |

*Tab. 4.1: Table showing the trace elements selected for analyses of augite phenocrysts in individual nakhlites. The conservative elements represent elements that are either known to resist to sub-solidus diffusional reactions in clinopyroxene (Van Orman et al., 2002) or which are believed to still represent the original distribution in augite from the nakhlites (Wadhwa and Crozaz, 1995). The compatible, incompatible and conservative behaviour of a selection of elements (taken from Fig. 4.39) is provided for general understanding and comparison for the nakhlites augite.*

distribution.

### 4.7.2 Tracking magma composition and differentiation through trace elements composition in separate mineral phases

#### Chemical characteristics of the early parent magmas as revealed by augite core geochemistry

Within all the nakhlites, the clinopyroxenes are believed to be the first-formed crystals (Treiman, 2005). Besides possibly olivine, augite is the only solid product of the subterranean magmatic processes. They crystallized from the most "primitive" (i.e. the least differentiated) parent magma(s). The early solid product of hypabysal magmatic activity (i.e. liquidus phase) is often better suited to document the mantle chemistry than their parent melts because magmas are easily contaminated and mixed en route to the surface with remnants of magma from previous magmatic activities or by interactions (i.e. thermal erosion) or assimilations of the host rocks. Apart from apatite, which are too small to be analysed using LA ICP-MS, augite is the main mineral host of trace elements in the nakhlites (Wadhwa et al., 2004). Clinopyroxenes have the capacity to accommodate many incompatible elements in their chemical structure, most than most mafic silicate minerals (Deer et al., 1992). They offer a great opportunity to access the very early composition of the parent magma(s), including some chemical characteristics of the mantle source(s). Critically, in the nakhlites, the cumulus augites display large cores that are believed to have largely retained their original composition (Wadhwa and Crozaz, 1995).

An interesting aspect of the nakhlites cumulate augites is their very similar incompatible trace element (REE, HFSE and LILE) patterns, although their respective abundances vary a few units between the meteorites. In general, Y 000749 and Nakhla have slightly more depleted augite core composition (lower REE abundances), followed by Y 000593, then NWA 998, MIL 03346, NWA 817 to finally NWA 5790. However, this general trend should be considered with care since the number of augite grains analysed is small and may not document the whole range of augite composition in each meteorite (i.e. sampling effect). Cumulus augites from all nakhlites are enriched in LREEs compared to HREEs but somewhat depleted in both La and Ce relative to Pr and Nd. Commonly, clinopyroxene including augite incorporate preferentially the HREEs relative to the LREEs (i.e. higher coefficient partitions, i.e. D, Fig. 4.38). The higher abundances of the most incompatible LREEs in the nakhlite cumulus augite probably reflect a general greater concentration of LREEs relative to the HREEs in the parent melts. The REE patterns and spider diagrams of augite rims (when analysed) and cores of NWA 817 and NWA 5790 show a negative Eu and Sr anomalies respectively, which indicates the presence of plagioclase on the liquidus. The absence of plagioclase in the glassy matrix of NWA 817 and NWA 5790 unlike the other nakhlites suggests that the two rocks crystallized from residual melts that previously experienced intense fractional crystallization of augite and plagioclase. The nakhlites' cumulus augites are generally depleted in LILEs relative to HFSEs especially in Th the most incompatible element (White, 2013).

Cumulus augites from all nakhlites display a similar Ti enrichment ($\sim$ 10000 enriched relative to CI-chondrite) and Zr depletion (ranging from 0.1 to 1 on the logarithmic scale) on normalized incompatible element plots (Fig. 4.23). The negative and positive anomalies of Zr and Ti respectively are also present in trace element plots of plagioclase and interstitial glass (Fig. 4.24 and 4.26). The quantification of the strength of Ti and Zr anomalies using Ti/Ti* and Zr/Zr* with

$$\mathrm{Ti}^{*}=\mathrm{Ti}/((1/2)(\mathrm{Sm}+\mathrm{Gd}))$$
$$\mathrm{Zr}^{*}=\mathrm{Zr}/((1/2)^{*}(\mathrm{Sm}+\mathrm{Gd}))$$

in augite measured from the different nakhlites show a gradual decrease in both anomalies during progressive crystallization (Fig. 4.41).

Despite a continuous increase in Ti and Zr abundances with the degree of crystallization (i.e. from core to rim), it can be noted that the relation between the two elements is not linear (Fig. 4.41). From a Ti concentration of $\backsim$ 1500 ppm, the incorporation of Ti tends to slow down whereas that of Zr continues to increase. In augite, Ti and Zr occupy the same lattice site (Deer et al., 1992). They are isovalent cations with a charge of $4^{+}$, but Ti has a smaller ionic size than Zr and thus is closer to the ideal lattice site radius of augite. The difference in ionic size between the lattice size radius and "foreign" cations is the most important factor controlling the partition coefficient of incompatible trace elements whatever their ionic charge (Onuma et al., 1968; Blundy and Wood, 2003). The element with the smallest cationic size is always preferentially incorporated onto crystal lattices. The preferential incorporation of Ti over Zr in augite is energetically favoured as it requires a smaller lattice distortion. However, the progressive preferential incorporation of Zr relative to Ti with increasing degree of crystallization suggests a more complex crystal control on the partitioning behaviour of Ti and Zr. An explanation could be the effect of the chemical variability of the augite crystal. The increase of element substitution with non ideal cationic size probably distorts the lattice site geometry allowing a greater incorporation of the larger cation Zr.

Deviations of Ti and Zr from smooth patterns on normalized spider diagrams are common in terrestrial igneous rocks (Salters and Shimizu, 1988). However, in the latter they are marked by sharp deficiencies of both elements with no obvious correlation between the two of them. In terrestrial volcanic rocks, the lack of correlation between both elements is believed to result from more complex processes

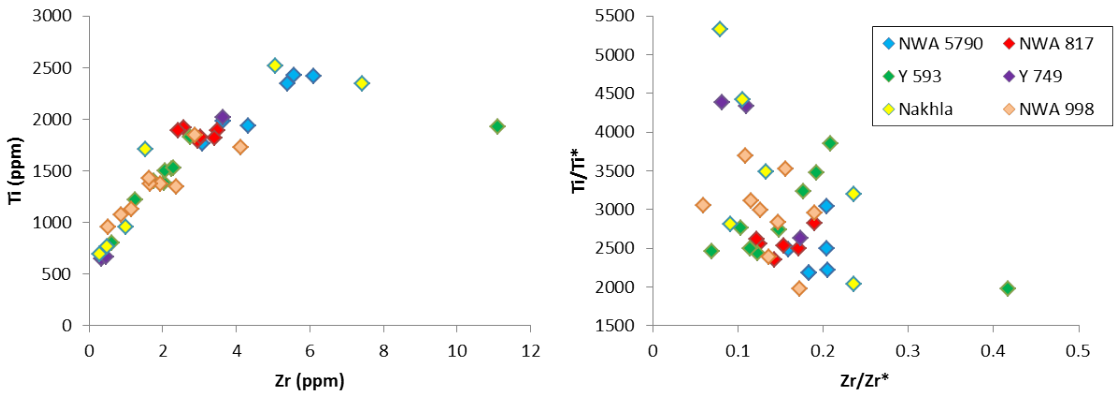

*Fig. 4.41: Ti vs. Zr and Ti/Ti* vs. Zr/Zr* in augite phenocrysts. The ratios represent a measure of the Ti and Zr depletion/enrichment relative to neighbouring elements on normalized incompatible element plots (Fig. 4.22). Such ratios are commonly used to quantify the strength of the positive or negative anomalies. Despite an increase of Ti with progressive crystallization, the strength of Ti anomalies decreases. Ti is less sensitive to fractional crystallization.*

than simple fractional crystallization that are commonly responsible for specific incompatible trace elements depletions/enrichments in magmas (Salters and Shimizu, 1988). The negative Ti and Zr anomalies in terrestrial volcanic rocks are believed to reflect chemical characteristics of the basaltic parent magmas and by extension, chemical characteristics of the mantle source or some obscure fractionation processes that occur in the mantle during partial melting events (Salters and Shimizu, 1988). In the nakhlites' cumulus augites, the respective positive and negative anomalies in Ti and Zr probably also reflect a relative enrichment and depletion of the two elements relative to other trace elements in the parent magma(s). The progressive decrease of Zr negative anomalies with melt differentiation indicates that Zr is relatively more sensitive than the other HFSEs to fractional crystallization processes and thus to the degree of melt differentiation. Zirconium negative anomalies in the nakhlites augite are chemical features of relatively un-fractionated basaltic rocks. With increasing degree of rock differentiation, the anomalies in augite tend to disappear. Augite phenocrysts in NWA 5790 have somewhat weaker Zr negative anomalies, such as the rims of augites from other nakhlites. Cumulus augites in NWA 5790 and NWA 817 probably crystallized from a residual melt that previously experienced a higher degree of fractionation involving both augite and plagioclase.

Other minor and trace elements in cumulus augites display abundance variations between the nakhlites (Fig. 4.42). In pyroxene, sub-solidus diffusion of Ti is known to be slower than Mg or Fe (Cherniak and Liang, 2012). Magnesium and Fe distribution throughout the augite rims in the different nakhlites may not represent the original abundances and distribution unlike Ti (Wadhwa and Crozaz, 1995). The distribution of Ti in the nakhlites' pyroxene can be used as an indicator for the extent of igneous fractionation experienced by the meteorites, as is common in terrestrial basaltic rocks. An interesting aspect of Ti abundance and distribution in cumulus augites is the range of concentration within individual nakhlite. The range of Ti concentration is wider for Nakhla and both Yamato nakhlites suggesting that the three meteorites crystallized their augite population from magmas experiencing more extreme differentiation processes (Fig. 4.42). In addition, augite grains from the three meteorites also have the lowest Ti concentration. This may result from a sampling effect. However, the relative depletion in Ti and both REEs and HFSEs of the augite cores from these three nakhlites, together with their less evolved bulk rock chemistry (TAS and REE patterns, Fig. 4.17 and 4.22), suggest that these meteorites began to crystallize from more "primitive" magmas. The "primitive" cores of cumulus augite (i.e. Ti $<$ 1500 ppm) from Nakhla, Y 000593 and Y 000749 have similar augite compatible element (i.g. Cr and Ni) and augite incompatible element (i.g. V, Y, Mn, etc.) abundances. From Ti $>$ 1500 ppm, the composition of augites in all nakhlites is more variable which supports the hypothesis that changes in augite composition cause variations in partition behaviour of incompatible elements (i.g. Ti and Zr).

Other interesting patterns are the relative similarities between Sc and Mn, Cr and Ni, and V, Y and Sr (Fig. 4.42). The elements of the apparent same "group" probably substitute onto the same lattice site. They also probably had similar substitution behaviours in augite. Augite rims are rarely thick enough to be measured using LA ICP-MS such that only one rim in NWA 817, Y 000593 and Y 000749 and two from Nakhla have been measured. The tight-to-scattered trends of incompatible Sc, Mn, V and Sr may reflect partial sub-solidus re-equilibration. However, by looking closely at for example Mn and Ni plots, we can see that the elemental patterns for each meteorite on both graphs are the exact inverse (like a symmetry effect) suggesting that the tight-to-scattered patterns may also reflect growth variations with a more complex substitutional behaviour during crystal growth from more evolved melt and with a certain degree of "co-dependency" between different elements substituting into the same lattice site. Diffusion-driven zoning in augite crystals appear to be difficult to clearly identify from crystal growth zoning as they result in similar elemental zoning in the pyroxene solid solution. However, even if cumulus augite were subject to partial sub-solidus diffusional re-equilibration (Wadhwa and Crozaz, 1995; Richter et al., 2016), it is unlikely that diffusive re-equilibration was the main process in the origin of such scattered patterns as it would have "fractionated" the different elements between themselves according to their specific diffusive behaviour and capacity.

Despite an apparent "coherent" behaviour of mildly incompatible elements during crystal growth (i.e. a gradual increase in elemental abundances from core to rim), mildly incompatible elements (i.e. Ti) in augite show a slowing down of their degree of incorporation during progressive crystallization of augite. Weakly incompatible elements (i.e. Sc, Mn, etc.) display more subtle variations and complex zoning patterns with an apparent more erratic behaviour during crystal growth. Both weakly incompatible elements and compatible elements in augite have been more sensitive than very incompatible elements to the evolution of physico-chemical conditions during and post crystal growths. The less incompatible an element is, the more complex its behaviour seems to become during progressive crystallization. Very incompatible elements may not be the best elements to identify different melt composition and/or progressive evolution in melt composition and conditions during fractional crystallization.

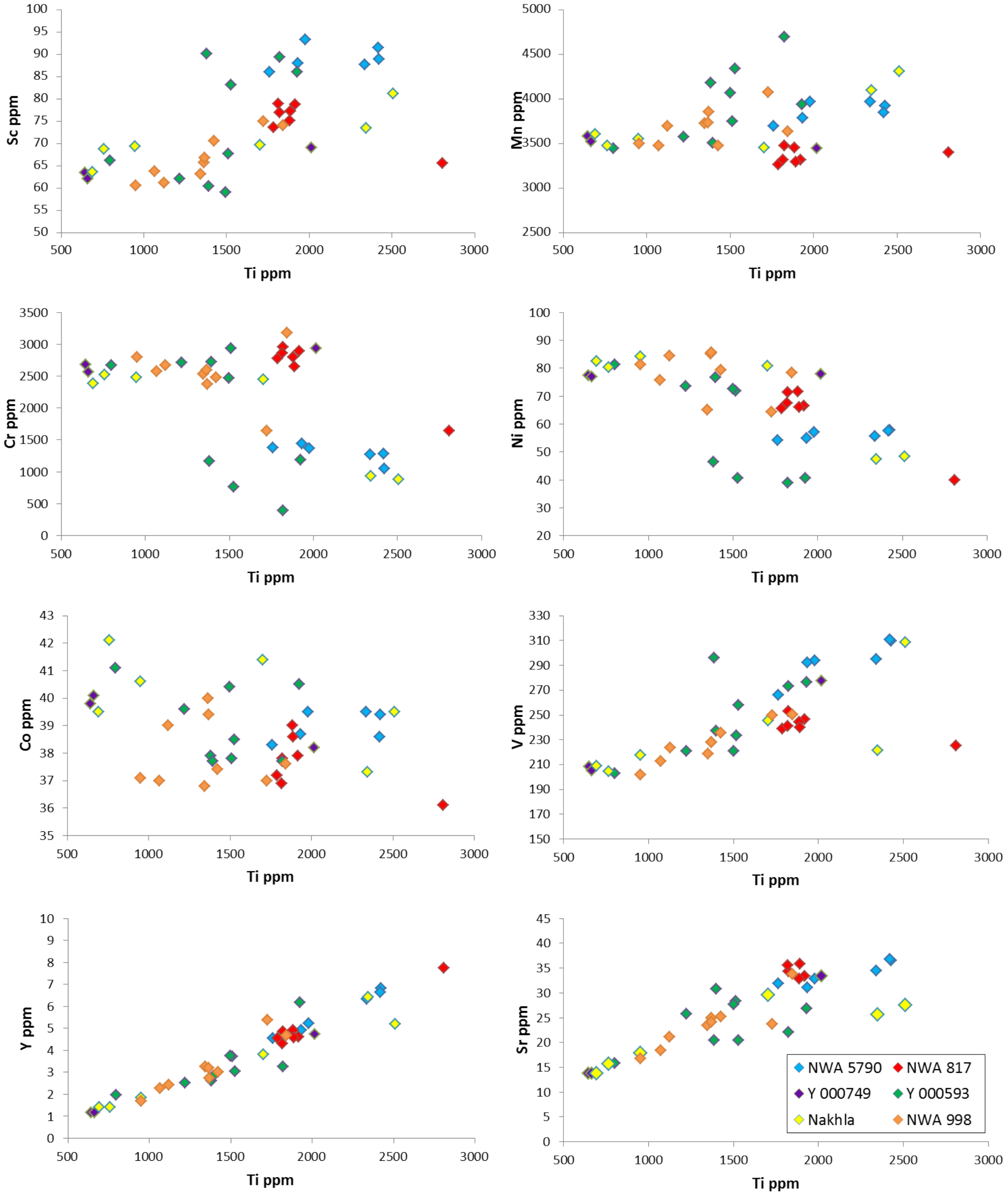

*Fig. 4.42: Trace element abundances in augite phenocrysts from different nakhlites. Despite their similar major element compositions, the trace element compositions of the augite phenocrysts vary (in both abundance and extent of zonation) between the nakhlites.*

Nakhlites NWA 817 and NWA 5790, which are believed to be the least reequilibrated nakhlites (Sautter et al., 2002; Jambon et al., 2010), have the most evolved augite core composition; they have the highest abundances in all of the most incompatible elements (i.g. Ti, Y, Sr, V). They also have the most evolved bulk rock chemical composition on both TAS and REE diagrams (Fig. 4.17, 4.22 and Jambon et al. (2010)). Both meteorites have their augite cores less extensively zoned in Ti, and Ti concentration plotting within the field of augite rims of the other nakhlites (Fig. 4.42). The augite cores from NWA 5790 display a small variation in Ti abundance, the augite rims of this nakhlite being too small to be analysed using LA ICP-MS. Augites of NWA 817 and NWA 5790 do not display significant abundance variations in most element analysed (including both compatible and incompatible) except in the most incompatible elements (i.e. Y or Sr) but have distinct elemental abundances in Cr, Ni, V, and Mn (Fig. 4.42). Manganese, Cr and Co with their ionic size similar to Mg are compatible elements in clinopyroxene. Augite cores from nakhlite NWA 5790 are enriched in Mn and Co relative to nakhlite NWA 817 but not in Cr. NWA 817 display smaller variations in minor and trace elements than any other nakhlites analysed in this study.

The higher incorporation of incompatible trace elements including Ti and Y in augite cores from NWA 817 and NWA 5790 could be the result of kinetic effects, a higher cooling and/or decompression rate which would have favoured crystal growth from the (compatible-depleted) diffusive boundary layers at the melt-solid interface (Lofgren et al., 2006). However, the relatively constant and high concentration of compatible elements in augite cores from NWA 817 argues against crystallization of augite cores under disequilibrium conditions. Furthermore, trace and minor element substitutions in augite show a crystal structure dependency. For example, the augite-compatible elements Cr and Ni and augite-incompatible Sr and Mn show similar patterns which not only reflect their similar substitution behaviour in the clinopyroxene but also their similar lattice site occupancy. Abundance variations in cumulus augite between these two meteorites probably reflect different element budgets in the melt. It is likely that both nakhlites crystallized their augite populations from more evolved basaltic magmas, but possibly from chemically distinct magmas. The composition of the clinopyroxene cores in NWA 817 is relatively homogeneous suggesting an overall attainment of chemical equilibrium of the magma at the time of augite core crystallization, unlike NWA 5790.

Olivine is the second mineral phase that possibly crystallized in the basaltic plumbing system (Treiman, 1990; Harvey and McSween, 1992). Unlike augite, olivine cannot incorporate significant amounts of trace elements including the REEs because of its simple crystal structure and chemistry (Foley et al., 2013). Olivine has two octahedral M1 and M2 sites which are both too small to suit most trace elements (De Hoog et al., 2010). Major elements in olivine have either a cationic charge of $2^+$ (Mg, Fe) or $4^+$ (Si). Substitution of cations with similar valences and size is straightforward but substitution of cations with different charges and sizes requires (charge-balanced) coupled substitution associated either with lattice distortion (that are energetically unfavourable) or with the generation of crystal vacancies (De Hoog et al., 2010). Amongst the elements that olivine can incorporate during its growth are the first series transition elements (i.g. Sc, Ti, Cr, Mn, Ni, Co, Zn, etc.). These elements can be used to identify the early fractional crystal-

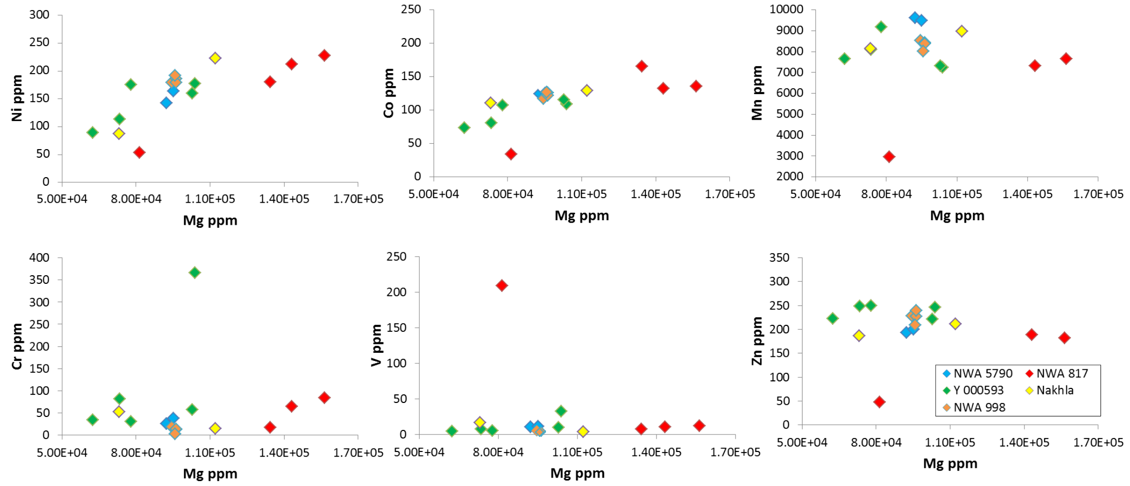

*Fig. 4.43: Selected trace elements in olivine phenocrysts and its high temperature oxidative replacement product (i.e laihunite, L) in Y 000593. Data from NWA 5790 represent measurements of the same large olivine grain.*

lization path although care has to be taken as they may have re-equilibrated during late-stage magmatic processes. During fractional crystallization, Ni, Mn, and Co partition preferentially into olivine relative to other silicate minerals because they have ionic radii close to Mg (De Hoog et al., 2010). They commonly show positive correlation with the forsterite content of olivine. The most compatible elements in olivine are Ni and Co; they are believed to be enriched in olivine relative to primitive mantle (De Hoog et al., 2010).

Figure 4.43 shows minor element contents in olivine phenocrysts. The minor elements are plotted *vs.* Mg although olivine was subject to intense sub-solidus Fe-Mg diffusional re-equilibration. In most nakhlites (except possibly NWA 5790 and NWA 817?), the Mg distribution no longer represents the original zonation and abundances. But as Fe-Mg re-equilibration occurs inward, olivine still display a progressive increase in Mg content toward the grain center (i.e. normal zoning). Post-crystallization exchanges have led to an increase in Fe content relative to Mg, an erasure of the fine-scale primary zoning and an apparent increase of rim zones relative to the core size. Nickel and Co abundances in olivine from all nakhlites analysed in this study generally increase with the Mg content (i.e. forsterite content), as expected in olivine. They are enriched in olivine relative to augite. On the other hand, V and Cr abundances are low in olivine from all nakhlites analysed. They do not fit well onto lattice sites of olivine because of their ionic size or charge (De Hoog et al., 2010). The high temperature oxidative alteration product of olivine (i.e laihunite) in Y 000593 and its host olivine shows a continuum of chemical composition in the studied minor elements. The late sub-solidus transformation of olivine into laihunite probably did not affect the original trace element distribution and/or has been affected by diffusional re-equilibration to the same extent as olivine.

Chromium is an important element in olivine because its diffusion is slow in this mineral phase (De Hoog et al., 2010). In olivine phenocrysts from the nakhlites, abundance variations in Cr may still represent the original abundances and distributions. Moreover, olivine in both NWA 817 and NWA 5790 have probably experienced incomplete sub-solidus re-equilibration because their parent magmas cooled very quickly. If correct, their olivine cores have retained their primary composition (i.e. not enough time for sub-solidus diffusion). Olivine phenocrysts in NWA 817 have a distinct chemical composition including elements that are believed to be "conservative" including Cr, a chemical feature already identified in its augite phenocrysts. Chromium abundance in olivine phenocrysts from NWA 5790 is lower than in the core of olivine phenocrysts from NWA 817 ($\backsim$ 25-50 ppm and $\backsim$ 50-75 ppm, respectively), a similar trend to these observed in augite phenocrysts from both meteorites. Variations in Cr abundance (a very compatible element in olivine) of the two phenocryst phases between NWA 5790 and NWA 817 most probably reflect different element budgets in the respective parent melts. Olivine cores in NWA 817 have a higher forsterite content than NWA 5790, but also the greatest Ni abundance (together with Nakhla), two features commonly attributed to olivine, which crystallizes from less differentiated (or more primitive) basaltic magmas. Crystallization of olivine in NWA 817 from a less fractionated magma is inconsistent with most previous data raising once again the question of the possibility of a distinct parent magma for NWA 817. Cobalt, Mn and Zn display similar zonation patterns in the different nakhlites suggesting that they had similar substitutional behaviour in olivine. They may still represent primary abundances.

### *Early magmatic differentiation recorded in augite rims*

Rare Earth Element graphs and HFSE spider diagrams of augite cores (the product of hypabyssal magmatic processes) and rims (the product of superficial magmatic processes) are nearly parallel to each other but with a general and consistent increase in abundances for the latter relative to the former in all nakhlites. The early intercumulus melts in a single nakhlite were genetically related to those that crystallized augite cores with no obvious chemical contaminations of the parent melts through magma mixing or host rock assimilation.

Minor and other trace elements (Fig. 4.42), including the augite compatible elements Cr and Ni, show a sharp change in elemental concentration between augite cores and rims in Y 000593 and Nakhla, augite rims from Y 000593 being the most depleted in both elements. This probably either reflects sudden changes in availability in Cr and Ni in the melt, associated with the co-precipitation of another mineral phase (olivine, oxides?), and/or sub-solidus diffusional re-equilibration. Vanadium, Mn and to less extent Sr in augite from Nakhla and Y 000593 show disruption (large elemental concentration variations at given Ti concentration) of the general trend (Fig. 4.42). Together with Ni and Co, their "inconsistent" zoning patterns in augite rims may reflect either complex changes in crystal composition during augite crystallization as explained above (associated or not with partial sub-solidus re-equilibration of these elements as suggested by Wadhwa and Crozaz (1995)), or again melt heterogeneity. Trace and minor element patterns suggest a more subtle crystal zoning than can be seen on BSE images, which may reflect the greater sensitivity of trace elements to magmatic conditions. The overall concentrations of incompatible elements (i.g. Y, Ti, Sr, V) of augite cores in NWA 817 and NWA 5790 are similar to the augite rims of the other nakhlites. Augite phenocrysts in NWA 5790 are depleted in Cr and Ni relative to those of NWA 817. These depletions are accompanied by an increase in Sc, Mn and V; a chemical trend expected from melts that experience intensive fractional crystallization. From our data, NWA 5790 crystallized from a residual melt more differentiated than any other nakhlites analysed in this study. Crystallization of the felsic mineral plagioclase played a major role in the degree of melt differentiation.

### *Evolutionary trends of inter-cumulus melt*

Based on textural observations, plagioclase in NWA 998, Y 000593, Y 000749 and Nakhla crystallized early from interstitial melts, during augite growth and accumulation and/or once augite accumulated but prior to augite rim formation. Rare Earth Element concentrations in plagioclase grains including their thin K-feldspar rims in Y 000593 and NWA 998 show typical patterns with an enrichment in LREEs relative to HREEs (higher partition coefficient of LREEs relative to HREEs, Fig. 4.38) and a general increase in REE abundances from plagioclase to K-feldspar (i.e. following magmatic differentiation, Fig. 4.24). Parallelism of REE patterns between plagioclase and K-feldspar rims suggest a crystallization in a closed-system as for augite core and rim. However, the incompatible trace elements in plagioclase and K-feldspar are more enriched in Y 000593 than in NWA 998, with similar trends observed on their respective spider diagram and bulk rock REE compositions (Fig. 4.21, 4.24). For example, feldspar in NWA 998 display strong negative anomalies in very incompatible Rb, Nb and Zr but do not display any La depletion typical of the nakhlites, chemical characteristics not observed in feldspar from Y 000593. The large plagioclase cores are compositionally homogeneous with respect to major elements within and between the nakhlites. Only the thin K-feldspar overgrowths show major element variations which can be attributed to various extent of melt differentiation achieved by the melts at the time of feldspar crystallization. The difference in incompatible trace elements between the plagioclase population from both nakhlites most probably reflects different trace element budget (compositions and abundances) in the respective melts from which the nakhlites respectively crystallized. Inter-cumulus melts between the two nakhlites have not been in contact with each other.

Trace element composition of cumulus augite in Y 000593 suggest that the meteorite crystallized its augite from magma experiencing more intense differentiation processes, leaving the melt post-augite crystallization more fractionated than that of other nakhlites including NWA 998. The higher trace element budget of plagioclase in Y 000593 can be explained by crystallization of plagioclase from these more evolved inter-cumulus melts with greater concentrations in incompatible trace elements. The crystallization of plagioclase in NWA 998 may have begun “earlier” than in Y 000593 in the crystallization history which is consistent with the larger feldspar grain size of this nakhlite. However, the larger grain size of plagioclase from NWA 998 may also be the result of the apparent slower cooling rate experienced by this nakhlite.

As in Y 000593, Nakhla is also one of the nakhlites that experienced intense early magmatic differentiation processes in the shallow magmatic system, as indicated by the trace element composition of its cumulus augite including its REE zonation (Fig.4.22). Trace element composition of its last residual melt found in pore corners is highly fractionated and evolved, more than most nakhlites analysed in this study (greater overall REE abundances especially the LREEs, Fig. 4.26). As with its augite population, the trace element composition of the last droplets of inter-cumulus melt in Nakhla indicate that this nakhlite (together with the Yamato meteorites) has experienced more intense differentiation processes than most nakhlites during its whole crystallization history.

The mesostasis of NWA 817 contains widespread nm-scale apatite grains embedded in glass and other larger grain of different mineral phases. At first sight, apatite in this specific nakhlite is homogeneously distributed and cannot be avoided during LA ICP-MS analyses. It is a mineral carrier of REEs and other incompatible elements in common minerals of basaltic rocks (e.g. Sr, P, etc.). The homogeneity in trace element composition of the poorly crystallized mesostasis of NWA 817 provides geochemical evidence for a homogeneous inter-cumulus melt composition including the distribution of apatite (Fig. 4.26). Cumulus augites in NWA 817 also show a compositional homogeneity with respect to incompatible trace element abundances. Hence, chemical melt homogeneity was already a characteristic of NWA 817' parent magma at the time augite crystallized.

### *Origin of compositional variations in trace elements: Deciphering mantle source from fractional crystallization processes*

Geochemical microanalyses of the nakhlites have revealed subtle differences in mineral trace and minor element budget (composition, distribution and abundance) between the different meteorites. Compositional variations with respect to trace and minor elements in separate mineral phases between the nakhlites have already been reported by Wadhwa and Crozaz (1995). They suggested that some nakhlites are more evolved than others, but because the range of compositional variation of minerals within a single nakhlite overlap with those reported between the nakhlites, their interpretation has been dismissed (Treiman, 2005). However, there are general consistencies in the relative enrichment/depletion of a wide range of elements in different mineral phases between the nakhlites. The specific chemical characteristics and zonation of the early-formed augite are further consistent with the compositions of the later-crystallized olivine and plagioclase of separate nakhlites and with the nakhlites differentiation trend on the TAS diagram and/or bulk rock trace element chemistry. The relative enrichment/depletion of augite between the individual nakhlites may not be a mere sampling effect. The nakhlites similarities suggest that they are genetically related but by which processes? Do the subtle geochemical variations in augite crystals between the nakhlites reflect mantle source variations, heterogeneity, partial melting dynamics, or are they the sole result of complex fractional crystallization-differentiation processes?

Mantle-derived primary magmas naturally display highly variable chemical compositions including trace element budgets. The chemistry of basaltic magmas can vary as a result of mantle source heterogeneities, the degree of partial melting (the smallest the most enriched in incompatible elements), changes in the melting dynamic process, mantle source history (if the source region experienced anterior episode(s) of partial melting which would have depleted the source region (i.e. remove the most incompatible elements), and efficiency of melt extraction (Kamenetsky and Maas, 2002). Furthermore, magma mixing with residua in the basaltic conduits and crustal assimilation are also efficient mechanisms that can significantly change the primary basaltic magma composition at any moment including prior to the onset of crystallization while it is still en route to the surface.

Changes in the chemistry of primitive basaltic magmas can also result from crystallization-differentiation processes with physical separation of early formed crystal and their parent melts in the magmatic environment either within the uppermost mantle or crust (Annen et al., 2006). Evolutionary trends of basaltic magmas are controlled by the physical conditions at which magmas emplace and/or stagnate and begin to crystallize because they determine the phase equilibria. The crystallization depth and pressure further determine the chemical composition of mineral assemblages and control the genesis of intermediate to felsic magma types (Annen et al., 2006). The chemistry of minerals is commonly used as an indicator of the physical conditions under which the specific mineral crystallized (Simkin and Smith, 1970; Thompson, 1974). Homogeneous primitive basaltic magmas can crystallize silicate minerals with different geochemistry because of different physical conditions (pressure, temperature, oxygen fugacity, etc.) in the basaltic conduits and generate multiple fractionated magmas at different stages of evolution that can be physically separated from the parent magma because of density contrast.

The nakhlites' bulk rock chemistries have very similar major element composition and trace element patterns (parallelism), which probably reflects crystallization of the different meteorites from geochemically similar parental magma(s). Together with their identical (within $2\sigma$) crystallization age and initial radio-isotopic composition (Nyquist et al., 2001), one can conclude that the nakhlites' parent melts originated from a common mantle source region and formed relatively contemporaneously. The nakhlites are all depleted in very incompatible elements relative to moderately incompatible elements, for example Th, U, Na and K (Treiman, 2005). They also have similar La and Ce abundances relative to other LREEs, which reflects the depleted nature of the mantle source and the existence of long-lived magmatic activity with anterior partial melting events and melt extraction processes. However, the nakhlites are all enriched in moderately incompatible elements relative to less incompatible elements (for example greater abundances of LREEs relative to HREEs). The nakhlites' parent magmas formed by small degrees of partial melting, which is consistent with a formation of the nakhlites' parent magma through heat generated by radioactivity in the mantle source region (Jones, 2003).

Clinopyroxene is an important constituent of basaltic rocks including the nakhlites. It crystallizes early (it is probably the liquidus phase in all the nakhlites) and has a complex crystalline chemistry and structure, which means that its chemical composition varies with the physico-chemical conditions that prevailed during its crystallization (Thompson, 1974). For example, with a decrease in temperature or increase in cooling rate, clinopyroxene becomes progressively depleted in Ca, Mg, $Fe^{2+}$ and Si and enriched in Na, $Fe^{3+}$, Al and Ti, or in other words the diopside and hederbergite components decrease while the Ca-Tschermark, jadeite, and enstatite increases, and the ferrosilite component remains constant (Mollo et al., 2010). Furthermore, under high cooling rate, clinopyroxenes are generally enriched in incompatible elements which is believed to reflect the growth of the clinopyroxene from the depleted layers that developed at melt-crystal interfaces, a crystallization process referred to as diffusion-controlled (Kirkpatrick, 1981).

Trace elements do not comprise the structure of common minerals and remain passive during magmatic processes (Blundy and Wood, 2003). The processes responsible for their incorporation in silicate minerals are complex. Their degree of incorporation in minerals (i.e. partition coefficient D) can be controlled by the crystal or melt chemistry or by variables such as pressure, temperature, cooling rate and oxygen fugacity (Gamble and Taylor, 1980). Experimental studies have shown that at constant pressure neither melt chemistry (i.e. major element composition) nor degree of melt polymerization (i.e. melt structure) affect the partition coefficient of trace elements in clinopyroxene (Lundstrom et al., 1994, 1998). Even if pressure and temperature have some influence on the crystal-melt partition coefficients, crystal chemistry and structure appear to be the main parameters controlling trace element incorporation under any physical magmatic conditions.

Effectively, multi-element partition coefficients for clinopyroxene and melt show a strong dependence on the content of tetrahedrally coordinated Al and octahedrally coordinated Na in clinopyroxene, either during equilibrium and non-equilibrium crystallization of basaltic melt under a wide range of natural isobaric and isothermal crystallization conditions (Skulski et al., 1994; Lundstrom et al., 1998; Blundy and Wood, 2003). The incorporation of incompatible trace elements in pyroxene is affected by the crystal chemistry of the pyroxene, especially the non-quadrilateral components because they provide excess free negative charge (enabling heterovalent substitutions) needed for the incorporation of the highly charged trace elements (Don and William, 2008). Yet, as intensive variables control the major and minor element composition of the pyroxene solid solution series, it also means that under identical physical conditions different basaltic magma types can crystallize pyroxene with very similar chemistry.

The nakhlites' cumulus augites are normally zoned with large cores of near uniform composition in major elements but with rims displaying wide ranges of composition. The nearly identical augite core composition in quadrilateral components suggests that the nakhlites began to crystallize under relatively similar physical conditions. The large and homogeneous augite cores (except in NWA 5790) indicate the possibility of very slow growth rate while the absence of oscillatory zonation or growth bands suggests continuous intra-crystalline diffusional re-equilibration of major elements in augite during crystal growth. Unlike the major elements, most trace element concentrations in clinopyroxene are mostly a function of their abundances in the melt with some influence by major element composition and structure of the minerals. Variations in intensive parameters are relatively unlikely to significantly fractionate trace elements with similar geochemical properties but rather affect their overall degree of incorporation in crystals, resulting in the formation of a different augite population, provided that variations of intensive parameters are large enough. The large homogeneous and nearly identical augite core composition (in quadrilateral and most but not all non-quadrilateral components) minimize interpretative uncertainties regarding the crystal chemical effect on trace element incorporation at least during the very early crystallization of the augite cores. Different trace element budgets in the cores of cumulus augites should reflect different melt chemistries, with the exception of variations in element abundances that exist in different oxidation states, which could also reflect different physical conditions in the basaltic plumbing system. Table 4.2 summarizes the behaviour of selected trace elements in augite phenocrysts in the nakhlites during crystallization.

| | |
|---|---|
| Compatible | Cr, Ni |
| Mildly incompatible | Sc, Mn, Co |
| Strongly incompatible | Ti, V, Y, Sr, REEs, Zr, Ba, Th, Rb, Hf |

*Tab. 4.2: Table summarizing the apparent behaviour of selected trace elements in augite during nakhlites crystallization. Compatible and mildly incompatible elements show complex zoning patterns reflecting both changes in element behaviour during augite growth and late sub-solidus re-equilibration.*

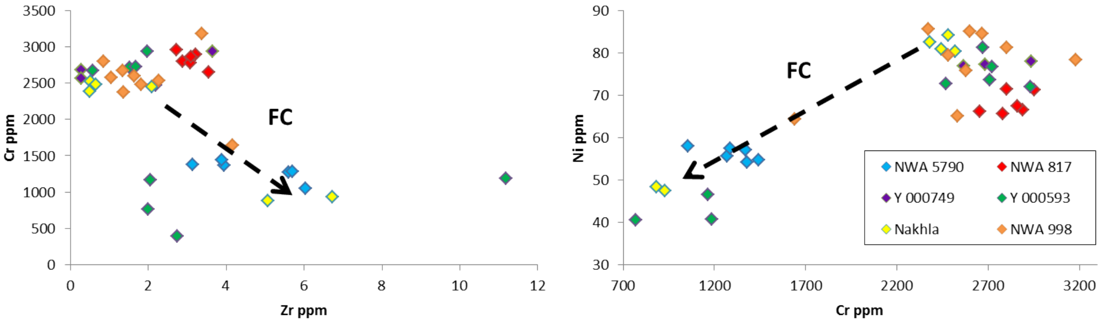

*Fig. 4.44: Binary diagram of Chromium (Cr) vs. Zirconium (Zr) and Nickel (Ni) in augite phenocrysts from different nakhlites. Chromium and Ni are compatible in augite, whereas Zr is incompatible. The arrows represent the magmatic evolution during fractional crystallization (FC) of Nakhla. A crystallization of the rocks through closed system FC should form overlapping trends.*

Formation of the nakhlites through fractional crystallization of a single magma pool should result in a gradual and consistent chemical evolution of compatible and incompatible elements. Figure 4.44 shows that the individual nakhlites have different element budgets. Cumulus augites of the individual nakhlites form two distinct groups with NWA 5790 commonly plotting outside of the other nakhlites cluster. Augite cores in NWA 5790 have a similar composition in compatible and incompatible elements to the augite rims of the other nakhlites suggesting that NWA 5790 began to crystallize from a chemically similar melt but one that had previously experienced more intense fractional crystallization. Augite cores from NWA 817 are slightly enriched in highly compatible Cr relative to other nakhlites although they are enriched in incompatible Zr and compatible Ni. Chromium is known to preferentially partition into clinopyroxene whatever the physical conditions of the magmatic system (De Hoog et al., 2010). Variations in Cr budget in augite reflect different abundances in the melt. The greatest concentration in Cr added to smallest concentration in Ni and Zr in augite from NWA 817 cannot be explained by a melt evolution of a common parent melt through progressive fractional crystallization processes of augite and plagioclase (with or without olivine) alone.

Nakhla and Y 000593 display parallel evolution trends of Cr *vs.* Ni from augite core to rim but with Nakhla consistently slightly more enriched in Ni for relatively similar Cr abundances. Augite rims in Nakhla are also enriched in Zr relative to Y 000593 for similar Cr abundances. Again, augite cores from NWA 998 display more variations in the three elements than the cores of augite from the other nakhlites analysed (Fig. 4.44). The variations are not correlated with augite grain size. The smallest grains are not necessarily the most chemically evolved with respect to all chemical elements. Cumulus augites in NWA 998 display chemical variations between the grains that most probably reflect melt heterogeneity. Furthermore, only augite cores from NWA 817 and NWA 5790 display chemical evidence for early plagioclase crystallization which argues against a formation of augite phenocrysts from all nakhlites from a slowly cooled shallow igneous body. Cumulus augites from the individual nakhlites display chemical characteristics that reflect different parent melt compositions, evolutions and crystal growth kinetics.

Common tests for identifying a genetic relationship of magmatic suites are to compare the ratio of incompatible elements between the rocks. Titanium and Al are mildly incompatible in clinopyroxene (Adam and Green, 1994). The degree of incorporation of both elements can be affected by the growth rate and the temperature and pressure conditions at the time of crystallization although variations in intensive parameters have to be relatively significant to be observable through Al and Ti concentration in clinopyroxene. In general, an increase in temperature increases the Al content in clinopyroxene but is unlikely to affect the Ti uptake, whereby an increase of pressure increases Ti and decreases Al abundances (Adam and Green, 1994). Aluminium/titanium ratios vary less significantly with intensive variables and may help to identify different melt compositions. Aluminium/titanium ratios in augite can also help to identify the crystallization of plagioclase (decrease of Al/Ti ratios) or magnetite (increase in Al/Ti ratios).

Figure 4.45 shows the Al/Ti ratios *vs.* Mg♯ of augite phenocryst core and rim from different nakhlites. A decrease in Mg♯ occurs as a result of melt differentiation during fractional crystallization in a closed system. The Mg♯ of the large augite cores is homogeneous (re-equilibrated distribution of Mg and Fe in augite cores) and relatively identical between all nakhlites analysed (∽ 0.62 - 0.65) with the exception of augite cores from NWA 5790, which have lower Mg♯ that further varies from ∽ 0.53 to 0.61. The lower Mg♯ and weaker Zr anomalies (amongst other) of augite cores from NWA 5790 reflects an early crystallization of this meteorite from a more evolved melt while the preservation of oscillatory zoning throughout the augite cores suggest a faster growth rate than the other nakhlites providing less time for intra-crystal diffusional re-equilibration. NWA 998 and Lafayette have somewhat the greatest Mg♯. Both nakhlites are the most coarsely crystallized with less abundant fully crystallized ground-mass. Intra-crystalline re-equilibration of the large core during augite formation may have been less efficient possibly due to a quicker physical separation (i.e. gravitational settling) of the augite grains from the magma pool.

Augite rims in all nakhlites (no obvious rims in augite from NWA 998 and Lafayette) display sharp changes in Mg♯ with a compositional gap between cores and rims in individual nakhlites that further varies between the meteorites. The sharp compositional gap may reflect a crystallization of augite rims from more evolved melt associated with sudden increase in the cooling rate to prevent further diffusional re-equilibration with the inter-cumulus melt. Effectively, an incomplete sub-solidus re-equilibration of the cumulus augites with the late inter-cumulus melts is also suggested by the lower Mg♯ of the nakhlites' bulk rocks (ranging from 0.35

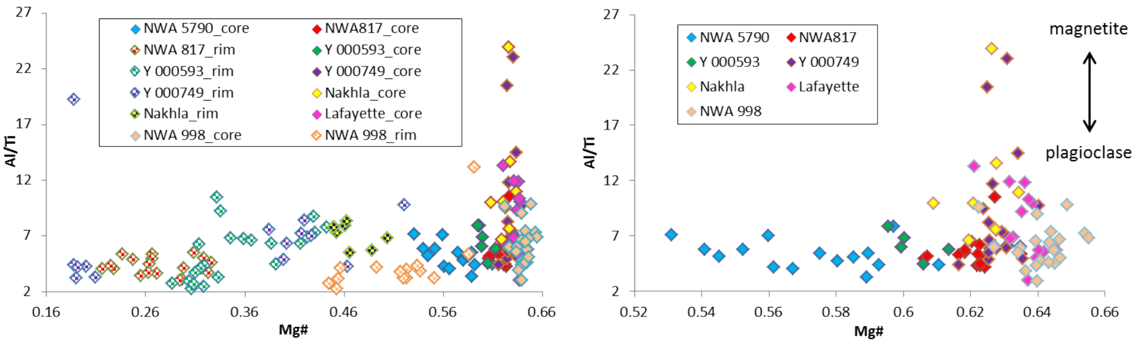

*Fig. 4.45: Aluminium/Titanium (Al/Ti) vs. Magnesium number (Mg♯) in augite phenocryst core and rim (left) and core (right). Ratio of the augite incompatible elements are less sensible to pressure and temperature conditions than Al and Ti concentrations and thus are interesting to track variations in melt chemistry. Al/Ti ratios of augite can also serve to identify the relative timing magnetite and plagioclase crystallization.*

to 0.4 with no data for NWA 5790; same references as for the TAS diagram Fig. 4.17) relative to that of their augite population. This also underlines that the nakhlites bulk rocks' composition is dominated by the inter-cumulus melts despite the greatest modal abundance of augite grains.

The Al/Ti ratios show large variations at similar Mg♯ in augite cores within individual nakhlites but the ratios strongly overlap between the individual nakhlites. These variations reflect not only the relative immobility of both elements to diffusive re-equilibration during and after mineral crystallization, unlike Fe and Mg, but also the precipitation of plagioclase relatively early in the crystallization history (prior to augite full growth), which is further consistent with the low Al/Ti ratios of augite rims. Rims of cumulus augites from the different nakhlites have different Mg♯ but reached similar Al/Ti ratios ($\backsim$ 2) whatever the Mg♯. Nakhlites Nakhla and Y 000749 have augite cores with the greatest Al/Ti ratios. The variations in elemental abundance may reflect a melt inhomogeneity or a gradual increase in the degree of melt fractionation (with the precipitation of plagioclase) that led instantaneously to changes in augite composition with an increase of Ti relative to Al. Furthermore, augite cores from the two meteorites have the most "primitive" composition. They may have began to crystallize at higher temperature as high temperature favours the incorporation of Al but has no effect on the incorporation of Ti in clinopyroxene. Augite cores in the other nakhlites display somewhat less variations in Al/Ti ratios than in their Mg♯ which may reflect different kinetic effects between the nakhlites. Augite cores in both NWA 5790 and NWA 817 do not display Al/Ti variation. They probably did not crystallized plagioclase during augite growth, which is consistent with their plagioclase-free glassy mesostasis. However, their relatively lower Al content relative to Ti suggests that the two meteorites crystallized from residual melts that crystallized plagioclase prior to melt separation, as already suggested the negative Eu anomalies of augite (Fig 4.22).

Because of their similar geochemical properties, incompatible elements such as the REEs, Ba, Sr, or the LILEs are not significantly fractionated by mantle pro-

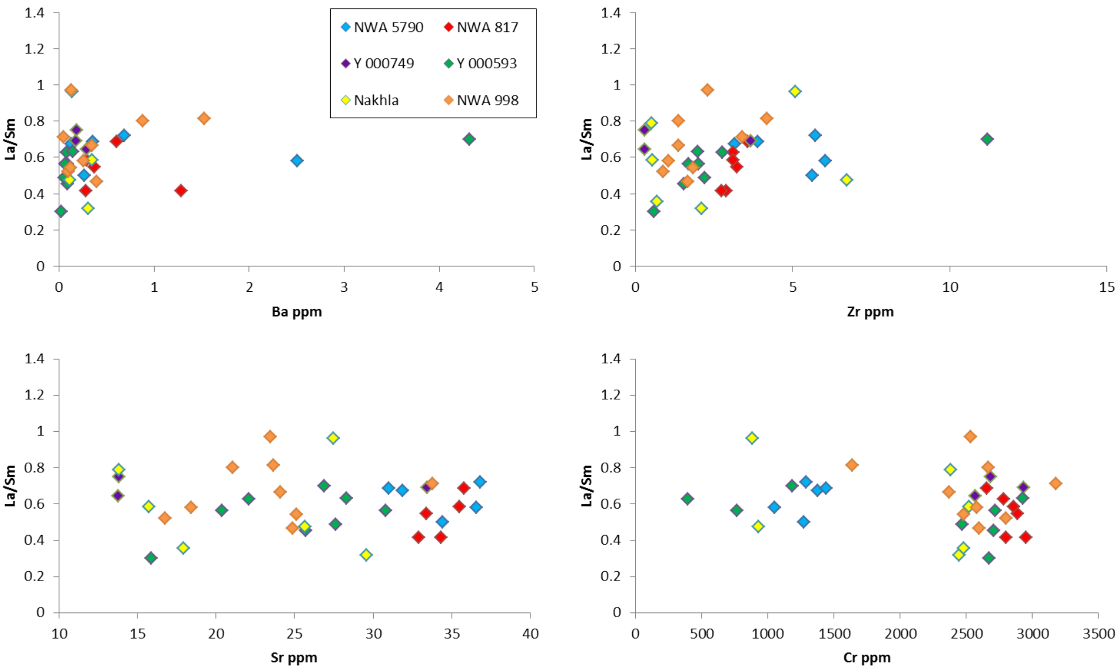

*Fig. 4.46: Light rare earth element ratio (i.e. Lanthanum/Samarium, i.g. La/Sm) vs. augite incompatible (i.e. Barium, Zirconium and Strontium, i.g. Ba, Zr, Sr) and compatible element (i.e. Chromium, i.g. Cr).*

cesses but ratios amongst them are. If we assume that the nakhlites crystallized from the same magma and subject there has been no competitive growth between two or more mineral phases, as is apparently the case for the early crystallization of the augite phenocrysts in the nakhlites, then the ratios of incompatible elements in augite from the individual nakhlites should positively correlate and/or show a single well-defined trend following the degree of differentiation. An increase in the degree of melt fractionation by augite and plagioclase (for NWA 817 and NWA 5790) crystallization should be traceable through the La/Sm ratios as La is slightly more incompatible than Sm while Ba and Sr commonly substitute to Ca in plagioclase. Cumulus augites display relatively large variations in La/Sm within individual nakhlite but the extend of variations is similar and overlap between the nakhlites without any obvious trend (Fig. 4.46). Surprisingly, NWA 5790 the most evolved nakhlites do not have the greatest La/Sm ratios. From the La/Sm ratios, there is no evidence that the individual nakhlites crystallized from melts with significant differences in the degree of differentiation. Lanthanum/Samarium ratios do not show decoupling trends with the incompatible element Ba between individual nakhlites. Zirconium abundances in augite phenocrysts show a slight progressive increase between the nakhlites while Sr abundances show still progressive but significant increase, NWA 5790 and NWA 817 been the most enriched in incompatible Sr. The increase in Sr, Cr and Zr in cumulus augites within and between the meteorites are not correlated with a change in La/Sm ratios.

However, these graphs show two interesting features of the naklites. First, increases of incompatible trace elements appear to be selective. Not all “conservative”

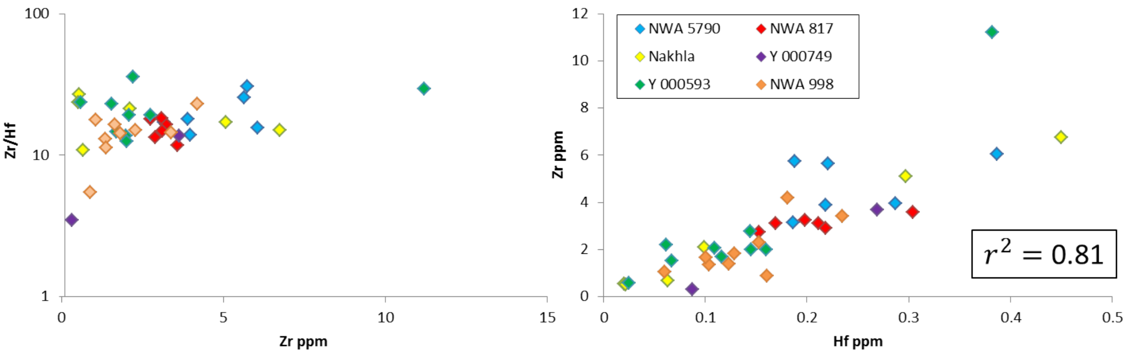

*Fig. 4.47: Zirconium/Hafnium (Zr/Hf) vs. Zr in augite phenocrysts. Both elements have similar substitution behaviour in clinopyroxene. The non-decoupling of element ratios between the nakhlites suggests that the meteorites are members of a genetically related suite of melts from a common parent magma.*

incompatible elements or ratio of incompatible elements show increases with the degree of melt fractionation (i.e. from augite core to rims). Secondly, the increase in specific incompatible element abundances are the same for all individual nakhlites. This suggests that augite chemistry and crystal structure played a major role in the incorporation of many trace elements.

A further test for identifying a genetic link uses a couple of incompatible trace elements with similar substitution behaviour in augite such as Nb/Ta or Zr/Hf. These paired elements have identical solid/liquid partition coefficient (Jochum et al., 1989), such that during partial melting (and whatever the degree of partial melting) the ratio of the mantle source is preserved. Despite their wide range of concentration in mafic and ultra-mafic terrestrial magmas, basaltic rocks have fairly similar (and chondritic) bulk rock Nb/Ta and Zr/Hf ratios. In the nakhlites cumulus augite, the concentration in Nb and Ta is very low and most of the time below detection limits using LA ICP-MS, which reflects their low partition coefficient in clinopyroxene (extremely high incompatibility) and low concentration in the parent melts, both been lower than Hf and Zr.

Cumulus augite amongst the nakhlites have similar Zr/Hf that do not vary with the progressive increase in Zr abundances (i.e. with increasing the degree of melt fractionation, or rimwards). Cumulus augite in all nakhlites are enriched in Zr relative to Hf (Fig. 4.47). Hf is slightly more compatible than Zr in clinopyroxene because of its smaller ionic radii (Hf = 71pm, Zr = 72pm). The greatest concentration of Zr relative to Hf probably reflects its greater concentration in the parent melt. Cumulus augite from the individual nakhlites crystallized augite from a melt with identical Zr/Hf ratios.

Henry's law behaviour for Zr and Hf (and other minor and trace elements) during augite crystallization is not demonstrable but questionable as both elements are present in very low concentration (Watson, 1985). However, crystallization of augite under equilibrium conditions in all nakhlites can be assumed because of their large homogeneous core and apparent slow growth rate. Furthermore, the coefficient of determination of Zr/Hf ratios in the nakhlites' cumulus augite, which gives the proportion of the variance of one variable that is predictable from the other variable, is $r^2 = 0.81$. The high $r^2$ value indicates a strong positive correlation between both elements suggesting that both had the same substitutional behaviour and have most probably obeyed Henry's Law during augite crystallization. The Zr and Hf concentrations in augite are proportional to those of the melts.

Parallelism of REE patterns, non-decoupling of paired incompatible trace element ratios and progressive evolution trends provide strong evidence that closed system fractional crystallization has been the dominant process in the nakhlites' formation. Difficulties with the core-rim-based approach using LA ICP-MS to establish the rocks' petrogenesis are the rough spatial resolution and thus the impossibility to analyse growth bands, which limits the ability to identify loss or gain of trace elements from the system by contamination or co-precipitation of two or more mineral phases (i.e. competitive partitioning). Inconsistent changes in crystal zoning patterns in general indicate that the recorded compositional variations reflect changes in the availability of specific trace elements in the melt unrelated to closed-system crystal fractionation. They show some contamination (either magma mixing or crustal assimilation), although they may also be the result of disequilibrium growth (i.e. kinetic factor), chemical heterogeneity of the parent magmas, or sub-solidus re-equilibration. None of the nakhlites display geochemical evidences for relatively significant contamination or sharp changes in trace element behaviour during augite crystallization, with the exception of post-emplacement rim formation, although this part of the crystallization history has been partially erased by sub-solidus diffusional re-equilibration. A further argument for crystallization of the nakhlites in a closed-system is the calculated REE composition of parental melts from which augite cores crystallized which is relatively parallel to the whole rock REE composition (Day et al., 2006).

However, different compositional and zoning patterns in the liquidus phase augite suggest the existence of distinct magma batches and/or intrusions with each magma body having its own crystallization history. These variations resulted from differences in parent magma composition but also from different extents of fractional crystallization and physical conditions including temperature and cooling rate experienced by the parent melts prior to and during augite crystallization. For example, augite cores in NWA 5790 are depleted in augite compatible Cr and Ni and enriched in augite incompatible Sc, Mn and V relative to other nakhlites, they have a lower and fluctuating Mg♯ and are depleted in Al relative to Ti. Together these chemical trends are characteristic of a melt that differentiated through fractional crystallization processes prior to augite crystallization. NWA 5790 crystallized from a cooler residual melt that further experienced a higher cooling rate including during augite crystallization. The similarity of trace element patterns with the other nakhlites suggests that the parent melt from which NWA 5790 but also NWA 817 formed experienced intense augite crystallization prior to melt extraction and the solidification of their early augite phenocrysts. The negative anomalies in Eu and Sr suggest also that plagioclase was on the liquidus prior to melt segregation.

On the other hand, increases in some incompatible and compatible element abundances in NWA 817 relative to other nakhlites are not consistent with closed system fractional crystallization involving the observed mineral phases. There is no evidence that NWA 817 experienced magmatic or crustal contamination. Hence, the unique geochemistry of cumulus augites from this meteorite probably reflects a different original melt chemistry probably not related with a higher degree of melt differentiation relative to most nakhlites (except NWA 5790). Cumulus augites within NWA 817 also display smaller concentration variations in all analysed elements whatever their behaviour (compatible or incompatible), which suggests a more homogeneous melt composition. The preservation of unique augite population in individual nakhlites suggests that the nakhlites' parent melts and their related augite population have physically been separated from each other pre-, syn- and post-eruption.

## 4.8 Estimation of the REE compositions of the nakhlites' parent magmas

A critical issue in interpreting the nakhlites petrogenesis is determining the composition (and likely number) of magmas at the origin of the individual rocks. Gaining an understanding of the composition of the melts may help unravel the nakhlites relationship, and provide information on the magmatic activity of Mars during the Middle Amazonian. Investigation of the rocks' texture and mineral relationship suggest a formation of augite early in the crystallization sequence, as previously recognized by Treiman (2005) to name a few. The chemical composition of minerals and bulk rocks suggests a crystallization of the individual nakhlites under closed-system conditions. The large core of augite phenocrysts most probably crystallized slowly and in equilibrium with the melts from which they crystallized (this study and Wadhwa and Crozaz (1995)), a pre-requisite for geochemical modelling. Consequently, the composition of the large core of augite phenocrysts should still retain some chemical fingerprints of the parental magmas, including the REE composition. Therefore, calculation of the REE composition of the melts that were in equilibrium with the augite cores in individual nakhlites by inverting the augite REE concentrations should provide an estimate of the trace element composition and budget of their respective parent melts (Wadhwa and Crozaz, 1995; Day et al., 2006). This can be determined using the relationship:

$$\mathrm{C}_{\mathrm{i(melt)}} = \mathrm{C}_{\mathrm{i(augite)}} \;/\; \mathrm{D}_{\mathrm{i}}$$

with $\mathrm{C}_{\mathrm{i}}$ the concentration of a given element i and $\mathrm{D}_{\mathrm{i}}$ the augite/melt coefficient partitioning for the element i. One of the main difficulties and uncertainties of such geochemical modelling is the determination and use of appropriate partition coefficient values because the partition coefficients strongly vary with melt and mineral composition and the physical conditions under which the mineral of interest crystallized (McKay et al., 1994; Oe et al., 2001). Estimation of reliable and accurate partition coefficients for clinopyroxene in the nakhlites have been previously calculated through experimental studies (McKay et al., 1994; Oe et al., 2001) and previously applied to different nakhlites (Wadhwa and Crozaz, 1995; Day et al., 2006). Figure 4.48 shows the partition coefficient calculated from experimental data for Martian meteorites including the Shergotites and Nakhlites (Oe et al., 2001).

However, geochemical modelling intrinsically bears uncertainties that have to be retained in mind. First, the variations of partition coefficients calculated from clinopyroxene/melt equilibria with different melt composition highlight the importance of the chemical composition of the parent melt onto the degree of trace

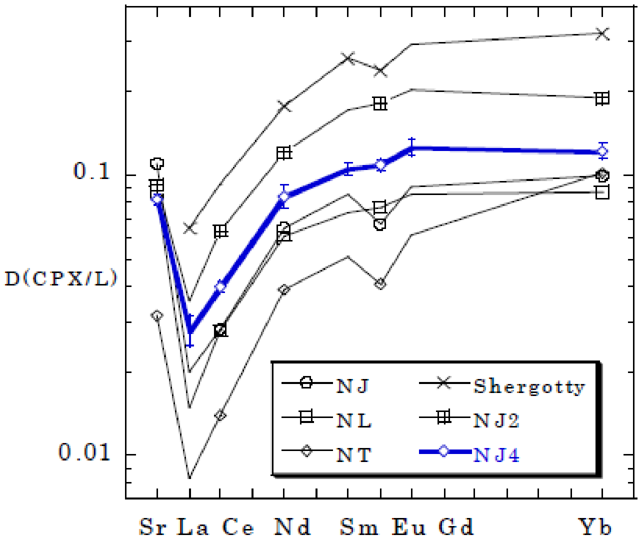

*Fig. 4.48: Partition coefficient (D) of REEs and Sr for clinopyroxene/liquid (CPX/L) equilibria calculated for nakhla and Shergotitty (Shergotitte-group of the SNC Martian meteorites) from experiemntal study (Oe et al., 2001). The partition coefficients of NJ4 have been obtained from a melt with a major element composition that resembles that of Nakhla and so are believed to represent the most accurate coefficient partitions for the nakhlites. The coefficient partitions used in this study have been directly read from this graph (presented on Tab. 4.3).*

element incompatibility in clinopyroxene (McKay et al., 1994; Oe et al., 2001). Consequently, if the individual nakhlites crystallized from melts with different composition or at different degree of differentiation, so the calculated REE abundances of the parent magma will not be accurate and will further deviate to different degree between the rocks according to the degree of their chemical variation from the melt composition used in the experiments. Nonetheless, despite variations in the absolute partition coefficient values, the general REE patterns of the various estimated partition coefficients are yet parallel to each other (Fig. 4.48). Consequently, the REE patterns of the calculated parental melts of the individual nakhlites (despite a likely crystallization of the rocks from different parent melt composition) should still be relatively representative (without absolute knowledge of their respective REE abundances). From our geochemical data, Nakhla and Y 000749 display the most "primitive" augite core composition and so, may have potentially crystallized from the least differentiated melt, while NWA 817 and NWA 5790 exhibit the most evolved augite core composition, Y 000593 and NWA 998 being intermediate. Therefore, it is expected that the partition coefficients of the REE in parent melt from the individual nakhlites will loose accuracy from Nakhla (the nakhlites used for the estimation of partition coefficients, Oe et al. (2001)) → Y 000593 → Y 000749 → NWA 998 → NWA 817 → NWA 5790.

A second uncertainty in the geochemical reconstruction of the parent magma composition is the average augite composition of the different nakhlites calculated in this study that probably do not truly represent an average of the most "primitive" augite core in the individual nakhlites. This is mostly due to (1) the small number of augite grains analysed that cannot represent the range of augite composition in the individual rocks, and (2) the use the LA ICP-MS (with large crater size) for measuring augite trace element composition. Accurate in situ analyses of trace elements using LA ICP-MS requires large volume of material to be ablated (a crater size of 50 $\mu$m in diameter has been selected in this study). Moreover, despite the apparent homogeneous composition of the large cores of augite phenocrysts using major elements, the augite cores yet display progressive growth zonation in trace element composition which have unavoidably been included during our LA ICP-MS measurements. Finally, another uncertainty is the relative timing of olivine crystallization that further may vary between the nakhlites. Olivine does not incorporate the REEs (Fig. 4.38), so if olivine co-crystallized with augite then the estimated REE abundances of the nakhlites' parent melts would be lower (and proportional to the abundance of olivine relative to augite) than the calculations. However, the REE patterns should not be affected by a possible augite-olivine co-precipitation. Olivine phenocrysts in the different nakhlites tend to form clusters (Treiman, 2005) that are further heterogeneously distributed throughout the rocks, hence the modal proportion of olivine in the small naklite meteorites may not be representative of the true proportion of olivine in the igneous bodies sampled by the nakhlites. There is also a possibility that most of the olivine grains that may have crystallized prior or contemporaneous to augite were not erupted with the parent magmas. The heavy olivine crystals may have been physically separated by crystal settling from the magma pool. The modal proportion of olivine in the nakhlites may not be representative of the true crystallization history of the rocks.

An average of REE abundances of augite core in individual nakhlites (measured in this study) has been calculated and are presented on Tab. 4.3 together with an estimate of the clinopyroxene/melt partition coefficients for REEs calculated for the Nakhla meteorite by Oe et al. (2001). The partition coefficient values have been directly read from the graph on Fig. 4.48 taken from Oe et al. (2001). The calculated values for NJ4 have been selected (as suggested by Oe et al. (2001)) because they were obtained from a melt with a major element composition potentially similar to the melt that crystallized the augite phenocrysts in Nakhla, which included low Al and Ti abundances. Indeed, it is largely recognised that the Martian meteorites (especially the nakhlites) crystallized from basaltic melts with Al and Ti abundances significantly lower than those in common basalts on Earth (Fig. 4.18 and 4.19).

Calculated REE composition of the parent melts at the origin of augite in different nakhlites assuming crystallization of the large augite core under equilibrium conditions and using the appropriate partition coefficients of Oe et al. (2001) are presented on Fig. 4.49. They are plotted with the average augite composition of the most “primitive” cores (analysed in this study) and bulk rocks' REE composition (concentrations taken from Treiman and Irving (2008)). However, as previously mentioned, the data presented on the graph are only given as a representation of the augite-melt system in the different nakhlites without any accuracy of absolute abundances. The first striking feature of the nakhlites is the parallelism of the REE patterns of the calculated parent melts of individual nakhlites and their respective measured bulk rock composition. This suggests a crystallization of the rocks in a closed-system, which is consistent with the parallelism of REE patterns of augite

| | La | Ce | Pr | Nd | Sm | Eu | Gd | Tb | Dy | Ho | Er | Tm | Yb | Lu |
|---|---|---|---|---|---|---|---|---|---|---|---|---|---|---|
| Partition coefficients | 0.02 | 0.03 | | 0.08 | 0.1 | 0.1 | 0.1 | | | | | | 0.1 | |
| NWA 5790 (n=4) | 0.623 | 2.522 | 0.502 | 3.150 | 1.014 | 0.317 | 1.344 | 0.187 | 1.240 | 0.238 | 0.629 | 0.075 | 0.468 | 0.081 |
| NWA 817 (n=6) | 0.464 | 1.965 | 0.405 | 2.620 | 0.860 | 0.228 | 0.907 | 0.142 | 0.962 | 0.173 | 0.466 | 0.062 | 0.395 | 0.068 |
| Y 000749 (n=3) | 0.26 | 1.30 | 0.21 | 1.27 | 0.37 | 0.11 | 0.52 | 0.09 | 0.51 | 0.09 | 0.26 | 0.02 | 0.20 | 0.04 |
| Y 000593 (n=7) | 0.33 | 1.52 | 0.28 | 1.77 | 0.56 | 0.18 | 0.62 | 0.09 | 0.59 | 0.11 | 0.28 | 0.04 | 0.29 | 0.04 |
| Nakhla (n=5) | 0.145 | 0.824 | 0.156 | 1.010 | 0.356 | 0.115 | 0.364 | 0.069 | 0.381 | 0.083 | 0.199 | 0.024 | 0.192 | 0.032 |
| NWA 998 (n=7) | 0.40 | 1.57 | 0.35 | 1.98 | 0.60 | 0.20 | 0.68 | 0.11 | 0.70 | 0.15 | 0.34 | 0.05 | 0.31 | 0.05 |

*Tab. 4.3: Estimated partition coefficients (i.e. D) calculated for Nakhla clinopyroxene of Oe et al. (2001) and average of REE abundances in ppm in augite cores in different nakhlites (measured in this work) with n the number of grains used to calculate the average.*

core and rim (Fig. 4.22) and plagioclase core and rim (Fig. 4.24) and previous estimations of the REE composition of the nakhlites' parent melts (Wadhwa and Crozaz, 1995; Day et al., 2006).

As previously observed in this study, the nakhlites' bulk rock REE abundances follow the apparent order of crystallization and accumulation of augite from bottom to top of the nakhlites cumulate pile model of Mikouchi et al. (2012) with NWA 998 the most depleted in REE and NWA 817 the most enriched (Fig. 4.21). They may represent a progressive crystallization of augite from a magma body that became more and more enriched in REEs as crystallization proceeded. However, the calculated parent melts of the nakhlites do not show such trend. The parent melt that crystallized augite in NWA 998 (and so assumed to be the first-formed and first accumulated augite) was probably not the least fractionated melt (i.e. most primitive) as would be expected from its position in the bottom of the cumulate pile. The discrepancy between NWA 998 measured bulk rock composition (apparently the most "primitive") and calculated parent melt composition (intermediate composition relative to other nakhlites) can be easily explained by the fact that the bulk rock composition of the rocks are not dominated by the augite chemistry (as indicate the different Mg ♯ of the naklites' bulk rock and their respective augite population, Fig. 4.45), and so the nakhlites' bulk rock composition is not representative of the composition of their parental magmas. The lower REE abundances of NWA 998's bulk rock (lower than other nakhlites) and the large variation in REE abundances between the early parent melt and bulk rock (larger than for the other nakhlites) probably reflect the full crystallinity of the rock and the likely escape of the interstitial melt during rock compaction. The respective calculated parent melt compositions of the different nakhlites analysed in this study correlate positively with the apparent nakhlites differentiation trend observed on the Total Alkali *vs.* Silica (TAS) diagram for volcanic rocks (Fig. 4.17). The progressive increase in $SiO_2$ and alkali ($Na_2O + K_2O$) abundances in the nakhlites' bulk rock and REE content in their respective calculated parent melts suggests that the individual nakhlites crystallized from co-genetic melts at different degree of differentiation with from the least to the most: Nakhla → Y 000593 → Y 000749 → NWA 998 → NWA 817 → NWA 5790.

The parallelism between the calculated REE patterns of the nakhlites' parent melt and their respective measured bulk rock composition suggests a crystallization of the rocks under closed-system conditions. A further test for a final rock solidification (after augite crystallization) in a geochemically closed system is to calculate the bulk rock REE concentrations using trace element concentrations in minerals and modal proportions of the rock-forming minerals. Unfortunately, the lack of laboratory time and the measurement of trace element compositions in minerals using the LA ICP-MS has not allowed the measurement of the fine mineral grains in the mesostasis (their grain size being generally $\leq 50$ $\mu$m). Therefore, the reconstruction of REE bulk rock composition has only been made for NWA 817 and NWA 998. Average of REE compositions used for bulk rock reconstruction for augite are the same than those used for the calculation of the parent melts REE composition (Tab. 4.3). The average of other different magmatic products used for bulk rock recalculation are presented on Tab. 4.4. Modal proportion of the different mineral phases in the two naklites are taken from Treiman (2005), with for NWA 817: 70

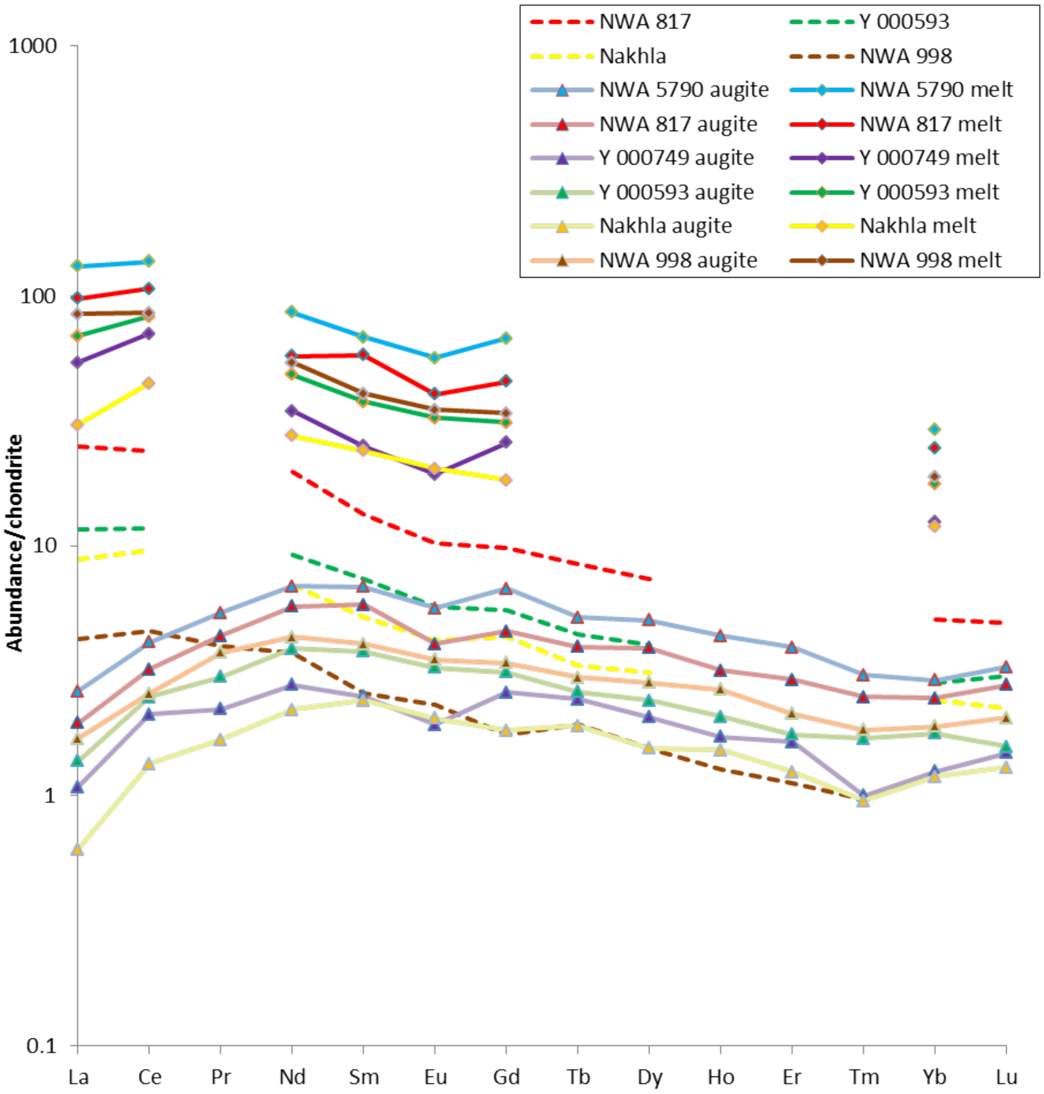

*Fig. 4.49: Average augite REE abundances and estimate of the REE composition of the parent magmas from which they crystallized using the partition coefficient of Oe et al. (2001) and normalization factors of McDonough and Sun (1995). Bulk rock REE composition (dashed lines) are provided for comparison. The REE patterns of the magmas that crystallized augite (assuming equilibrium conditions) are parallel to the nakhlites' bulk rock suggesting closed-system crystallization.*

% augite, 10 % olivine and 20 % mesostasis; and for NWA 998: 68 % augite, 2 % orthopyroxene, 10 % olivine, 19 % mesostasis (assumed 100 % plagioclase) and 1 % glass.

NWA 817 comprises large augite and olivine phenocrysts forming the framework for a glassy finely crystallized mesostasis. The crystal grains in the mesostasis consists of Fe-oxide (avoided during measurements), fayalitic olivine, abundant nano-scale apatite grains and very rare pyrrhotite (Fig. 4.8). However, fayalitic olivine and apatite are relatively homogeneously distributed while the glassy matrix seem to be chemically homogeneous (Fig. 4.26). Therefore, the REE bulk rock composition of NWA 817 should reflect an average of the relative proportion of the REE abundances in augite and bulk mesostasis, olivine been refractory to the incorporation of REE in its crystalline structure. On the other hand, NWA 998 is fully crystallized with grain size generally $\geq 50$ $\mu$m and glass present only along grain boundaries and pore corners (Fig. 4.11). Therefore, an average of the REE abundances of the main mineral phases (augite, plagioclase, low-Ca pyroxene and glass) relative to their respective modal proportion should provide a good estimate of the bulk rock composition.

The measured and calculated REE compositions and abundances of the nakhlites' bulk rock normalized to CI chondrite (McDonough and Sun, 1995) are presented on Fig. 4.50. They are relatively parallel and with a similar range of element abundances. As previously observed, the mesostasis of NWA 817 is mineralogically and chemically homogeneous, which includes the large distribution of naturally REE-rich fine apatite grains. NWA 998 displays some variations in REE abundances and compositions. However, in our calculation of the bulk rock composition, we have estimated a rock matrix only composed of plagioclase (which accounts for the strong Eu positive anomalies relative to the bulk rock). Plagioclase commonly display large feldspar rims. Feldspar do not incorporate as much Eu as plagioclase because of its crystal chemistry (i.e. lack of Ca for common Eu-Ca subtitution), which may accounts for the strong Eu positve anomalies in the calculated REE pattern. Olivine has not been included in our calculation but as guessed from its naturally REE-free chemical structure and as evidence the calculated bulk rock REE pattern of NWA 817, olivine does not affect the general REE pattern of the rock. In NWA 998, the rock matrix comprises a few cluster of large (20 $\mu$m-thick) apatite grains that have not been measured during our LA ICP-MS analyses and thus have been excluded in our calculation. As apatite preferentially incorporates the LREEs relative to HREEs, including REE compositions of apatite in the calculation will change the calculated bulk rock REE pattern and abundances. The greater HREE content on the calculated REE patterns relative to the measured bulk rock probably reflect an overestimation of plagioclase and augite and underestimation of low-Ca pyroxene, feldspar and apatite. The measured and recalculated bulk rock REE composition are consistent with each other but with some uncertainties regarding the proportion of the mineral phases in NWA 998. As already suggested from the trace element compositions of augite and their variations in extent of zonation, the nakhlites crystallized in closed system but most probably within multiple igneous bodies and/or magma discharges.

NWA 817

| | La | Ce | Pr | Nd | Sm | Eu | Gd | Tb | Dy | Ho | Er | Tm | Yb | Lu |
|---|---|---|---|---|---|---|---|---|---|---|---|---|---|---|
| Glass (n=2) | 19.785 | 48.35 | 6.685 | 29.95 | 6.47 | 1.675 | 5.335 | 0.801 | 4.775 | 0.992 | 2.66 | 0.3375 | 2.315 | 0.307 |

NWA 998

| | La | Ce | Pr | Nd | Sm | Eu | Gd | Tb | Dy | Ho | Er | Tm | Yb | Lu |
|---|---|---|---|---|---|---|---|---|---|---|---|---|---|---|
| Pyroxene (n=10) | 2.347 | 8.672 | 1.478 | 9.597 | 3.107 | 0.681 | 4.388 | 0.821 | 6.41 | 1.574 | 5.158 | 0.88 | 6.73 | 1.265 |
| Plagioclase (n=1) | 3.14 | 4.37 | 0.326 | 1.12 | 0.128 | 1.52 | | | | | | | | |
| Glass (n=3) | 8.993 | 24.513 | 3.363 | 14.663 | 3.276 | 1.005 | 2.653 | 0.492 | 3.23 | 0.569 | 1.53 | 0.179 | 1.67 | 0.226 |

*Tab. 4.4: Average of REE abundances in ppm in glass, feldspar and low-Ca pyroxene in NWA 817 and NWA 998, with n the number of analysed grains averaged.*

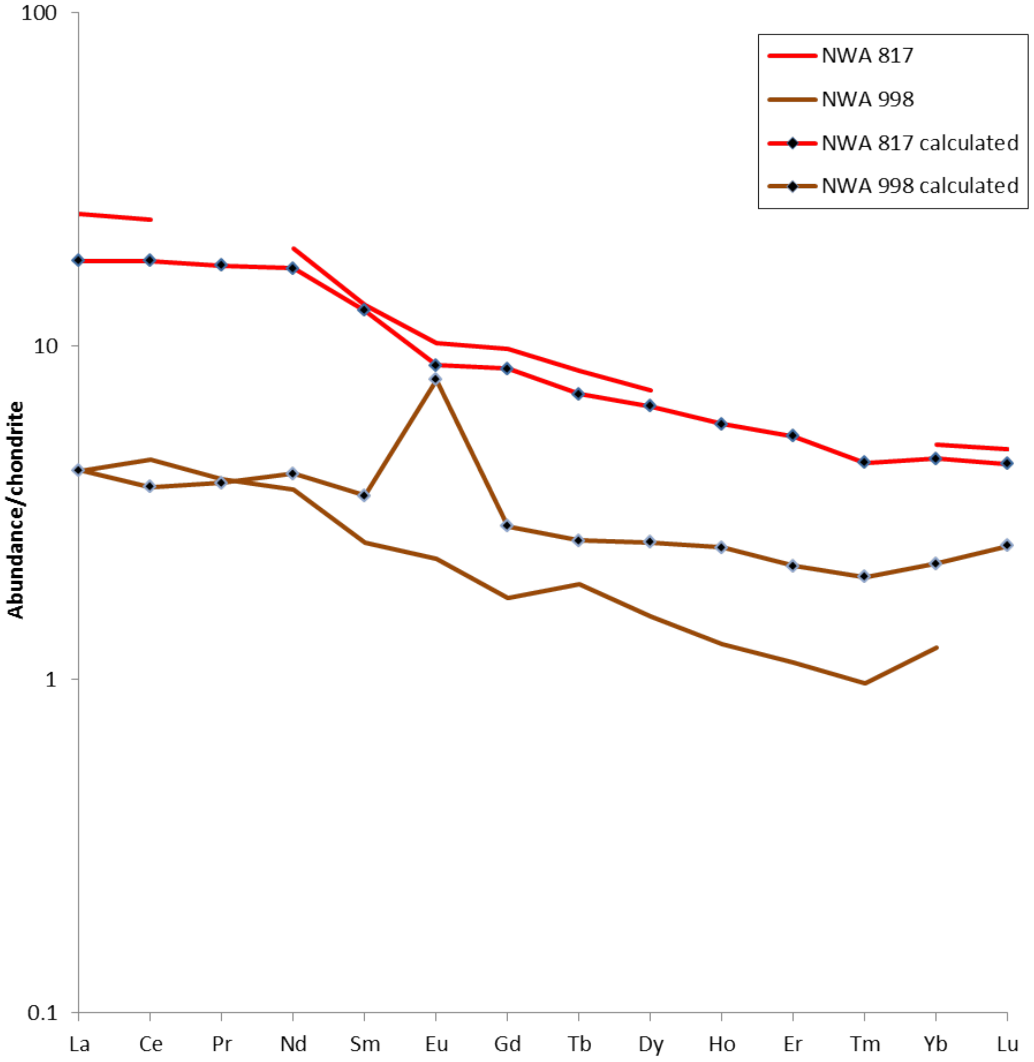

*Fig. 4.50: Bulk rock composition of NWA 817 and NWA 998 measured by Treiman and Irving (2008) and calculated using average composition of the rock-forming minerals (this study) and their relative modal proportion in the rocks. Percentage of the different mineral phases are taken from (Treiman, 2005) with for NWA 817: 70 % augite, 10 % olivine and 20 % mesostasis; and for NWA 998: 68 % augite, 2 % orthopyroxene, 10 % olivine, 19 % mesostasis (assumed 100 % plagioclase) and 1 % glass. The rock compositions are normalized to CI chondrite using the normalization factors of McDonough and Sun (1995). The calculated and measured bulk rocks have relatively similar REE patterns suggesting an evolution of the rocks through fractional crystallization under closed-system condition. The high Eu anomalies in the calculated bulk rock composition of NWA 998 and high HREE abundances relative to the measured bulk rock reflect the assumption that the mesostasis is only composed of plagioclase whereas it contains also apatite a mineral that preferentially incorporates the LREEs relative to the HREEs.*

### 4.8.1 Summary of crystallization sequences and history

Based on the detailed petrographic investigations of the individual nakhlites (including mineral texture, chemistry and relationship), crystallization sequences of the nakhlites has been established. Order of mineral crystallization in the different nakhlites are presented in their relative position with the cumulate pile model of Mikouchi et al. (2012) (Fig. 1.6) with NWA 5790, NWA 817 and MIL 03346 representing the top of the igneous body (Tab. 4.5), Yamato 749, Y 000593 and Nakhla sampling the interior (Tab. 4.6) and Lafayette and NWA 998 the bottom of the cumulate pile (Tab. 4.7). The determination of the order of mineral sequences is not always clear because the different mineral phases have continued to grow while the next mineral phase(s) appeared on the liquidus (i.e. co-precipitation), for example augite rim/overgrowth and plagioclase. The order of mineral crystallization is generally the same in all the nakhlites analysed, although the meteorites display some differences in their mineral composition. For example, NWA 5790 and NWA 817 do not contain plagioclase, orthopyroxene and cristobalite; cristobalite being also absent in Lafayette and NWA 998. Variations in the mineralogy of the rock matrix probably result from the varying cooling rate experienced by the individual nakhlites. Both NWA 5790 and NWA 817 have probably solidified their mesostasis too quickly to crystallize plagioclase and orthopyroxene and reach silica saturation through intense fractional crystallization of the interstitial melt, whereas the absence of silica in Lafayette and NWA 998 may result from late peritectic reactions.

A scenario for the nakhlites crystallization history taken from Imae et al. (2005) is provided on Fig. 4.51. It summarizes the order of crystallization of the main mineral phases and their likely environment of crystallization. The individual nakhlites probably began crystallization with homogeneous nucleation of augite, olivine and oxide in a large magma reservoir prior to magma extrusion and crystallization of abundant plagioclase (list of minerals not exhaustive). Crystallization of the nakhlites parent melt(s) once in a (sub-)surface environment were likely contemporaneous to crystal accumulation to form cumulate pile(s). However, the scenario taken from (Imae et al., 2005) is probably not truly representative as there is a very likely possibility that the nakhlites sample multiple igneous bodies including lava flows and shallow intrusions and/or may even represent the solid products of multiple magma pulses in the large shallow magmatic reservoir. Variations in the degree of crystallinity between the rocks may not be either representative of the relative depth of final emplacement of the individual nakhlites. The glassy mesostasis of some nakhlites may represent the chilled margins of near-surface sills while more crystallized rocks may sample the bottom of lava flows.

## 4.9 Conclusions

The nakhlite meteorites are basalt-derived igneous rocks from Mars. Their bulk chemical compositions plot within the basalt field of the TAS diagram. They are clinopyroxenites with approximate crystallization ages of 1.3 Ga (Nyquist et al., 2001). Most nakhlites were excavated and ejected into space by a single (?) impact of meteorite $\sim$ 11 Ma ago. Only NWA 5790 displays a cosmic-ray exposition age 3 Ma younger, which suggests an excavation during a separate impact-launch event

| Pre-emplacement crystallization sequences | | | | | | | | |
|---|---|---|---|---|---|---|---|---|
| augite | | | | | | | | |
| augite | olivine | | | | | | | |
| Post emplacement crystallization sequences | | | | | | | | |
| augite | olivine | magnetite | | | | | | |
| augite | olivine | magnetite | fayalite | | | | | |
| augite | olivine | magnetite | fayalite | augite | pyrrhotite | | | |
| augite | olivine | magnetite | fayalite | augite | pyrrhotite | apatite | | |
| augite | olivine | magnetite | fayalite | augite | pyrrhotite | apatite | cristobalite* | |
| augite | olivine | magnetite | fayalite | augite | pyrrhotite | apatite | cristobalite* | glass |

*Tab. 4.5: Approximate sequences of mineral crystallization in the quickly cooled nakhlites NWA 5790, NWA 817 and MIL 03346. Cristobalite* has only been found in MIL 03346.*

| Pre-emplacement crystallization sequences | | | | | | | | | |
|---|---|---|---|---|---|---|---|---|---|
| augite | | | | | | | | | |
| augite | olivine | | | | | | | | |
| augite | olivine | magnetite | | | | | | | |
| Post emplacement crystallization sequences | | | | | | | | | |
| augite | olivine | magnetite | | | | | | | |
| augite | olivine | magnetite | plagioclase | | | | | | |
| augite | olivine | magnetite | plagioclase | fayalite | | | | | |
| augite | olivine | magnetite | plagioclase | fayalite | pyroxene$^{**}$ | | | | |
| augite | olivine | magnetite | plagioclase | fayalite | pyroxene$^{**}$ | pyrrhotite | | | |
| augite | olivine | magnetite | plagioclase | fayalite | pyroxene$^{**}$ | pyrrhotite | apatite | | |
| augite | olivine | magnetite | plagioclase | fayalite | pyroxene$^{**}$ | pyrrhotite | apatite | cristobalite | |
| augite | olivine | magnetite | plagioclase | fayalite | pyroxene$^{**}$ | pyrrhotite | apatite | cristobalite | orthopyroxene$^{***}$ |

Tab. 4.6: *Approximate sequences of mineral crystallization in the nakhlites Y 000749, Y 000593, Nakhla and Lafayette. Pyroxene$^{**}$ is used as a generic term for low-Ca pyroxene (including pigeonite and orthopyroxene). The last mineral to crystallize is orthopyroxene$^{***}$, it corresponds to a mineralogical re-equilibration from olivine-plagioclase. Its abundance in the nakhlites increases with the degree of crystallinity.*

| Pre-emplacement crystallization sequences | | | | | | | |
|---|---|---|---|---|---|---|---|
| augite | | | | | | | |
| augite | olivine | | | | | | |
| augite | olivine | magnetite | | | | | |
| Post emplacement crystallization sequences | | | | | | | |
| augite | olivine | magnetite | | | | | |
| augite | olivine | magnetite | plagioclase | | | | |
| augite | olivine | magnetite | plagioclase | pyroxene** | | | |
| augite | olivine | magnetite | plagioclase | pyroxene** | pyrrhotite | | |
| augite | olivine | magnetite | plagioclase | pyroxene** | pyrrhotite | apatite | |
| augite | olivine | magnetite | plagioclase | pyroxene** | pyrrhotite | apatite | orthopyroxene*** |

Tab. 4.7: *Approximate sequences of mineral crystallization in NWA 998. Pyroxene** is used as a generic term for low-Ca pyroxene (including pigeonite and orthopyroxene). The last formed orthopyroxene*** corresponds to a mineralogical re-equilibration from the previously stable mineral assemblage olivine-plagioclase. It is abundant in NWA 998.*

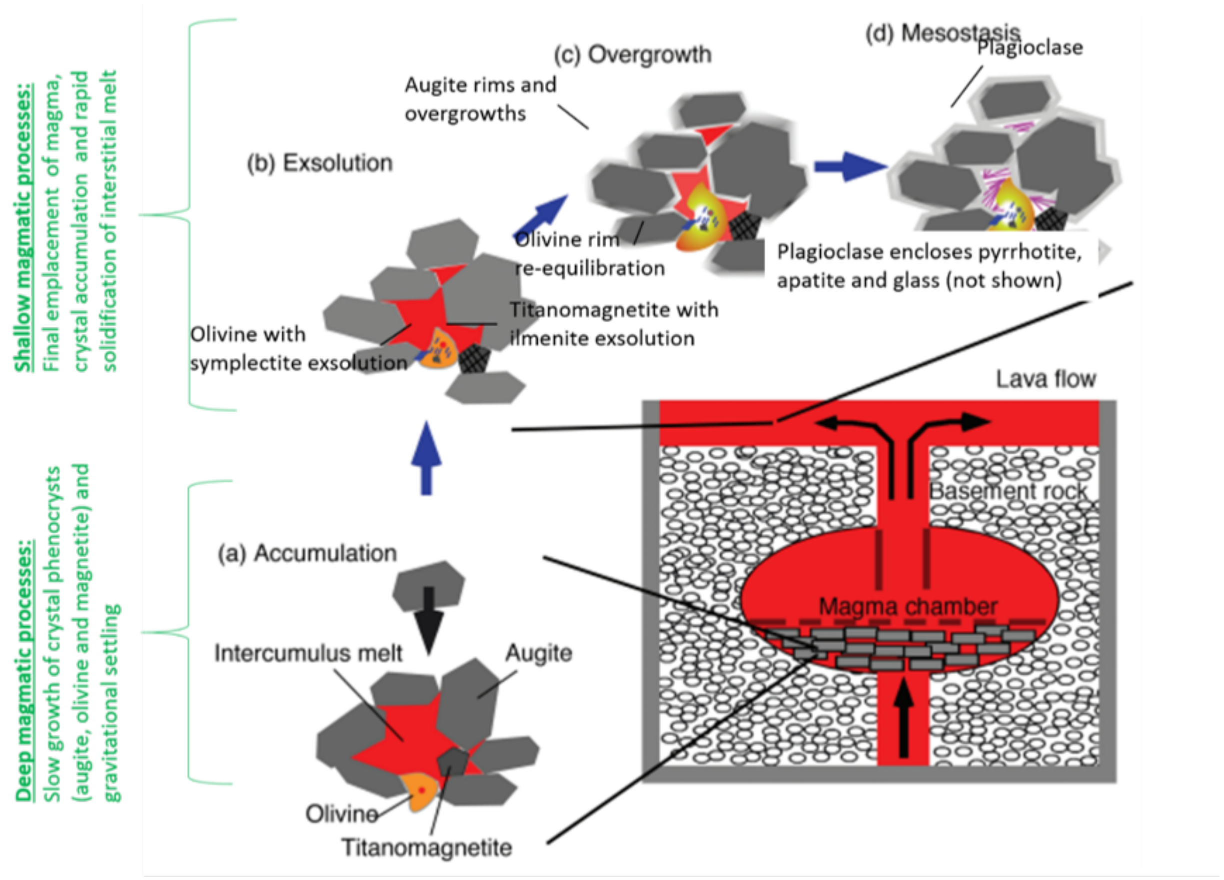

Fig. 4.51: *Sketch modified from Imae et al. (2005) illustrating the two-stage crystallization history of the nakhlites (with the likely environments of crystallization of the main mineral phases) that served as a basis for the further investigation of the nakhlites geological history in the second part of this chapter. This included the petrological link of the individual rocks using trace element geochemistry. Based on trace element geochemistry of the various mineral phases of the nakhlites, the different rocks are not the product of a single lava flow but rather represent the solidified products of multiple magma pulses or bodies that were emplaced relatively contemporaneously.*

and possibly site (Wieler et al., 2016). The nakhlites are all differentiated basaltic rocks formed by fractional crystallization and cumulate processes. They have the same mineralogy and bulk chemistry including a depletion of the most incompatible elements, similar incompatible element ratios and an enrichment in moderately incompatible elements relative to less incompatible elements. The nakhlites' parent magmas formed by small degree of partial melting within a mantle source that experienced previous melt extraction processes. There is no geochemical evidence indicating that the nakhlites formed from different mantle sources.

The nakhlites' petrogenetic history began with the crystallization of augite phenocrysts, now preserved as mineral inclusions in olivine. The crystallization of stable augite at the expense of olivine suggests that the nakhlites' parent magmas began to crystallize under moderate pressure and anhydrous conditions, which is consistent with the absence of water-bearing primary minerals in the rocks. The similarly developed large cores of cumulus augite (except in NWA 5790) and their homogeneous major element composition (including equilibrated distribution of Mg and Fe) indicate that they crystallized slowly most probably from large and stagnant magma pools. However, the sharp zonation of augite core with respect to trace elements provides evidence for an augite growth from strongly fractionating magmas. The degree of melt fractionation achieved prior to augite crystallization and during augite grow vary between the nakhlites. There is no chemical or textural evidences suggesting that augites crystallized during magma ascent toward the surface as they would show partial resorption features (minerals forming at depth being rarely stable in a low-pressure environment) and sharp chemical zoning in compatible elements of augite cores (the coefficient of partition of compatible elements being strongly pressure-dependent).

The cores of the nakhlites' cumulus augite have similar quadrilateral components but still display some variations in non-quadrilateral components including trace and minor elements that are difficult to conceive with a contemporaneous crystallization of augite within a single buoyant magma sat in a shallow magmatic chamber or later sub-solidus reactions. Variations in augite composition could reflect the existence of a zoned magma chamber, that commonly develops as a result of intensive fractional crystallization, with the augite population from individual nakhlites each growing within a “separate” layer before settling at the base of the magma chamber. However, it is expected that stratified magma chambers follow differentiation trends controlled by fractional crystallization which are unlikely to result in decoupling compatible and incompatible elements as observed in augites from the diverse nakhlites. Another mechanism than the development of a zoned magma chamber by fractional crystallization of augite with or without olivine and plagioclase alone must be responsible for the compositional variability of the augites.

Despite quite different REE abundances, the overall REE patterns of equilibrium melts and cumulus augite cores are very similar and parallel to the measured bulk rock composition which suggests that the nakhlites crystallized from parent melts geochemically similar and in closed-system condition but at different degree of differentiation. The variations in augite properties (composition and zoning patterns and extents) between the nakhlites (despite their obvious consanguinity) suggest that the different meteorites correspond to multiple discharges of magma at depth where augite crystallized. Source-controlled variations (i.e. source heterogeneity or partial melting dynamics) and/or other physical processes such as magma segregation in the basaltic conduits and formation of separate igneous bodies could explain the variations in augite chemistry between the nakhlites. Distinguishing source variations from magmatic processes is very challenging and may remain unresolved. A possibility would be a better resolution of crystallization age of the different nakhlites but age difference between the rocks has to be greater than the precision of radioisotopic dating techniques, which is unlikely if the igneous bodies emplaced nearly contemporaneously.

The occurrence of melt inclusions with an evolved composition in the cores of cumulus augites provides evidence that the nakhlites began to crystallize from fractionated basaltic melts although the nature of these early fractionation processes are obscure. The primitive magmas have probably left behind crystal residues before crystallizing the nakhlites. The parent magmas at the origin of the nakhlites are probably not primitive but may rather be residua of progenitors that experienced cryptic fractionation mechanisms in the deep magmatic environment. The degree of differentiation of the parent melts between the nakhlites prior to and during augite crystallization varied. Bulk rock compositions and augite geochemnistry suggest that both NWA 5790 and NWA 817 represent melt residuas that previously crystallized abundant augite and plagioclase. Today, nothing is certain about the physical conditions under which the nakhlites' parent magmas crystallized their augite. We have incomplete if not largely unknown knowledge of the pressure and temperature conditions experienced by the nakhlites' parent magmas in the subterranean basaltic system. Hence, the composition and evolutionary paths of the nakhlites' parent magmas cannot be extrapolated with complete confidence. However, all our data disfavour a formation of the nakhlites from a single igneous body that differentiate in situ by intense fractional crystallization.

The unique chemical characteristics and zoning patterns of augite from the individual nakhlites are further consistent with the degree of chemical evolution of the igneous materials forming the inter-cumulus spaces in the respective nakhlites. The occurrence of evolved mineral phases (plagioclase, K-feldspar, Ti-magnetite, silica, Cl-apatite and Fe-sulfide) provides evidences of intense fractional crystallization processes experienced by the inter-cumulus melts while sub-solidus re-equilibration and disequilibrium texture between cumulus mineral phases and interstitial melts indicate that these fractionated melts have been redistributed probably during crystal accumulation and compaction. The nakhlites' parent igneous bodies were chemically structured. The higher Mg$\sharp$ of cumulus augite cores relative to those of the bulk rock provide evidence that augite did not completely re-equilibrate with the last inter-cumulus melt. The dominant mineral phase augite does not control the bulk rock composition of the nakhlites.

The small grain size and presence of glass in the inter-cumulus assemblage in some of the nakhlites indicate a sudden increase in the rocks cooling rate most likely associated with an extrusion of the augite-bearing magma near or at the surface prior to cumulate processes and final solidification. On the other hand, the development of orthopyroxene in the other nakhlites through reactions between olivine, plagioclase and the last droplets of melts together with subsequent intensive pyroxene exsolution suggest that the rocks experienced slow cooling rate during their whole crystallization history and have remained at sub-solidus temperatures up to almost complete rock solidification. Mechanical rock compaction during the very late-stage igneous processes may have expelled and unevenly redistributed the last residual melts. The existence of reactive silica-rich melts eventually destabilized the previously stable primocryst association olivine-plagioclase and set off the solid-state replacement of both mineral phases by low-Ca pyroxenes without changes in physical conditions (i.g. oxygen fugacity or temperature).

The parent magmas of the nakhlites were most probably dry. With the exception of apatite, the meteorites do not contain common basaltic primary water-bearing minerals (either amphibole or biotite). Apatite in the nakhlites appear to be largely depleted in OH but enriched in both Cl and F, providing further evidence of the lack of water in the magmatic environment, either primary or hydrothermal. However, the pervasive occurrence in the nakhlite MIL 03346 of Cl-amphibole in tens of µm large augite-hosted melt inclusions attests to the presence of high temperature Cl-rich fluids within the early magmatic environment. Chlorine was probably the main volatile element in the nakhlites' parent magmas. The lack of Cl in apatite within the mesostasis in MIL 03346, and NWA 5790, may result from Cl degassing prior to apatite crystallization suggesting a juvenile origin of Cl and the rock possibly crystallizing in a shallower environment than the other nakhlites.

# 5. MINERALOGY AND HYDROCHEMISTRY OF A YOUNG MARTIAN AQUIFER

## *5.1 Introduction*

The question of where, when and the nature of aqueous fluids that existed on Mars throughout its history is an ongoing debate. Defining the history and distribution of liquid water on Mars is fundamental because it is inherently linked to the climate and atmosphere history of the planet and plays a central role in the potential habitability of Mars (Jakosky and Phillips, 2001). With its mean pressure and temperature conditions close to 6 mbar and 220 K, modern Mars does not allow liquid water stability on its surface (Jakosky and Phillips, 2001). Yet, traces of hydrated minerals that only formed in liquid water have been detected within the basaltic materials forming the young Amazonian Martian crust (Carter et al., 2013). The existence of liquid water on modern Mars is a mystery, especially as water molecules in Mars' volatile reservoirs (polar ice caps and atmosphere) are almost completely non-existent (Jakosky and Phillips, 2001). So, is it possible that Mars still contains water beneath its surface? And if so, how much water can be stored? And what geological processes may be responsible for the sporadic activation of the groundwater? The purpose of this chapter is to better understand the history and properties of the hydrologic systems that existed in Mars' sub-surface during a recent past by studying the hydrated secondary minerals delivered to Earth by the nakhlite meteorites.

The nakhlite meteorites are fragments of a young Martian sub-surface basaltic crust that interacted with ephemeral, and possibly episodic, aqueous fluids over the last billion year (Bridges et al., 2001). During the fluid-rock interactions, a variety of secondary minerals demonstrably of Martian origin have been formed, many of which contain hydrous molecules (Treiman et al., 1993). The water-bearing secondary minerals are the irrefutable scientific proof that liquid water was at least once present in Mars' subsurface and had some influence on Mars' basaltic crust (Leshin and Vicenzi, 2006). To date, Mars sub-surface remains inaccessible to the space probes and rovers that analyse the surface of Mars. Hence, to deepen our knowledge of the nature and property of crustal water on modern Mars, high-precision laboratory investigations of the secondary minerals present in the nakhlites provide a unique opportunity.

The presence of water-bearing minerals in the young nakhlites formed during secondary processes testifies to aqueous activity on Mars during the Amazonian time, and is not a matter of debate any more. However, the physico-chemical conditions under which the products of aqueous activity formed and the nature of the crustal aqueous fluids that existed on Mars in the recent past remain a mystery. The products of aqueous activity present in the nakhlites are very scarce; they make up less than 1% of the rocks (Leshin and Vicenzi, 2006). However, they can provide information about the large-scale watery environments of Mars because their chemistry and mineralogy reflect the chemistry of the fluid from which they precipitated and the physical conditions that prevailed in Mars' sub-surface at the time of their formation (Tosca et al., 2004; Changela and Bridges, 2010). Unfortunately, because of their scarcity and inherent fragility, mineralogical or chemical information on the secondary minerals has proven difficult to extract and to date their exact nature remains unknown. The secondary minerals have been loosely termed "iddingsite" because of their rough mineralogical similarity with the alteration materials, a mixture of clay minerals and Fe-oxide, commonly formed during the weathering of terrestrial basaltic rocks especially olivine (Bunch and Reid, 1975). But unlike the latter, the Martian iddingsite-like alteration assemblage also contains carbonates, sulphates and halides, evidencing complex geochemical aqueous environments in Mars' subsurface (Bridges et al., 2001).

Understanding the nature of groundwater in the Amazonian crust of Mars, its chemical composition, origin and distribution, remains to date one of the biggest outstanding issues and major goals of future Mars scientific exploration and research. The nakhlites as available fragments of Mars regolith are important to better understand the properties of Mars' crust. They can serve as ground-tracking data for future Mars exploration returned sample missions such as ExoMars (Vago et al., 2006), for astrobiological models (especially with identification of the environmental limitations of the development of life such as the availability of bio-genetic elements (C, H, N, O) in the aqueous fluids (Des Marais et al., 2008)), or to predict where past or present water-rich environments can be found on Mars. Furthermore, identification of the evaporite and clay mineral assemblages deposited from concentrated Martian groundwater in the nakhlite meteorites can provide key information about the history of crustal water flow systems, their sources and the paleo-environment and climate under which they formed. The objectives of this chapter are to describe the aqueous alteration textures and chemical features of the nakhlites to gain insight to the nature of the groundwater inflows and their geological history, including the hydrochemical evolution and secondary mineralization processes prior to fluid evanescence.

## 5.2 Aqueous alteration: Definition and comprehensive model

### 5.2.1 General understanding of water-rock reactions

By definition, aqueous alteration refers to transformation of a rock's composition, either chemical or mineralogical, because of chemical reactions between aqueous fluids and the rock-forming minerals (Ming et al., 2007). Aqueous alteration is a chemical breakdown of rocks that proceeds whenever a rock comes into contact with an aqueous fluid (whether ice, liquid or vapour) at ambient (a process called weathering) or hydrothermal temperatures. The process of aqueous alteration is exothermic, the chemical reactions release energy. In other words, once triggered, aqueous alteration proceeds up to complete consumption of the limiting reactants. Aqueous alteration leads to the transfer of chemical components between the host rock and fluids and the formation of new chemical combinations (Velbel, 2012).

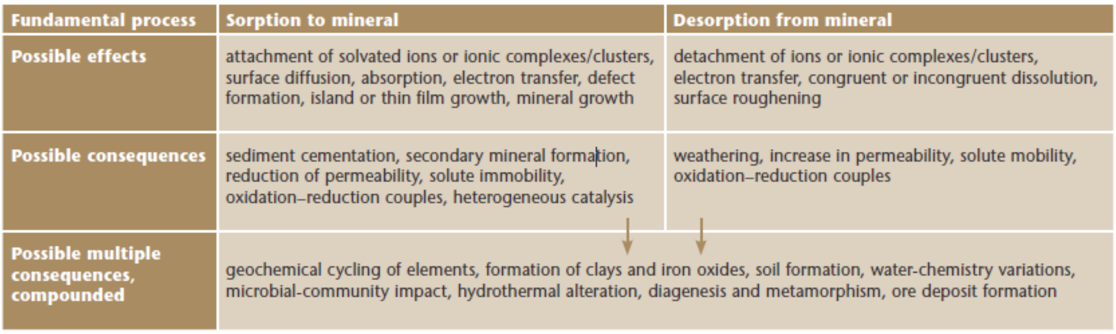

| Fundamental process | Sorption to mineral | Desorption from mineral |
|---|---|---|
| Possible effects | attachment of solvated ions or ionic complexes/clusters, surface diffusion, absorption, electron transfer, defect formation, island or thin film growth, mineral growth | detachment of ions or ionic complexes/clusters, electron transfer, congruent or incongruent dissolution, surface roughening |
| Possible consequences | sediment cementation, secondary mineral formation, reduction of permeability, solute immobility, oxidation–reduction couples, heterogeneous catalysis | weathering, increase in permeability, solute mobility, oxidation–reduction couples |
| Possible multiple consequences, compounded | geochemical cycling of elements, formation of clays and iron oxides, soil formation, water-chemistry variations, microbial-community impact, hydrothermal alteration, diagenesis and metamorphism, ore deposit formation | |

*Fig. 5.1: Fundamental processes, effects and consequences of fluid-mineral interactions (Hochella and White, 1990).*

Eventually, some of the new formed molecules precipitate to form secondary minerals in thermodynamic equilibrium with the new environmental conditions (Velbel, 2012). On Earth, aqueous alteration contributes to the local but also global redistribution of chemical species including the geological cycling of elements between the different superficial geological reservoirs: atmosphere, hydrosphere, and lithosphere (Hochella and White, 1990; Hellmann et al., 2012).

Although aqueous alteration can have fundamental implications for the large-scale geochemical aqueous environment, it always begins to operate at the atomic scale (Putnis, 2009). The chemical reactions responsible for aqueous alteration involve two mechanical processes that occur along the fluid-mineral interfaces: chemical species detachment (i.e. desorption) and chemical species attachment (i.e. sorption) (Hochella and White, 1990). They are responsible for a wide range of reactions: mineral growth/dissolution, oxidation/reduction, hydration, ion exchange, and hydrolysis (Fig. 5.1). The dynamics of such processes are strongly controlled by the chemical composition and structure of reactive minerals (Casey and Bunker, 1990). Mafic rocks contain silicate minerals whose crystal lattice are dominated by strong covalent bonds between O and Si or Al. The breaking of these (strong) covalent bonds by interactions with hydrous molecules through Van der Waals forces is difficult. It may be promoted by an increase in temperature because thermal agitation lowers the energy barrier of the covalent bonds, or by the presence of protons (i.e. $H^+$) that modifies the surface charge of silicate minerals. Hence, even though most mafic silicate minerals are chemically relatively resistant, they may be dissolved away by aqueous fluids including through low-temperature weathering-type reactions.

Amongst the silicate minerals that dissolve with difficulty are the tectosilicates (Casey and Bunker, 1990). Their relative resistivity to aqueous attack is due to their strongly cross-linked structure. However, they may still be selectively leached along their surfaces (through the preferential removal of the most soluble elements) by aqueous fluids. Mineral leaching creates pore spaces in the crystal, a process called incongruent dissolution, but is not sufficient to breakdown the general crystal structure of tectosilicates. On the other hand, silicates with poorly connected fabric are likely to dissolve quickly and more homogeneously. An extreme case is olivine. With its isolated silica units (tetrahedrons) bonded to each other by metallic cations, olivine has a loose molecular structure. In contact with the natural acidity of water, the metallic components ionize which is sufficient to completely (congruently) breakdown the olivine structure (Casey and Bunker, 1990), such as

$$(\mathrm{Mg,\ Fe})_2\mathrm{SiO}_4 + 4\ \mathrm{H}^+ \rightarrow 2\ (\mathrm{Mg,\ Fe})^{2+} + \mathrm{H}_4\mathrm{SiO}_{4(\mathrm{aq})}$$

The chemical breakdown of crustal materials during weathering processes is the main source of solute load of naturally dilute groundwater (Tosca and McLennan, 2006). Consequently, the chemistry and mineralogy of the bedrock control the solute composition of subsurface water. The chemical species present in the most susceptible minerals will be released to the fluids first while those present in the least reactive minerals will be released later. Mafic rocks are composed of a variety of silicate minerals whose specific reactivity releases at different rate chemical components to crustal fluids. The rate at which specific minerals dissolve (crystal susceptibility) in nature is impossible to predict (Hellmann et al., 2012). As we have seen above, it is strongly controlled by the crystal structure (i.e. the type of chemical bonding) (Weissbart and Rimstidt, 2000), but also by the micro-topography (or roughness) and presence of structural defects such as vacancies or dislocation planes near the mineral surfaces partly because they increase the mineral reactive surface area (Hochella and White, 1990). The abundance of the aqueous solutions, their initial chemical composition and pH also exert a strong control on the specific reactivity of minerals (Casey and Bunker, 1990) and the nature of secondary minerals that can potentially precipitate (Velbel, 2012; Tosca and McLennan, 2006).

The bedrock provides the chemical loads for the formation of crustal brines, but saturation of crustal fluids and eventually precipitation of soluble secondary minerals requires progressive evaporative processes of the crustal brines to saturate the dilute aqueous solutions (Hardie and Eugster, 1970; Tosca and McLennan, 2006). This presupposes that to precipitate secondary minerals sufficient inflow of water enters the bedrock and remains for sufficient time to react with the host rock. This also implies that solid precipitation is the main process responsible for the compositional evolution in space and time of crustal brines (Hardie and Eugster, 1970).

In general crustal aqueous fluids are initially charged (Putnis, 2009; Hellmann et al., 2012). They contain a certain quantity of chemical components gained from previous chemical reactions with atmosphere, lithosphere or other liquid or gaseous fluids with which they came into contact. The compositions of the crustal aqueous fluids are strongly influenced by their history (origin, chemistry and mineral composition of the host rock that further supply solutes, and lifetime) and have a very transient nature. Unlike minerals whose chemical compositions are definite (with the exception of some substitutions), fluids exist in an infinity of compositions and conditions (Lagasa, 1998). They are in constant evolution, both spatially and temporally. They never reach chemical equilibrium with the host rock which further increases the complexity of the thermodynamic of aqueous systems (Lagasa, 1998).

Fluid-rock interactions arise because the surfaces of minerals are not inert. Along their surfaces, minerals have their atomic bonding or coordination environment distorted or partly missing (Parks, 1990). Thus, surfaces of minerals have an excess of free energy and adsorption capacity which makes them highly sensitive to surrounding aqueous conditions. Chemical species (from both solid or fluid) along the mineral-fluid interfaces are highly mobile (Hellmann et al., 2012). They can diffuse along the surface or into the aqueous fluid/mineral, or attach/detach to specific sites along the mineral surfaces. In general, aqueous alteration is responsible for the breaking of specific chemical bonds in minerals and the formation of solutes in the fluid phase. Regardless of the silicate mineral and its crystal structure, at some early stages of the aqueous alteration, or in the presence of restricted amount of aqueous fluids, minerals are leached (Casey et al., 1993). Silicate minerals and glass are dissolved incongruently by selected removal of chemical elements which results in the development of leached layers at the solid-fluid interfaces (Hellmann et al., 2012). Leached layers are rarely stable and tend to be re-polymerized by solid state processes to form new and less reactive secondary product(s), a process called mineral replacement or pseudomorphic replacement (Casey et al., 1993; Putnis, 2009).

Leached layers have very specific properties (Casey and Bunker, 1990; Casey et al., 1993). They are largely composed of insoluble products of mineral and fluid (in general Si and Al), the most soluble elements having been lost to the fluid phase (Casey and Bunker, 1990; Weissbart and Rimstidt, 2000). Leached layers contain high concentrations of hydrous molecules, especially $H^+$ which serves as charge balanced component for the removed (structural) cations in the host solid (Casey et al., 1993; Hellmann et al., 2012). The leached layers form a porous silica network that are highly reactive. They tend to concentrate solutes from the adjacent aqueous fluids; leached layers are not representative of the bulk fluid composition and condition (Casey and Bunker, 1990).

The kinetics of aqueous reactions along mineral-fluid interfaces (dissolution and precipitation) are strongly controlled by the availability of aqueous reactants (either $H^+$ or $OH^-$) and the transport of aqueous components to and from the mineral reactive sites (Putnis, 2009). The capacity of a particular fluid to transport species before supersaturation and subsequent precipitation is very variable. It depends on the specific aqueous mobility of the chemical species released form the minerals, initial fluid load (with respect to the chemical composition of the rock-forming minerals), availability of reactive components (or ligands) in the fluid, and the water-to-rock ratio (Stroncik and Schmincke, 2002). Complete or partial removal of the most soluble chemical species from the aqueous environment (open system) is likely if large amount of aqueous solutions move freely, while stagnation of small amount of aqueous fluids should preserve the bulk chemical composition of the host rock together with that of the fluids (closed system), a process referred to as isochemical (Ming et al., 2007). If the water-to-rock ratio is very low, chemical gradients leading to diffusion are likely to be the most effective driving force for elements mobility and their localized redistribution from the reaction fronts. The chemical compositions of secondary minerals that precipitate in a closed system represents both the fluid chemistry and the elements released from the host rock (Ming et al., 2007). The efficiency of a fluid to transport (and spatially fractionate) chemical species determines the sites of secondary minerals precipitation and the nature of the secondary minerals that form. The removal or retention of chemical species from an aqueous system is controlled by the water-to-rock ratio.

Aqueous environments are dynamic systems, highly sensitive to local (i.e. atomic) conditions and reactions (Tosca et al., 2004; Tosca and McLennan, 2006). The infinite possibility of aqueous solutions, their spatial and temporal inhomogeneity and evanescent nature preclude any detailed understanding and prediction of aqueous alteration processes (Lagasa, 1998). Unfortunately, aqueous solutions are rarely retained within the alteration products while fluid inclusions are rare and often too small to be analysed, which is even more true in the case of meteorites. Direct chemical analyses of aqueous fluids are rarely possible. Hence, to constrain the nature of the aqueous solutions that reacted with a crustal material, analysing the leftover alteration products often remains the only opportunity.

Petrological studies of secondary minerals can still provide a comprehensive insight (although incomplete) into the mineral-water interactions of a given system with clues about the chemistry and conditions of the solutions. Effectively, secondary minerals precipitate only when supersaturation of its constituent components is reached, which means that at least these elements were present in excess in the fluids at the site of precipitation. The chemical composition of the alteration minerals reflects to a certain extent the prevailing mobility of chemical species during aqueous processes (Stroncik and Schmincke, 2002). However, it does not mean that the secondary mineral constituents were the only chemical species present in the fluids at the time of precipitation. The chemical composition of secondary minerals does not reflect the bulk chemistry of the solutions; they are biased chemical leftovers of the aqueous solutions. In general clay minerals offer a better opportunity to access the chemistry of fluids than salts or oxides as they can trap (absorb) in their interlayer spaces many chemical species from the fluids without structural constraint. Clay minerals are sensitive indicators of environmental conditions, either past or present (Eberl, 1984). They are good proxies of hydrous environments including the time-scale and conditions of aqueous alteration. They can provide further information on the source, type, and volume of aqueous solutions (Eberl, 1984). However, they are difficult to characterize because of their small crystal size, variable structural composition and ion-exchange properties.

### *5.2.2 Understanding of the nakhlites aqueous environment from the atom scale: What to expect*

The end products of Martian aqueous activity delivered to Earth by the nakhlite meteorites can provide an invaluable opportunity to access information about the near-surface aqueous environments of Mars and the nature, condition and evolution of the aqueous fluids present on the planet during the last 1.3 billion years (Fig. 5.2). The nakhlites exhibit primary lithology with only rare minerals of low-temperature aqueous origin. As already discussed, preferential dissolution of surfaces of reactive minerals provide the chemical ingredients of dilute ground water but also create porosity in the rock needed for further fluid ingress and secondary mineralisation. Identifying reactive sites along mineral surfaces in the nakhlites should provide clues about the aqueous fluid pathway through the rocks and the processes of crustal fluid maturation, including the identification of components potentially provided by the nakhlite parent host rock; while characterization of the chemistry of the secondary minerals should enable us to potentially identify foreign elements (i.e. elements that cannot be explained by in situ dissolution of primary minerals), and thus to determine the initial composition of the aqueous fluids including possible atmospheric or volatile volcanic components. Identification (or not) of atmospheric and/or volatile volcanic components is fundamental as it should provide information regarding the origin (magmatic, crustal or atmospheric) of the aqueous fluids that circulated in the Martian crust and/or the possible interactions between the different volatile reservoirs of Mars (Fig. 5.3).

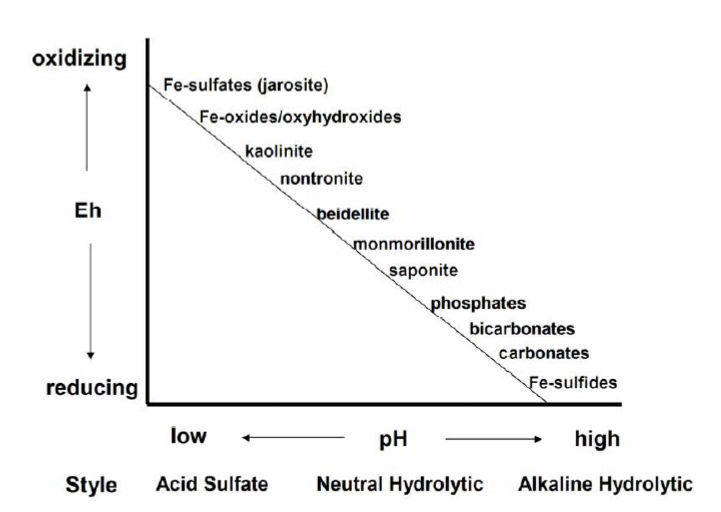

*Fig. 5.2: Secondary minerals identified on Mars or in Martian meteorites and their respective general environmental conditions and style of formation, figure taken from Ming et al. (2007).*

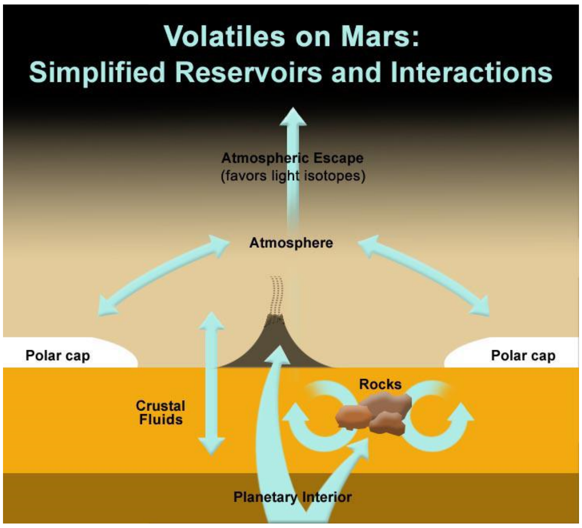

*Fig. 5.3: Schema illustrating the different reservoirs of volatiles on Mars and their interactions (http://photojournal.jpl.nasa.gov/jpeg/PIA16463.jpg).*

The mineralogy and chemical composition of the secondary minerals are not only controlled by the chemistry and quantity of the reacting fluids, but also by the transport distance of the fluids and relative element mobility under the prevailing aqueous conditions. Therefore, in the presence of a restricted amount of water, as suspected on Mars, one should expect a sharp spatial stratification of the secondary mineral composition with the least soluble crystallizing early from the most dilute and abundant fluids and the most soluble crystallizing from the most concentrated (vanishing) brines. Furthermore, as secondary mineral precipitate, the residual fluid composition evolves modifying the subsequent precipitation path of the resulting brines (Tosca and McLennan, 2006). The hydrodynamic, water chemistry and secondary mineralogy are interconnected. The nakhlites are very similar in bulk chemistry and mineralogy (Treiman, 2005), hence the secondary mineral composition of the nakhlites should reflect the spatial and temporal structure of the young aquifer of Mars that interacted with the nakhlites parent rocks and not intrinsic properties of different bedrock.

## *5.3 Recent hydrologic activity on Mars: Evidences from the Nakhlites*

The nakhlites contain a variety of secondary minerals indicative of aqueous processes, some of which are clearly from Mars. A pre-terrestrial origin of at least one part of the nakhlites' alteration products has been strongly established based on petrography and micro-stratigraphy relationships and chemical and isotopic composition (Reid and Bunch, 1975; Treiman et al., 1993; Gooding, 1986; Gooding et al., 1991; Swindle et al., 2000). Two of the nakhlite meteorites (Nakhla and Lafayette) have intra-crystalline alteration veins truncated by the fusion crust (the outer skin of the meteorite formed by frictional heating during the meteorite's entrance into the terrestrial atmosphere, Bevan and De Laeter (2002)); and alteration products that display (heat-induced) de-volatilization features at the vicinity of the fusion crust (Treiman et al., 1993; Gooding et al., 1991). Moreover, the K-Ar age (estimated at 670+/- 91 Ma) obtained from the bulk secondary mineral assemblages in Lafayette undoubtedly exceed the terrestrial residence time of the meteorite, while the presence of Kr and Xe in the alteration products reflect the (shock-induced) incorporation of the fractionated Martian atmosphere during the impact-launched event (Swindle et al., 2000). Further evidence of a Martian origin has been provided by the oxygen isotopic compositions of the secondary minerals that reveal precipitation from a non-terrestrial water reservoir (Karlsson et al., 1992).

However, although a Martian origin of the secondary minerals has been clearly demonstrated, interactions of the nakhlites with the terrestrial environment during their long terrestrial residence time have been inevitable. Terrestrial contaminations are thought minor in all nakhlites but remain poorly documented in separate meteorites (Stopar et al., 2013). Nakhla, the only nakhlite fall to date (Prior, 1912), has probably been the least contaminated by terrestrial fluids although it is not completely improbable either (Hallis et al., 2012). Aqueous alteration of the nakhlites in the dry terrestrial environments is difficult to identify because its characteristic features (textures and products) are very similar to those produced on Mars (Gooding, 1986; Wentworth et al., 2005; Hallis, 2013). Terrestrial aqueous alteration of the nakhlites may have led to the further dissolution of primary materials associated or not with secondary mineralization, exchanges of chemical species with the secondary Martian minerals and partial or complete redistribution of Martian hydrophile chemical species throughout the rock including the possibility of complete removal of the most soluble elements.

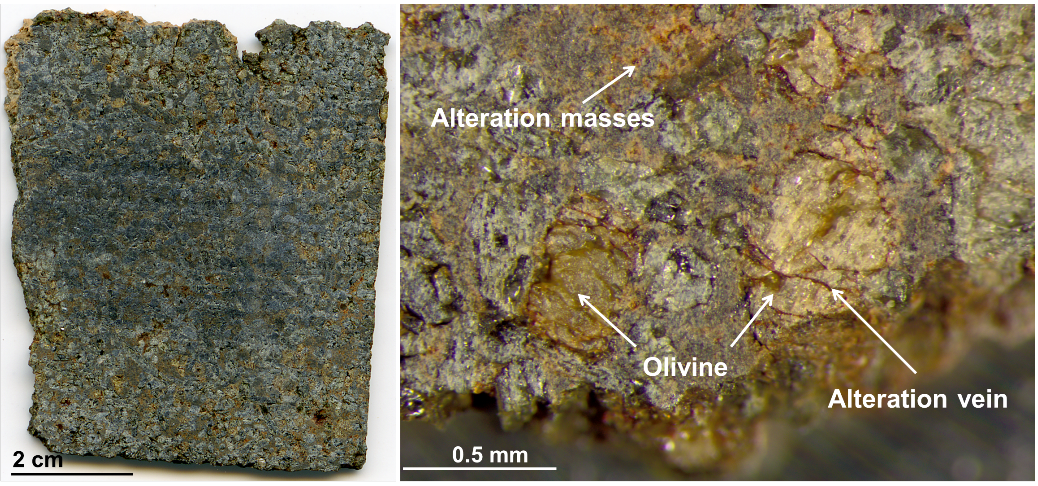

*Fig. 5.4: Pictures of the nakhlite meteorite NWA 817. The rock displays reddish-brown rock staining unevenly distributed. Secondary minerals are strongly associated with olivine where they form veins and thin films cross-cutting and surrounding the olivine grains respectively. In the mesostasis they form patches of alteration.*

## 5.4 Aqueous alteration textures: Tracking fluid-rock interactions in the nakhlites

The purpose of this section is to identify and characterise alteration textures formed during aqueous processes along mineral interfaces. Whenever a rock comes into contact with an aqueous fluid its mineral constituents begin to dissolve. Identifying the mineral dissolution features should enable us to define how the aqueous fluids circulated throughout the rock. It should also provide information about the origin of the solute (i.e. discriminating between chemical species that can have derived from in situ reactions or from earlier reactions that took place outside of the nakhlites' parent bedrock).

The most conspicuous effects of aqueous alteration on the nakhlite meteorites are the pervasive reddish-brown staining of the rocks, often referred as 'rust' in the literature, and secondary mineralization easily identifiable thanks to their porous nature and apparent absence of crystallinity (Fig. 5.4). With the naked eyes, the secondary minerals are unevenly but widely distributed throughout the rocks. They are not constrained within a network of fractures cross-cutting the rocks. Such alteration textures and distribution of secondary minerals suggest that the aqueous fluids most probably percolated through the rock using some natural rock porosity, while the widespread secondary mineralization gives evidence of abundant chemical species within the Martian aqueous solutions. With the exception of NWA 5790, all the nakhlites display similar rock staining. Unfortunately, none of our nakhlites thin sections has a fusion crust so deciphering a terrestrial *vs.* Martian origin will require further investigation.

At the microscopic scale, the secondary minerals are strongly associated with olivine. The secondary minerals fill disconnected, very irregular, sometimes curved veins and form thin films that partially cross-cut and surround the olivine grains, respectively (Fig. 5.4). Olivine veins do not radiate into surrounding materials.

The mesostasis also displays significant traces of aqueous alteration products, but in this petrographic setting, they form masses and not well-defined veins as in the olivine grains. Such alteration features suggest that the aqueous fluids did not circulate within brittle fractures but rather permeated their way through the rocks.

Surprisingly, although augite dominate the nakhlites mineralogy, the silicate minerals seem to have remained largely unaltered by the aqueous fluids. The relative greater susceptibility of olivine to alter in the presence of aqueous fluids relative to other mineral phases is already known (Velbel, 2009), and is due to its chemistry (mostly composed of highly soluble Fe and Mg) and crystal structure (isolated $SiO_4$ tetrahedrons bound to each other by the soluble Fe and/or Mg cations). The apparent relative non-reactivity of the silicate minerals augite and plagioclase within the nakhlite meteorites further suggests the likely short life time of the crustal aqueous fluids on Mars.

### 5.4.1 Olivine phenocryst alteration

Olivine is the most altered primary product in all nakhlite meteorites. Only NWA 5790 does not display any characteristic Martian aqueous alteration features, either texture or product, including within the ultra reactive olivine grains (Tomkinson et al., 2015). Hence, this nakhlite meteorite will not be further discussed here. Olivine from other nakhlites display subtle differences in their alteration texture that might reflect slightly contrasting aqueous processes, conditions or brine properties. Commonly, the olivine grains are cross-cut by intra-crystalline veins of alteration products. However, even within a single nakhlite, the olivine grains appear more heavily altered (displaying more or larger veins) in some areas or sections than others suggesting uneven aqueous fluid circulation throughout the nakhlites parent rocks. Although the olivine veins tend to be curved, they are roughly parallel. Using EBSD, the orientation of the veins have been determined. They all tend to have developed along the trace of the {001} plane of olivine suggesting a crystallographic control (Fig. 5.5).

Olivine veins display different textures between the nakhlites. Both NWA 817 and Lafayette have the largest alteration veins (few tens of micron large). The veins have irregular and saw-tooth margins. The alteration products also form sometimes disconnected rhombic-shaped areas within the olivine grains (Fig. 5.6). The edges of the veins and rhombic-shaped areas follow the {021} planes demonstrating a crystallographic control of the development of the veins. The veins do not radiate or intrude into surrounding materials. On Earth, olivine commonly alters and dissolves (i.e. weathers) in the presence of low-temperature aqueous fluids in similar textural patterns (Velbel, 2009). Certain nakhlites display veins of alteration that partially enclose symplectites (augite-magnetite inter-growths formed by high temperature exsolution) further suggesting that veins have enlarged through dissolution-precipitation processes, with the symplectites being less soluble than the olivine host. The preservation of the alignment of the symplectites provides evidence for a temporal coupling between olivine dissolution and secondary mineral precipitation.

The olivine alteration products within MIL 03346 also are at the scale of a few tens of micron but form irregular masses with often rounded margins rather than proper veins (Fig. 5.6). The olivine veins within both Yamato meteorites

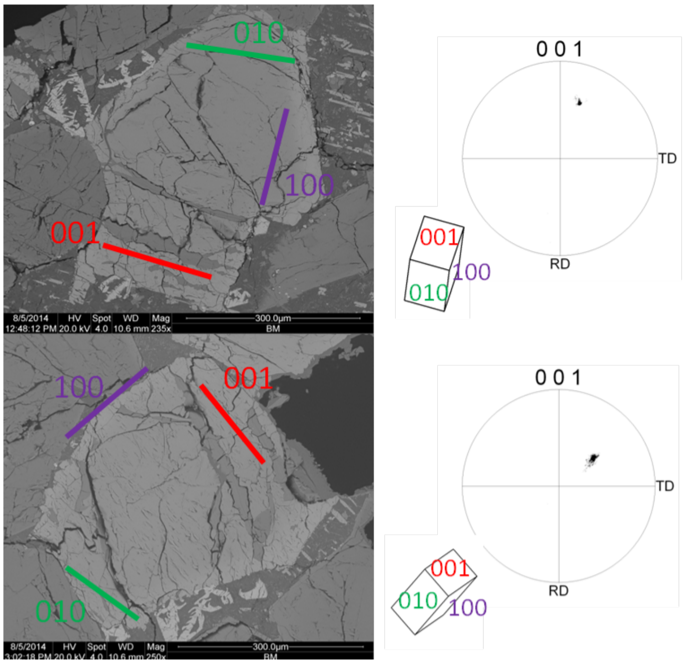

Fig. 5.5: *Crystallographic orientation of olivine grains (pole figures olivine forsterite 92) in NWA 817. The red, green and purple strips correspond respectively to the trace of the {100}, {010}, and {001} planes normal to the olivine grains. The veins are roughly parallel to the trace of the {001} planes.*

and Nakhla are only few micron thick (Fig. 5.6). They are very finely serrated and display along their margins, lamellar, sometimes curved, micro-structures that penetrate into the unaltered olivine. The micro-tunnels are either filled or devoid of alteration products. The complex alteration textures have been previously identified as laihunite (Noguchi et al., 2009). The laihunite-like alteration texture form lamellae that are parallel to each other. The lamellae seem to have developed from hairline fractures and penetrated perpendicularly from the fractures into the surrounding unaltered olivine crystal (Fig. 5.6). Such textures highlight the importance of the initial presence of hairline fractures in the formation and further development of the laihunite, especially for the circulation of fluids and chemical species into and from the olivine grains. Surprisingly, in our Y 000749 samples, no laihunite-like lamellae have been found although the presence of laihunite has already been established in this nakhlite using Raman spectroscopy, Synchrotron radiation X-ray diffraction (SRXRD) and electron microscopy techniques (SEM and TEM) (Noguchi et al., 2009). Lafayette also contains rare micro-tunnels at the olivine-secondary mineral interfaces intruding into olivine, especially at the tips of the sawtooth veins (only visible at very high magnification). The olivine grains within the meteorite NWA 998 are the least altered (Fig. 5.6). They have the thinnest alteration veins, which do not exceed 1 µm in thickness, with very sharp and straight margins. Outside of these veins, the olivine grains are largely unaltered. There is no textural evidence of dissolution features.

At the micro-scale (using the SEM), the alteration products in olivine from all the nakhlites except Lafayette do not display any obvious crystallinity. However,

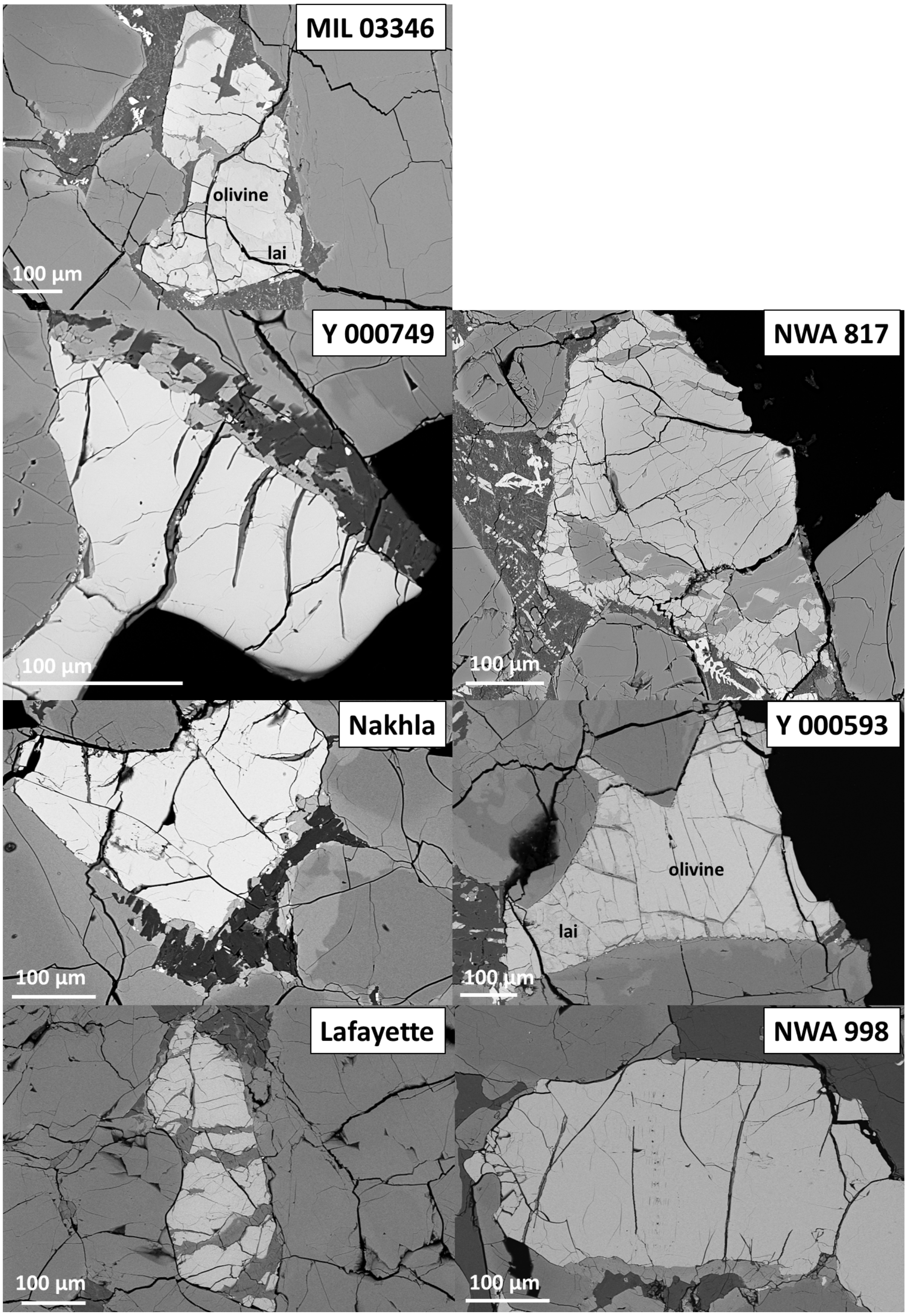

*Fig. 5.6: BSE images of the different alteration textures in olivine phenocrysts from the different nakhlites. Lafayette and NWA 817 have the largest veins with saw-tooth margins, while Y 000593 and MIL 03346 are the only nakhlites with abundant channel-like alteration textures identified as laihunite (lai) by Noguchi et al. (2009).*

alteration veins display strong compositional zoning along the margins of some veins. The marginal products overgrowth the alteration product central to the veins. In all nakhlites, the zoned products become progressively porous and coarse grained towards the contact with olivine suggesting different conditions of precipitation for the central and marginal alteration products. Both zoning feature and texture (cross-cutting relationship and overgrowing) suggest multiple episodes of deposition.

Olivine phenocrysts in all of the studied nakhlites contain intra-crystalline veins with common serrated and/or irregular margins (Fig. 5.6) and multiple thin films of alteration products coating their surfaces (Fig. 5.8). The coating layers cover in a non-uniform fashion the olivine surfaces but are orientated parallel to the grain surfaces. The contacts between the successive thin layers are sharp. Detailed examination using SEM technique of the products forming the surface layers does not reveal any obvious crystal faces or porosity (such as those filling the veins) although the deepest layers directly at the contact with olivine surfaces display some roughness including reversed bumpiness that "mirror" the microscopic morphology of the olivine altered surfaces. Furthermore, olivine surface layers show a network of "cracks" forming a "patchwork" texture or desiccation crack-like appearance. Olivine surfaces underneath these "cracks" are more heavily altered than where alteration products have remained; the "cracks" may have served as pathway for the aqueous solutions to the olivine surfaces.

Underneath the thin films of alteration products and along olivine-vein boundaries, olivine grains are generally corroded over few µm (Fig. 5.8 and 5.9). Outside of these areas, olivine phenocrysts are unaltered. Some of the corrosive textures are devoid of any secondary mineralization although they are directly in contact with the alteration products. The corrosive textures of olivine comprise funnel-shaped etch pits and denticulation that seem to have developed from fluid-mineral interfaces inwards (Fig. 5.9). They represent the interface-limited processes of fluid-mineral reactions and mark the progressive advancing front of aqueous alteration, i.e. the infiltration front of aqueous fluid into olivine grain. The denticulations on the olivine surfaces are parallel to each other while the conical etch pits seem to occur along hypothetical hairline fractures or planes along which they spread side-by-side and base-to-base (Fig. 5.8). The hypothetical hairline may represent possible zones of weakness (cleavage planes ?) or hairline fractures (dislocations ?) within the olivine grains. Regardless where the planes and chains of etch pits and denticulations are located (intra-crystalline or along the grain surfaces), on a given surface they all show a common orientation, suggesting a possible crystallographic control of the development of the alteration textures (Velbel, 2009). The further growth of corrosive textures occurred through side-by-side coalescence to form larger and deeper ones.

Existing crystal lattice defects may have served as pathways for aqueous fluid ingress into olivine grains and removal of the dissolved chemical species of olivine. The persistence of porosity (empty denticulation) underneath the thin film of alteration products (leached layers) along the olivine grain surfaces has probably enabled the retention of a contact between the primary minerals and aqueous fluids. On Earth, such corrosion textures commonly occur on silicate minerals through weathering processes (Velbel, 2009). However, within the nakhlites, it is impossible to determine the origin of the corrosive textures. They may either have formed on

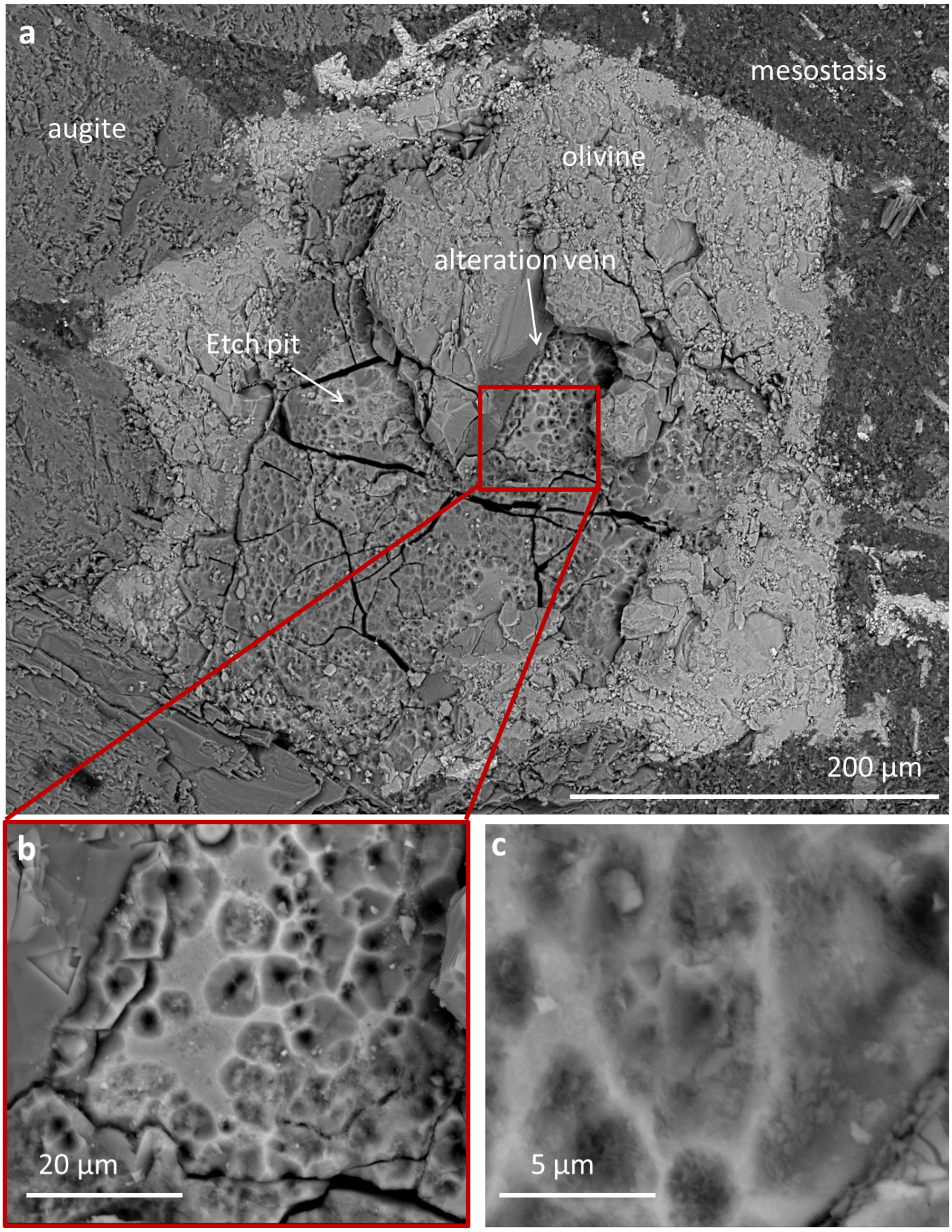

Fig. 5.7: *BSE images of a rough surface of olivine from NWA 817 showing the presence of funnel-shape etch pits with a common orientation (a) and their likely growth by coalescence to form larger ones (b). Some of the etch pits are coated with clay minerals, possibly smectite, as suggest by the mineral crystallinity (c).*

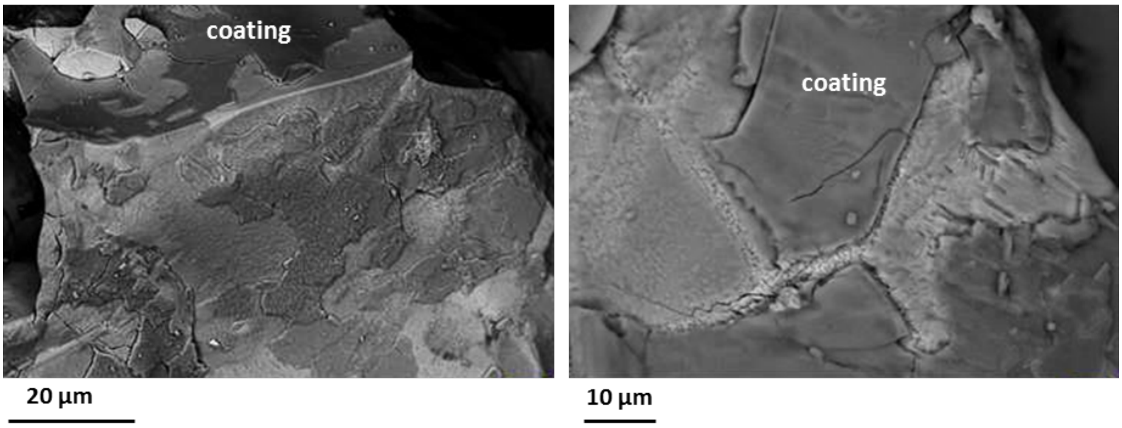

*Fig. 5.8: BSE images of a rough olivine grain from Nakhla showing the presence of a succession of coating layers that developed parallel to the grain surfaces. Below the thin films of alteration products, the olivine surface is heavily altered and show abundant denticulations intruding into the olivine grain. The coating layers display a dessication crack-like pattern. Underneath the cracks, olivine is more altered suggesting that the successive layers of alteration products have somewhat protected olivine from the fluids but were inefficient to prevent fluid access to the olivine surface.*

Mars through aqueous processes similar to terrestrial weathering or by terrestrial weathering during their residence time on Earth's surface.

### 5.4.2 Mesostasis alteration

Alteration products are also present within the mesostasis of the nakhlite meteorites. In this petrological setting, they form uneven and irregular aggregates rather than well-defined veins. The nakhlite NWA 817 contains a relatively high alteration products content within its mesostasis relative to other nakhlites. However, the alteration products are strongly associated with the numerous skeletal, fayalitic fayalite grains from which they seem to have grown (Fig. 5.10). Remnants of unconsumed fayalite are common within the alteration masses. The alteration products within the NWA 817 mesostasis occur as replacement products of the chemically and structurally weak olivine. The alteration masses replacing small fayalite grains do not present obvious crystallinity but display the same smooth texture than the alteration products within the olivine veins but without any compositional zoning feature.

Skeletal olivine within the mesostasis of MIL 03346 have also been largely altered, but unlike in NWA 817, in MIL 03346 it has been altered into laihunite (Fig. 5.11). In our samples of MIL 03346, no unaltered skeletal fayalite grains have been found. The laihunite seems to be depleted in aqueous alteration products (especially if compared to NWA 817), although it is not clear if the laihunite grain surfaces have been coated or not by very thin films of alteration products. The laihunite might have been more stable than fayalite under aqueous conditions, perhaps because of its higher oxidation state.

In the other nakhlites, small fayalite grains have been locally partially replaced

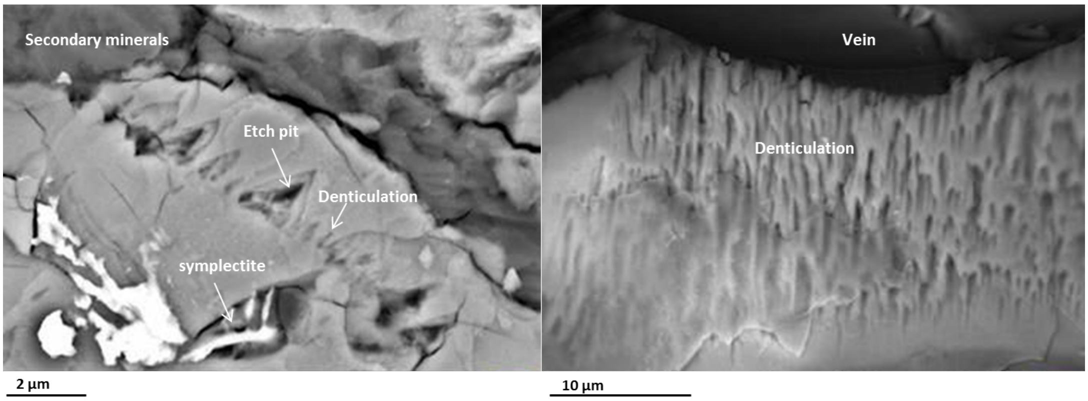

*Fig. 5.9: BSE images of a rough olivine grain from Nakhla showing veins at different stages of evolution. On the left image, one of the vein is filled by secondary minerals displaying no obvious crystal faces. A second vein is marked by fine denticulations and etch pits spreading side-by-side and base-to-base. The poorly developed vein illustrates the early stage of vein formation that results from fluid ingress probably flowing an intra-crystalline plane defect and subsequent removal of selected elements from olivine. Image on the right shows the denticulated surface of olivine at the contact with a vein.*

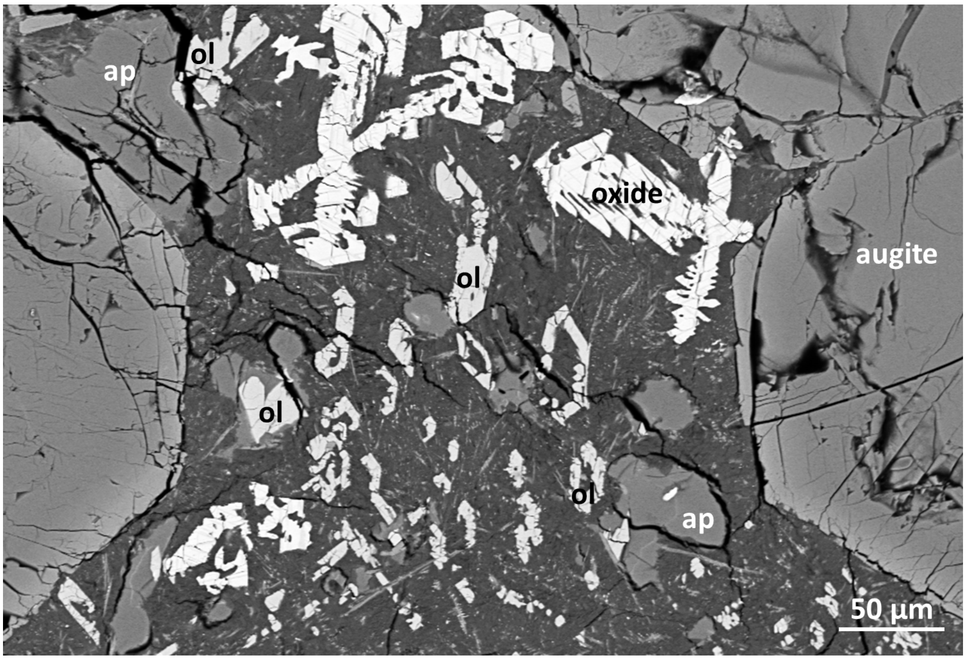

*Fig. 5.10: BSE image of the alteration products (ap) partially replacing skeletal olivine (ol) in the mesostasis of NWA 817.*

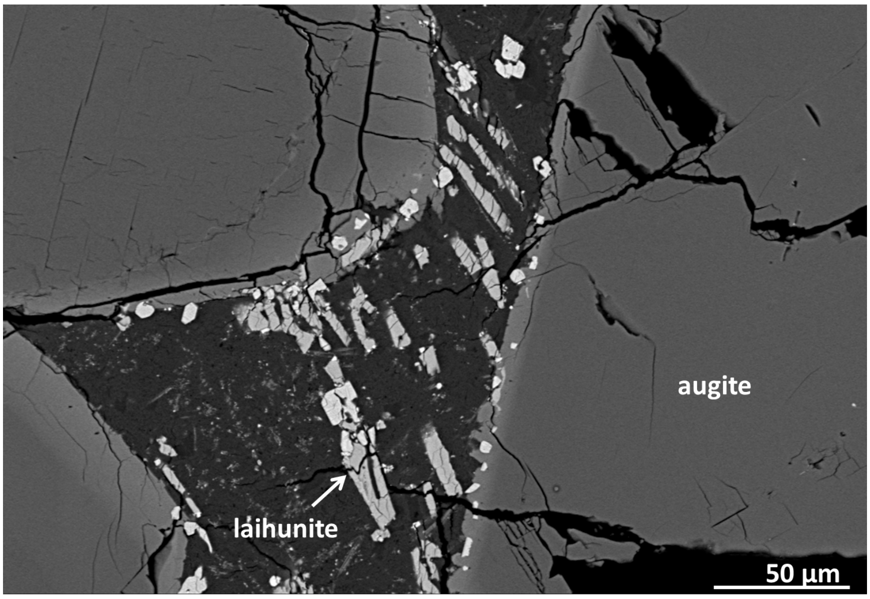

*Fig. 5.11: BSE image of laihunite (the high temperature aqueous oxidative product of olivine) in the mesostasis of MIL 03346. In our sample of MIL 03346, all skeletal olivine grains have been transformed into laihunite.*

by alteration products along veins but to less extent than in NWA 817. Small olivine grains in the mesostasis of Y 000593 also contain laihunite (Fig. 5.11). Laihunite has developed from the grain margin inward leaving the core of the crystal unaltered. The "fresh" part of olivine have veins of alteration. Other mineral phases within the mesostasis especially pyrrhotite have been altered in specific areas by aqueous fluids but display characteristic textural and chemical features unique to each meteorite. The alteration products associated with these other mineral phases contrast from those replacing olivine. Sulfide is a mineral in meteorites that is commonly altered during terrestrial weathering. Both the contrasting alteration products and alteration of pyrrhotite raise the question of possible terrestrial contamination.

Aqueous alteration within all the nakhlites has led to the common partial dissolution of olivine. The aqueous fluids have permeated their way through the nakhlite parent rocks. The presence of olivine was an important factor during aqueous processes. Olivine dissolution provided not only spaces for secondary precipitation but also solute to the fluid phase. Although other primary mineral phases may have contributed to the solute load even if they do not display obvious dissolution textures, components from olivine largely dominated the solute composition from in situ reactions within all nakhlites. Excess Fe, Mg and Si are thus to be expected in the Martian alteration products.

## 5.5 Secondary mineralogy and elemental composition

Most nakhlite meteorites contain traces of aqueous alteration products. A surprising variety of secondary minerals have been recognized so far but because of their scarcity and inherent fragile nature which precludes the use of many common ana-

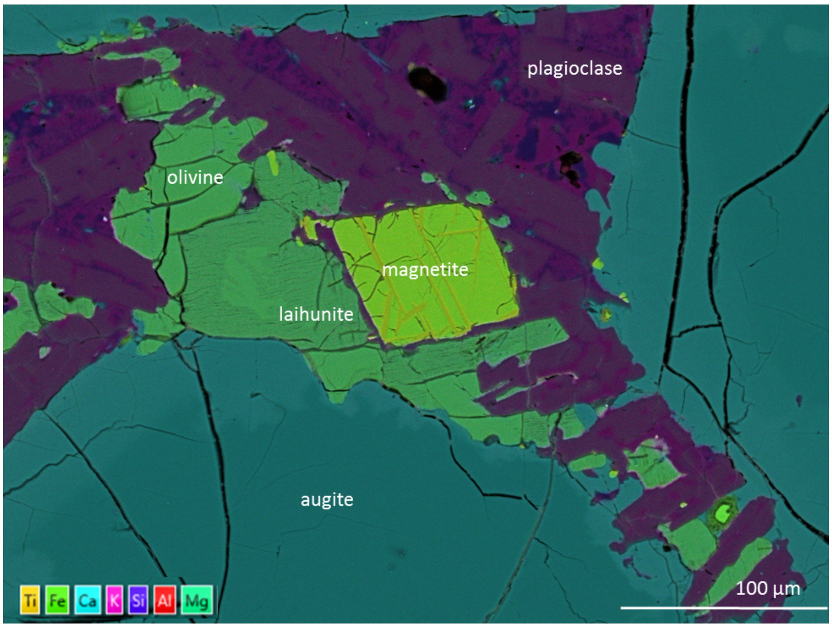

*Fig. 5.12: EDS map of an altered olivine grain in the mesostasis of Y 000593. Some parts of the olivine grain are transformed into laihunite (the high temperature aqueous oxidative product of olivine). The "fresh" parts of olivine contain small veins of alteration products.*

lytical techniques, their full and detailed characterization including crystal structure and structural formula remained only partial and sometimes even impossible. Their mineralogical identification is mostly based on morphological crystallography and qualitative elemental analyses using electron microscopy. But as they often occur as fine inter-growths of multiple phases, the distinction among several possible mineralogical interpretations is not always clear and remains controversial.

### 5.5.1 NWA 817

The alteration products within the olivine-hosted veins of the nakhlite NWA 817 appear mostly homogeneous, with the exception of some chemical and possibly mineralogical zoning along the vein axis and margins (Fig. 5.13). The first alteration product has only been found along the olivine-hosted vein axis. It occurs as straight, thin (<< 1 µm) "veinlets" composed of a fibrous, Mg-Si-rich and Fe-poor material. This alteration product does not seem to be present in the mesostasis and has never been found in any other nakhlite so far. If we assume that the veins formed by progressive dissolution-precipitation, then these "veinlets" probably represent the first alteration product formed, the crystallization occurring from micro-fissures via which aqueous fluids entered the olivine. These "veinlets" are sometimes difficult to follow within a single vein. They seem to have been partially recrystallized. As such, it is impossible today to define their initial thickness. This alteration product may also have been initially present within the mesostasis of other nakhlites and been completely re-crystallized later during the aqueous processes or during another aqueous event.

The second alteration product comprises most of the alteration products (Fig.

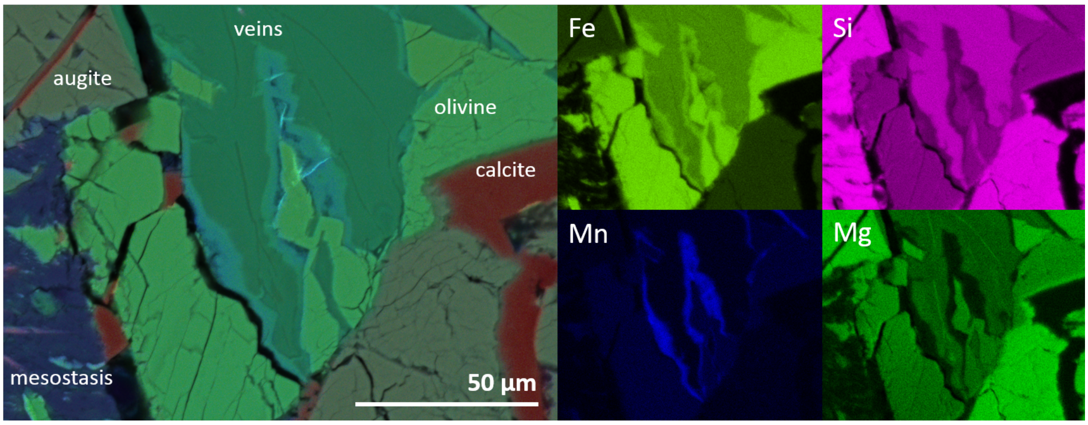

*Fig. 5.13: EDS maps of the olivine alteration products in NWA 817 comprising an Mg-rich product central to the veins, an Si-rich product making most of the veins and a marginal product rich in Fe and Mn.*

5.13). It is present in both olivine phenocrysts and mesostasis where it partially replaces small fayalitic olivine grains. It is structureless and Si-rich. Relative to its host olivine (either phenocrysts or small grains), it is depleted in Fe. It does not display obvious crystallinity at $\mu$m scale, or textural variation whether it is replacing olivine phenocryst or skeletal olivine in the mesostasis. However, it does display small chemical variations. When replacing small fayalitic olivine grains, the silicate alteration product is enriched in Mg relative to the host olivine, whereas when replacing olivine phenocrysts it is depleted in Mg, although olivine phenocrysts are less fayalite-rich. Furthermore, the Si-rich alteration product contains small amounts of S but only within the olivine phenocryst-hosted veins.

The third alteration product has only been found as a replacing product of olivine phenocrysts along the margins of some veins (Fig. 5.14). Unlike the other alteration products, it comprises two finely intermixed alteration products that can be identified by their different texture and chemistry (different grey scale on BSE images). They appear slightly coarse grained, although the crystallinity remained difficult to clearly identify using the SEM. Because of their small size and intermixed nature, it is not possible to properly analyse their chemical composition separately. As a whole, they are depleted in Si and Mg relative to their host olivine but are enriched in Fe, Mn and to a certain extent Ca. Their chemical composition provides evidence for an evolution of the complexity of the aqueous fluid chemistry. This marginal poly-mineralic assemblage partially cross-cuts and overgrows the Si-rich product, confirming that it crystallized last. Their occurrence in textural and chemical disequilibrium with the other alteration products suggests episodic deposition of materials under contrasting conditions. In our samples, no C, P, Cl, or S have been detected within this last alteration product.

All the olivine phenocrysts within our samples of the NWA 817 nakhlite meteorite display textural and chemical evidence of aqueous alteration. But, their degree of alteration is highly variable even when the olivine grains are only separated by one hundred $\mu$m (Fig. 5.15). The secondary marginal zoning is not always present within the olivine veins but does not seem to be related to the size of the veins.

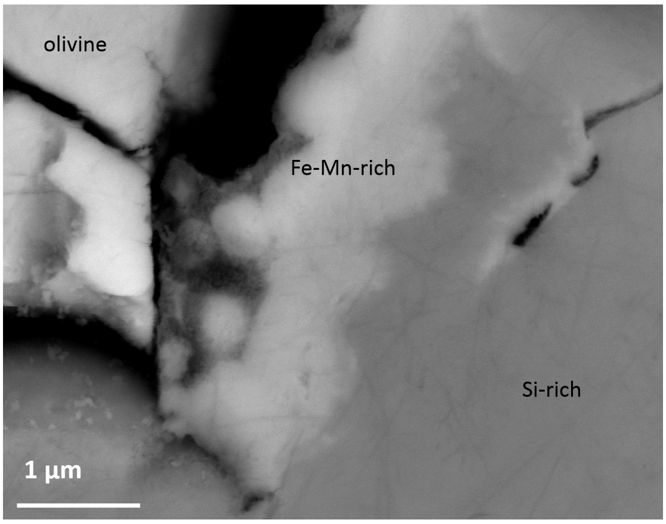

*Fig. 5.14: BSE image of the fine inter-growth of alteration products along the margins of olivine veins in NWA 817.*

The unusually largely altered olivine phenocryst has most probably been altered by the same fluids under the same physico-chemical conditions than the least altered olivine phenocrysts but most likely reflect an uneven fluid distribution. Such patterns can also been found in the mesostasis. In certain mesostasis pockets almost all skeletal fayalitic olivine have been altered into alteration products, while in other places, the mesostasis displays no obvious secondary mineralization, including associated within the small fayalitic olivine grains.

Our NWA 817 samples contain a network of fractures, up to several tens of $\mu$m-thick, fully cemented by calcite (recognized using Raman spectroscopy), a typical terrestrial contaminant of hot deserts. The contact between the fractures and primary material is sharp, and there is no textural evidence suggesting dissolution-precipitation along the fracture walls. The calcite veins cross-cut all primary material unlike the previous alteration products that are spatially restricted to olivine. The terrestrial calcite is physically constrained into the fractures and has not been found elsewhere either filling initial porosity or as replacement product of olivine grains, or intermixed product within the olivine-bounded alteration products, although minor Ca occurs in the porous silicate secondary minerals (Fig. 5.15). The aqueous fluids that have precipitated the calcite seem to have mainly circulated within the network of fractures. However, the calcite has been found in contact with the veins-bearing silicate and the Fe-Mn materials. At the contact with calcite, the Mn-Fe-rich mineral phases have been partially dissolved away. Nonetheless, at first sight, the terrestrial fluids do not seem to have significantly exchanged chemical elements (except possibly Ca) or penetrated within the (most probable) Martian olivine-hosted alteration products.

Sulfide minerals are generally very small ($< 1$ $\mu$m-thick) within the nakhlite NWA 817. However, rare large grains up to 100 $\mu$m of pyrrhotite do occur. Some of the large pyrrhotite grains have been largely replaced by an Si-Fe-rich product (Fig. 5.16). The secondary silicate does not contain S providing evidence that all the S has been lost to the fluid phase and possibly largely removed from the

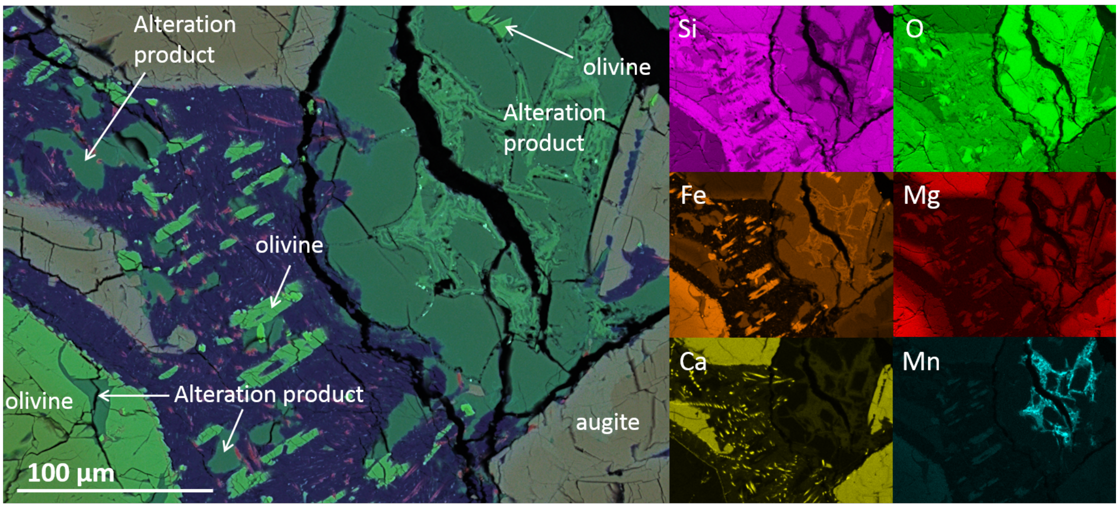

Fig. 5.15: *EDS maps of an unusually heavily altered olivine phenocryst next to a relatively unaltered one in the NWA 817 naklite. This probably reflect a very uneven fluid circulation throughout the rock.*

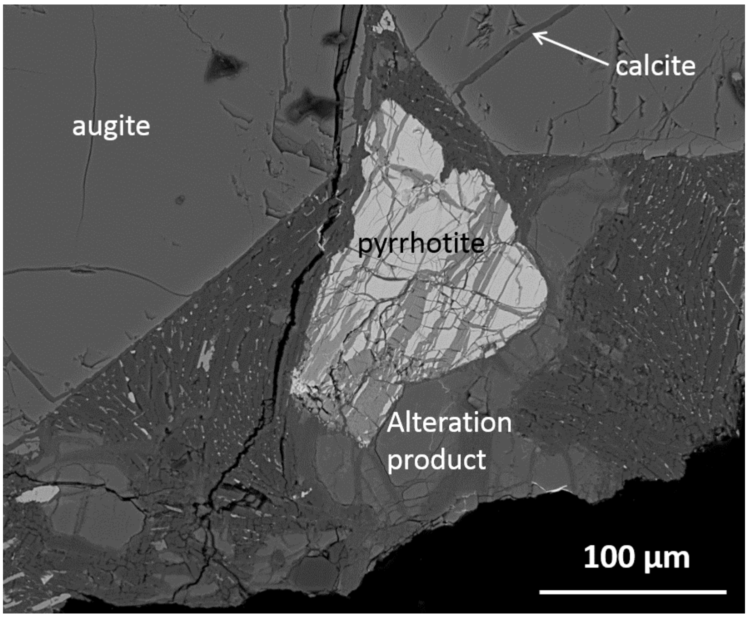

Fig. 5.16: *BSE image of an unusually large altered pyrrhotite in NWA 817. Pyrrhotite dissolution brought acidity which has enhanced glass alteration. The "darker' veins are terrestrial calcite.*

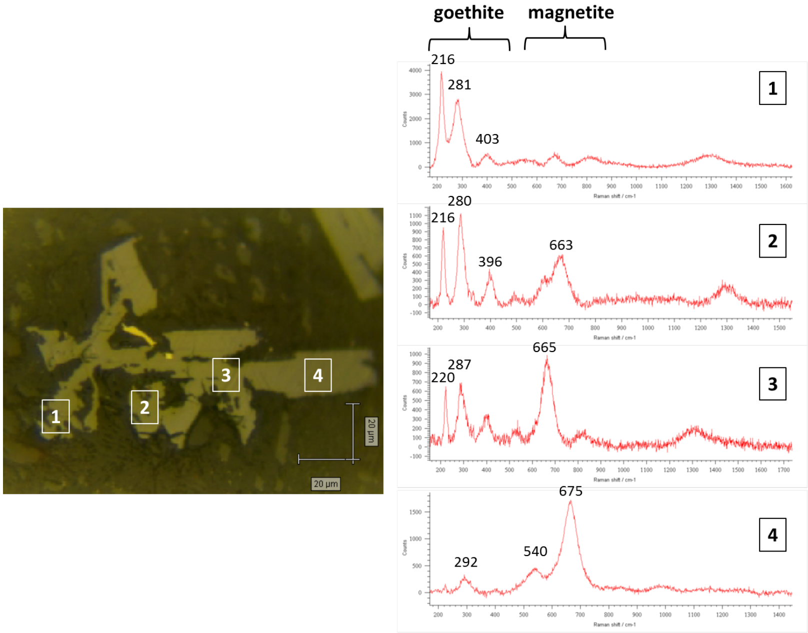

Fig. 5.17: *Photomicrograph (reflective light) of skeletal Fe-oxide in NWA 817 and Raman spectra showing the progressive pseudomrphic replacement of magmatic magnetite by secondary goethite.*

meteorite as no sulphate minerals have been identified within the meteorite (except rare S within the Si-rich product of most likely different origin, as will be discussed later). Commonly, the glassy mesostasis surrounding the pyrrhotite grains is heavily altered and replaced by uneven patches of secondary minerals (devoid of S). The dissolution of pyrrhotite by sulfide oxidation reactions may have brought localised acidity in the aqueous fluids that has enhanced the dissolution of the surrounding glass.

$$\mathrm{FeS_2\ (pyrite) + 15\ 0_2 + 8\ H_2O = 2\ Fe_20_3 + 8\ S0^{2-}_4 + 16\ H^+}$$

A Raman investigation of the mesostasis mineralogy has revealed the large presence of pseudomorphic goethite (Fig. 5.17), a common alteration product of Fe-bearing minerals. On Earth, a transformation of ferrous ferric oxide magnetite ($(\mathrm{Fe^{2+},Fe^{3+}})_3\mathrm{O}_4$) to ferric haematite ($\mathrm{Fe^{3+}O_4}$) and finally goethite ($\mathrm{Fe^{3+}O(OH)}$) is widespread and results from reactions with aqueous fluids either liquid or vapour at high or low temperature conditions. In NWA 817, goethite progressively replaces magnetite from the grains boundaries (Fig. 5.17). During the pseudomorphic replacement, the crystalline structure of magnetite has been preserved, such as it is not possible to identify goethite using an electron microscope. The presence of goethite in all mesostasis pockets suggests that tiny amounts of fluid have circulated throughout the whole rock (most probably along grain boundaries) despite the apparent lack of characteristic alteration textures at the vicinity of the magnetite/goethite.

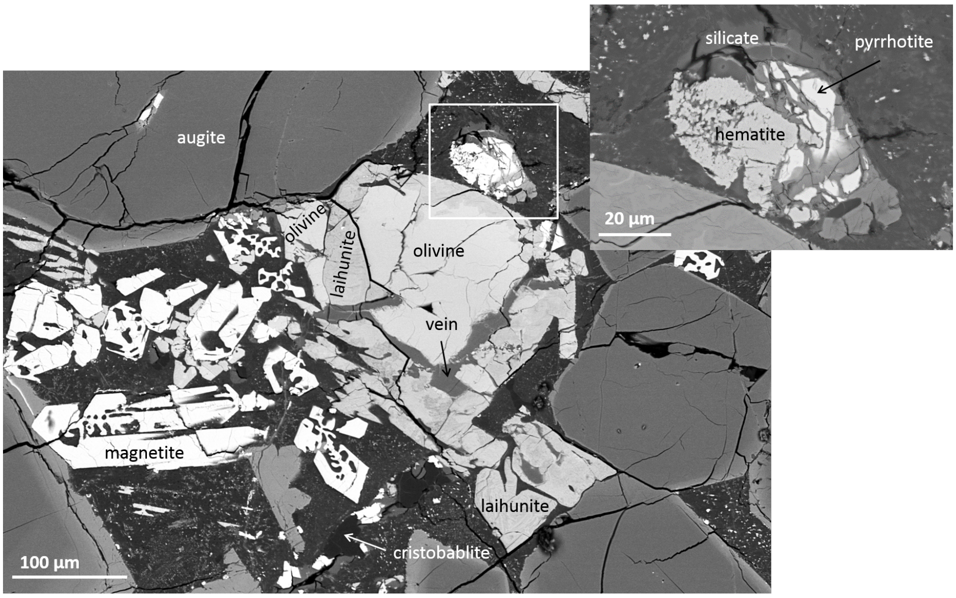

*Fig. 5.18: BSE image of an olivine phenocryst from MIL 03346 with its characteristic alteration texture including laihunite along grain boundaries and intra-crystalline veins of secondary silicate. Pyrrhotite are also commonly altered and replaced by secondary silicate forming veins similar those in olivine and pseudomorphic replacements of secondary Fe-oxide (hematite). The magmatic magnetite grains appear largely unaltered.*

### 5.5.2 MIL 03346

The nakhlite MIL 03346 contains a wide range of products of aqueous alteration. All olivine phenocrysts in our samples are pervasively altered (Fig. 5.18). They all contain laihunite, recognizable by its channelized texture, and elongate masses (or veins) of alteration products a few tens of $\mu$m thick. Both laihunite and alteration veins enclose symplectite exsolution suggesting formation by progressive replacement processes for both alteration products (Fig. 5.19). The laihunite is very unevenly distributed but seems to have developed from the grain surfaces inwards. Commonly, the cores of the olivine phenocrysts have remained unaltered, whereas the small olivine grains within the mesostasis have been completely transformed into laihunite as suggested by the channelized texture of the small grains.

Laihunite appears to be chemically very similar to the olivine rim composition. The transformation of fayalitic olivine into laihunite does not seem to have been accompanied by significant changes in major elements. Laihunite is best identified by its characteristic channelized texture rather than its chemical composition. On backscattered electron images, laihunite appears darker and “dirtier” than unaltered olivine (Fig. 5.18). However, laihunite does contain minor amounts of P and S. At the $\mu$m-scale, there is no textural evidence for the presence of inter-growths of salts within the laihunite suggesting that the ions may be present as adsorbed components. They may have been deposited either during the laihunite formation or during a latter aqueous event of Martian or terrestrial origin.

The olivine-hosted veins do not display a regular textural (sawtooth) pattern as in NWA 817. They are chemically very heterogeneous even at the $\mu$m-scale within

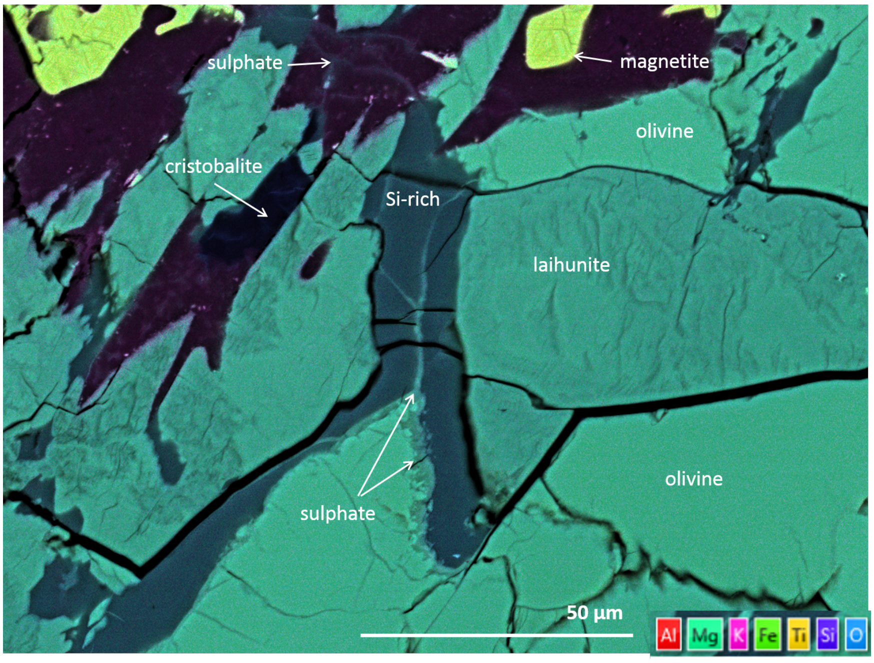

*Fig. 5.19: EDS map of an olivine alteration veins comprising an Si-rich product and Fe-sulphate in MIL 03346. The sulfate cross-cuts the Si-rich product and can be traced through the mesostasis.*

a single vein. The alteration products are generally enriched in O and can either be enriched or depleted in Si and be either constant or depleted in Fe relative to the host olivine. No enrichment in Mg has been qualitatively measured. However, all alteration veins contain a certain proportion of Al that appears to be relatively homogeneously distributed within and amongst the veins. Such (relative) Al content has not been detected within olivine veins from NWA 817. The alteration veins are commonly zoned along the vein margins. The marginal product does not contain Si but S and Fe. This alteration product could be jarosite, a hydrous sulphate of K and Fe that commonly forms as a result of Fe-sulfide oxidation ($KFe^{3+}{}_3(OH)_6(SO_4)_2$), but in our samples no K has been detected within the alteration veins. The S-rich product does not contain Ca either which eliminates the possibility of the presence of gypsum or anhydrite. The marginal Fe-S product sometimes cross-cut through the vein thickness suggesting that it crystallized last, most possibly from a separate aqueous event. Unlike the laihunite, the alteration products within the veins do not contain P- or Cl-rich alteration products.

As within the nakhlite NWA 817, large pyrrhotite grains within the mesostasis of MIL 03346 have largely been altered by aqueous fluids (Fig. 5.18). They commonly contain a network of veins composed of an Fe-Si-rich product, but also clusters of tiny grains of Fe-oxide. The texture of the Fe-oxide, including the small crystal size and preservation of the host pyrrhotite crystal shape, suggests a formation during secondary processes. Although alteration of pyrrhotite is common in most nakhlites, MIL 03346 is the only one displaying Fe-oxide secondary replacement of pyrrhotite. Surrounding the pyrrhotite grains, the glassy mesostasis has been heavily altered and transformed into Fe-Si-rich product similar to those within the pyrrhotite. The random alteration of the glassy mesostasis without obvious pseudomorphic replacement or vein formation within primary grains only occurs surrounding the heavily altered pyrrhotite suggesting that their dissolution brought localized acidity that has enhanced glass dissolution. The alteration products associated with pyrrhotite alteration are texturally smooth and relatively similar to those within olivine phenocrysts, such as their chemical composition.

The aqueous fluids circulation within the nakhlite MIL 03346 can be easily traced throughout the rock because the aqueous fluids have heavily reacted and redistributed chemical species within the rock along its way (Fig. 5.20). Most of the alteration products are not constrained within brittle fractures but rather spread unevenly over the primary materials, including glass. Outside of these patches of alteration, which form a river-like pattern, the meteorite is largely unaltered. The aqueous fluids were probably scarce and have unevenly circulated throughout the rock, such as for NWA 817, although the latter nakhlite does not display such river-like alteration areas. The aqueous fluid circulation within the mesostasis has led to a preferential removal of Si, Al, Na, Ca, and K from the glass and a deposition of Fe and S. The secondary minerals do not display any crystal faces at the micron-scale. Crystal faces of augite phenocrysts that came into contact with the aqueous fluids are depleted in Mg and Fe but not in Si or Ca although there is no textural evidence that the grain surfaces experienced leaching processes (i.e. creation of porosity).

Finally, our samples of the meteorite MIL 03346 are also cross-cut by a network of brittle fractures a few µm-thick filled with quartz, but also tiny fractures ($<< 1$ $\mu$m) that contain Fe-oxide (Fig. 5.21). Both secondary mineral phases have never been found together in the same fracture. The quartz-filling fractures do not seem to be related with the igneous $SiO_2$ blobs identified as cristobalite using Raman spectroscopy technique. Unlike in NWA 817, no calcite veins have been detected within MIL 03346. Furthermore, our samples seem to lack the Ca-sulphates (gypsum, anhydrite or bassanite?) and K-Fe-sulphates (jarosite?), as K has never been measured in association with the Fe-S-rich product, as previously found and properly identified in MIL 03346 (Hallis, 2013; Stopar et al., 2013). However, their occurrence restricted to the terrestrially exposed areas eliminates a Martian origin. None of our thin sections include the fusion crust, and possibly the external surfaces of the meteorite that have been exposed to atmospheric components, which may explain the apparent lack of the well-identified Ca- and K-Fe-sulphate. Commonly, chemical species are mobilized at different rate during aqueous processes while aqueous fluids were most probably scarce and unevenly distributed throughout the rock, which may explain the different chemical and mineralogical composition of the secondary minerals within our samples including the sulphate relative to other samples of this meteorite previously analysed.

### *5.5.3 Y 000749*

Nakhlite Y 000749 is a complexly altered meteorite. Almost all olivine phenocrysts have abundant veins which display sharp chemical and mineralogical zoning (Fig. 5.22). The olivine-bounded alteration veins very rarely exceed 10 $\mu$m in thickness, unlike the two previous nakhlites NWA 817 and MIL 03346. Along the vein axis, as common to most nakhlites, lies the smooth texture-less Si-rich alteration product (Fig. 5.23). It forms bands possibly separated by Fe-oxide (white strips on

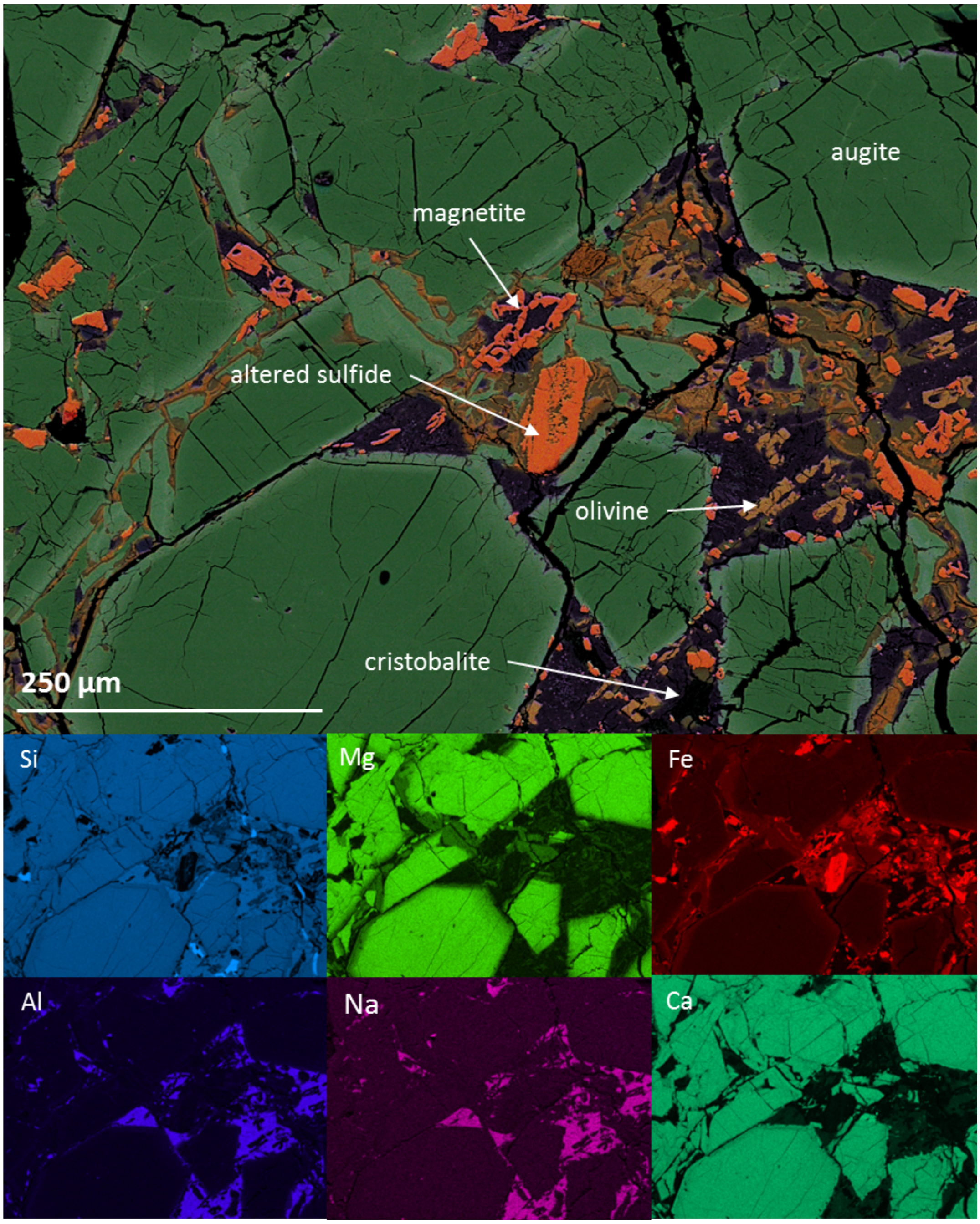

*Fig. 5.20: EDS map of a heavily altered area of MIL 03346. The aqueous fluids have partly dissolved the primary material and precipitated secondary minerals. For example, the sulfide grains have been completely re-crystallized into Fe-oxides. To be noted: at the contact with the aqueous fluids augite grains have been partly corroded and have lost through their altered rims their structural Fe and Mg (probably by solid-state diffusion).*

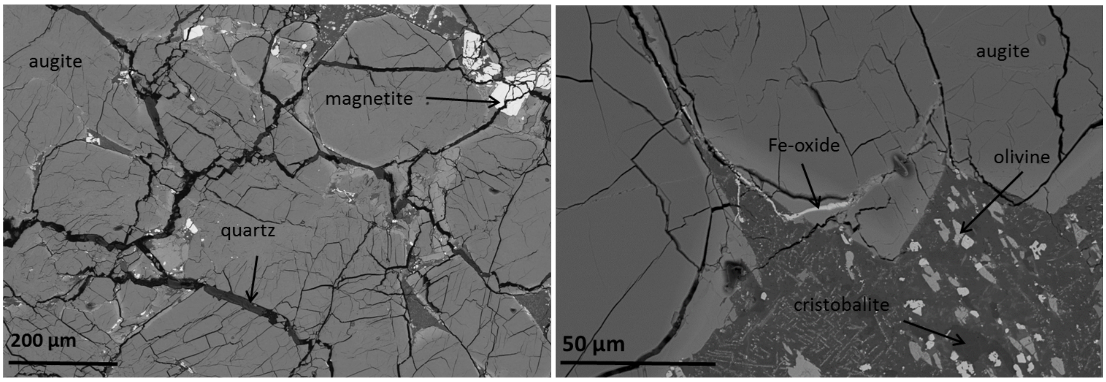

*Fig. 5.21: BSE images of quartz and Fe-oxide filling impact-induced fractures in nakhlite MIL 03346.*

Fig. 5.23). This product also contains a significant content of Mg but is largely depleted in Fe relative to the host olivine. The alteration product is surrounded by another alteration product with a more heterogeneous chemical composition, even at the $\mu$m scale within a single vein. Once again, the marginal alteration product does not display obvious crystallinity at the $\mu$m scale. It sometimes overgrowths onto the Si-rich product providing evidence for at least two different episodes of precipitation with the marginal product crystallizing last. The marginal alteration product contain traces of Si and Mg but does contain a significant amount of Fe (Fig. 5.23). In certain veins, it is enriched in Mn, while it can locally contains rare K, Ca and Al but also the semi-volatile S and more rarely possible traces of P. No Cl has been detected in any alteration products as is common in some of the nakhlites. It probably is siderite, a Fe-rich carbonate.

The Fe-rich carbonate within olivine veins display fine-scale interpenetration textures along the vein margins suggesting a partial dissolution of the host olivine (Fig. 5.22, 5.23). The channel-like texture (poorly developed laihunite?) surrounding the veins is sometimes devoid of alteration products but when at the contact with carbonates, the tunnel-shaped porosity is filled with siderite. The channel-like alteration texture is very similar to laihunite, but a very poorly developed one. The channels may have served as pathways for the aqueous fluids and chemical components in and out of the reactive front. The aqueous fluids were probably very under-saturated relative to olivine composition. They

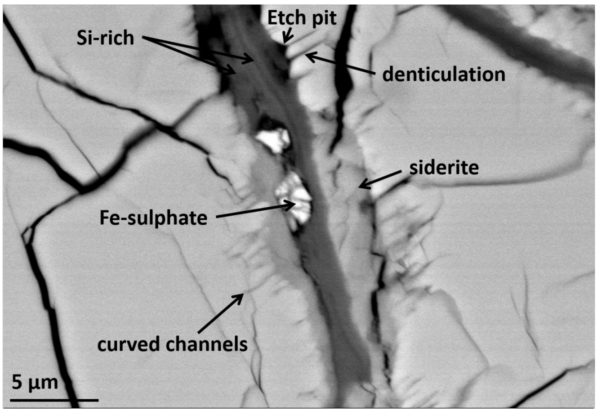

*Fig. 5.22: BSE image of an alteration vein in Y 000749 with bands of Si-rich products with Fe-oxide (light grey strips), siderite, Fe-sulphate. Olivine alteration textures include empty etch pits and denticulation and filled curved channels.*

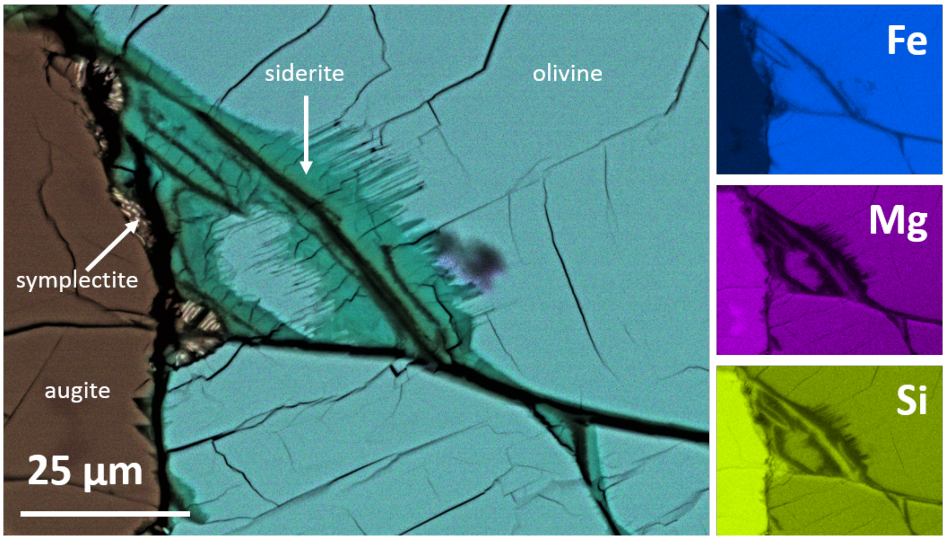

*Fig. 5.23: EDS maps of the olivine-bounded alteration products in Y 000749. The alteration product central to the veins is strongly enriched in Si and Mg and is surrounded by siderite, a Fe-rich carbonate.*

may have reacted and dissolved the
olivine, precipitating afterwards the dissolved components of the olivine including Fe.

The alteration veins extend over augite-magnetite symplectite exsolutions (Fig. 5.23). The symplectite exsolutions have partly reacted with the aqueous fluids, including both augite and magnetite, but can still be optically traced through the alteration veins, further providing evidence for a formation of the veins through dissolution-precipitation processes with the symplectites being less soluble than the olivine. A final alteration product occurs within the olivine-bounded alteration veins. It seems to fill brittle fractures and voids. It has never been found in any other petrological setting. It forms relatively coarse grains of Fe-sulphate (jarosite?) cemented on another product of unknown chemical composition (Fig. 5.22). This alteration product is widely present in one of our samples but not present in all olivine-hosted veins or in our other of samples of Y 000749. However, its poor bonding to the rest of the alteration products may have resulted in its almost complete loss during sample preparation. Its occurrence in voids and fractures suggests that it crystallized last, after the previous alteration products.

The meteorite mesostasis does not present obvious secondary mineralization except partial replacements of small pyrrhotite and fayalitic olivine grains. The alteration product is devoid of S in both petrological settings but contains abundant Fe and Si and minor Al. Pyrrhotite alteration has not led to the formation of Fe-oxide or dissolution of surrounding materials as in MIL 03346. There is no trace of calcite or Ca-rich alteration products anywhere in our samples of Y 000749.

### 5.5.4 Y 000593

The Y 000593 meteorite is heavily altered, more than its paired Y 000749. All olivine phenocrysts display complex alteration features (Fig. 5.24). The alter-

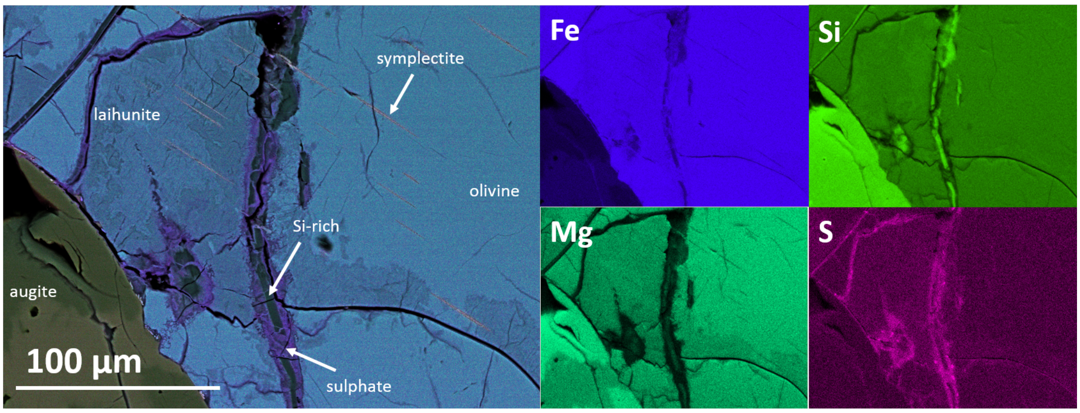

*Fig. 5.24: EDS maps of olivine with laihunite (dirty patches) and alteration veins in Y 000593. The veins are zoned with an Si-Mg-rich product surrounded by an Si-Fe ±S-and P- (not shown) rich product. Alteration products enclose symplectite suggesting a formation through dissolution-precipitation, the symplectite being less soluble than the olivine.*

ation products commonly enclose symplectites suggesting that they formed after the high temperature augite-magnetite intergrowths by selective replacement of olivine. Most of the alteration products are confined within veins a few micron-thick cross-cutting olivine. Outside of these veins, olivine is discontinuously replaced by an alteration product with the fine-scale channel-like micro-texture characteristic of laihunite Noguchi et al. (2009). The distribution of the laihunite is strongly controlled by grain boundaries, lamellae symplectites and veins from which it seems to have developed. In their study, (Noguchi et al., 2009) found that the laihunite has decomposed into amorphous silicate and Fe-oxide at the vicinity of the fusion crust suggesting a pre-terrestrial origin of the laihunite. X-ray elemental imaging of the laihunite reveals no major compositional difference relative to unaltered olivine (Fig. 5.24). It shows only a slight depletion in Fe and sometimes Mg and enrichment in O suggesting partial dissolution of olivine by water-bearing fluids with preferential removal of the highly soluble Fe and to some extent Mg and possibly oxidation of the olivine ferrous Fe to ferric Fe. The laihunite X-ray spectra show traces of S most probably present as adsorbed ions within the channels.

Laihunite is a mineral similar to olivine but with a distorted structure with abundant planar vacancies and a non-stoichiometric composition. Laihunite can be identified on high resolution TEM images as they form dark contrast nano-lamellae on olivine (Fig. 5.25). On Fig 5.25, the semi-ordered texture (planar vacancies or nano-tunnels) of laihunite can be easily seen. The presence of cluster of black diamond-shaped grains with laihunite suggests the presence of goethite.

"Iddingsite" veins within olivine phenocrysts are zoned with a complex secondary mineral assemblage. The alteration products occurring along vein axes do not show evident crystal faces at the SEM scale. They are enriched in Si, Mg, and O with lower concentration in Fe and rare Al. This material is commonly surrounded by a discontinuous, fine layer of Fe-Mn-oxide. Both mineral phases represent the Martian"iddingsite" common to most nakhlites. The "iddingsite" has largely been replaced by coarse grained minerals enriched in Fe, Mn, Al, S, P, and very rare Cl

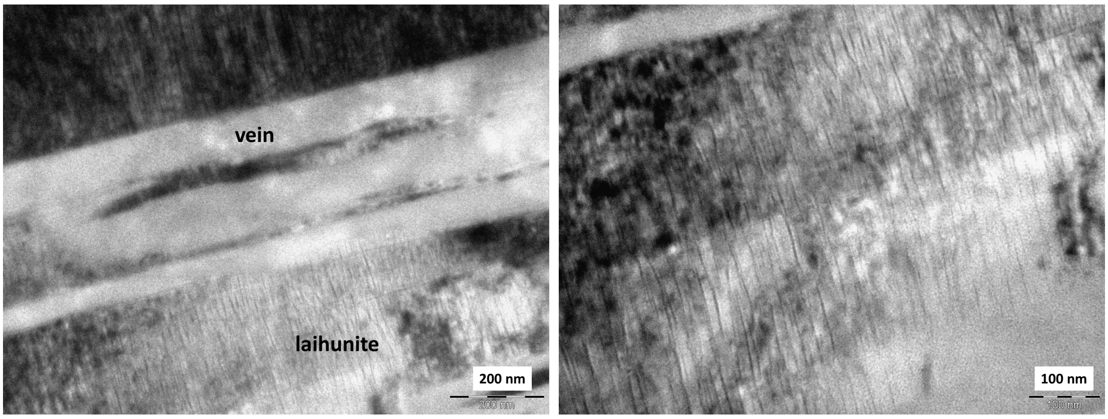

*Fig. 5.25: High resolution bright field images of laihunite (dark strips) and alteration veins in an olivine phenocryst from Y 000593. The black diamond shaped grains within the laihunite are most probably goethite.*

(unlike Y 000749) whose proportions vary at the (sub)micron-scale. The aqueous fluids that pervaded Y 000593 were probably more concentrated in ion components than those that circulated in Y 000479. The marginal alteration products are depleted in Si and Mg relative to the alteration product central to the veins. Finally, the different materials are cross-cut by a K-Fe-S-bearing mineral phase (jarosite?). The presence of different mineral phases in cross-cutting and overgrowing relationships points toward multiple episodes of secondary mineral deposition.

The mesostasis also contains significant amounts of alteration products. They are not restricted to veins but rather form concentrated masses replacing different igneous phases forming the mesostasis, especially pyrrhotite, Ti-magnetite, augite, and plagioclase feldspar (Fig. 5.26, 5.27). The alteration products are composed of a fine mixture of two different types of secondary mineral. Their texture and chemistry is very similar whatever the primary product they are replacing. The first alteration product forms layers surrounding and replacing primary minerals although it has never been found associated with altered olivine. This alteration product is fibrous and composed of Si, Fe, Mn, Mg, and Al. Traces of P, Cl and S have been detected although it may reflect mixed analyses with the other alteration products. Both its micro-structure and chemical composition suggest that it is a phyllosilicate.

The second alteration product occurs mostly within the phyllosilicates. It is highly porous, fibrous and composed mostly of Fe and Mn, with low concentrations of Si and variable P, S, and Cl. The occurrence of Si and the fibrous texture suggest once more the presence of a phyllosilicate mineral. The ionic components may represent either a co-precipitation of salts with the phyllosilicate mineral or a substitution of interlayer $OH^-$ molecules by anions. This alteration product is similar in composition (albeit poorer in Si) and texture to that overgrowing the olivine-hosted“iddingsite”, suggesting that they may have precipitated from the same fluid but with a micro-environmental control on the fluid chemistry. It was most probably the last to crystallize and may be of terrestrial origin. The occurrence of anions may be the result of dissolution of primary minerals such as pyrrhotite and Cl-apatite. Although augite is the most abundant mineral, it contains only

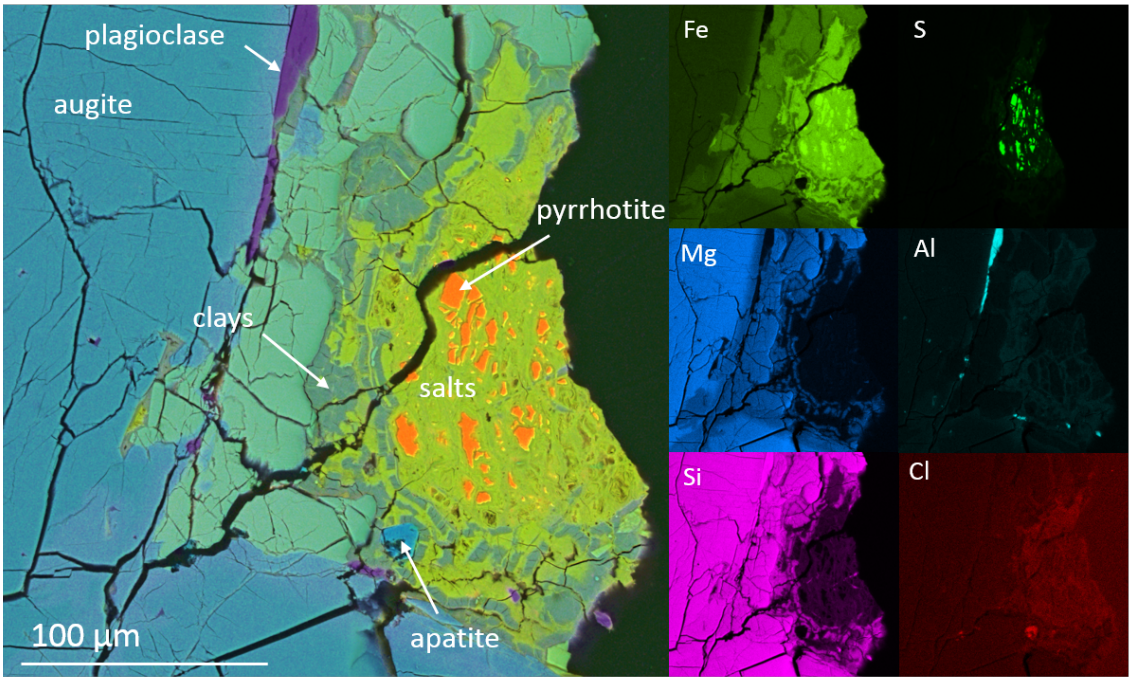

*Fig. 5.26: EDS maps of a heavily altered pyrrhotite grain replaced by Fe-sulphate and Mg-rich clay minerals (recognized by their crystallinity) in Y 000593.*

rare traces of secondary minerals which include Ca-sulphate filling fractures and phyllosilicate replacement, once again recognized by their habit and crystallinity.

Areas of heavy aqueous alteration within the meteorite occur. In these areas, the mesostasis has largely disappeared: only remnants of unconsumed feldspar still attest that the mesostasis once laid at these specific sites. Chemically the alteration products of olivine phenocrysts and primary materials within the mesostasis are very similar nonetheless, they are much coarse grained in the latter. Unlike in NWA 817, the texture-less Si-rich product has not been found in the mesostasis. The Y 000593 nakhlite meteorite is also cross-cut by a network of fractures that are largely filled with a Fe-P-rich, and locally Cl-rich, secondary product. The fractures are spatially related to the mesostasis and olivine alteration products raising the question about latter terrestrial or Martian contamination.

### 5.5.5 Nakhla

Nakhla is the only nakhlite meteorite observed to fall and is consequently the only nakhlite potentially not contaminated by terrestrial fluids. At first sight, the meteorite appears to be one of the least altered of the nakhlites. The olivine-hosted alteration veins are sparse and amongst the smallest in both length and thickness (Fig. 5.28 right). Olivine displays dissolution features along its grain boundaries that are devoid of secondary mineralization (Fig. 5.28 left). Outside of the olivine veins and grain surfaces, olivine grains are largely unaltered. There is no textural evidence for the chemical breakdown through aqueous processes (i.e. corrosive texture) of any primary material forming the mesostasis, including the highly reactive pyrrhotite grains. Only very rare hairline veins following plagioclase grain bound-

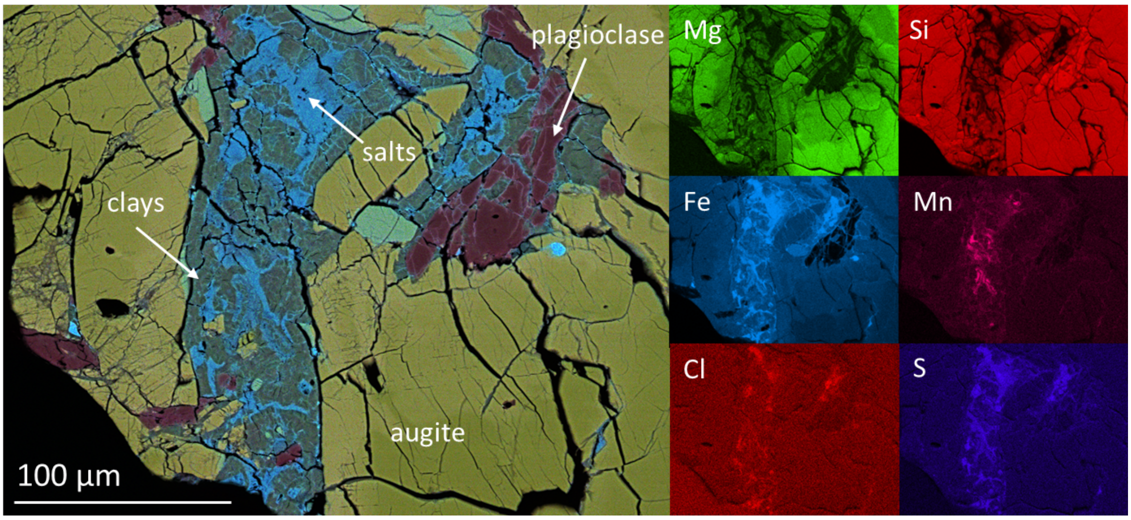

*Fig. 5.27: EDS maps of a completely altered area where once lays the mesostasis (identified thanks to the presence of remnants of plagioclase) containing salts and Mg-Si-rich fibrous phyllosilicates (clays) in Y 000593. Both silicate minerals displays the same bulk texture and mineralogy than those replacing the large pyrrhotite grain on Fig. 5.26.*

aries mostly composed of Fe and Mg have been identified within the mesostasis. The veins do not contain Si, P, S or Cl suggesting that they are most probably filled with Fe-Mg-oxide. The interstitial glass does not seem to have reacted with the aqueous fluids that have precipitated the Fe-Mg-oxide.

The olivine-hosted alteration veins in Nakhla are very similar to those in the Yamato meteorites in term of both texture and possibly chemistry. As with the Yamato meteorites, the olivine-hosted alteration veins in Nakhla are zoned with central to the veins a Si-rich alteration product. As in other nakhlites, it does not display obvious crystallinity at the $\mu$m scale. The silicate alteration product is depleted in both Fe and Mg relative to olivine, but it locally contains Mn and Na, rare S (more or less at detection limits) and widely distributed Cl (although only detected using EDX mapping). No P has been measured within the olivine-hosted alteration product. Nakhla is the only nakhlite with Y 000593 which contains relatively abundant Cl.

The vein margins are often composed of an Fe-rich alteration product (Fig. 5.28 right). The marginal alteration product tends to overgrow olivine and the Si-rich product suggesting a deposition of the different aqueous products during distinct aqueous events. The vein margins display fine-scale inter-penetration textures spreading inward in the host olivine suggesting a progressive dissolution of olivine prior to precipitation of alteration products.

The olivine-hosted alteration veins are very thin ($< 10$ $\mu$m) and their alteration products poorly crystallized (Fig. 5.28), such that the alteration products are often dissolved away during sample preparation. The study of rough olivine grains has revealed the presence of nano-meter scale well crystallized grains within the olivine phenocryst-hosted alteration veins that might not survive sample preparation (Fig. 5.29). Because of their very small size, both chemical and mineralogical

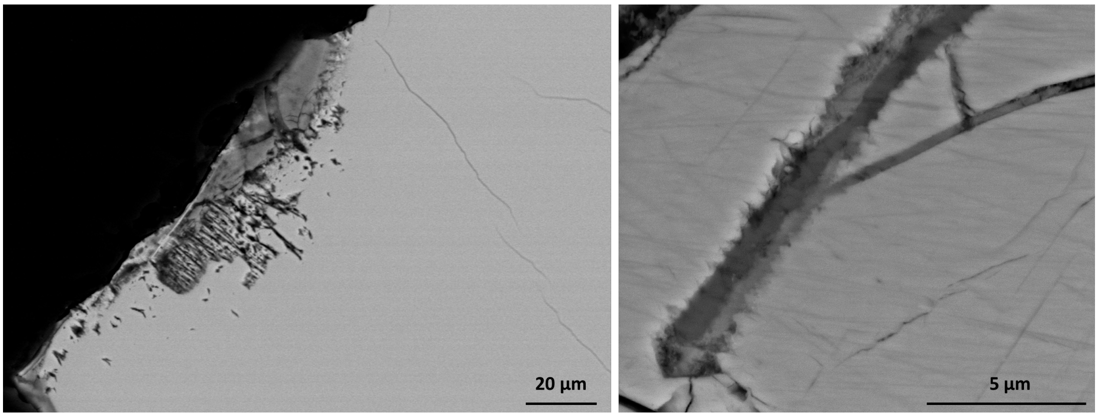

*Fig. 5.28: BSE images of olivine dissolution textures (left) along a grain boundary and alteration vein (right) in Nakhla. Outside of these localized areas, olivine is unaltered.*

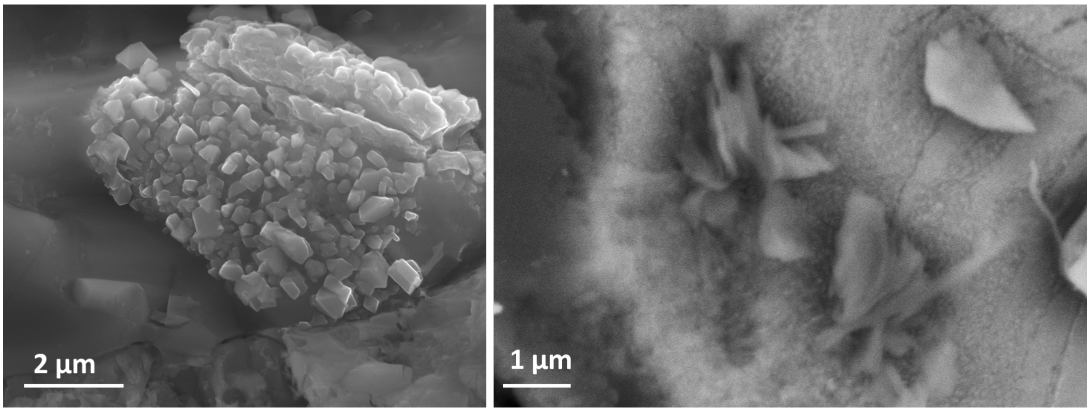

*Fig. 5.29: BSE images of nm-scale secondary minerals filling olivine veins from a non-polished sample of Nakhla.*

identification are impossible to obtain using the SEM as the volume of interaction is larger than the pictures (5 $\mu$m). However, analysis of the alteration products using EDS spectra (qualitative analysis) have not revealed the presence of P or S but a very small amount of C and Cl. The absence of sample preparation rules out a possible Cl contamination in the laboratory, while the absence of carbon coating prior to analysis suggests the presence of carbonate minerals. Similar crystal grains of Ca-carbonate with smooth and degraded texture have been found in Chassigny (Wentworth et al., 2005). Chlorine is contained within the fibrous product. Surprisingly, the alteration products in the image a is very similar in crystal shape, size, association and petrological setting but not in chemical composition (?) to the Fe-sulphate filling voids in Y 000749 (Fig. 5.22).

### 5.5.6 Lafayette

Lafayette is the most altered nakhlite found to date. It contains alteration products replacing its abundant olivine grains but also the feldspar forming the rock matrix

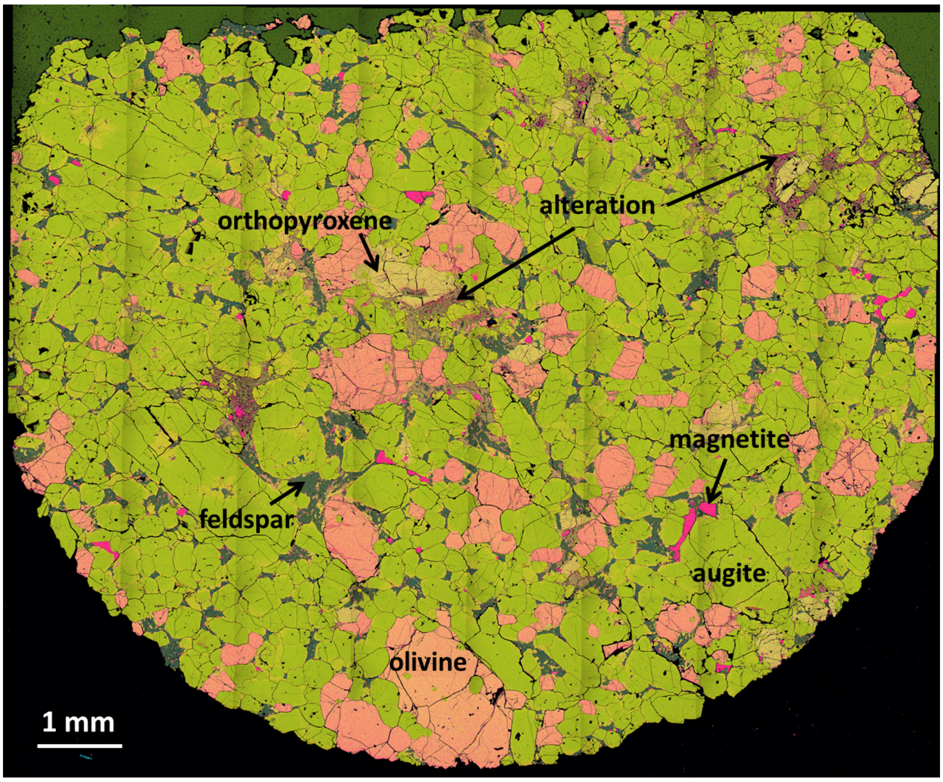

*Fig. 5.30: EDX montage map of a thin section of lafayette with localized alteration "rims" surrounding augite, olivine and orthopyroxene grains.*

(Fig. 5.30). All olivine grains bear alteration products but the rock matrix is only locally (although completely) replaced by secondary minerals. Thin films of water were probably largely present throughout the rock but uneven larger water influx probably moved through the rocks, dissolving the rock matrix and precipitating abundant clay minerals along their path (Fig. 5.31).

The numerous olivine grains in Lafayette contain abundant disconnected alteration veins displaying relatively large sawtooth margins similar in size and shape to those in olivine from the NWA 817 meteorite (Fig. 5.32). The veins are commonly thicker along the grain boundaries and do not radiate or intrude into surrounding materials. Olivine veins in Lafayette have the most complex mineralogy and chemistry of all nakhlites, especially the presence of abundant carbonates and well crystallized fibrous silicate (Fig. 5.33). Olivine veins are zoned with a very fine layer of the apparently structureless Si-rich product central to the veins. But unlike most nakhlites, the Si-rich product in Lafayette also contains relatively abundant Mg. The Si-rich product is surrounded by a discontinuous fine layer of hydrous Fe-oxide goethite (measured by Raman spectroscopy) with no obvious crystal faces at the $\mu$m-scale, and fibrous silicate whose crystals grew perpendicular to the goethite-Si-rich products (transversal to the veins). The fibrous silicate contains Si, Fe, Mg, K and Al. It is the most texturally and chemically mature alteration product present in olivine in all the nakhlite meteorites. The texture and chemical composition of the silicate are consistent with minerals from the phyllosilicate family. The phyllosilicate minerals have been identified as inter-growths of smectite and illite

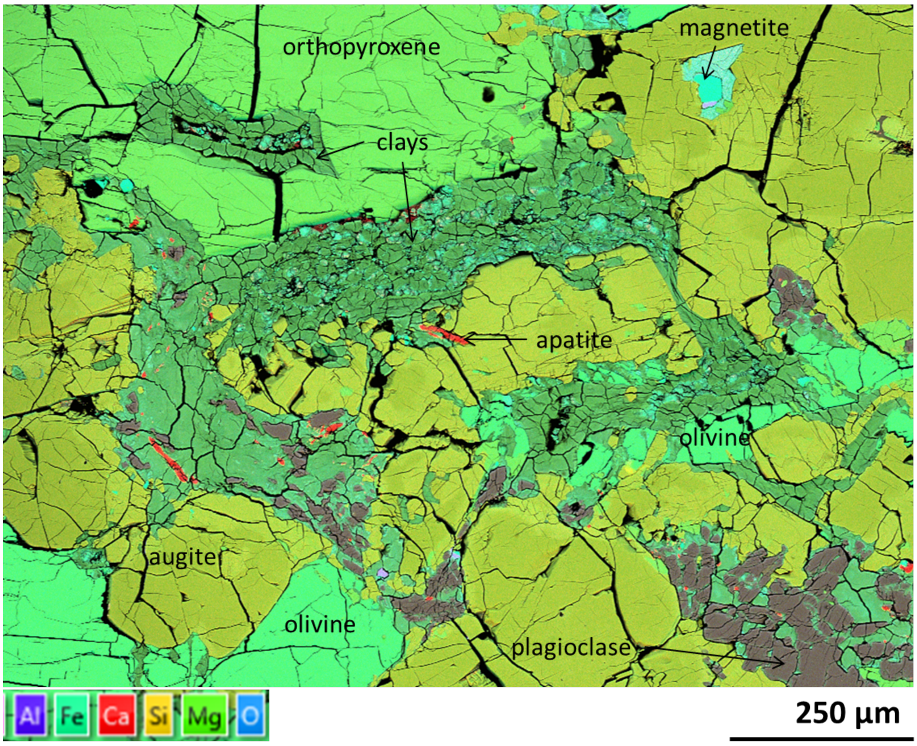

*Fig. 5.31: EDX map of a heavily altered area in lafayette with abundant clays replacing plagioclase, olivine, augite and orthopyroxene.*

(Bridges and Grady, 2001). The phyllosilicate replacing the rock matrix have identical chemical composition including the alkali and alkali earth elements and element abundances. The fluids were relatively chemically homogeneous. The secondary silicates contain a certain quantity of S but no Cl has been detected associated with secondary minerals in our sample.

The vein margin in Lafayette are commonly composed of carbonate whose individual crystals are not obvious at the $\mu$m scale. The carbonates are largely unevenly distributed between olivine grains but tend to concentrate in the largest veins. The veins comprising carbonates do not display the common sawtooth margin of non-carbonate-bearing veins. The different vein textures suggest different water-mineral interaction processes and/or conditions. The carbonates are rich in Ca and Fe, and locally enriched in Mn but contain only traces of Mg. The carbonates do not display obvious zoning in metallic components through the vein thickness which could reflect a change or evolution of the fluid conditions. Along the vein margins, the carbonates contain rosettes of fibrous phyllosilicate (Fig. 5.33). The rosettes may represent traces of thin veins that developed perpendicular to that on the images. Both phyllosilicate and carbonates are never inter-mixed but physically well separated.

### *5.5.7 NWA 998*

NWA 998 appears to be the least aqueously altered nakhlite meteorite. Only some olivine grains display rare and thin alteration veins composed of Si-rich material

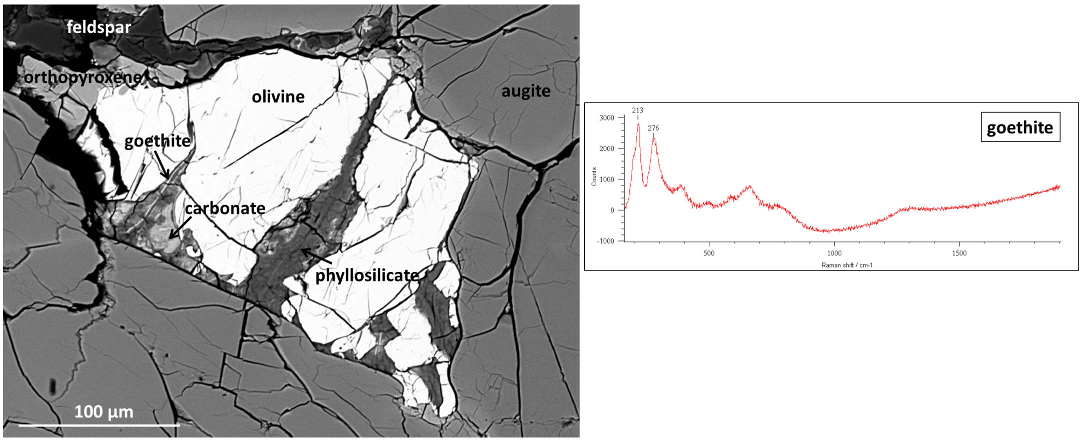

Fig. 5.32: *BSE image of the complex alteration products within olivine veins from Lafayette. Goethite has been identified using Raman Spectroscopy.*

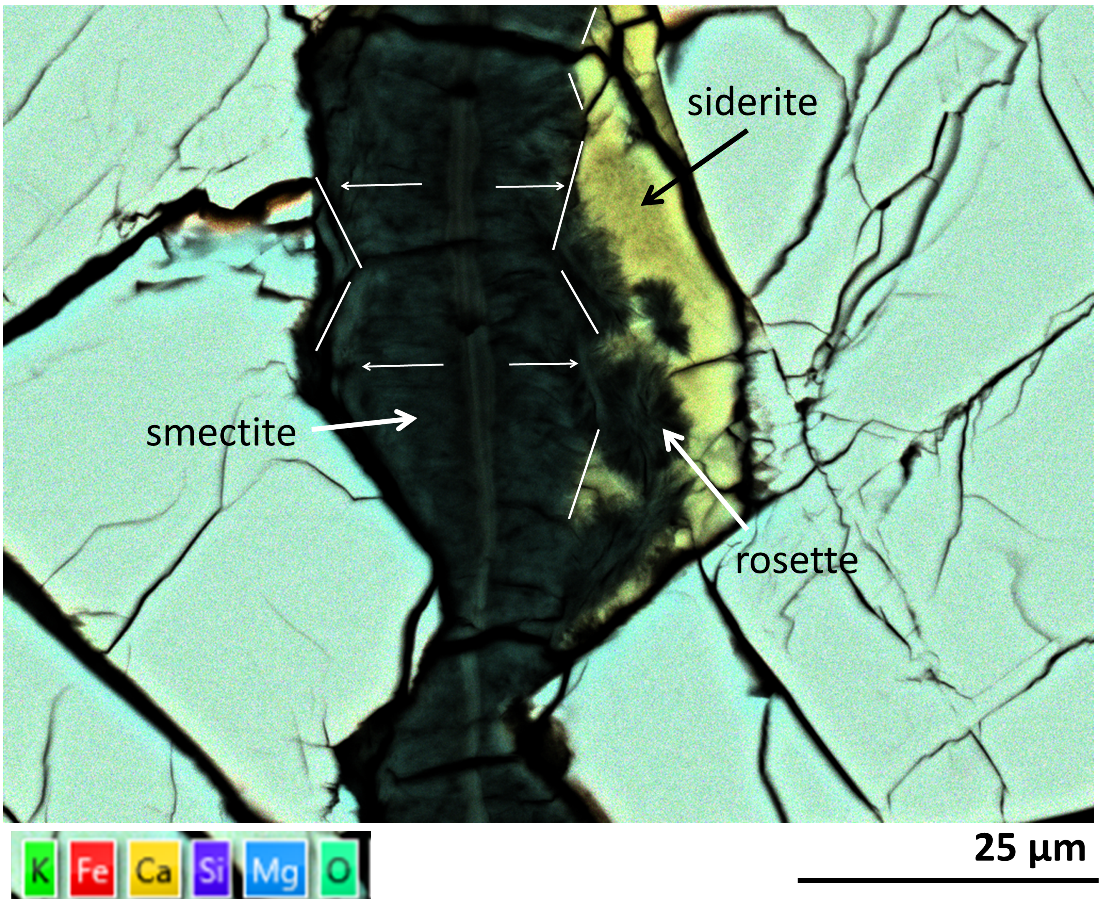

Fig. 5.33: *EDX map of well-organised smectite spreading perpendicular to the vein walls or forming rosette and siderite in Lafayette. To be noted: the preservation of the saw tooth shape and symmetry of the "double layer" of phyllosilicate.*

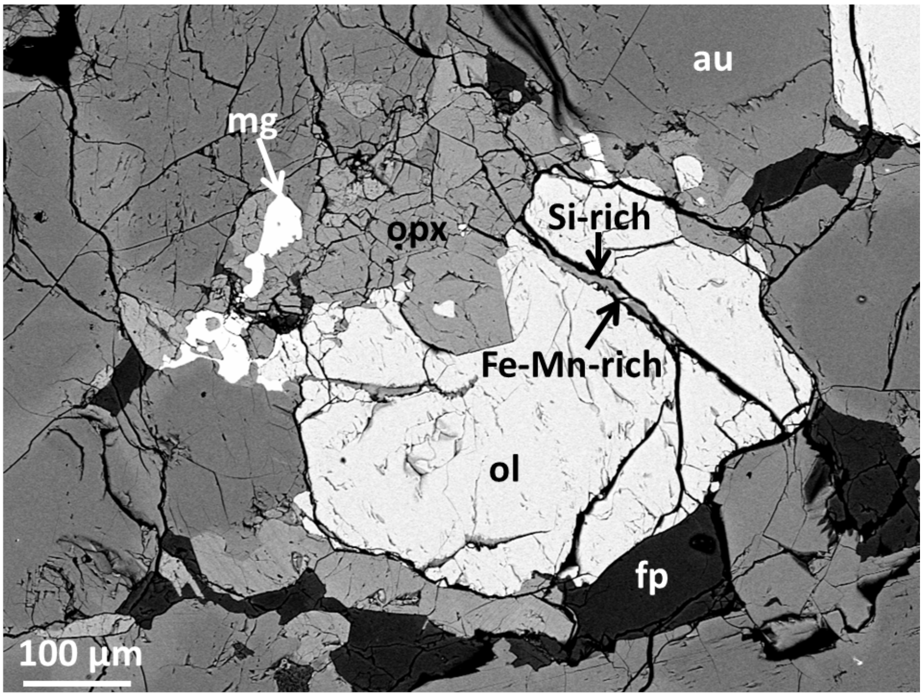

*Fig. 5.34: BSE image of an olivine phenocryst from NWA 998. Olivine contains thin veins filled with a texture-less Si-rich alteration product and rare "patchy" Fe-Mn product along vein margins and transversal fractures cross-cutting the Si-rich product.*

with no obvious crystal faces at the $\mu$m-scale (Fig. 5.34). The alteration product is largely depleted in both Fe and Mg relative to olivine but contains minor Ca relatively homogeneously distributed. The alteration veins also contain another very rare alteration product only found along the vein margins and rare transversal fractures (desiccation cracks?) cross-cutting the Si-rich alteration product suggesting that it crystallized last, possibly from a different aqueous event. It is too small (at the nano-meter scale) to be chemically characterised but it is generally enriched in Fe and Mn and more rarely Mg, contains some Ca and depleted in Si. Its nature is difficult to identify. It may be a carbonate as in Lafayette or a Si-poor silicate mineral as in NWA 817.

Most of olivine grains have been partially replaced by orthopyroxene during late magmatic processes. The alteration veins do not intrude the latter. The orthopyroxenes have remained unaffected by aqueous fluids. Apart from olivine replacements by orthopyroxene (magmatic) and iddingsite-like alteration products (secondary), olivine is unaltered. Like NWA 817, NWA 998 contains a network of fractures that cross-cut all primary materials. The fractures are filled with calcite, a typical contaminant of terrestrial fluids in hot desert. No other secondary minerals have been detected within this meteorite.

## 5.6 Chemistry of the nakhlites mineralising brines

Characterization of the mineralogy and chemistry of indigenous secondary minerals in the nakhlite meteorites is very important to better understanding the geochemistry of the recent, low temperature superficial aqueous environments of Mars. Unfortunately, at the $\mu$m-scale, the secondary mineral assemblage displays very rarely obvious individual crystals and is finely intermixed between clay minerals and salts, which largely prevents any detailed crystalline structure and structural formula for the individual clay minerals to be clearly established. However, insights into the chemistry of the mineralizing crustal fluids can still be gained through the general chemistry and zonation of the solidified end products. The composition of crustal fluids at their climax of saturation prior to evaporative concentration is the critical factor that defines the nature and chemistry of the minerals that precipitate and the chemical evolution of the residual brines (Hardie and Eugster, 1970). Crustal ionic waters are typical mineralizing fluids in closed-basin. The sources of their solutes (metallic and ionic components) are often uncertain. However, the formation of saline deposits from crustal brines undoubtedly requires intense evaporative processes which presuppose semi-arid to arid climate where water inflow is much lower than water evaporation (Hardie and Eugster, 1970). Evaporitic basins are usually restricted and ephemeral. At the contact of even tiny amount of water the highly soluble salts are unavoidably dissolved away and transported elsewhere (Velbel, 2012).

Clay minerals are also good indicator of environmental conditions (Eberl, 1984). The type of clay minerals that form depends on the abundance of water (intrinsically related to the climate) and soil drainage. Clays composed of relatively insoluble elements such as (Al-rich) gibbsite form in environments where water flows profusely (Eberl, 1984). The soil experiences severe leaching conditions while only sparingly soluble elements such as Al can remain. Clays composed of soluble elements such as the ferro-magnesian clay minerals from the smectite family form commonly in environments where cations can accumulate, which reflects a dry climate and poor soil drainage (Eberl, 1984). The association of both evaporite and smectite are proxies for dry climate conditions and closed-basins where brines accumulate prior to evaporative crystallization (Eberl, 1984).

### 5.6.1 Fine phyllosilicate

The composition of the volumetric dominant alteration phase occurring in olivine phenocrysts in all nakhlites is largely dominated by Si, Mg and Fe, a chemical composition that resembles the smectite family. The low and constant analytical totals (commonly 80-85 wt%) suggest the presence of hydrous molecules that cannot be detected using electron microscopy. High-Resolution TEM (HRTEM) bright field images from NWA 817 reveal the presence of very poorly-crystallized and ill-organized clay mineraloids with lattice fringes of 0.9 nm (Fig. 5.35). These *d*-spacing are typical of clay minerals from the smectite group, 0.9 nm corresponding to the fully collapsed state of smectite. High precision textural investigation of the Si-Fe rich product of the other nakhlites has not been undertaken in this study however undulating lattice fringes have previously been detected in the Si-Fe rich product of Nakhla (Gooding et al., 1991). Fine clay mineraloids from the smectite

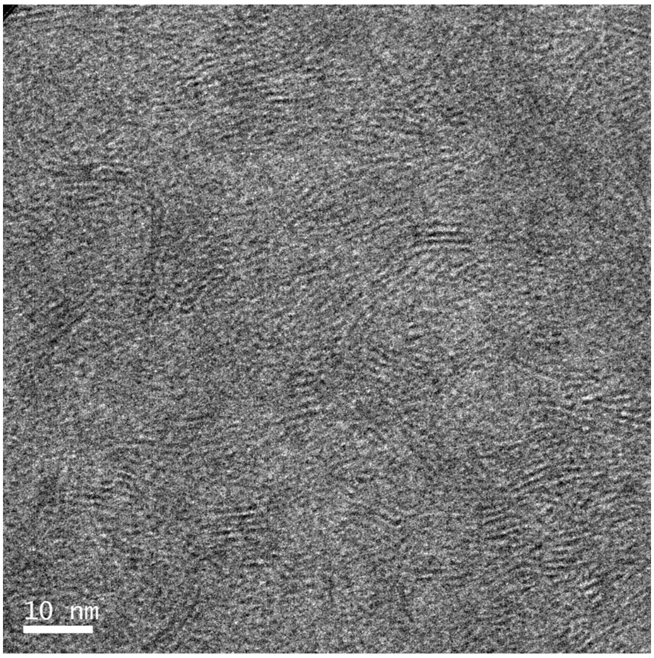

*Fig. 5.35: High resolution TEM bright field image of poorly crystallized and ill organized smectite from NWA 817. Bright field images are density contrast images, the lightest grey zones represent areas of low density.*

family may have randomly formed in the material precursor of smectite (i.e. the Si-rich product) in the different nakhlites.

The presence of trace elements (including K, Na, Ca, and Al) in the material precursor of smectite probably reflects their low concentration in the Martian solutions and the apparent general resistivity of the primary materials (other than olivine) to aqueous attack, probably because of the short life time and scarcity of the aqueous fluids. The low availability of K, Na, Ca, and Al was a limiting factor in the formation of chemically more evolved clay minerals like montmorillonite or vermiculite and the entrapment of cations in the inter-layer spaces as is common in smectite grains. The lack of obvious inter-elemental correlations suggests also that the material precursor of smectite is a single phase with compositional heterogeneity, a hypothesis further confirmed by high-resolution investigations of the material precursor of smectite using the TEM. The smectite in the nakhlite mesostasis contain some alkali and alkali earth elements but apparently not sufficiently either to have precipitated chemically (and texturally) mature clay minerals, except in Y 000749 and Y 000593 although in the later they may be of terrestrial origin (see section 5.8). The clays in the mesostasis are proportionally depleted in total metallic components relative to those precipitated in olivine phenocrysts.

Traces of halogens including S (except in NWA 998) and more rarely Cl (only in Nakhla) have been detected within the fine smectite or material precursor of smectite. None of the high-resolution bright field images of the smectite have revealed the presence of separate salt crystal grains (or even oxide grains) intermixed with the fine clays which suggests that the ionic components are somewhat related to the smectite mineraloids. Saline species may have been trapped in the inter-layer spaces of the clay mineral or may reflect chemisorption processes (solutes in natural water that are taken up by solids at their contact), both mechanisms could have been promoted by the severe evaporative conditions. Chlorine has only been detected in smectite from Nakhla during EDX mapping using AZTEC software although its presence has not been confirmed by spot analyses using the INCA software. Unfortunately, we do not have a Cl standard for quantitative analyses calibration, which may explain the failure to detect Cl despite its selection in the list of element analysed. Under the conditions of analyses, the theoretical X-ray peaks of Cl maybe did not match those measured or Cl may be very heterogeneously distributed and have not been "spotted". Sulphur is a very common trace element in smectite from all nakhlites. Its concentration seems to be roughly homogeneous within a nakhlite but varies slightly between the meteorites. Chlorine and S are not present within the smectite in the mesostasis. Both halogens are highly soluble. The crustal brines probably circulated more freely in the rocks' matrix than in the olivine open spaces leading to its physical removal in the rock matrix. Phosphorous has not been detected within the poorly-crystallized smectite from any nakhlite.

### 5.6.2 Salts-phyllosilicate admixture

The poorly crystallized smectite is commonly surrounded by a mixture of alteration minerals whose nature is difficult to identify. They occur with parsimony mainly in olivine veins. They are also significantly present in the mesostasis of the Yamato meteorites and Nakhla although in the latter meteorites they are most probably terrestrial (see section 5.8). Their chemistry as a whole is complex. They are depleted in Si relative to the previous fine smectite but enriched in metallic cations (Fe and Mn). They contain some alkali (K and Na) and halogens (Cl, S and rare P in some nakhlites, an element absent within the fine smectite). In NWA 817, the alteration assemblage is in general porous and contains well developed fibres poorly connected to each other. The presence of Si and fibres suggest that silicate minerals are components of the alteration assemblages. The fibres have a *d*-spacing of 1.1 nm which indicates the presence of minerals from the smectite family (Fig. 5.36). The "well-formed" clays and significant presence of metallic cations suggest that smectite crystallized under more favoured fluid conditions despite their spatially and volumetric restricted precipitation. A balance between silica and metallic components may have been reached. The *d*-spacing of the "coarse" smectite suggest the presence of inter-layer components, either hydrous molecules or cations. No salt components have been detected in the coarse silicate in NWA 817 (Fig. 5.36). However, because of the porosity and poor bounding of the different mineral phases and their general ill organized texture in NWA 817, the saline minerals may have been largely lost during sample preparation while the clays are largely amorphized during FIB thinning

In Y 000749, Y 000593 and Nakhla, the marginal products contains abundant salt deposits (mostly Fe-sulphate and/or carbonate) and rare Fe-oxides and clay minerals, Nakhla containing traces of halite too. MIL 03346 also contains scarce S but no salt deposits (except terrestrial, see section 5.8) have been found in our samples. The presence of ionic components within the mineral assemblages is not restricted to salt deposits but is inter-mixed within rare clays. The relationships between the secondary silicates and salt crystals are difficult to determine. They

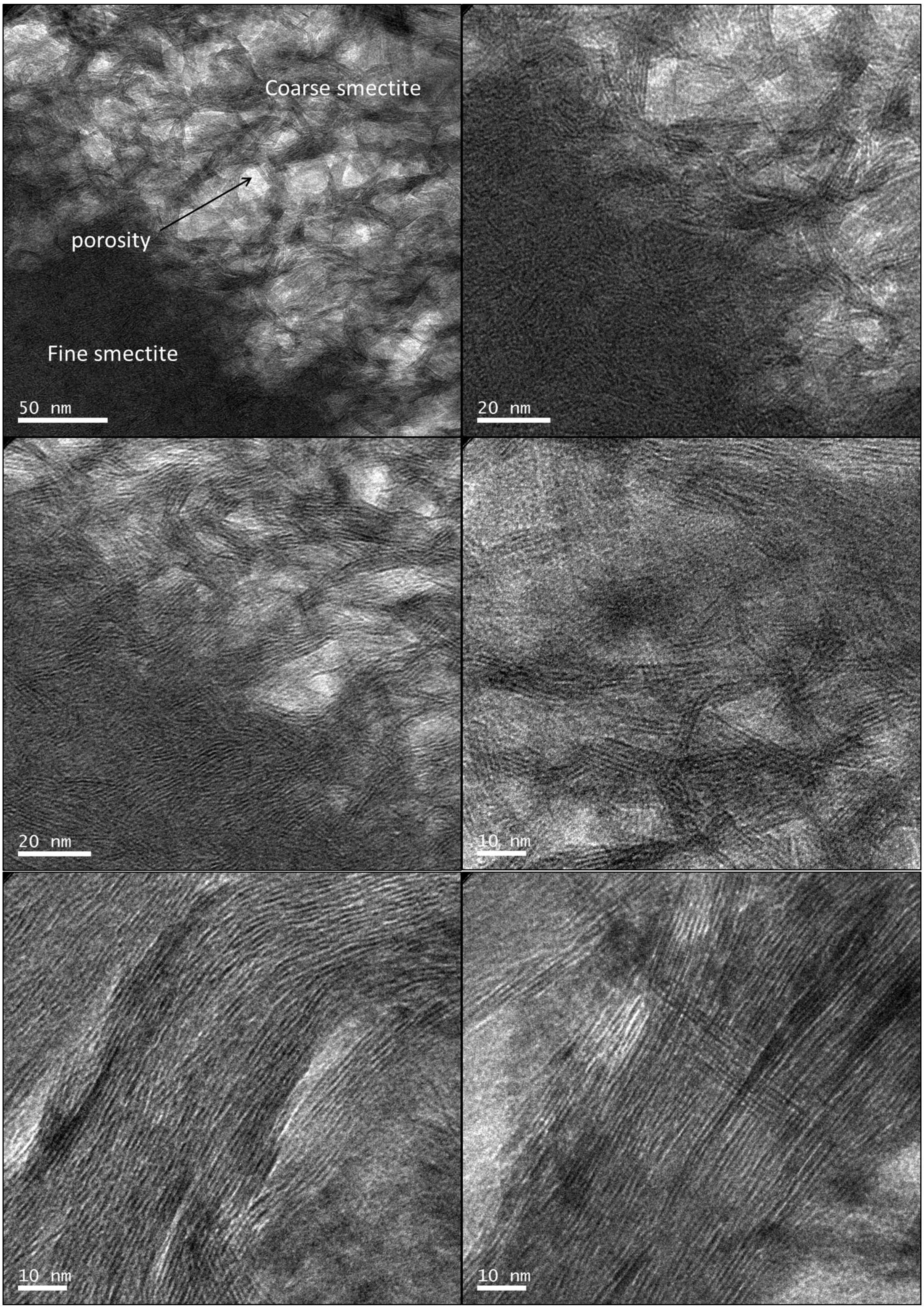

*Fig. 5.36: High resolution TEM bright field images of "coarse" smectite from NWA 817 at different magnification. The coarse smectite spread between olivine vein walls (not shown on the image) and the fine poorly crystallized smectite making the olivine vein center.*

may have co-precipitated or may represent two distinct fluid inflows, the salt crystals crystallizing last within the natural porosity of the clays. It is impossible to estimate how much salts were initially present with the clays. Their respective abundances and distribution in the prepared samples can only represent a lower limit and possibly a biased distribution. In our samples, the salt component represents less than 1 wt% of the composition of the clays but their ionic composition seems to vary locally within a single nakhlite, one or another component locally dominating the total halogen content. There is no obvious chemical or spatial relationship or apparent affinity between the different ionic components. However, as the separate ion concentrations are below detection limits their respective abundances may not be completely trustful. The composition of the mineralizing fluids that percolated throughout the separate nakhlite was probably heterogeneous and have precipitated a variety of minerals distinct in each nakhlites but chemically contrasting from the fluids that precipitated the widely-distributed and volumetrically dominant poorly crystallized material precursor of smectite.

### 5.6.3 The unique alteration products of Lafayette

Lafayette is a unique nakhlite as it contains (1) abundant carbonates and (2) very well crystallized and organized and chemically matures phyllosilicate minerals, a mixture of smectite and illite identified by Bridges and Grady (2001). The greatest abundance of alteration products in Lafayette suggests that, relative to the other nakhlites, significant amount of aqueous fluids invaded the rock while the localized massive plagioclase feldspar replacement suggests that these fluids existed over a sufficient length of time to react with mineral phases with different aqueous susceptibility (Fig. 5.31). However, a fluid-rock reactions at greater temperatures can also be considered for the greater mineral reactions. The smectite/illite minerals (identified by Bridges and Grady (2001)) contain some alkali and alkali earth elements and a few wt% of Ca but no obvious ionic compounds. Only rare S has been detected in some spot analyses. The fluids that precipitated the clay minerals were relatively chemically homogeneous whereas the apparent lack of S may reflect a greater fluid flow than in the other nakhlites to transport chemical species in and out of the rock.

## 5.7 Terrestrial contaminations

Even though a Martian origin of some of the aqueous alteration products has been demonstrated, it is very important to bear in mind that the meteorites have also unavoidably reacted to an unknown extent with terrestrial fluids during their long residence on Earth' surface (over millennial time-scales!) prior to recovery. Meteorites are also known to quickly react with terrestrial moisture and oxidants even in laboratory or Museum storage (Velbel, 2014). The terrestrial contamination can have either resulted in the deposition of new alteration products including along post-landing fractures or in the natural rock porosity, or in chemical exchanges between the terrestrial fluids and naturally porous Martian secondary minerals. A further difficulty is the great similarity between Martian and terrestrial aqueous alteration textures and products (Wentworth et al., 2005; Hallis, 2013; Stopar et al.,

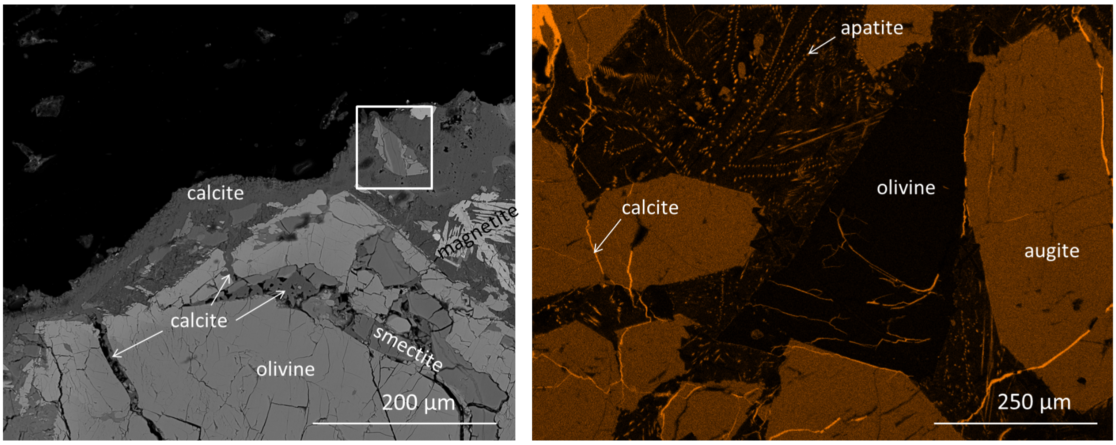

*Fig. 5.37: BSE image (left) and Ca $K_\alpha$ EDX map (right) of terrestrial calcite in NWA 817. Calcite contains fragments of olivine with its alteration products (white square). Textural relationships between calcite and olivine-bounded veins suggest that the veins are of Martian origin. Calcite fills post-landed fractures that cross-cut the meteorite.*

2013). Hence, establishing a Martian *vs.* terrestrial origin of each specific alteration product is not straightforward and requires strong petrographic evidence for each meteorite (Gooding et al., 1991). However, a Martian origin of the olivine-bounded clay minerals (the structureless Si-rich product precursor of smectite) in most nakhlites have already been largely demonstrated through micro-texture, petrographic relationships and isotopic composition and will not be further developed here (Bunch and Reid, 1975; Gooding et al., 1991; Treiman et al., 1993).

The most obvious terrestrial contaminant in nakhlites discovered in the Sahara desert is calcite (Fig. 5.37), a typical terrestrial contaminant of meteorites found in hot desert (Gillet et al., 2002). Calcite has been found forming a layer on one of the external surfaces of NWA 817 (Fig. 5.37, left) but also filling a network of nm- to $\mu$m-thick brittle (post-landing) fractures that cross-cut all igneous materials (Fig. 5.37, right). The thick layer of calcite coating one of the meteorite surface contains fragments of igneous material including olivine with its alteration products. Textural relationships between olivine, the texturally and chemically zoned smectite minerals and calcite suggest that smectite minerals (including both fine and coarse smectite) formed prior to olivine fragmentation and thus are most probably pre-terrestrial.

In NWA 817, terrestrial calcite has been found in contact with the Martian alteration veins raising questions about the interactions between terrestrial fluids and the Martian clays. The alkaline terrestrial fluids have partially dissolved away the coarse smectite (but not the fine smectite) and precipitated calcite with locally Mn-rich carbonates in the porosity created by the dissolution of the Martian clays but also in the intrinsic porosity associated with the poorly organized texture of the clays (Fig. 5.38). The spatial relationship between C, Ca and Mn suggests that both Ca and Mn are terrestrial contaminants. Chemical analyses of the Martian smectite at the vicinity of calcite have not revealed the presence of Mn or Ca, an element that easily enter in the smectite interlayer spaces because of its characteristic

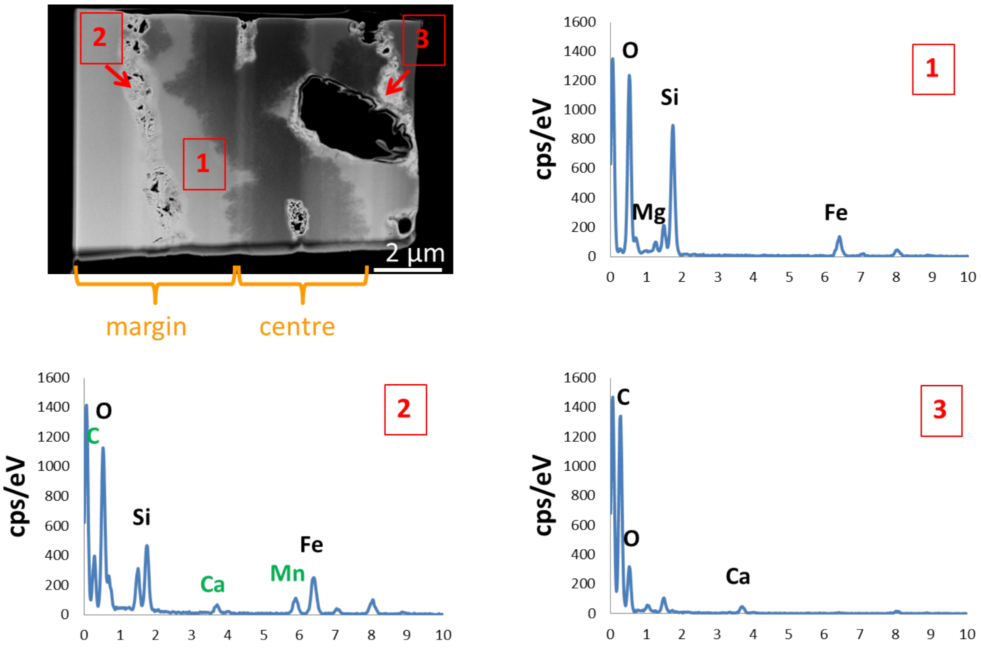

*Fig. 5.38: BSE/STEM image of a FIB section of an olivine-bounded vein in NWA 817. EDS spot analyses reveal the presence of (Mn-bearing) calcite filling porosity created by the dissolution of the Martian clay minerals by terrestrial fluids. Ca and Mn are most probably terrestrial contaminants.*

swollen properties. This shows that the Martian smectite have probably not significantly reacted and exchanged with terrestrial fluids, most probably because of their poor crystallinity and fully collapsed state which is consistent with the Martian D/H ratio measured for the alteration products in the rock by Gillet et al. (2002). The terrestrial fluids probably only flowed through the porosity between the coarse smectite grains. There is no textural or chemical evidence indicating that terrestrial fluids moved through the fine smectite, further suggesting a Martian origin for the highly soluble S adsorbed onto the fine smectite.

Other products that formed through interactions with terrestrial fluids are commonly found in landing impact-generated brecciated areas (Fig. 5.39). The brecciated areas are rare and never exceed a few tens of $\mu$m long. They are composed of fragments of augite, olivine and plagioclase abutting each other. Along grain boundaries, clay minerals (recognized by their chemistry and fibrous texture) occur. Brecciated areas with clay minerals are present in nakhlites discovered in both hot and cold deserts. They have very similar chemical composition than the Martian smectite. They contain mostly Si and Fe with rare Mg and Al, a chemical composition similar to the poorly crystallized clay minerals from the smectite family. However, contrary to Martian smectite, they contain significant amounts of Mn and Ca in the nakhlites found in hot desert. Clay minerals from the brecciated areas in the Yamato meteorites are inter-mixed with a product that contains S and less P and Cl. Pyrrhotite grains in the Yamato mesostasis are heavily altered and dissolved away. Sulfide alteration by terrestrial fluids is common in meteorites (Gillet et al., 2002) and may be the origin of the S found in the nakhlite terrestrial

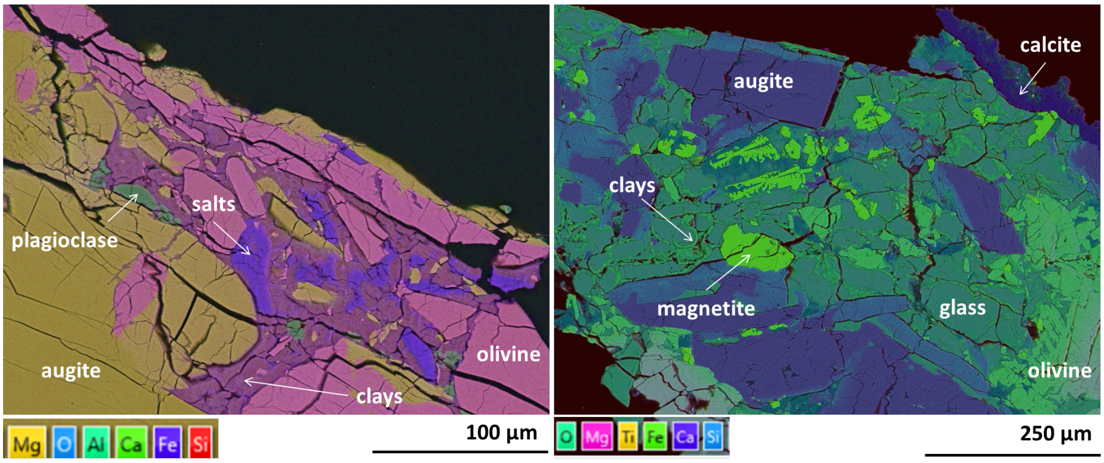

*Fig. 5.39: EDS map of impact-generated brecciated areas with their terrestrial alteration products, a mixture of clay minerals and P-S-Cl-rich salts in Y 000593 (left) and Fe-Mn-rich clay minerals in NWA 817 (right).*

weathering products.

Terrestrial clay minerals in meteorites discovered in Antarctica and in the Sahara desert are chemically distinct, despite the fact that they both seem to contain terrestrial Mn. While the terrestrial weathering products in nakhlites from Antarctica contain abundant ionic compounds, those found in Morocco contain calcite. The presence of ionic compounds in the terrestrial alteration product in the Yamato meteorites raises the question about the origin of the salt minerals found in association with the coarse smectite. A close look at the olivine-bounded veins in the Yamato meteorites at the vicinity of brecciated areas has revealed the presence of a distinct alteration product with cross-cutting and overlapping relationships with the fine and coarse smectite (Fig. 5.40). The overlapping alteration product has a similar smooth texture and chemistry (it contains also S and rare Cl and P) than that in the brecciated areas. It may be the same terrestrial alteration product that crystallized last in the brecciated areas. Circulation of terrestrial aqueous fluids in the natural porosity of secondary Martian minerals has been unavoidable and the consequences on the Martian alteration assemblages are impossible to estimate. Terrestrial fluids may have brought terrestrial ionic compounds into the Martian products especially if the terrestrial solutions were heavily charged or removed Martian ionic components if the solutions were relatively abundant and/or under-saturated. The presence of salt crystals of Martian origin in the nakhlites is relatively well documented and certain but the current secondary Martian ionic budget (composition, abundance and distribution) in the nakhlite meteorites is probably not representative any more of their original composition.

To summarize, terrestrial contaminations in the meteorites discovered in the hot Saharan desert have led to the deposition of calcite (locally enriched in Mn), whereas terrestrial depositions in the meteorites discovered in the cold desert of Antarctica are composed of S-P-Cl-rich salts mostly along grain boundaries in the mesostasis and fractures in olivine grains. The last secondary minerals of terrestrial origin in the nakhlites whatever their site of discovery are clay minerals in impact-generated

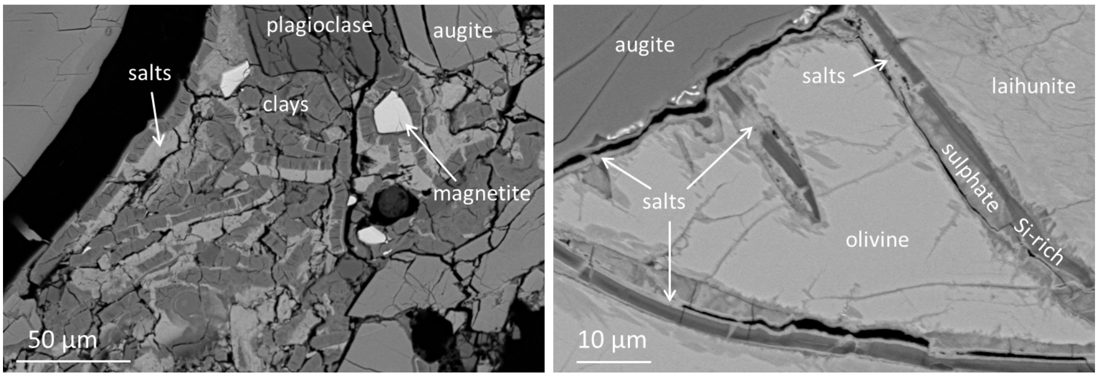

*Fig. 5.40: BSE images of terrestrial weathering products rich in ionic compounds (light grey shown by the white arrows) in the mesostasis (left) and olivine-bounded veins (right) in Y 000593. The ion-rich products in the mesostasis form bands along and intruding into the sheet of clay minerals. In the olivine veins, the ion-rich products follow fractures and cross-cut the Martian alteration assemblage.*

brecciated areas. The clay minerals are recognized by their crystal structure and chemistry. Alteration products from terrestrial and Martian fluids are very similar as previously recognized by Wentworth et al. (2005), Hallis (2013) and Stopar et al. (2013). However, discrimination between terrestrial *vs.* Martian can still be determined through petrographic relationships. However, it is important to retain in mind that chemical exchanges between the terrestrial fluids and solidified Martian alteration products are more than probable and unfortunately difficult to identify, if not impossible.

## 5.8 Insights into the dynamic, structure and geological history of the Nakhlites aquifer

The presence of corrosive texture on olivine surfaces at the contact with alteration products (Fig. 5.8 and 5.9) provides evidence for subtle weathering-like processes on Mars (Velbel, 2009). Chemical weathering along crystal surfaces and intra-crystal lattice defects has caused progressive dissolution of olivine suggesting that olivine has been altered prior to and/or during secondary deposition. If we think that aqueous fluid initially access olivine grains flowing through crystal “ruptures” and subgrain boundaries and further permeated their way toward the interior of the crystal through progressive dissolution and precipitation processes, then the first-formed product should lies central to the vein while lateral zonation should represent an evolution of the aqueous alteration over time. Understanding the controlling mechanisms of olivine-fluid interactions and the interplay between olivine dissolution and secondary deposition is important to correctly interpret environmental conditions and changes over time (Velbel, 2009, 2012; Hellmann et al., 2012).

Weathering processes consist in a sequence of steps that operates in a specific order (Putnis, 2009; Velbel, 2012). To begin, aqueous solutions must be put into contact with mineral surfaces. Because of the natural acidity of water, mineral dissolution takes place. For aqueous alteration to proceed aqueous reactants must continue to access reaction interfaces which implies that, once dissolved, the solutes must be removed from the reaction fronts (Putnis and Putnis, 2007; Putnis, 2009). The capacity of a fluid to transport (and spatially fractionate according to their specific aqueous mobility) chemical species from the reactive fronts is crucial as it determines the sites of secondary mineralization and the nature and chemistry of the secondary minerals that can potentially form (Velbel, 2012). The chemical composition of the secondary minerals reflects the chemistry of the fluid and host rock, the reactivity of the rock-forming mineral and the specific element mobility in the water-rock system (Stroncik and Schmincke, 2002; Tosca et al., 2004; Tosca and McLennan, 2006; Putnis, 2009). However, if secondary minerals remain in contact with the aqueous fluids for a certain time after precipitation, they are highly likely to continue to interact with the fluids and chemically and texturally mature (Velbel, 2012; Hellmann et al., 2012). In this context, it is very important to investigate in detail the physical properties, texture, mineralogical and chemical composition and zonation of alteration products together with the mechanisms and kinetics of the overall aqueous alteration processes (Putnis, 2009).

### *5.8.1 Early mineral-water reactions and deposition of material precursor of smectite-group minerals*

Olivine phenocrysts display evidence for weathering-like type of alteration along surfaces that were once into contact with aqueous fluids (Fig. 5.7, 5.8 and 5.9). They include corrosive textures (etch pits and denticulations) and secondary precipitates that developed along grain surfaces (Fig. 5.8) and planar lattice defects (Fig. 5.9). The geometrical shape (serrated margins) of the intra-crystalline veins provides evidences for a formation of the veins through progressive dissolution with a strong crystallographic control on the way olivine has altered (Velbel, 2009). The corrosive textures reflect the non-uniformity of aqueous attack on olivine surfaces, i.e. incongruent dissolution, that commonly develop during the very early stage of aqueous alteration reactions (Velbel, 2009). The aqueous fluids were not saturated with respect to olivine composition while olivine dissolution was controlled by surface chemical reactions. The creation and preservation of tunnel-shaped microporosity at olivine reaction fronts (an early, transient feature of aqueous alteration) at the contact with the material precursor of smectite reflects the insufficient availability of fluid and a cessation of aqueous activity for congruently dissolve olivine. The development of corrosive textures perpendicular to the fluid-mineral interfaces suggests some kind of control by the chemical structure of olivine (Velbel, 2009).

The occurrence of alteration veins spreading through the fayalitic-rich zones of olivine and along the sharp the forsterite-fayalite boundary of olivine of NWA 817 without intruding into the forsterite component indicates the higher solubility of Fe relative to Mg in the Martian aqueous environment. The common presence of alteration veins along core-rim boundaries suggests that the veins developed along possible lattice misfits between the olivine Mg- and Fe-rich zones, possibly reflecting a sudden change in melt chemistry. Along the forsterite-rich side, olivine do not display evident corrosive textures suggesting that the Mg-rich core of olivine was less reactive to aqueous attack than the Fe-rich rim. The rate at which olivine has dissolved in the Martian aqueous environment and the thickness of the veins were probably controlled not only by the water-to-rock ratio and fluid life time but also by the chemical resistivity of the olivine (Mg-rich vs. Fe-rich) to alter in the presence of reactive fluids.

The development of denticulations and etch pits along fluid-mineral interfaces result from preferential loss of the most soluble element of olivine including Fe to the fluid phase and its mobilization by some sort of transport mechanism from the fluid-rock interfaces at least in the very early stages of aqueous alteration (Velbel, 2009). The continuous access of aqueous reactants to the "fresh" parts of olivine requires the creation of spaces in the olivine crystal structure and thus the dissolution of some species of olivine that must further leave the reaction fronts (Stroncik and Schmincke, 2002). The generation of interconnected porosity in minerals is an important process for fluid infiltration deep into the minerals (Putnis, 2009; Ruiz-Agudo et al., 2014). The probably very low permeability of the nakhlite rocks (as suggests the absence of apparent natural porosity/vesicles in the basaltic rocks and fractures) suggests a very slow motion of fluids along grain boundaries and their probable subsequent stagnation as aqueous activity decreases. Mass transfer probably occurred by diffusion driven by chemical gradient. The continuation of the leaching process allowed an enlargement of the denticulation through side-by-side coalescence to form etch pits that further grew through similar process (Fig. 5.7 and 5.9) and a progressive and complete (i.e. congruent) breakdown of the loose structure of olivine throughout the heavily altered rims.

The apparent passive release of silica from olivine by progressive coarsening of corrosive textures probably exceeded its diffusion rate leading to silica precipitation very near the reaction fronts and, under certain circumstances, its subsequent random polymerization into sheets together with a fixation of some metallic cations. The material precursor of smectite probably represents the unstable precipitates that commonly form at the very early stages of aqueous alteration and generally recrystallized through solid state reactions (Casey et al., 1993; Putnis, 2009). The apparent higher crystallinity of the olivine-hosted alteration products of NWA 817 relative to other nakhlites underlined by the presence of randomly organized micro-crystallites of smectite may represent a greater maturity of the precipitate, i.e. a more advanced stage in the evolutionary process of the alteration products (Stroncik and Schmincke, 2002). The formation of poorly developed grains of smectite and their fully collapsed state are indicative of a restricted amount of water to prevent a flushing out of the clays during the wetting event and severe evaporative conditions, while the ill-organized structure of the smectite suggests sluggish solid state reactions possibly due to the cold and arid conditions of Mars and a poor solute concentration of the brines. In the presence of micro-solutions, the dissolution rate of silica from olivine probably exceeded its diffusion rate leading to a random silica polymerization into sheets and a fixation of some metallic cations. A balance between silica and metallic cations in the clays has probably not been attained.

The deposition of material precursor of smectite has required a more advanced stage of aqueous alteration than olivine dissolution. The apparent absence of solute background (i.e. elements that cannot be explained by olivine dissolution) in the aqueous solutions resulted in the strong dependence of olivine to provide the chemical species required for secondary precipitation. Both secondary precipitation and precipitation growth rate are time-dependent (Putnis, 2009) and in the nakhlites were inevitably controlled by the rate of dissolution of olivine (i.e. fluid saturation), transport mechanism of the charged solutions and some kind of "evaporative" mechanism to concentrate the aqueous solutions. Secondary precipitation was apparently more sensitive to the degree of saturation than the fluid composition. The absence of precipitates in olivine micro-porosity at the contact with the material precursor of smectite suggests that fluid supersaturation was somewhat pore-size dependent. The fate of the nakhlites' crustal brines and precipitates were sealed at the onset of fluid evaporation, as from this stage the reactivity of the fluids has probably decreased drastically such as mass transfer from the solid to the fluid phase and subsequent transport of the charged solutions became insignificant, then nil (Hardie and Eugster, 1970). The evolutionary process of the metastable layers into more organised structure may have been prevented by the scarcity and transient nature of the Martian aqueous fluids. The general high mobility of Fe and immobility of Si in the Martian water-rock system suggest that an intensification of olivine leaching processes during aqueous alteration could have led to an almost complete loss of Fe and the deposition of opaline (hydrated amorphous) silica rather than a material precursor of clay minerals from the smectite family. Nano-particles of opaline silica has been detected in both Nakhla and on Mars by rover-based spectroscopy (Lee et al., 2015).

The material precursor of smectite in the mesostasis contains traces of alkali. Commonly, alkali and alkali earth elements concentrate in situ during weathering processes (Stroncik and Schmincke, 2002). In the nakhlites, alkali and alkali earth elements were probably provided locally by the adjacent materials forming the rock mesostasis. The absence of alkali and alkali earth elements in olivine-bounded veins indicate that the fluids were not present for a sufficiently long time to homogenise at the mm-scale either through physical transport or driven by chemical gradients. The micro-scale chemical variations in the precipitates provide evidences for the control exerted by fluid composition at the fluid-mineral boundary onto the nature and chemistry of the secondary precipitates in the nakhlites, as common during mineral-rock interactions with restricted amount of water (Stroncik and Schmincke, 2002).

### 5.8.2 Complex evolution of the nakhlites aquifer and crystallization of salt and clay mineral assemblage

The material precursor of clay minerals from the smectite family is commonly surrounded by a mixture of alteration minerals. They are easily identifiable on BSE images with their common low grey scale colour although the number and type of secondary mineral phases forming the marginal products vary between the nakhlites. The lower grey colour probably reflects the common lower Si content of the marginal products whatever the nakhlites. The marginal products only occur along some olivine vein margins and their occurrence does not always reach the tip of the veins (for example Fig. 5.22 and 5.32). The bands they formed are sometimes thicker at the periphery of the olivine grains and have partly overgrown onto the material precursor of smectite-group minerals. The aqueous fluids that have deposited them may not have circulated through the entire length of the veins which probably reflects the poor inter-connectivity of the tunnel-shaped denticulation through olivine reacted rims and the lack of porosity of the material precursor of clay minerals from the smectite family. The partial dissolution of the proto-smectite by the aqueous fluids that deposited the marginal products suggests a variation in the fluid conditions over time which is further underlined by the different mineralogy and chemistry of the secondary precipitates and texture of olivine at the reactive fronts that further vary between the nakhlites.

In Nakhla, Y 000593 and Y 000749, the chemical interactions between the "second" fluids and olivine have not led to the formation of etch pits or straight and parallel tunnel-shaped porosity but abundant undulating micro-channels that are further filled with secondary deposition (Fig. 5.23), mostly Fe-carbonates and less abundant Fe-sulphates (except in Y 000593). Neither carbonate nor sulphate minerals display obvious crystal faces at the micro-scale except some rare coarser crystals of Fe-sulphate that probably crystallized later from a distinct aqueous event. The olivine alteration fronts at the contact with the carbonates and sulphates do not display serrated margins but irregular advancing fronts without obvious porosity between olivine and secondary precipitation (Fig. 5.22, 5.23 and 5.32). The fluid-rock interactions at the origin of the carbonate/sulphate deposition were not controlled by olivine crystallography suggesting that the fluid properties (pH, temperature, etc.) might have been an important parameter in the way olivine has dissolved.

The presence of siderite in the undulating micro-channels (Fig. 5.22 and 5.23) suggests a process of fluid super-saturation not completely dependent on olivine dissolution to saturate the aqueous fluids and evaporative concentration of the saline brines to super-saturate the solutions and precipitate secondary minerals (unlike for the proto-smectite deposition). Carbonate ions in the fluid phase were probably not the limiting factor for carbonate mineral precipitation. The absence of obvious porosity at the sharp olivine-carbonate interfaces suggests a better coupling between dissolution and precipitation. Olivine carbonation process probably involved the release of Fe from olivine by dissolution and a reaction of the aqueous Fe with hydrous carbonate ions to form carbonate minerals such as

$$1/2\ \mathrm{Fe_2SiO_4} + \mathrm{CO_2} \rightarrow \mathrm{FeCO_3} + 1/2\ \mathrm{SiO_2}$$

The replacement of olivine by siderite was sensu stricto pseudomorphic, dissolution and precipitation were closely coupled in space and time. The rate-limiting step for olivine carbonation might have been the release of divalent cations from olivine. The pervasive presence of siderite in the micro-porosity of olivine might have slowed down the rate of olivine dissolution but did not inhibit it. Inhibition of mineral dissolution by a precipitating phase is known to be more effective when there is a close crystal structural match between the dissolving and precipitating phases (Putnis, 2009; Stockmann et al., 2011).

### *5.8.3 Mineralogical evidence for multiple fluid pulses*

The material precursor of smectite (i.e. Si-rich product) and evaporate-clay assemblage are in textural disequilibrium and have contrasting chemistry which suggests that they deposited during discrete fluid pulses from brines with different properties, the "pure" poorly crystallized smectite crystallizing from the first event (Fig. 5.41). The sharp disequilibrium cannot be explained by a progressive evolution of the same crustal brine. The best argument for multiple wetting events is probably the occurrence of the evaporate-clay assemblage filling desiccation cracks (?)

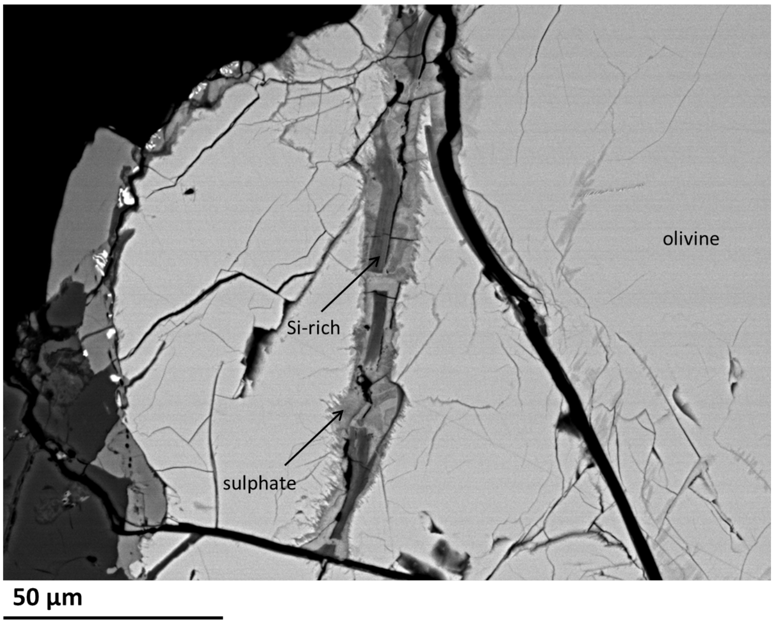

*Fig. 5.41: Secondary mineral assemblage in Y 000593 with the material precursor of smectite (Si-rich) surrounded by Fe-sulphate. Fe-sulphate overgrow and cross-cut the proto-smectite suggesting that it crystallized last probably from a separate aqueous pulse.*

partially cross-cutting the fine smectite. The different brine conditions between the multiple aqueous events are dictated by the variation in ionic components and abundances. A schematic diagram illustrating the different steps at the origin of the formation of alteration veins in olivine phenocryst (here Lafayette) over discrete aqueous events with different brine properties are provided on Fig. 5.42.

The formation of successive surface layers of material precursor of smectite on olivine grains, their common orientation parallel to the olivine surfaces and their sharp boundaries (Fig. 5.8) also suggest a deposition of material precursor of smectite over discreet aqueous events with probably a temporal de-coupling between olivine dissolution and secondary precipitation. The precipitation of silica and some Fe from the back of the reactive surfaces of olivine inwards, i.e. from the former grain boundaries inwards, reflects the general incapacity of the fluid to transport silica and a progressive decrease of the aqueous activity to maintain some Fe prior to or contemporaneously to silica deposition. The more altered surface of olivine underneath "cracks" in the surface layers reveals the protective nature of the secondary coating (Fig. 5.8). The coating of olivine grains by alteration products have slow down the transport of aqueous reactants to and from the olivine surfaces (probably due to the absence of porosity in the silica layers) and the rate of aqueous reactions but were inefficient to completely prevent further weathering processes of olivine. The formation of successive and distinct surface layers and their subsequent fracturing suggests possible episodic aqueous event(s) with a cessation of aqueous activity in between.

Variations in ionic composition absorbed onto the clay minerals between the first and second wetting event in NWA 817 suggest that the first-formed proto-

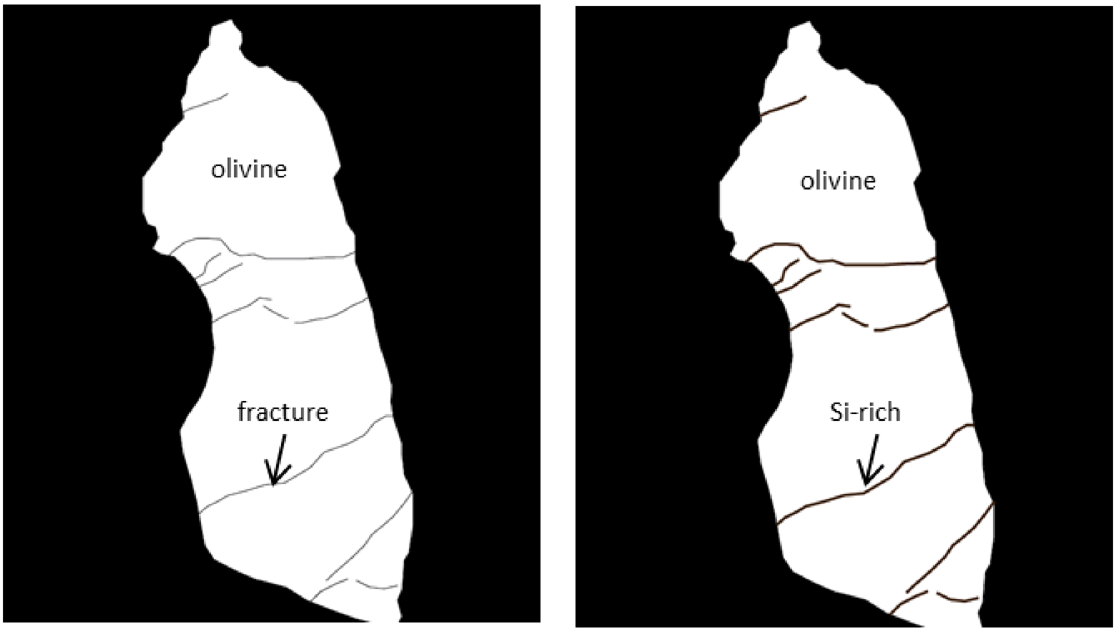

1- Formation of intra-crystalline fractures

2- Deposition of Si-rich poorly crystallized material

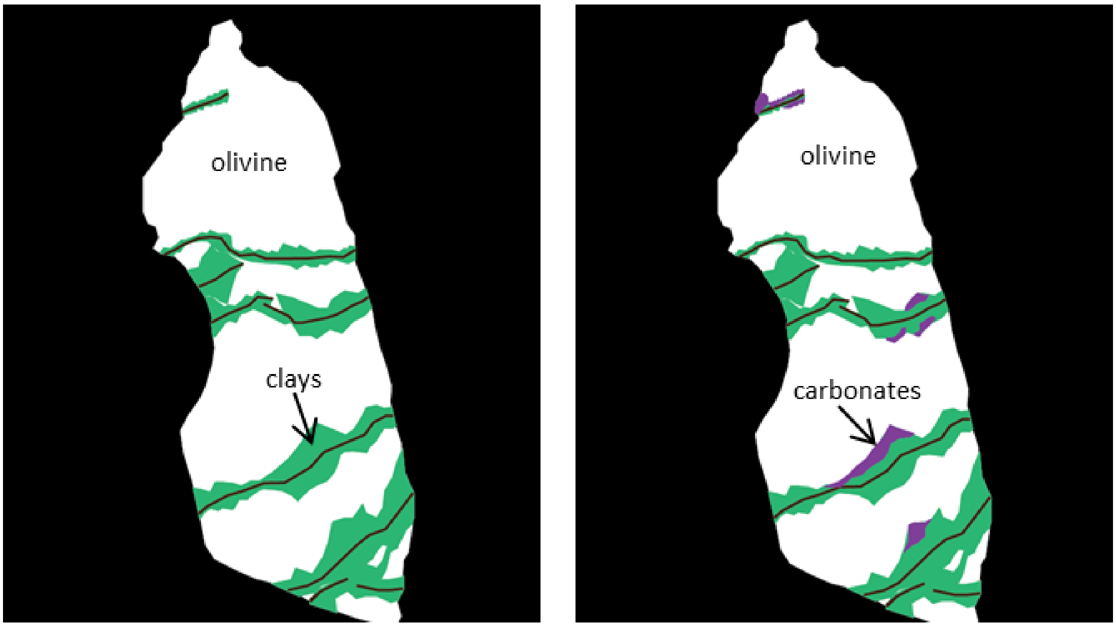

3- Vein enlargement and deposition of clays

4- Precipitation of carbonate along the vien margins

*Fig. 5.42: Schematic diagram illustrating the different stages of vein formation and mineralization in olivine phenocryst in Lafayette during multiple aqueous pulses. (1) Aqueous fluids probably entered into olivine grains following intra-crystalline fractures. (2) Fluid-rock interactions led to a partial dissolution of olivine and in situ deposition of insoluble component of olivine. (3) Further progressive dissolution of olivine and fluid maturity have led to the formation of well organized clay minerals that grew from, and perpendicular to, the Si-rich product. (4) Later infiltration of scarce* $CO_2$*-rich fluids in the rock resulted in the precipitation of carbonate in some of the veins between the clay minerals and olivine.*

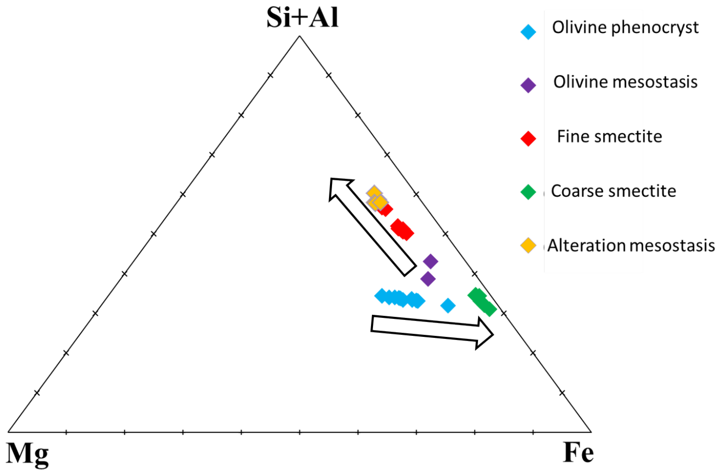

*Fig. 5.43: Composition of olivine (phenocryst and mesostasis) and their respective clay mineral populations in NWA 817. Fine smectite are enriched in insoluble Si and Al reflecting a loss of metallic components to the fluids while coarse smectite are enriched in soluble Fe indicating a very restricted amount of fluids and a poor circulation of the solutions. Both smectite probably crystallized during distinct aqueous event and reflect the changes of aqueous conditions over time.*

smectite did not re-equilibrate with the aqueous fluid that precipitated the coarse smectite. A hypothesis that seems to be valid for the other nakhlites. The fully collapsed state of the smectite may have prevented ion exchange processes between the fluids and fine smectite. The different chemical compositions of the smectite (first formed and second formed) in NWA 817 suggest a formation of the fine and coarse smectite under different brine conditions probably associated with a reducing of the aqueous activity over time (Fig. 5.43). The fine smectite is enriched in insoluble Si and Al relative to olivine suggesting severe leaching conditions. The absence of metallic components suggests that these elements have been physically removed from the reaction fronts and the rock by the fluids. The fine smectite replacing the skeletal olivine is more depleted in Fe than those replacing the olivine phenocrysts despite the fact that skeletal olivine is enriched in fayalite component relative to the olivine phenocrysts. The selective loss of Fe and Mg suggests that fluid transport was an efficient mechanism in spatially segregating elements from one another. The removal of Fe and Mg from the rocks despite the obvious restricted amount of water present in the rocks could be explained by repeated discrete pulses of water inflow leaving behind leached layers that polymerized under unfavourable conditions. Discrete and uneven water inflows throughout the rocks can also explain the apparent inhomogeneity at the mm-scale of the fluids, for example the absence of alkali and alkali earth in olivine-bounded smectite. It is also possible that ionic compounds were more abundant in the brines than it seems. Most may have not been deposited and/or flushed away with the metallic cations by the repeated water pulses.

The coarse smectite in NWA 817 is enriched in highly soluble Fe and depleted in the less soluble Mg relative to the host olivine (Fig. 5.43). During the alteration processes, Fe has been preferentially leached from the grain surfaces and retained near the alteration fronts, which indicates a very low water-rock ratio to only remove Fe from the olivine and a poor fluid circulation to keep Fe at the reaction fronts. The common channelized texture of olivine at the olivine-vein boundaries also indicates an olivine alteration through leaching processes. The non-stoichiometric dissolution of olivine emphasises the very short-lived nature of the Martian aqueous fluids and their restricted abundances. The preservation of Fe near the reaction fronts suggests that the micro-solutions that entered into olivine porosity evaporated in situ depositing their whole solute load. There is no evidence that the aqueous solutions that entered into the nakhlites bedrock brought chemical species at the exception of the ionic components.

### *5.8.4 Spatio-temporal evolution of environmental conditions in the nakhlites aquifer*

The more complex chemistry of the last-formed alteration products in other nakhlites that include abundant ionic compounds such as S and Cl reflects the existence of uneven percolating micro-brines in Mars subsurface that became acidic with time, allowing sulphate, halide and Fe-oxide to co-precipitate with rare clay minerals and/or carbonates. As aqueous activity vanished, the wetting events became more subtle, chemically complex and probably sharply stratified (no ions in the coarse smectite of NWA 817). The pervasive presence of Cl in all alteration products in Nakhla suggests that this meteorite precipitated its secondary products from relatively late brines that previously crystallized “abundant” clayish material which would have increased Cl content (by $H_2O$ uptake) or was subject to more extreme evaporative condition (Tosca and McLennan, 2006). The presence of carbonate in some of the most coarsely crystallized nakhlites (as a proxy for a deeper crustal environment) suggests less acidic conditions with depth. The presence of Fe-sulphate within the carbonate deposits provides evidence for some S ions in the carbonate-rich aqueous fluids. The proportion of both secondary mineral phases varies between Nakhla, Y 000593 and Y 000749. In our sample Y 000749 is enriched in carbonate relative to sulphate while Y 000593 is enriched in sulphate and contains rare (if any) carbonates, Nakhla being somewhat intermediate. The precipitation of both mineral phases was dependent on the release of Fe from olivine. Hence the preferential precipitation of one mineral phase relative the other should reflect the fluid properties (or ratio of carbonate *vs.* sulphate ions) at the olivine interfaces. The presence of scarce halite associated with Fe-sulphate suggests that sulphate and halite crystallized from late-stage brines, from the evaporation of small amount of residual solutions remaining along olivine surfaces. The volumetric dominance of siderite over sulphate in Y 000749 and sulphate over carbonate in Nakhla together with halite suggests that carbonate → sulphate → halite represent the progressive crystallization path of the Martian brines upon evaporation in some nakhlites, a hypothesis consistent with experimental data of evolution path of Martian brines (Tosca and McLennan, 2006) but apparently not valid for the all nakhlites including NWA 817 and NWA 998 as they do not contain apparent salt deposits.

The alteration products in Lafayette indicate the existence of non acidic aqueous conditions in Mars subsurface, no sulphate or halite minerals have been detected. Phyllosilicate crystallizes under near neutral to slightly alkaline conditions while carbonate precipitates under alkaline conditions (Fig. 5.2). Chemical weathering of the rock probably buffered the natural fluid acidity and has allowed it to gaining solute and precipitating chemically more complex clay minerals. More abundant water inflows, longer lived aqueous fluids, possibly greater temperature and subsequent chemical weathering of the rock materials are probably responsible for the better development of clay minerals. Which of the clays or carbonates crystallized first is not easy to determine. However, few textural relationships suggest that the clays precipitated first. The symmetry and thickness of the double clay layers are preserved and the saw-tooth feature can still be seen (Fig. 5.33). The latter suggests that the clays were once the only alteration product and have completely filled the veins. The tips of the clays still marked the former olivine vein boundaries. Another argument in favour of an earlier clay mineral precipitation is the higher solubility of carbonates in aqueous fluids than the phyllosilicates. If the very finely carbonates had experienced a latter aqueous event, they most probably would not have survived it.

Figure 5.44 illustrates the variations in the secondary mineral assemblage present in the nakhlites with their relative proportion. Variations in secondary minerals between the nakhlites do not show any correlation relative to the cumulate pile model of Mikouchi et al. (2012) that could reflect a fluid evolution through secondary mineral precipitation with depth. Both NWA 817 and Lafayette display the most altered olivine phenocrysts with respect to vein thickness and crystallinity. They are the only nakhlites to display well crystallized clay minerals although they sample the top and bottom of the cumulate pile model of Mikouchi et al. (2012). The nakhlites sampling the interior of the cumulate pile (Y 000749, Y 000593 and Nakhla) are the only rocks containing sulphate deposits. They also contain carbonates (Y 000593?) as does Lafayette. Abundance of carbonate decreases from lafayette → Y 000749 → Nakhla while the sulphate abundances decrease from Y 000593 → Nakhla → Y 000749. This may be a coincidence or the different rocks could reflect the progressive evolution of the brines through both space and time.

The origin of the ionic components in the alteration products of the nakhlites is difficult to identify, but they may have been brought by the aqueous fluids into the nakhlites bedrock. The presence of S could be explained by a partial dissolution and/or exchanges with sulfide minerals (i.e. pyrrhotite grains present in the rocks mesostasis), while the large absence of P in most alteration products argues against apatite dissolution as a principal source of Cl. Sulphur and Cl are common degassed volcanic compounds on Mars while $CO_2$ is the main component of the Martian atmosphere (Tosca and McLennan, 2006) but also cryosphere.

With the exception of NWA 5790, the only nakhlite apparently devoid of any Martian aqueous product (Tomkinson et al., 2015), the ejection ages of the other nakhlites form a well-defined cluster which presumably represents a single impact event and launch site (McSween, 2008). The variations in the marginal alteration products between the nakhlites may reflect a progressive heterogeneous evolution or stratification of the conditions in the aqueous environment at the launch site. Previous petrological studies suggest that the nakhlites represent a stratigraphical sampling of a single thick differentiated igneous body (Friedman-Lentz et al., 1999), the different depths at which specific nakhlites have been excavated may spread over kilometres. On young Amazonian volcanic terrains, the plausible impact launch site of the nakhlites has been estimated as 3 km large at the minimum (Head et al.,

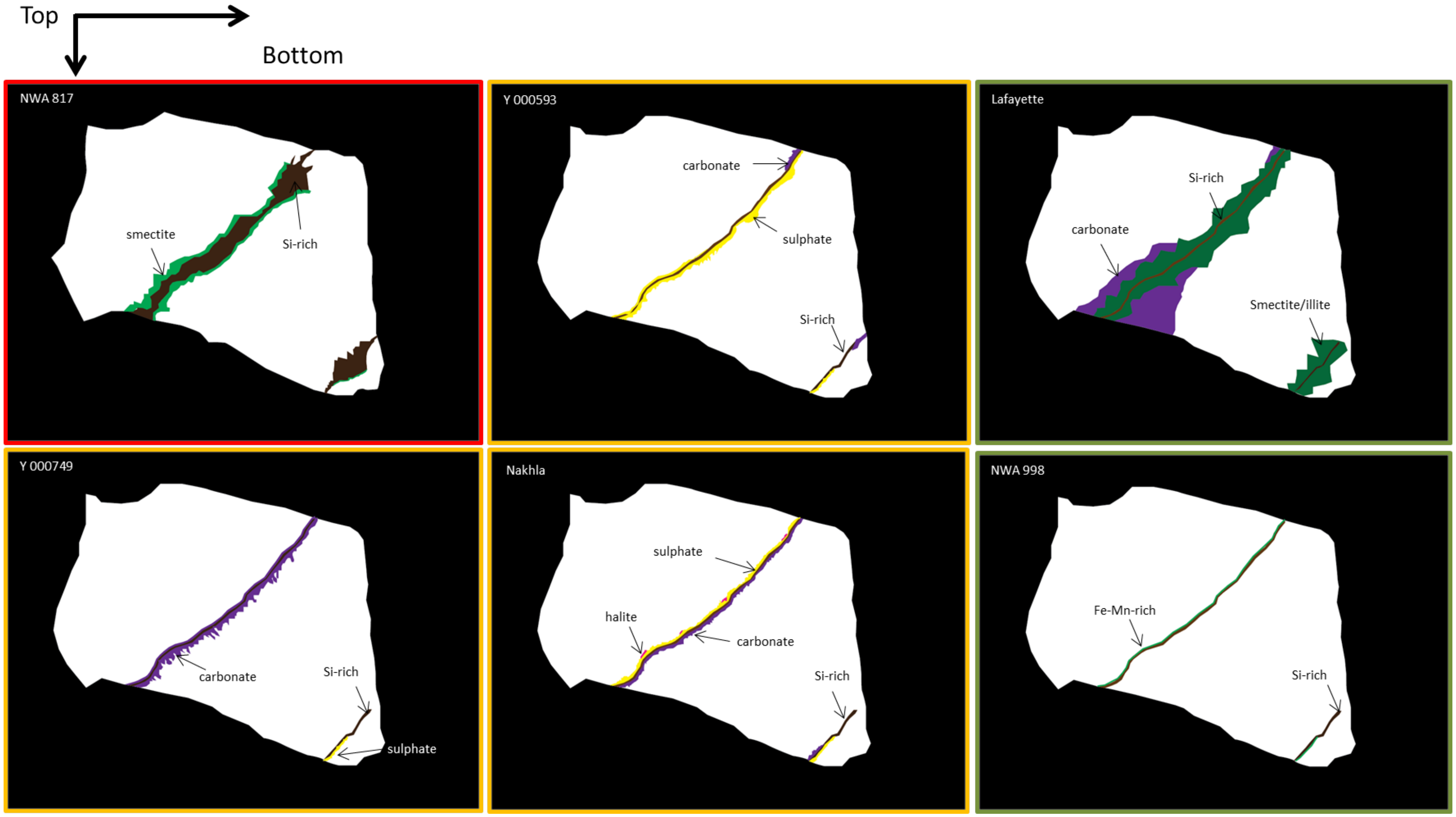

*Fig. 5.44: Schema of olivine alteration veins showing the different mineral assemblage found in the individual nakhlites with their relative proportion and position in the veins. The nakhlites are presenting in their stratigaphic position according to the pettrographic model of Mikouchi et al. (2012), with NWA 817 sampling the top of the cumulate pile (red), Nakhla, Y 000749 and Y 000593 forming the interior of the igneous body (yellow) and Lafayette and NWA 998 the bottom (green).*

2002). Therefore, the secondary mineral assemblages may reflect not only vertical changes of the brine properties (Changela and Bridges, 2010) but also lateral evolutions, or even intrinsic localized heterogeneity in the brines' properties whatever their original depth of emplacement.

## 5.9 Conclusions

Pre-terrestrial clay minerals from the smectite family are ubiquitous in all nakhlite meteorites except NWA 5790. They offer a unique mineralogical record of a young aqueous environment and history on Mars. Smectite is the first formed and dominant product of aqueous alteration of olivine. The smectite forms bands of variable thickness, each with their own structural and chemical properties. The Martian clay minerals have been responsive to the local environmental conditions under which they precipitate and reflect an evolution of the brines property over discrete aqueous events. Yet, some information about the separate aqueous events have been preserved. Smectite mineraloids have not significantly reacted with the aqueous fluid during the next wetting events by ion exchange or layer transformation as common with clay minerals. The relative un-reactivity of the smectite was probably due to the natural slow reaction rate of clay minerals in cold environments and the gradual waning of Martian aqueous activity through time.

The formation of smectite minerals resulted from incongruent dissolution of olivine along surfaces that were exposed for some time to aqueous fluids, together with the contemporaneous precipitation of some dissolved species at the mineral-fluid interfaces. The crystallization of clay minerals was accompanied by mobilization of aqueous species and transport segregation of the dissolved elements of olivine. The chemical immaturity of the smectite probably mirrors the poor chemical complexity of the aqueous solutions. There is no chemical evidence from the leftover products that the fluids that entered the nakhlites bedrock were significantly charged with compounds gained from previous chemical reactions with the lithosphere.

The variations in chemical composition of the smectite mineraloids between the layers reflect the prevailing elements mobility in the water-rock system during the individual aqueous events, which were controlled by the fluid properties such as fluid flow rate, abundance, lifetime and pH. The volumetrically dominant fine smectite probably formed through repeated short-lived pulses of micro-solutions which have progressively dissolved olivine and removed the soluble metallic components from the mineral-fluid interfaces leaving a chemically unbalanced layer of poorly polymerized insoluble elements of olivine. The rate of metal diffusion through the aqueous medium exceeded the rate of release, which suggests that the chemical weathering occurred in the presence of very under-saturated fluids.

The formation of coarse smectite and salt deposits shows a sharp change in the physical conditions of water-rock interactions over time that further vary between the nakhlites. In NWA 817, the micro-solutions that penetrated into the porosity created during previous alteration events have further dissolved olivine. The restricted availability of stagnant water has largely favoured the dissolution of the most soluble constituent of olivine (i.e. Fe) from the surfaces, progressively enriching the solution in Fe. The rate of Fe release from the olivine surfaces exceeded the rate of diffusion. The physical incapacity of the fluids to transport Fe further from the reaction fronts has led to the development of Fe-rich smectite. The presence and immobility of metallic elements (elements constituent of clay minerals) at the reaction fronts may have favoured the development of better crystallized smectite grains. A “stoichiometric” balance between Si and metallic cations may have been reached during the formation of coarse smectite. The preservation of Fe at the reaction fronts suggests that the chemical weathering did not intensify during or after the crystallization of the coarse smectite. The formation of smectite with contrasting chemistry and texture in the nakhlites may be explained by kinetic constraints linked to the fluid properties.

The nakhlites all experienced similar aqueous processes with “intense” chemical weathering processes (despite restricted availability of aqueous fluids) leading to the precipitation of a material precursor of smectite followed by a more subtle chemical weathering leading to salt deposition with rare clay minerals (except in NWA 817) that is temporally distinct. Moreover, the salt composition (either sulphate or carbonate) and their respective proportion differ between the rocks, which implies sharp local variations in the conditions of alteration in the Martian subsurface. For example, the presence of a certain quantity of Al in smectite from MIL 03346 may reflect the general higher degree of aqueous alteration experienced by this nakhlite which includes alteration of the glassy mesostasis, while the precipitation of relatively abundant salts in Y 000749, Y 000593, Nakhla and Lafayette reflects the existence of concentrated brines in the Martian subsurface that were not present in the area sample by NWA 817 (no ionic compounds detected in the coarse smectite).

The material precursor of smectite commonly contain adsorbed ionic compounds while vein zonation include salt deposits finely inter-mixed with rare clays. Some salts and ionic compounds are probably of Martian origin. They include the ubiquitous presence of S in the fine smectite and probably some S and Cl in the coarse smectite from all nakhlites (not always present) and Fe carbonate and sulphate. However, even if the fine smectite may have remained unaffected by terrestrial fluids thanks to its fully collapsed state, and hence still represents the Martian record, nothing is less sure as to the abundances and distribution of S and Cl in the coarse smectite. The salt deposits inter-mixed with the clays display devolatilization texture which indicates the presence of significant amounts of ionic components in the Martian aqueous solutions. However, it is also obvious that terrestrial fluids containing S, Cl and P have flowed through the coarse smectite and may have removed the Martian adsorbed ions onto the smectite and redeposited them further away together with the terrestrial ones. Variations in salt composition and relative proportion between the nakhlites indicate that the Martian aqueous system was sharply stratified. Because of the high probability of terrestrial contamination, ionic component chemisorbed onto the coarse smectite should not be used as a proxy for Martian aqueous alteration. Terrestrial contaminants in the nakhlites include the ions S, P and Cl especially in the nakhlites discovered in the Antarctic region but also calcite in the nakhlites discovered in the Sahara desert. Manganese is commonly spatially associated with terrestrial alteration products from both hot and cold deserts and may be of terrestrial origin.

The alteration products of Lafayette (well crystallized smectite/illite and abundant carbonates) suggest the existence of a wide range of aqueous conditions in

Mars sub-surface during the recent past. The clay minerals and carbonates require alkaline and respectively near-neutral to basic conditions which contrast with the more acidic conditions (associated with the deposition of evaporite minerals) that was experienced by the other nakhlites during water-rock interactions. The aqueous fluids that circulated in Lafayette were probably more abundant and “long”-lived. They reacted not only with olivine but also with plagioclase and possibly augite (if not terrestrial ?). More intense chemical weathering probably buffered the natural acidity of water and formed aqueous fluids with contrasting conditions and chemical state that have allowed the development of mature clay minerals, although a formation of the clay minerals at greater temperature may also be considered. The mechanism of olivine dissolution during aqueous processes were probably influenced by the fluid pH. For example, olivine dissolution by $CO_2$-rich fluids was not controlled by its crystallography and had not led to the formation of funnel-shaped corrosive features at the mineral-fluid interfaces.

# 6. SUMMARY

The nakhlite meteorites have revealed many geochemical, mineralogical and physical properties of a young Amazonian basaltic crust that cannot yet be obtained from Mars' orbiters and rovers. The nakhlites are differentiated rocks formed by fractional crystallization of basaltic magmas and accumulation of pyroxene at the base of the igneous bodies. As the nakhlites experienced crystal-melt segregation and intensive sub-solidus re-equilibration during their solidification, the physical and chemical conditions of the parent magmas at the origin of the rocks are difficult to constrain. The nakhlites exhibit similar bulk rock composition, mineralogy (dominated by calcic clinopyroxene, ferroan olivine and sodic plagioclase) and almost identical radio-isotope compositions (within error bar) including crystallization and cosmic ray exposure age (Nyquist et al., 2001; McSween, 2008). They probably come from a same magmatic complex fed by a unique mantle source region and emplaced during a short amount of geologic time. They are likely related to the same magmatic event. The depletion in highly incompatible elements of the nakhlites' bulk rock suggests that the meteorites are the magmatic products of a long-lived mantle source and are not the product of anomalous magmatic activity (Treiman, 2005). The geochemistry of cumulus augite (the apparent first-formed crystal) of the nakhlites are not the solidified product of primitive magmas either; the nakhlites parent magmas probably evolved from primary magmas via cryptic differentiation processes in the deep magmatic environment. The primitive magmas may have moved through dykes and sills and stagnated during their ascent throughout the thick Martian crust probably leaving behind crystal residues whose nature is obscure.

Current models on the nakhlites petrogenesis based on comparative petrology with terrestrial analogue suggests a possible formation of the nakhlites from a common parent magma with a early crystallization of chemically homogeneous augite in a shallow magma chamber and a later eruption of the augite-bearing magma to an environment where the augite accumulated and the interstitial magma cooled down at varying rates (Treiman, 2005; Day et al., 2006; Mikouchi et al., 2012). Once in their final emplacement, the nakhlites experienced intense differentiation processes to form a thick stratified cumulate pile (Friedman-Lentz et al., 1999; Mikouchi et al., 2012). The nakhlites display similar mineralogy and mineral paragenesis, but they differ in their mesostasis textures and abundances, and extent of mineral zoning and replacements/reactions (Treiman, 2005; Mikouchi et al., 2012). All petrological variations between the rocks are believed to be the sole result of post-cumulate or late magmatic processes and can be directly linked to the various cooling history experienced by the individual nakhlites post-emplacement (Treiman, 2005). The specific mineral and textural variations between the different rocks show a positive correlation (summarized on the cumulate pile model of Mikouchi et al. (2012) on

Fig. 1.6), such correlated petrographic features commonly developed in thick differentiating igneous bodies and reflect the internal thermal structure and history of the igneous body, which provides a strong argument to support the single cumulate pile model (Mikouchi et al., 2012). However, there is still a possibility that the nakhlites crystallized from multiple similarly structured igneous bodies that emplaced over a short geological time. Consequently, a critical issue in interpreting the petrogenesis and relationship of the nakhlites is the composition (and number) of magmas at the origin of the rocks. One possibility to identify some chemical characteristics in the parental magma composition is to look at the chemical composition of the core of the first-crystallized augite phenocrysts using a series of trace elements because they are less sensitive to diffusional re-equilibration than major elements (Wadhwa and Crozaz, 1995). Trace element composition of the augite should still represent the original composition and could provide some clues about the parent melt composition from which augite in the different nakhlites crystallized (Wadhwa and Crozaz, 1995).

The detailed petrological and mineralogical investigation undertaken in this thesis on a large suite of nakhlites has provided new information about the magmatic history and relationship of the nakhlites with, despite an obvious consanguinity, a more likely formation of the rocks from multiple parent magmas that separate early in the deep magmatic environment and have remained separated up to complete crystallization. Indeed, the detail examination of trace element composition of augite from individual nakhlites, the solidified product of early magmatic activity in the sub-surface environment, has revealed subtle but distinct igneous mineral compositions with a de-coupling between compatible and incompatible elements between the rocks and zoning patterns inconsistent with an early crystallization of the nakhlites from a large single magma reservoir experiencing fractional crystallization. The systematic chemical differences of augite between the nakhlites probably reflects different degrees of attainment of melt differentiation early in the crystallization history, even prior to (and during) augite crystallization which indicates that the parent melts at the origin of the individual rocks were already (1) fractionated to different extent in the large sub-surface magmatic reservoir and (2) separated in space (possibly within different magmatic intrusions) if not in time. The systematic changes without following any bulk rock evolution trend, the absence of convergence of incompatible element ratios of the more evolved rock compositions and de-coupling of compatible/incompatible elements between the nakhlites suggest that the variability in parental magma compositions between the rocks are more likely the result of deep magmatic processes (probably associated with both mantle source characteristics and deep level magma differentiation) than progressive fractional crystallization in a shallow magma chamber involving augite alone.

The lower Mg$\sharp$ of the meteorites' bulk rock compared to those of the cumulus augite indicates that the nakhlites' bulk rock chemistry is not dominated by the augite composition. Chemical consistency between early-formed augite and inter-cumulus mineral phases further suggests that the chemical characteristics of the early magmas (pre-augite crystallization) of the different nakhlites were preserved during emplacement. The different parent melts and their respective augite population have not been in contact with each other. The nakhlites are probably genetically linked but their varying mineralogical properties suggest complex magmatic activity and volcanic system with a likely formation from a possible common parent magma that separated early en route to the surface and possibly at different stages of magma differentiation into different igneous bodies where augite began crystallization. However, there is also a possibility that the unique mantle source region of the nakhlites magmatic suite was episodically active for a certain period of time around 1.3 Ga ago, while the individual extraction events (represented by different nakhlites) cannot be resolved using radio-isotope dating technique.

Determining exactly how many magmas are at the origin of the nakhlite magmatic suites is not possible from the limited number of geochemical data obtained in this study. The too small amount of augite grain analysed per nakhlites cannot document the whole range of mineral composition while the poor spatial representation of trace element composition and distribution in augite using the LA ICP-MS (with large ablation size) cannot give the composition of the very inner "primitive" core and range of chemical zonation of augite throughout core mantle and rim. A better understanding of the early crystallization history and path taken by the individual nakhlites required more analyses of augite grains to access the whole range of composition, ideally with a technique that allows a better spatial representation such as the ion probe (i.e. Secondary Ions Mass Spectrometer SIMS). Of special interest is the crystallization path of NWA 5790. The REE budget and pattern of its augite phenocryst are similar to those of the augite rims of other nakhlites (except NWA 817) including the Eu negative anomalies indicating the presence of plagioclase on the liquidus. The geochemical composition of augite in NWA 5790 provides evidence for a crystallization of the rock from a more fractionated melt despite the similar quadrilateral components of their augites' core relative to other nakhlites. NWA 5790 could have crystallized from a melt that separated from the nakhlites parent melt later (after and/or during plagioclase crystallization) in the sub-surface environment. The more fractionated (and less dense) melt may have escaped by an effect of gravity. But it is not clear why a melt that crystallized Fe-rich clinopyroxene has continued to crystallize augite in NWA 5790. It is also not clear why NWA 5790, the meteorite that represents the most evolved parent melt of the nakhlite suites, do not show an evolution of incompatible trace element ratios relative to other nakhlites as expected from magmatic rock suites. A possibility would be a strong crystal chemical effect of augite (augite from the different nakhlites display all similar quadrilateral components) into the incorporation of incompatible trace elements in the pyroxene. NWA 5790 may also represent the late solidified products of a distinct magma batch in the shallow magmatic plumbing system.

The nakhlites are the products of protracted crystallization of basaltic magmas. The presence of droplet-shaped magmatic cristobalite and silica-rich melts attest to the formation of silicic magmas in Mars' subsurface. The nakhlite meteorites provide evidence that while dominated by basaltic activity Mars has produced silicic igneous products through magmatic processes analogous to those occurring in volcanic complexes on Earth. Intensive fractional crystallization and gravity-driven mineral-melt separation played an important role in the formation of infinitesimal quantity of silicic melts from basaltic magmas. However, the formation of significant amounts of highly evolved magmas on Mars associated with the nakhlites magmatic activity is unlikely as it would have required deep stagnation of large volumes of primary magmas because the volume ratio of crystal residue to silicic melt has to be high and the presence of hydrous molecules which would have lowered the mineral solidus. The nakhlites are rich in incompatible elements including the LREEs providing strong evidence for a formation of their parent magmas by small degrees of partial melting and not during extensive partial melting events, while the absence of hydrous primary minerals (i.e. amphibole, biotite, etc.) or hydrous molecules in primary water-bearing mineral (i.e. apatite) suggest the absence of abundant primary water in the nakhlites' parent magmas.

The nakhlites display minimal traces of aqueous alteration but the alteration minerals are unquestionable indicators of the existence of recent short-lived water-rich environments in the Martian subsurface, at least in the region and depth sampled by the nakhlites. Small quantities of poorly crystallized alteration minerals, a mixture of clay minerals from the smectite family and salts, prove that thin films of crustal water interacted with the rock-forming minerals releasing chemical species from the bedrock into the aqueous solutions. The texture of the alteration minerals and their crystal hosts are consistent with a secondary mineralization from low temperature aqueous solutions (i.e. weathering processes). The secondary minerals precipitated in situ in the space created by mineral dissolution during intense evaporative saturation of these micro-solutions. The poor development of lattice fringes (energetically unfavourable) within the clay minerals probably reflects the naturally slow reaction rate in the cold Martian sub-surface environments.

The preservation of the fine chemical sediments in the nakhlites indicates that rock exposure to aqueous fluids was limited in volume and duration while the precipitate zonation suggests a deposition over brief and multiple episodes of wetting events. The rapid dissolution of olivine compared to other silicate minerals in the nakhlites means that metallic cations (i.e. Fe and Mg) and silica had been preferentially liberated during the basaltic weathering processes. The dissolved species of olivine are indeed the main constituents of the nakhlites' secondary minerals. The lack of evidence of significant chemical species in the secondary mineral assemblages other than those provided by the olivine and ionic compounds suggests that the fluids were largely diluted prior to entry in the nakhlites bedrock. The relative abundant deposition and polymerization of silica without much metallic cations at olivine-fluid interfaces indicate that aqueous fluids existed for a sufficient time to have mobilized the metallic cations but not for a long-time after initial silica deposition. The preservation of polymerized silica attests to the poor availability of water in the subsequent aqueous events. The origin of the ionic compounds chemisorbed onto the clays or deposited as salt minerals is not clear. Most are probably terrestrial but certain are of Martian origin and are possibly external to the nakhlites bedrocks. The existence of $CO_3^-$-rich fluids that permeated their way through Y 000749, Nakhla and Lafayette provide evidence for the presence of more complex fluid chemistry on Mars. The greatest alteration of Lafayette by aqueous fluids suggest that brines at the depth sample by the meteorite have probably survived for a longer period of time to interact with different chemical reservoirs prior to entering the nakhlites bedrocks.

However, variations in structural Fe and Mg content of the clays and salts mineralogy within and between the meteorites are strong indicators of spatial and temporal variabilities of the brines property. The variations in the brines' property are directly linked to the water-to-rock ratios. Areas which experienced relatively more intense aqueous alteration processes (i.e. higher water-to-rock ratio) display the most complex secondary mineral assemblages and mineral chemistry. The crustal brines gained their solute load through in situ chemical reactions (i.e. leaching) with the rock-forming mineral with which they entered into contact. The general low water-to-rock ratio prevented intense dissolution of the rock-forming minerals and the precipitation of more complex secondary mineral assemblages. The development of immature clay minerals with no obvious inter-layer components probably reflects the weak solute load prior to evaporitive saturation and youth of the aqueous fluids from which the secondary minerals precipitated. The chemical and mineralogical evolution of the secondary minerals deposited over the brief episodes of aqueous activity, further consistent in all meteorites, testify to a progressive reducing of water availability with time.

Clay minerals from the smectite family have been the most stable minerals during the brief water-rich environments of Mars sub-surface. The dominance of immature clay minerals in the alteration assemblages suggests that neutral-to-alkaline conditions predominated in the sub-surface aqueous environments at least during the first wetting events experienced by the nakhlites, which contrasts with the highly acidic conditions of Mars' surface over the Amazoninan time. Yet, the presence of either sulfate or carbonate in the nakhlites within the alteration products deposited in the last aqueous event(s) testifies of the existence of briny liquids with various conditions in Mars subsurface. This suggests that both slightly alkaline and acidic aqueous environments have existed in the Martian crust at some period during the late Amazonian. They may have coexisted, spatially isolated from one another. Physical isolation of the brines may either reflect an intrinsic depth stratification of the Martian crustal fluids or regional variations in the brines condition. The absence of relatively significant salt deposition (except carbonates in Lafayette) proves that the salt components in the aqueous solutions were either very diluted or have been swept away (together with Fe) during the repetitive liquid water pulses.

# BIBLIOGRAPHY

J. Adam and T.H. Green. Trace-element partitioning with application to magmatic processes the effects of pressure and temperature on the partitioning of ti, sr and REE between amphibole, clinopyroxene and basanitic melts. *Chemical Geology*, 117:219 – 233, 1994.

C. B. Agee, N. V. Wilson, F.M. McCubbin, K. Ziegler, V. J. Polyak, Z. D. Sharp, Y. Asmerom, M. H. Nunn, R. Shaheen, M. H. Thiemens, A. Steele, M.L. Fogel, R. Bowden, M. Glamoclija, Z. Zhang, and S. M. Elardo. Unique meteorite from early Amazonian Mars: Water-rich basaltic breccia NorthWest Africa 7034. *Science*, 339:780 – 785, 2013.

D. J. Anderson, D. H. Lindsley, and P. M. Davidson. QUILF: A PASCAL program to asses equilibria among Fe-Mg-Mn-Ti oxides, pyroxenes, olivine, and quartz. *Computers and Geosciences*, 19:1333 – 1350, 1993.

C. Annen, J. D. Blundy, and R. S. J. Sparks. The genesis of intermediate and silicic magmas in deep crustal hot zones. *J. Petrol.*, 47:505 – 539, 2006.

V. R. Baker, R. G. Strom, V. C. Gulick, J. S. Kargel, G. Komatsu, and V. S. Kale. Ancient oceans, ice sheets and the hydrological cycle on Mars. *Nature*, 352:589 – 594, 1991.

J. F. Banfield, D. R. Veblen, and B. F. Jones. Transmission electron microscopy of subsolidus oxidation and weathering of olivine. *Contrib. Mineral Petrol*, 106:110 – 123, 1990.

J. J. Bellucci, A. A. Nemchin, M. J. Whitehouse, J. F. Snape, P. Bland, and G. K. Benedix. The Pb isotopic evolution of the Martian mantle constrained by initial Pb in Martian meteorites. *J. of Geophys. Res.: Planets*, 120:2224 – 2240, 2015.

J. L. Berkley, K. Kiel, and M. Prinz. Comparative petrology and origin of Governador Valadares and other nakhlites. *Proc. Lunar and Planet. Sci. Conf.*, 10: 1089 – 1102, 1980.

C. M. Bertka and Y. Fei. Density profile of an SNC model Martian interior and the moment-of-inertia factor of Mars. *Earth Planet. Sci. Lett.*, 157:79 – 88, 1998.

A. Bevan and J. R. De Laeter. *Meteorites: A journey through space and time.* Smithsonian Institution Press, 2002.

J. Blundy and K. Cashman. Petrologic reconstruction of magmatic system variables and processes. *Reviews in Mineralogy and Geochemistry*, 69:179–239, 2009.

J. Blundy and B. Wood. Partitioning of trace elements between crystals and melts. *Earth Planet. Sci. Lett.*, 210:383 – 397, 2003.

L. Borg and M. J. Drake. A review of meteorite evidence for the timing of magmatism and of surface or near-surface liquid water on Mars. *J. Geoph. Res.*, 110:1 – 10, 2005.

N. L. Bowen. Evolution of the Igneous Rocks. *Dover Pubns*, page 334, 1928.

J. C. Bridges and M. M. Grady. Evaporite mineral assemblages in the nakhlite (Martian) meteorites. *Earth Planet. Sci. Lett.*, 176:267 – 279, 2001.

J. C. Bridges and P. H. Warren. The Snc meteorites: Basaltic igneous processes on Mars. *J. Geolog. Soc.*, 163:229 – 251, 2006.

J. C. Bridges, D. C. Catling, J. M. Saxton, T. D. Swindle, I. C. Lyon, and M. M. Grady. Alteration assemblages in martian meteorites: Implications for near-surface processes. *Space Science Reviews*, 96:365 – 392, 2001.

T. E. Bunch and A. M. Reid. The nakhlites, Part I: Petrography and mineral chemistry. *Meteoritics,*, 10:303 – 305, 1975.

F. Burragato, G. Cavaretta, and R. Funiciello. The new Brazilian achondrite of Governador Valadares (Minas Gerais). *Meteoritics*, 10:374 – 375, 1975.

M. H. Carr and J. W. III Head. Geologic history of Mars. *Earth Planet. Sci. Lett.*, 294:185 – 203, 2010.

J. Carter, F. Poulet, J.-P. Bibring, N. Mangold, and S. Murchie. Hydrous minerals on Mars as seen by the CRISM and OMEGA imaging spectrometers: Updated global view. *J. Geophys. Res.: Planets*, 118:831 – 858, 2013.

W. H. Casey and B. Bunker. Leaching of mineral and glass surfaces during dissolution. *Reviews in Mineralogy*, 23:397 – 426, 1990.

W. H. Casey, H. R. Westrich, J. F. Banfield, G. Ferruzzi, and G. W. old. Leaching and reconstruction at the surfaces of dissolving chain-silicate minerals. *Nature*, 2366:253 – 256, 1993.

J. Chadwick, P. McGovern, M. Simpson, and A. Reeves. Late Amazonian subsidence and magmatism of Olympus Mons, Mars. *J. Geophys. Res. Planets*, 120:1585 – 1595, 2015.

H. G. Changela and J. C. Bridges. Alteration assemblages in the nakhlites: Variation with depth on Mars. *Meteorit. Planet. Sci.*, 45:1847 – 1867, 2010.

D. J. Cherniak and Y. Liang. Rare earth element diffusion in natural enstatite. *Geochim. Cosmochim. Acta*, 71:1324 – 1340, 2007.

D. J. Cherniak and Y. Liang. Ti diffusion in natural pyroxene. *Geochim. Cosmochim. Acta*, 98:31 – 47, 2012.

F. Christen, O. Eugster, and H. Busemann. Mars ejection times and neutron capture effects of the nakhlites Y000593 and Y000749, the olivine-phyric shergottite Y980459, and the lherzolite NWA1950. *Antarct. Meteorite Res.*, 18:117 – 132, 2005.

G. Crozaz, C. Floss, and M. Wadhwa. Chemical alteration and {REE} mobilization in meteorites from hot and cold deserts. *Geochim. Cosmochim. Acta*, 67:4727 – 4741, 2003.

J. M. D. Day, L. A. Taylor, C. Floss, and H. Y. Jr. McSween. Petrology and chemistry of MIL 03346 and its signifcance in understanding the petrogenesis of nakhlites on Mars. *Meteorit. Planet. Sci.*, 41:581 – 606, 2006.

G.-J. L. M. De Haas, T. G. Nijland, P. J. Valbracht, C. Maijer, R. Verschure, and Andersen T. Magmatic versus metamorphic origin of olivine-plagioclase coronas. *Contrib. Mineral. Petrol.*, 143:537 – 550, 2002.

J. C. M. De Hoog, L. Gall, and D. H. Cornell. Trace-element geochemistry of mantle olivine and application to mantle petrogenesis and geothermobarometry. *Chemical Geology*, 270:196 – 215, 2010.

W. A. Deer, R. A. Howie, and Zussman J. An introduction to the rock-forming minerals. *Min. Mag.*, 666, 1992.

D. J. Des Marais, B. M. Jakosky, and B. M. Hynek. Astrobiological implications of Mars' surface composition and properties, in Bell J. F. III (ed.), The Martian surface: Composition, mineralogy, and physical properties. *Cambridge University Press*, 599 - 623, 2008.

F. Don and M. William. Aluminum-dependent trace element partitioning in clinopyroxene. *Contrib. Mineral. Petrol.*, 156:439 – 451, 2008.

G. T. R. Droop. A general equation for estimating $Fe^{3+}$ concentrations in ferromagnesian silicates and oxides from microprobe analyses, using stoichiometric criteria. *Min. Mag.*, 51:431 – 435, 1987.

D. D. Eberl. Clay mineral formation and transformation in rocks and soils. *Phil. Trans. R. Soc. Lond. A*, 311:241 – 257, 1984.

R. F. Egerton. Physical Principles of Electron Microscopy: An Introduction to TEM, SEM, and AEM. *Springer Science*, 357, 2005.

R. F. Egerton. Electron energy-loss spectroscopy in the electron microscope. *Springer Science+Business Media, LLC*, 491, 2011.

S. F. Foley, D. Prelevic, T. Rehfeldt, and D. E. Jacob. Minor and trace elements in olivines as probes into early igneous and mantle melting processes. *Earth Planet. Sci. Lett.*, 363:181 – 191, 2013.

R. C. Friedman-Lentz, G. J. Taylor, and A. H. Treiman. Formation of a Martian pyroxenite: A comparative study of the naklite meteorites and Theo's Flow. *Meteorit. Planet. Sci.*, 34:919 – 932, 1999.

E. J. Gaidos. Cryovolcanism and the recent flow of liquid water on Mars. *Icarus*, 153:218 – 223, 2001.

R. P. Gamble and L. A. Taylor. Crystal/liquid partitioning in augite: Effects of cooling rate. *Earth Planet. Sci. Lett.*, 47:21 – 33, 1980.

L. A Giannuzzi and F. A. Stevie. Introduction to Focused Ion Beams: Instrumentation, Theory, Technique and Practice. *Springer*, 357, 2004.

Ph. Gillet, J.A. Barrat, E. Deloule, M. Wadhwa, A. Jambon, V. Sautter, B. Devouard, D. Neuville, K. Benzerara, and M. Lesourd. Aqueous alteration in the Northwest Africa 817 (NWA 817) Martian meteorite. *Earth Planet. Sci. Lett.*, 203:431 – 444, 2002.

J. A Gilmour, J. D. and. Whitby and G. Turner. Disentangling xenon components in Nakhla: Martian atmosphere, spallation and Martian interior. *Geochim. Cosmochim. Acta*, 65:343 – 354, 2001.

J. D. Gilmour, J. A. Whitby, and G. Turner. Martian atmospheric xenon contents of Nakhla mineral separates: Implications for the origin of elemental mass fractionation. *Earth Planet. Sci. Lett.*, 166:139 – 147, 1999.

C. B. Gomes and K. Keil. Brazilian stone meteorites. *University of New Mexico Press*, page 159, 1980.

J. L. Gooding. Clay-mineraloid weathering products in antarctic meteorites. *Geochim. Cosmochim. Acta*, 50:2215 – 2223, 1986.

J. L. Gooding, S. J. Wentworth, and M. E. Zolensky. Aqueous alteration of the Nakhla meteorite. *Meteoritics*, 326:135 – 143, 1991.

T. L. Grove, M. B. Baker, and R. J. Kinzler. Coupled CaAl-NaSi diffusion in plagioclase feldspar: Experiments and applications to cooling rate speedometry. *Geochim. Cosmochim. Acta*, 48:2113 – 2121, 1984.

L. J. Hallis. Alteration assemblages in the Miller Range and Elephant Moraine regions of Antarctica: Comparisons between terrestrial igneous rocks and Martian meteorites. *Meteorit. Planet. Sci.*, 48:165 – 179, 2013.

L.J. Hallis, G.J. Taylor, K. Nagashima, G.R. Huss, A.W. Needham, M.M. Grady, and I.A. Franchi. Hydrogen isotope analyses of alteration phases in the nakhlite martian meteorites. *Geochim. Cosmochim. Acta*, 97:105 – 119, 2012.

L. A. Hardie and H. P. Eugster. The evolution of closed-bassin brines. *Mineral. Soc. Amer. Spec.*, 3:273 – 290, 1970.

W. K. Hartmann. Martian cratering: Isochron refinement and the chronology of Mars. *Icarus*, 174:294 – 320, 2005.

R. P. Harvey and H. Y. McSween. Petrogenesis of the nakhlite meteorites: Evidence from cumulate mineral zoning. *Geochim. Cosmochim. Acta*, 56:1655 – 1663, 1992.

J. N. Head, H. J. Melosh, and B. A. Ivanov. Martian meteorite launch: High speed ejecta from small craters. *Science*, 298:1752 – 1756, 2002.

P. J. Heaney, E. P. Vicenzi, L. A. Giannuzzi, and K. J. T. Livi. Focused ion beam milling: A method of site-specific sample extraction for microanalysis of Earth and planetary materials. *Am. Min.*, 86:1094 – 1099, 2001.

R. Hellmann, R. Wirth, D. Daval, J.-P. Barnes, J.-M. Penisson, D. Tisserand, T. Epicier, B. Florin, and R. L. Hervig. Unifying natural and laboratory chemical weathering with interfacial dissolution–reprecipitation: A study based on the nanometer-scale chemistry of fluid–silicate interfaces. *Chemical Geology*, 294–295: 203 – 216, 2012.

E. Hill, B. J. Wood, and J. D. Blundy. The effect of Ca-Tschermaks component on trace element partitioning between clinopyroxene and silicate melt. *Lithos*, 53: 203 – 215, 2000.

M. F. Jr. Hochella. Nanoscience and technology: the next revolution in the Earth sciences. *Earth Planet. Sci. Lett.*, 203:593 – 605, 2002.

M.F. Jr. Hochella and A.F. White. Mineral-water interface geochemistry: An overview. *Reviews in Mineralogy*, 23:1 – 15, 1990.

F. Hofer, F. P. Schmidt, W. Grogger, and G. Kothleitner. Fundamentals of electron energy-loss spectroscopy. *IOP Conf. Series: Materials Science and Engineering*, 109:1 – 9, 2016.

M. B. Holness, G. Stripp, M. C. S. Humphreys, I. V. Veksler, T. F. D. Nielsen, and C. Tegner. Silicate liquid immiscibility within the crystal mush: Late-stage magmatic microstructures in the Skaergaard intrusion, East Greenland. *J. Petrol.*, 52:175 – 222, 2011.

M. C. S. Humphreys. Chemical evolution of intercumulus liquid, as recoreded in plagioclase overgrowth rims from the Skaergaard intrusion. *J. Petrol.*, 50:127 – 145, 2009.

N. Imae, Y. Ikeda, and H. Kojima. Petrology of the Yamato nakhlites. *Meteorit. Planet. Sci.*, 40:1581 – 1598, 2005.

A. J. Irving, S. M. Kuehner, K. Ziegler, R. Andreasen, M. Righter, T. J. Lapen, and Pitt D. Chlorophaeite-bearing nakhlite Northwest Africa 10153: Petrology, oxygen and hafnium isotopic composition, and implications for magmatic or crustal water on Mars. *78th Annual Meeting of the Meteoritical Society*, A5251, 2015.

S. E. Jackson. Calibration strategies for elemental analysis by LA–ICP–MS. *Mineralogical Association of Canada*, 40, 2008.

B. M. Jakosky and R. J. Phillips. Mars' volatile and climate history. *Nature*, 412: 237 – 244, 2001.

A. Jambon, J.-A. Barrat, C. Bollinger, V. Sautter, O. Boudouma, R. C. Greenwood, I. A. Franchi, and D. Badia. Northwest Africa 5790. Top sequence of the Nakhlite pile. *41st Lunar and Planet. Sci. Conf.*, A1696, 2010.

K. P. Jochum, W. F. McDonough, H. Palme, and B. Spettel. Compositional constraints on the continental lithospheric mantle from trace elements in spinel peridotite xenoliths. *Nature*, 340:548 – 550, 1989.

K. P. Jochum, M. Willbold, I. Raczek, B. Stoll, and K. Herwig. Chemical characterisation of the USGS reference glasses GSA-1G, GSC-1G, GSD-1G, GSE-1G, BCR-2G, BHVO-2G and BIR-1G using EPMA, ID-TIMS, ID-ICP-MS and LA-ICP-MS. *Geostandards and Geoanalytical Research*, 29(3):285 – 302, 2005.

K. P. Jochum, B. Stoll, K. Herwig, and M. Willbold. Validation of LA-ICP-MS trace element analysis of geological glasses using a new solid-state 193 nm Nd:YAG laser and matrix-matched calibration. *J. Anal. At. Spectrom.*, 22:112 – 121, 2007.

J. H. Jones. Constraints on the structure of the Martian interior determined from the chemical and isotopic systematics of SNC meteorites. *Meteorit. Planet. Sci.*, 38:1807 – 1814, 2003.

V. S. Kamenetsky and R. Maas. Mantle-melt evolution (dynamic source) in the origin of a single morb suite: A perspective from magnesian glasses of Macquarie Island. *J. Petrol.*, 43:1909 – 1922, 2002.

J. S. Kargel and R. G. Strom. Ancient glaciation on Mars. *Geology*, 20:3 – 7, 1992.

H. R. Karlsson, R. N. Clayton, E. K. Gibston, and Mayeda T. K. Water in the SNC meteorites: evidence for a Martian hydrosphere. *Science*, 255:1409 – 1411, 1992.

J. Karner, J. J. Papike, and C. K. Shearer. Comparative planetary mineralogy: Pyroxene major- and minor-element chemistry and partitioning of vanadium between pyroxene and melt in planetary basalts. *Am. Min.*, 91:1574 – 1582, 2006.

A. J.R. Kent. Melt inclusions in basaltic and related volcanic rocks. *Reviews in Mineralogy and Geochemistry*, 69:273 – 331, 2008.

H. H. Kieffer and T. N. Titus. TES mapping of Mars' North Seasonal Cap. *Icarus*, 154:162 – 180, 2001.

R. J. Kirkpatrick. Kinetics of crystallization of igneous rocks. *Reviews in Mineralogy and Geochemistry*, 8:321–395, 1981.

K. Kunze, S. I. Wright, B. L. Adams, and D. J. Dingley. Advances in automatic EBSP single orientation measurements. *Textures and Microstructures*, 20:1 – 4, 1993.

A. C. Lagasa. Kinetic theory in the Earth Sciences. *Princeton University Press*, pages 1 – 811, 1998.

J. Laskar, A. C. M. Correia, M. Gastineau, F. Joutel, B. Levrard, and P. Robutel. Long term evolution and chaotic diffusion of the insolation quantities of Mars. *Icarus*, 170:343 – 364, 2004.

D. C. Lee and A. N. Halliday. Core formation on Mars and differentiated asteroids. *Nature*, 388:854 – 857, 1997.

M. R Lee. Transmission electron microscopy (TEM) of Earth and planetary materials: A review. *Min. Mag.*, 74:1 – 27, 2010.

M. R Lee, P. A. Bland, and Graham G. Preparation for tem samples by focused ion beam (fib) techniques: applications to the study of clays and phyllosilicates in meteorites. *Min. Mag.*, 67:581 – 592, 2003.

M. R. Lee, I. MacLaren, S. M. L. Andersson, A. Kovács, T. Tomkinson, D. F. Mark, and C. L. Smith. Opal-a in the nakhla meteorite: A tracer of ephemeral liquid water in the Amazonian crust of Mars. *Meteorit. Planet. Sci.*, 50:1362 – 1377, 2015.

L. A. Leshin and E. Vicenzi. Aqueous processes recorded by Martian meteorites: Analyzing Martian water on Earth. *Elements*, 2:159 – 164, 2006.

Y. S. Liu, Z. C. Hu, M. Li, and S. Gao. Applications of LA-ICP-MS in the elemental analyses of geological samples. *Chinese Science Bulletin*, 58:3863–3878, 2013.

G. E. Lofgren. Effect of heterogeneous nucleation of basaltic textures: a dynamic crystallization study. *J. Petrol.*, 24:229 – 255, 1983.

G. E. Lofgren, G. R. Huss, and G. J. Wasserburg. An experimental study of trace element partitioning between Ti-Al-clinopyroxene and melt: Equilibrium and kinetic effects including sector zoning. *Am. Min.*, 91:1596 – 1606, 2006.

J. Longhi. Complex magmatic processes on Mars - inferences from the SNC meteorites. *Proc. 21st Lunar Planet. Sci. Conf.*, 21:695 – 709, 1991.

J. Longhi and V. Pan. The parent magmas of the SNC meteorites. *Proc. 19th Lunar Planet. Sci. Conf.*, pages 451 – 464, 1989.

C. C. Lundstrom, H. F. Shaw, F. J. Ryerson, D. L. Phinney, J. B. Gill, and Q. Williams. Compositional controls on the partitioning of U, Th, Ba, Pb, Sr and Zr between clinopyroxene and haplobasaltic melts: Implications for uranium series disequilibria in basalts. *Earth Planet. Sci. Lett.*, 128:407 – 423, 1994.

C. C. Lundstrom, H. F. Shaw, F. J. Ryerson, Q. Williams, and J. Gill. Crystal chemical control of clinopyroxene-melt partitioning in the Di-Ab-An system: Implications for elemental fractionations in the depleted mantle. *Geochim. Cosmochim. Acta*, 62:2849 – 2862, 1998.

T. Maitland and S. Sitzman. Electron backscattered diffraction (EBSD) technique and materials characterization examples. in scanning microscopy for nanotechnology: Techniques and applications. *Springer*, 533, 2007.

M. C. Malin and K. S. Edgett. Evidence for recent groundwater seepage and surface runoff on Mars. *Science*, 288:2330 – 2335, 2000.

B. Marty, K. Th. Marti, and Monod Consortium. Noble gases in new SNC meteorites NWA 817 and NWA 480. *Meteorit. Planet. Sci.*, 36:A122–123, 2001.

F. K. Mazdab. The diversity and occurrence of potassium-dominant amphiboles. *Can. Mineral.*, 41:1329 – 1344, 2003.

F. M. McCubbin, S. M. Elardo, C. K. Jr. Shearer, A. Smirnov, E. H. Hauri, and D. S. Draper. A petrogenetic model for the co-magmatic origin of the chassignites and nakhlites: Inferences from chlorine-rich minerals, petrology, and geochemistry. *Meteorit. Planet. Sci.*, 48:819 – 853, 2013.

W. F. McDonough and S. S. Sun. The composition of the Earth. *Chem. Geol.*, 120: 223 – 253, 1995.

G. McKay, L. Le, and J. Wagstaff. The Nakhla parent melt: REE partition coefficients and clues to major element composition. *25th Lunar and Planet. Sci. Conf.*, A883:965 – 966, 1994.

H. Y. McSween. SNC meteorites: Clues to Martian petrologic evolution? *Reviews of Geophysics*, 23:391 – 416, 1985.

H. Y. Jr. McSween. Martian meteorites as crustal samples, in The Martian Surface: Composition, Mineralogy, and Physical Properties J.F. Bell III, ed. *Cambridge University Press*, pages 383 – 395, 2008.

H. Y. Jr. McSween, G. J. Taylor, and M. B. Wyatt. Elemental composition of the Martian crust. *Science*, 324:736 – 739, 2009.

T. Mikouchi, J. Makishima, T. Kurihara, V. H. Hoffmann, and M. Miyamoto. Relative burial depths of the nakhlites revisited. *43th Lunar and Planet. Sci. Conf.*, A2363, 2012.

D. W. Ming, R. V. Morris, and B. C. Clark. Aqueous alteration on Mars, in The Martian Surface: Composition, Mineralogy, and Physical Properties J.F. Bell III, ed. *Cambridge University Press*, 44:519 – 540, 2007.

K. Misawa, K. Kojima, N. Imae, and N. Nakamura. The Yamato nakhlite consortium, Antarctic Meteorite Research. *Ant. Meteorite Res.(NIPR)*, 16:1 – 12, 2003.

K. L. Mitchell and L. Wilson. Mars: A geologically active planet. *Astronomy & Geophysics*, 44:4.16 – 4.20, 2003.

S. Mollo, P. Del Gaudio, G. Ventura, G. Iezzi, and P. Scarlato. Dependence of clinopyroxene composition on cooling rate in basaltic magmas: Implications for thermobarometry. *Lithos*, 118:302 – 312, 2010.

S. V. S. Murty, R. R. Mahajan, J. N. Goswami, and N. Sinha. Noble gases and nuclear tracks in the nakhlite MIL 03346. *36th Lunar and Planet. Sci. Conf.*, A1280, 2005.

G. Neukum, R. Jaumann, H. Hoffmann, E. Hauber, J. W. Head, A. T. Basilevsky, S. C Ivanov, B. A. and. Werner, S. Van Gasselt, J. B. Murray, T. McCord, and The HRSC Co-Investigator Team. Recent and episodic volcanic and glacial activity on Mars revealed by the High Resolution Stereo Camera. *Nature*, 432: 971 – 979, 2004.

F. Nimmo and K. L. Tanaka. Early crustal evolution of Mars. *Ann. Rev. Earth Planet. Sci.*, 33:133 – 166, 2005.

H. H. Nininger. The Lafayette meteorite. *Popular Astronomy*, 43:404 – 408, 1935.

K. Nishiizumi, D. J. Hillegonds, L. R. McHargue, and A. J. T. Jull. Exposure and terrestrial histories of new Lunar and Martian meteorites. *35th Lunar and Planet. Sci. Conf*, A1130, 2004.

T. Noguchi, T. Nakamura, K. Misawa, N. Imae, T. Aoki, and S. Toch. Laihunite and jarosite in the Yamato 00 nakhlites: Alteration products on Mars? *J. of Geophys. Res.*, 114:1 – 13, 2009.

L. E. Nyquist, D. D. Bogard, C.-Y. Shih, A. Greshake, D. Stoffer, and O. Eugster. Ages and geologic histories of Martian meteorites. *Space Science Reviews*, 96:105 – 164, 2001.

L. E. Nyquist, C.-Y. Shih, F. M. McCubbin, A. R. Santos, C. K. Shearer, Z. X. Peng, P. V. Burger, and C. B. Agee. Rb-Sr and Sm-Nd isotopic and REE studies of igneous components in the bulk matrix domain of Martian breccia Northwest Africa 7034. *Meteorit. Planet. Sci.*, 51:483 – 498, 2016.

K. Oe, G. McKay, and L. Le. Ree and strontium partition coefficients for Nakhla pyroxenes. *32nd Lunar and Planet. Sci. Conf*, A2174, 2001.

N. Onuma, H. Higuchi, H. Wakita, and H. Nagasawa. Trace element partition between two pyroxenes and the host lava. *Earth Planet. Sci. Lett.*, 5:47 – 51, 1968.

J. Orloff, M. Utlaut, and L. Swanson. High Resolution Focused Ion Beams: FIB and its Applications. *Earth Planet. Sci. Lett.*, 304, 2002.

J Orloff, M. Utlaut, and L. Swanson. High resolution ion beams. *Kluwer Academic*, 2003.

J. J. Papike. Pyroxene as a recorder of cumulate formational processes in asteroids, Moon, Mars, Earth: Reading the record with the ion microprobe*. *American Mineralogist*, 81:525 – 544, 1996.

G. A. Parks. Surface energy and adsorption at mineral-water interfaces: An introduction. *Reviews in Mineralogy*, 23:133 – 176, 1990.

J. C. Pearl, M. D. Smith, B. J. Conrath, J. L. Bandfield, and P. R. Christensen. Observations of Martian ice clouds by the Mars Global Surveyor Thermal Emission Spectrometer: The first Martian year. *J. of Geophys. Res.: Planets*, 106: 12325 – 12338, 2001.

R. J. Phillips, M. T. Zuber, S. C. Solomon, M. P. Golombek, B. M. Jakosky, W. B. Banerdt, D. E. Smith, R. M. E. Williams, B. M. Hynek, O. Aharonson, and Steven A. Hauck II. Ancient geodynamics and global-scale hydrology on Mars. *Science*, 291:2587 – 2591, 2001.

A. Poldervaart and H. H. Hess. Pyroxenes in the crystallization of basaltic magma. *J. Geol.*, 59:472 – 489, 1951.

G. T. Prior. The meteoritic stones of El Nakla El Baharia (Egypt). *Min. Mag.*, 16: 274 – 281, 1912.

A Putnis. Mineral replacement reactions,. *Reviews in Mineralogy & Geochemistry*, 70:87 – 124, 2009.

A. Putnis and C. V. Putnis. The mechanism of reequilibration of solids in the presence of a fluid phase. *Journal of Solid State Chemistry*, 180:1783 – 1786, 2007.

A. M. Reid and T. E. Bunch. The nakhlites II: where, when, and how. *Meteoritics*, 10:317 – 324, 1975.

F. Richter, M. Chaussidon, R. Mendybaev, and E. Kite. Reassessing the cooling rate and geologic setting of Martian meteorites MIL 03346 and NWA 817. *Geochim. Cosmochim. Acta*, 182:1 – 23, 2016.

H. R. Rollinson. Using Geochimcal Data: Evaluation, Presentation, Interpretation. *Longman geochemistry series, UK*, pages 1 – 352, 1993.

E. Ruiz-Agudo, C.V. Putnis, and A. Putnis. Coupled dissolution and precipitation at mineral–fluid interfaces. *Chemical Geology*, 383:132 – 146, 2014.

V. J. M. Salters and N. Shimizu. World-wide occurrence of HFSE-depleted mantle. *Geochim. Cosmochim. Acta*, 52:2177 – 2182, 1988.

V. Sautter, J. A. Barrat, A. Jambon, J. P. Lorand, Ph. Gillet, M. Javoy, J. L. Joron, and M. Lesoud. A new Martian meteorite from Morocco: the nakhlite North West Africa 817. *Earth Planet. Sci. Lett.*, 195:223 – 238, 2002.

V. Sautter, A. Jambon, and O. Boudouma. Cl-amphibole in the naklite MIL 03346: Evidence for sediment contamination in a Martian meteorite. *Earth Planet. Sci. Lett.*, 252:45 – 55, 2006.

A. J. Schwartz, M. Kumar, B. L. Adams, and D. P. Field. Electron Backscatter Diffraction in Materials Science. *Spinger*, 402, 2010.

C.-Y. Shih, L. E. Nyquist, Y. Reese, and A. Jambon. Sm-Nd isotopic studies of two nakhlites, NWA 5790 and Nakhla. *41st Lunar and Planet. Sci. Conf.*, A1367, 2010.

T. Simkin and J. V. Smith. Minor-element distribution in olivine. *J. Geol.*, 78:304 – 325, 1970.

R. B. Singer and H.Y. Jr. McSween. The igneous crust of Mars: compositional evidence from remote sensing and the SNC meteorites. *Resources of near-Earth space*, pages 709 – 736, 1970.

T. Skulski, W. Minarik, and E. B. Watson. High-pressure experimental trace-element partitioning between clinopyroxene and basaltic melts. *Chemical Geology*, 117:127 – 147, 1994.

J. R. Smyth and D. L. Bish. Crystal structures and cation sites of the rock-forming minerals. *J. Geol.*, 332, 1989.

G. J. Stockmann, D. Wolff-Boenisch, S. R. Gislason, and E. H. Oelkers. Do carbonate precipitates affect dissolution kinetics? 1: Basaltic glass. *Chemical Geology*, 284:306 – 316, 2011.

D. Stoffler. Maskelynite confirmed as diaplectic glass: Indication for peak shock pressures below 45 Gpa in all Martian meteorites. *31st Lunar and Planet. Sci. Conf.*, A1170, 2000.

D. Stojakovic. Electron backscatter diffraction in materials characterization. *Processing and Application of Ceramics*, 6:1 – 13, 2012.

J. D. Stopar, G. J. Taylor, M. A. Velbel, M. D. Norman, E. P. Vicenzi, and L. J. Hallis. Element abundances, patterns, and mobility in Nakhlite Miller Range 03346 and implications for aqueous alteration. *Geochim. Cosmochim. Acta*, 112: 208 – 225, 2013.

N. A. Stroncik and H.-U. Schmincke. Palagonite – a review. *International Journal of Earth Sciences*, 91(4):680–697, 2002.

T.D. Swindle, A. H. Treiman, D. J. Lindstrom, M. K. Burkland, B. A. Cohen, J. A. Grier, B. Li, and E. K. Olson. Noble gases in iddingsite from the Lafayette meteorite: Evidence for liquid water on Mars in the last few hundred million years. *Meteorit. Planet. Sci.*, 35:107 – 115, 2000.

R. Thomas. Practical guide to ICP-MS: A tutorial for beginners. *CRC Press*, pages 1 – 446, 2013.

R. N. Thompson. Some high-pressure pyroxenes. *Min. Mag.*, 39:768 – 787, 1974.

J. E. Tillman, N. C. Johnson, P. Guttorp, and D. B. Percival. The Martian annual atmospheric pressure cycle: Years without great dust storms. *J. of Geophys. Res.: Planets*, 98:10963 – 10971, 1993.

T. Tomkinson, M. R. Lee, D. F. Mark, K. J. Dobson, and I. A. Franchi. The northwest africa (NWA) 5790 meteorite: A mesostasis-rich nakhlite with little or no Martian aqueous alteration. *Meteorit. Planet. Sci.*, 50:287 – 304, 2015.

N. J. Tosca and S. M. McLennan. Chemical divides and evaporite assemblages on Mars. *Earth Planet. Sci. Lett.*, 241:21 – 31, 2006.

N. J. Tosca, S. M. McLennan, D. H. Lindsley, and M. A. A. Schoonen. Acid-sulfate weathering of synthetic Martian basalt: The acid fog model revisited. *J. of Geophys. Res.: Planets*, 109:1 – 29, 2004.

A. H. Treiman. The nakhlite meteorites: augite-rich igneous rocks from Mars. *18th Lunar and Planet. Sci. Conf.*, A1022, 1987.

A. H. Treiman. Complex petrogenesis of the Nakhla (SNC) meteorite: Evidence from petrography and mineral chemistry. *Proc. Lunar Planet. Sci. Conf.*, 20:273 – 280, 1990.

A. H. Treiman. The parental magma of the Nakhla (SNC) achondrite, inferred from magmatic inclusions. *Geochim. Cosmochim. Acta*, 57:4753 – 4767, 1993.

A. H. Treiman. The nakhlite meteorites: Augite-rich igneous rocks from Mars. *Chem. Erde*, 65:203 – 270, 2005.

A. H. Treiman and A. J. Irving. Petrology of Martian meteorite Northwest Africa 998. *Meteorit. Planet. Sci.*, 43:829 – 854, 2008.

A. H. Treiman, R. A. Barrett, and J. Gooding. Preterrestrial aqueous alteration of the Lafayette (SNC) meteorite. *Meteoritics*, 28:86 – 97, 1993.

A. Udry, H. Y. Jr. McSween, P. Lecumberri-Sanchez, and R. J. Bodnar. Paired nakhlites MIL 090030, 090032, 090136, and 03346: Insights into the Miller Range parent meteorite. *Meteorit. Planet. Sci.*, 47:1575 – 1589, 2012.

J. L. Vago, B. Gardini, and P. Baglioni. ExoMars: ESA's mission to search for signs of life on the Red Planet. *37th Lunar Planet. Sci. Conf.*, A1871, 2006.

J. A. Van Orman, T. L. Grove, and N. Shimizu. Diffusive fractionation of trace elements during production and transport of melt in earth's upper mantle. *Earth Planet. Sci. Lett.*, 198:93 – 112, 2002.

E. M. Varela, G. Kurat, and R. Clocchiatti. Glass-bearing inclusions in nakhla (SNC meteorite) augite: Heterogeneously trapped phases. *Min. and Petrol.*, 71: 155 – 172, 2001.

E. M. Varela, G. Kurat, and R. Clocchiatti. Reply to comment: "The Nakhla Martian meteorite is a cumulate igneous rock" by A. Treiman. *Min. and Petrol.*, 77:279 – 285, 2003.

M. A. Velbel. Dissolution of olivine during natural weathering. *Geochim. Cosmochim. Acta*, 73:6098 – 6113, 2009.

M. A. Velbel. Aqueous alteration in Martian meteorites: Comparing relations in igneous-rock weathering of Martian meteorites and in the sedimentary cycle of mars, Grotzinger J. P. and Milliken R. E., ed. *Society for Sedimentary Geology Special Publication*, 102:97 – 117, 2012.

M. A. Velbel. Terrestrial weathering of ordinary chondrites in nature and continuing during laboratory storage and processing: Review and implications for Hayabusa sample integrity. *Meteorit. Planet. Sci.*, 49:154 – 171, 2014.

M. Wadhwa and G. Crozaz. Trace and minor elements in minerals of nakhlites and chassigny: Clues to their petrogenesis. *Geochim. Cosmochim. Acta*, 59:3629 – 3645, 1995.

M. Wadhwa, G. Crozaz, and J.-A. Barrat. Trace element distributions in the Yamato 000593/000749, NWA 817 and NWA 998 nakhlites: Implications for their petrogenesis and mantle source on Mars. *Antarct. Meteorite Res.*, 17:97 – 116, 2004.

E. B. Watson. Henry's law behavior in simple systems and in magmas: Criteria for discerning concentration-dependent partition coefficients in nature. *Geochim. Cosmochim. Acta*, 49:917 – 923, 1985.

J. D. Webster. Chloride solubility in felsic melts and the role of chloride in magmatic degassing. *J. Petrol.*, 38:1793–1807, 1997.

B. P. Weiss, H. Vali, F. J. Baudenbacher, J. L. Kirschvink, S. T. Stewart, and D. L. Shuster. Records of an ancient Martian magnetic field in ALH84001. *Earth Planet. Sci. Lett.*, 201:449 – 463, 2002.

E. J. Weissbart and D. J. Rimstidt. Wollastonite: Incongruent dissolution and leached layer formation. *Geochim. Cosmochim. Acta*, 64:4007 – 4016, 2000.

S. J. Wentworth, K. E. Gibson, M. A. Velbel, and D. S. McKay. Antarctic dry valleys and indigeneous weathering in Mars meteorites: Implications for water and life on mars. *Icarus*, 174:383 – 395, 2005.

W. M. White. Geochemistry. *Wiley-Blackwell*, 660, 2013.

R. Wieler, L. Huber, H. Busemann, S. Seiler, I. Leya, C. Maden, J. Masarik, M. M. M. Meier, K. Nagao, R. Trappitsch, and A. J. Irving. Noble gases in 18 Martian meteorites and angrite Northwest Africa 7812—exposure ages, trapped gases, and a re-evaluation of the evidence for solar cosmic ray-produced neon in shergottites and other achondrites. *Meteorit. Planet. Sci.*, 51:407 – 428, 2016.

D. B. Williams and B. C. Carter. Transmission electron microscopy. *Springer US*, 804, 2009.

R. K. Workman and H. R. Stanley. Major and trace element composition of the depleted MORB mantle (DMM. *Earth Planet. Sci. Lett.*, 231:53 – 72, 2005.

# Appendices

# *Appendix A*

| | Trace Element concentration (in µg/g) in augite of NWA 5790 | | | | |
|---|---|---|---|---|---|
| La | 0.6 ± 0.09 | 0.682 ± 0.099 | 0.499 ± 0.077 | 0.835 ± 0.091 | 0.548 ± 0.08 |
| Ce | 2.67 ± 0.27 | 2.85 ± 0.18 | 1.94 ± 0.15 | 2.91 ± 0.18 | 2.24 ± 0.17 |
| Pr | 0.497 ± 0.054 | 0.607 ± 0.065 | 0.358 ± 0.047 | 0.621 ± 0.071 | 0.425 ± 0.055 |
| Nd | 3.66 ± 0.34 | 3.74 ± 0.48 | 2.26 ± 0.36 | 3.6 ± 0.44 | 2.49 ± 0.35 |
| Sm | 1.2 ± 0.18 | 1.17 ± 0.18 | 0.74 ± 0.14 | 1.16 ± 0.22 | 0.8 ± 0.15 |
| Eu | 0.342 ± 0.047 | 0.402 ± 0.054 | 0.204 ± 0.044 | 0.407 ± 0.06 | 0.251 ± 0.04 |
| Gd | 1.44 ± 0.24 | 1.59 ± 0.23 | 1.02 ± 0.18 | 1.54 ± 0.2 | 1.13 ± 0.21 |
| Tb | 0.204 ± 0.029 | 0.216 ± 0.031 | 0.164 ± 0.028 | 0.203 ± 0.033 | 0.146 ± 0.029 |
| Dy | 1.35 ± 0.2 | 1.41 ± 0.13 | 0.91 ± 0.12 | 1.56 ± 0.15 | 0.97 ± 0.15 |
| Ho | 0.265 ± 0.035 | 0.266 ± 0.033 | 0.165 ± 0.027 | 0.278 ± 0.04 | 0.224 ± 0.028 |
| Er | 0.696 ± 0.099 | 0.838 ± 0.079 | 0.438 ± 0.072 | 0.73 ± 0.11 | 0.443 ± 0.088 |
| Tm | 0.09 ± 0.019 | 0.084 ± 0.016 | 0.045 ± 0.013 | 0.101 ± 0.02 | 0.056 ± 0.016 |
| Yb | 0.43 ± 0.12 | 0.63 ± 0.12 | 0.34 ± 0.091 | 0.58 ± 0.13 | 0.36 ± 0.1 |
| Rb | 0.01 ± 0.14 | 0.04 ± 0.15 | bd | 0.01 ± 0.15 | bd |
| Ba | 0.27 ± 0.14 | 2.51 ± 0.53 | 0.13 ± 0.1 | 0.69 ± 0.26 | 0.36 ± 0.16 |
| Th | bd | bd | bd | bd | bd |
| Nb | 0.002 ± 0.005 | bd | 0.002 ± 0.005 | bd | bd |
| Sr | 34.4 ± 1.9 | 36.57 ± 0.98 | 31.9 ± 1.2 | 36.8 ± 1.2 | 31 ± 1.1 |
| Zr | 5.38 ± 0.82 | 5.57 ± 3.09 | 3.09 ± 0.57 | 6.1 ± 0.87 | 4.32 ± 0.64 |
| Ti | 2340 ± 150 | 2426 ± 52 | 1762 ± 68 | 2420 ± 100 | 1936 ± 66 |
| Sc | 87.5 ± 4.7 | 88.7 ± 2.6 | 85.8 ± 3.4 | 91.3 ± 3.5 | 87.8 ± 2.7 |
| V | 295 ± 24 | 309.5 ± 7.2 | 266 ± 6128 | 311 ± 15 | 292 ± 11 |
| Cr | 1270 ± 110 | 1054 ± 27 | 1380 ± 74 | 1288 ± 64 | 1441 ± 60 |
| Mn | 3960 ± 380 | 3915 ± 81 | 3690 ± 190 | 3840 ± 190 | 3780 ± 150 |
| Co | 39.5 ± 3.7 | 39.4 ± 1.3 | 38.3 ± 2.3 | 38.6 ± 1.9 | 38.7 ± 1.8 |
| Ni | 55.6 ± 5.5 | 57.9 ± 2.7 | 54.2 ± 4 | 57.5 ± 3.8 | 54.8 ± 3.3 |
| Y | 6.33 ± 0.5 | 6.82 ± 0.37 | 4.54 ± 0.28 | 6.64 ± 0.4 | 4.93 ± 0.31 |

bd: below detection

| Trace Element concentration (in µg/g) in olivine of NWA 5790 | | |
|---|---|---|
| V | 10.61 ± 0.47 | 11.48 ± 0.5 |
| Cr | 26.1 ± 2.9 | 38 ± 3.6 |
| Mn | 9580 ± 170 | 9460 ± 170 |
| Co | 123.6 ± 3 | 127 ± 2.7 |
| Ni | 4.9 ± 2.6 | 5 ± 4 |
| Zn | 6.3 ± 0.283 | 6.9 ± 0.2 |

Trace Element concentration (in µg/g) in augite of NWA 817

| | | | | | | | |
|---|---|---|---|---|---|---|---|
| La | 0.472 ± 0.073 | 0.378 ± 0.062 | 0.496 ± 0.085 | 1.39 ± 0.18 | 0.576 ± 0.087 | 0.405 ± 0.062 | 0.455 ± 0.066 |
| Ce | 1.9 ± 0.16 | 1.89 ± 0.15 | 1.96 ± 0.17 | 5.32 ± 0.54 | 2.21 ± 0.17 | 2.02 ± 0.14 | 1.81 ± 0.15 |
| Pr | 0.39 ± 0.064 | 0.389 ± 0.069 | 0.397 ± 0.064 | 0.82 ± 0.093 | 0.429 ± 0.064 | 0.446 ± 0.062 | 0.376 ± 0.056 |
| Nd | 2.32 ± 0.35 | 2.69 ± 0.48 | 2.92 ± 0.42 | 4.91 ± 0.67 | 2.26 ± 0.37 | 2.8 ± 0.45 | 2.73 ± 0.42 |
| Sm | 0.86 ± 0.19 | 0.91 ± 0.22 | 0.72 ± 0.17 | 1.49 ± 0.27 | 0.92 ± 0.19 | 0.97 ± 0.17 | 0.78 ± 0.17 |
| Eu | 0.253 ± 0.043 | 0.211 ± 0.05 | 0.208 ± 0.046 | 0.512 ± 0.074 | 0.202 ± 0.04 | 0.242 ± 0.052 | 0.253 ± 0.045 |
| Gd | 0.98 ± 0.17 | 0.83 ± 0.17 | 0.94 ± 0.16 | 1.29 ± 0.2 | 0.77 ± 0.17 | 0.9 ± 0.15 | 1.02 ± 0.2 |
| Tb | 0.133 ± 0.027 | 0.158 ± 0.029 | 0.159 ± 0.033 | 0.235 ± 0.035 | 0.112 ± 0.026 | 0.144 ± 0.026 | 0.148 ± 0.027 |
| Dy | 0.91 ± 0.17 | 0.91 ± 0.14 | 1.09 ± 0.19 | 1.64 ± 0.18 | 0.85 ± 0.13 | 1.01 ± 0.17 | 1 ± 0.15 |
| Ho | 0.178 ± 0.026 | 0.151 ± 0.032 | 0.163 ± 0.026 | 0.28 ± 0.042 | 0.17 ± 0.03 | 0.206 ± 0.028 | 0.169 ± 0.025 |
| Er | 0.445 ± 0.083 | 0.47 ± 0.1 | 0.47 ± 0.11 | 0.89 ± 0.12 | 0.461 ± 0.072 | 0.49 ± 0.1 | 0.462 ± 0.081 |
| Tm | 0.075 ± 0.019 | 0.071 ± 0.02 | 0.057 ± 0.016 | 0.119 ± 0.026 | 0.059 ± 0.017 | 0.046 ± 0.017 | 0.061 ± 0.017 |
| Yb | 0.41 ± 0.11 | 0.39 ± 0.11 | 0.43 ± 0.15 | 0.71 ± 0.15 | 0.4 ± 0.12 | 0.37 ± 0.11 | 0.37 ± 0.12 |
| Rb | 0.29 ± 0.12 | 0.09 ± 0.15 | bd | 2.03 ± 0.34 | 0.16 ± 0.15 | bd | 0.09 ± 0.13 |
| Ba | 0.37 ± 0.18 | 0.28 ± 0.17 | 0.61 ± 0.23 | 1370 ± 99 | 278 ± 15 | 0.29 ± 0.33 | 0.29 ± 0.17 |
| Th | bd | bd | bd | 0.128 ± 0.031 | 0.004 ± 0.006 | bd | bd |
| Nb | bd | bd | bd | 0.44 ± 0.13 | bd | bd | bd |
| Sr | 33.4 ± 0.9 | 32.88 ± 0.98 | 35.8 ± 1.3 | 456 ± 27 | 116.5 ± 6 | 34.3 ± 1.3 | 35.49 ± 0.97 |
| Zr | 2.57 ± 0.53 | 2.41 ± 0.71 | 3.49 ± 0.89 | 16.3 ± 2.3 | 2.96 ± 0.63 | 3.02 ± 0.65 | 3.41 ± 0.66 |
| Ti | 1920 ± 42 | 1885 ± 48 | 1892 ± 41 | 2810 ± 170 | 1789 ± 51 | 1823 ± 58 | 1818 ± 37 |
| Sc | 78.6 ± 1.6 | 75 ± 2.1 | 77.1 ± 2 | 65.4 ± 1.8 | 73.5 ± 2.4 | 76.8 ± 2.7 | 78.7 ± 1.7 |
| V | 246.5 ± 5.7 | 244.5 ± 5.2 | 240 ± 6 | 225.3 ± 6.1 | 239 ± 6.6 | 252.9 ± 8.6 | 240.9 ± 4.8 |
| Cr | 2888 ± 56 | 2802 ± 68 | 2654 ± 66 | 1640 ± 86 | 2780 ± 86 | 2951 ± 90 | 2861 ± 50 |
| Mn | 3313 ± 56 | 3447 ± 77 | 3291 ± 73 | 3397 ± 94 | 3260 ± 110 | 3470 ± 110 | 3311 ± 59 |
| Co | 37.9 ± 1.3 | 39 ± 1.3 | 38.6 ± 1.4 | 36.1 ± 1.5 | 37.2 ± 1.6 | 37.8 ± 1.7 | 36.9 ± 1.2 |
| Ni | 66.6 ± 3.2 | 71.5 ± 3.9 | 66.1 ± 3.6 | 39.8 ± 3 | 65.6 ± 3.9 | 71.3 ± 4 | 67.5 ± 3.6 |
| Y | 4.62 ± 0.26 | 4.92 ± 0.36 | 4.57 ± 0.3 | 7.76 ± 0.59 | 4.55 ± 0.29 | 4.85 ± 0.31 | 4.29 ± 0.22 |

bd: below detection

| Trace Element concentration (in µg/g) in melt of NWA 817 | | |
|---|---|---|
| La | 14.97 ± 0.9 | 24.6 ± 1.1 |
| Ce | 39.4 ± 2.1 | 57.3 ± 2.2 |
| Pr | 5.43 ± 0.36 | 7.94 ± 0.4 |
| Nd | 25.6 ± 1.5 | 34.3 ± 2.1 |
| Sm | 6.03 ± 0.51 | 6.91 ± 0.53 |
| Eu | 1.51 ± 0.13 | 1.84 ± 0.15 |
| Gd | 5.07 ± 0.54 | 5.6 ± 0.47 |
| Tb | 0.785 ± 0.07 | 0.817 ± 0.07 |
| Dy | 4.6 ± 0.36 | 4.95 ± 0.37 |
| Ho | 0.006 ± 0.076 | 0.978 ± 0.081 |
| Er | 2.53 ± 0.24 | 2.79 ± 0.21 |
| Tm | 0.347 ± 0.048 | 0.328 ± 0.041 |
| Yb | 2.4 ± 0.28 | 2.23 ± 0.27 |
| Rb | 10.8 ± 1.1 | 17.51 ± 0.82 |
| Ba | 611 ± 76 | 359 ± 14 |
| Th | 1.22 ± 0.14 | 2.4 ± 0.17 |
| Nb | 4.6 ± 0.56 | 13.88 ± 0.72 |
| Sr | 563 ± 50 | 523 ± 14 |
| Zr | 70.7 ± 5.4 | 84.9 ± 4.8 |
| Ti | 3740 ± 150 | 3120 ± 120 |

| Trace Element concentration (in µg/g) in olivine of NWA 817 | | | | |
|---|---|---|---|---|
| V | 10.95 ± 0.65 | 12.37 ± 0.69 | 208.9 ± 5.1 | 7.89 ± 0.65 |
| Cr | 65 ± 4.1 | 83.8 ± 5.5 | 2054 ± 62 | 17.4 ± 3.7 |
| Mn | 7290 ± 200 | 7620 ± 140 | 2942 ± 48 | 13470 ± 360 |
| Co | 131.6 ± 3.9 | 134.9 ± 3.1 | 32.92 ± 0.92 | 164.5 ± 5.5 |
| Ni | 211.4 ± 7.4 | 226.3 ± 6.5 | 52.5 ± 2.7 | 179.2 ± 9.6 |
| Zn | 189.1 ± 8 | 182.2 ± 7.4 | 47.9 ± 3.3 | 414 ± 16 |

Trace Element concentration (in µg/g) in augite of Y 000593

| | core | | | | | rim | |
|---|---|---|---|---|---|---|---|
| La | 0.244 ± 0.046 | 0.361 ± 0.056 | 0.431 ± 0.076 | 0.4 ± 0.077 | 0.401 ± 0.072 | 0.39 ± 0.08 | 0.287 ± 0.053 |
| Ce | 1.22 ± 0.13 | 1.7 ± 0.16 | 1.61 ± 0.17 | 2 ± 0.21 | 1.72 ± 0.18 | 1.86 ± 0.17 | 1.41 ± 0.14 |
| Pr | 0.231 ± 0.044 | 0.298 ± 0.048 | 0.314 ± 0.55 | 0.328 ± 0.068 | 0.316 ± 0.054 | 0.362 ± 0.067 | 0.268 ± 0.051 |
| Nd | 1.7 ± 0.28 | 2.01 ± 0.32 | 1.89 ± 0.27 | 2.11 ± 0.33 | 1.91 ± 0.37 | 2.18 ± 0.28 | 1.76 ± 0.26 |
| Sm | 0.62 ± 0.12 | 0.57 ± 0.11 | 0.36 ± 0.1 | 0.82 ± 0.17 | 0.71 ± 0.14 | 0.62 ± 0.12 | 0.51 ± 0.1 |
| Eu | 0.24 ± 0.046 | 0.227 ± 0.044 | 0.136 ± 0.036 | 0.239 ± 0.054 | 0.201 ± 0.04 | 0.24 ± 0.046 | 0.19 ± 0.039 |
| Gd | 0.53 ± 0.14 | 0.81 ± 0.13 | 0.54 ± 0.1 | 0.65 ± 0.16 | 0.64 ± 0.13 | 0.66 ± 0.14 | 0.66 ± 0.13 |
| Tb | 0.084 ± 0.017 | 0.112 ± 0.022 | 0.094 ± 0.02 | 0.122 ± 0.022 | 0.092 ± 0.02 | 0.103 ± 0.019 | 0.094 ± 0.021 |
| Dy | 0.441 ± 0.086 | 0.74 ± 0.11 | 0.61 ± 0.1 | 0.72 ± 0.13 | 0.557 ± 0.094 | 0.76 ± 0.11 | 0.57 ± 0.1 |
| Ho | 0.101 ± 0.021 | 0.149 ± 0.023 | 0.11 ± 0.02 | 0.123 ± 0.023 | 0.093 ± 0.019 | 0.123 ± 0.02 | 0.114 ± 0.021 |
| Er | 0.265 ± 0.056 | 0.388 ± 0.054 | 0.245 ± 0.058 | 0.369 ± 0.063 | 0.23 ± 0.048 | 0.334 ± 0.055 | 0.258 ± 0.04 |
| Tm | 0.05 ± 0.012 | 0.051 ± 0.012 | 0.043 ± 0.013 | 0.038 ± 0.012 | 0.043 ± 0.013 | 0.033 ± 0.009 | 0.041 ± 0.009 |
| Yb | 0.276 ± 0.079 | 0.396 ± 0.091 | 0.208 ± 0.068 | 0.3 ± 0.87 | 0.25 ± 0.1 | 0.366 ± 0.07 | 0.278 ± 0.082 |
| Rb | 0.01 ± 0.11 | bd | 0.19 ± 0.1 | 0.11 ± 0.16 | 0.16 ± 0.12 | 0.05 ± 0.13 | bd |
| Ba | 0.105 ± 0.092 | 0.29 ± 0.15 | 0.69 ± 0.3 | 0.039 ± 0.06 | 0.09 ± 0.092 | 0.084 ± 0.084 | 0.053 ± 0.068 |
| Th | bd | 0.005 ± 0.005 | 0.016 ± 0.009 | bd | bd | 0.005 ± 0.005 | bd |
| Nb | 0.025 ± 0.018 | bd | 0.066 ± 0.029 | bd | bd | bd | bd |
| Sr | 25.7 ± 1.5 | 28.3 ± 1.2 | 20.4 ± 1.1 | 27.6 ± 2.4 | 30.8 ± 2.1 | 22.1 ± 1.3 | 20.4 ± 1.4 |
| Zr | 1.24 ± 0.34 | 2.24 ± 0.49 | 2.05 ± 0.44 | 2.07 ± 0.49 | 1.75 ± 0.41 | 2.75 ± 0.58 | 2.28 ± 0.54 |
| Ti | 1221 ± 65 | 1515 ± 48 | 1385 ± 76 | 1500 ± 130 | 1397 ± 99 | 1823 ± 88 | 1529 ± 98 |
| Sc | 62 ± 3 | 67.6 ± 2.1 | 90 ± 4.1 | 58.9 ± 4.3 | 60.3 ± 4.7 | 89.2 ± 3.9 | 83 ± 4.7 |
| V | 221 ± 11 | 233.6 ± 8.2 | 296 ± 19 | 221 ± 18 | 237 ± 17 | 273 ± 14 | 258 ± 16 |
| Cr | 2710 ± 150 | 2930 ± 100 | 1166 ± 65 | 2470 ± 180 | 27.20 ± 190 | 393 ± 23 | 768 ± 46 |
| Mn | 3770 ± 200 | 3740 ± 140 | 4170 ± 250 | 4060 ± 290 | 3500 ± 250 | 4690 ± 260 | 4330 ± 260 |
| Co | 39.6 ± 2.6 | 37.8 ± 1.8 | 37.9 ± 2.6 | 40.4 ± 3.1 | 37.7 ± 2.7 | 37.7 ± 2 | 38.5 ± 2.3 |
| Ni | 73.6 ± 5.3 | 71.9 ± 4.2 | 46.5 ± 3.5 | 72.6 ± 5.9 | 76.7 ± 6 | 38.9 ± 2.9 | 40.6 ± 2.7 |
| Y | 2.53 ± 0.21 | 3.71 ± 0.23 | 2.61 ± 0.22 | 3.74 ± 0.38 | 2.83 ± 0.27 | 3.27 ± 0.26 | 3.04 ± 0.23 |

bd: below detection

Trace Element concentration (in µg/g) in plagioclase and orthopyroxene of Y 000593

| | plagioclase | | orthopyroxene | | |
|---|---|---|---|---|---|
| La | 2.07 ± 0.24 | 9.6 ± 1.3 | 0.366 ± 0.066 | 0.303 ± 0.077 | 0.326 ± 0.064 |
| Ce | 7.66 ± 0.58 | 53.2 ± 3.8 | 1.41 ± 0.13 | 0.93 ± 0.14 | 1.78 ± 0.19 |
| Pr | 0.496 ± 0.089 | 2.86 ± 0.37 | 0.283 ± 0.051 | 0.103 ± 0.035 | 0.263 ± 0.048 |
| Nd | 1.8 ± 0.36 | 11.8 ± 1.4 | 2.04 ± 0.39 | 0.67 ± 0.18 | 1.96 ± 0.34 |
| Sm | 0.27 ± 0.1 | 2.37 ± 0.43 | 0.52 ± 0.12 | 0.36 ± 0.1 | 0.57 ± 0.15 |
| Eu | 1.31 ± 0.16 | 1.49 ± 0.17 | 0.186 ± 0.044 | 0.127 ± 0.044 | 0.122 ± 0.034 |
| Gd | 0.31 ± 0.12 | 1.88 ± 0.38 | 0.59 ± 0.11 | 0.243 ± 0.078 | 0.74 ± 0.14 |
| Tb | 0.036 ± 0.015 | 0.27 ± 0.053 | 0.115 ± 0.022 | 0.079 ± 0.018 | 0.112 ± 0.018 |
| Dy | 0.303 ± 0.094 | 1.5 ± 0.25 | 0.67 ± 0.14 | 0.48 ± 0.1 | 0.69 ± 0.13 |
| Ho | 0.031 ± 0.012 | 0.305 ± 0.043 | 0.126 ± 0.03 | 0.103 ± 0.024 | 0.125 ± 0.03 |
| Er | 0.098 ± 0.042 | 0.7 ± 0.16 | 0.378 ± 0.074 | 0.417 ± 0.08 | 0.384 ± 0.071 |
| Tm | 0.011 ± 0.008 | 0.074 ± 0.022 | 0.056 ± 0.016 | 0.065 ± 0.02 | 0.043 ± 0.013 |
| Yb | 0.135 ± 0.068 | 0.69 ± 0.19 | 0.207 ± 0.075 | 0.54 ± 0.14 | 0.224 ± 0.09 |
| Rb | 30.1 ± 2.9 | 61.1 ± 4 | 0.17 ± 0.15 | 0.91 ± 0.27 | bd |
| Ba | 537 ± 36 | 304 ± 22 | 0.37 ± 0.19 | 29.2 ± 5.1 | 0.077 ± 0.089 |
| Th | 1.42 ± 0.16 | 4.73 ± 0.49 | bd | 0.184 ± 0.035 | 0.019 ± 0.011 |
| Nb | 10.9 ± 2.3 | 26.6 ± 5.4 | bd | 0.08 ± 0.036 | bd |
| Sr | 557 ± 23 | 436 ± 27 | 28.3 ± 1.2 | 53.2 ± 8.8 | 21.53 ± 0.88 |
| Zr | 96 ± 22 | 460 ± 150 | 1.61 ± 0.44 | 3.93 ± 0.9 | 2.63 ± 0.53 |
| Ti | 730 ± 120 | 1050 ± 240 | 1514 ± 56 | 572 ± 29 | 1815 ± 73 |

bd: below detection

| Trace Element concentration (in µg/g) in olivine of Y 000593 | | | | | |
|---|---|---|---|---|---|
| | olivine | | laihunite | | |
| V | 50.36 ± 0.39 | 32.5 ± 6 | 9.61 ± 0.53 | 7.46 ± 0.5 | 4.68 ± 0.42 |
| Cr | 30.5 ± 3.2 | 366 ± 83 | 56.8 ± 4.8 | 80.9 ± 5.8 | 34.5 ± 3.1 |
| Mn | 9160 ± 360 | 7230 ± 200 | 7300 ± 140 | 8080 ± 210 | 7620 ± 180 |
| Co | 107 ± 4.1 | 108.1 ± 3 | 114.7 ± 3.3 | 79.7 ± 2.6 | 72.6 ± 2 |
| Ni | 174.4 ± 7.7 | 176.3 ± 5.7 | 158.8 ± 6.9 | 112.9 ± 5.1 | 88.3 ± 3.3 |
| Zn | 250 ± 11 | 246.5 ± 8.1 | 221.7 ± 6.8 | 248.8 ± 9.1 | 222.4 ± 18.9 |

| Trace Element concentration (in µg/g) in augite of Y 000749 | | | |
|---|---|---|---|
| La | 0.566 ± 0.088 | 0.115 ± 0.038 | 0.089 ± 0.03 |
| Ce | 2.54 ± 0.18 | 0.82 ± 0.12 | 0.544 ± 0.095 |
| Pr | 0.421 ± 0.064 | 0.08 ± 0.029 | 0.117 ± 0.034 |
| Nd | 2.93 ± 0.33 | 0.39 ± 0.16 | 0.49 ± 0.19 |
| Sm | 0.82 ± 0.17 | 0.153 ± 0.071 | 0.138 ± 0.07 |
| Eu | 0.211 ± 0.046 | 0.059 ± 0.025 | 0.056 ± 0.026 |
| Gd | 1.08 ± 0.19 | 0.251 ± 0.089 | 0.251 ± 0.089 |
| Tb | 0.174 ± 0.027 | 0.04 ± 0.011 | 0.04 ± 0.011 |
| Dy | 1.1 ± 0.17 | 0.208 ± 0.06 | 0.208 ± 0.06 |
| Ho | 0.191 ± 0.033 | 0.043 ± 0.013 | 0.043 ± 0.013 |
| Er | 0.534 ± 0.09 | 0.095 ± 0.032 | 0.095 ± 0.032 |
| Tm | 0.047 ± 0.013 | 0.0131 ± 0.0081 | 0.0131 ± 0.0081 |
| Yb | 0.404 ± 0.098 | 0.1 ± 0.057 | 0.1 ± 0.057 |
| Rb | 0.11 ± 0.17 | bd | bd |
| Ba | 0.18 ± 0.19 | 0.19 ± 0.16 | 0.29 ± 0.19 |
| Th | bd | bd | bd |
| Nb | bd | bd | bd |
| Sr | 33.43 ± 0.84 | 13.8 ± 0.48 | 13.79 ± 0.55 |
| Zr | 3.63 ± 0.81 | 0.33 ± 0.2 | 0.46 ± 0.25 |
| Ti | 2018 ± 38 | 648 ± 15 | 666 ± 18 |
| Sc | 68.9 ± 1.5 | 63.4 ± 1.5 | 205 ± 5.7 |
| V | 277.3 ± 4.6 | 208.2 ± 4.6 | 666 ± 18 |
| Cr | 2936 ± 50 | 2682 ± 63 | 2566 ± 75 |
| Mn | 3437 ± 47 | 3572 ± 79 | 3515 ± 92 |
| Co | 38.2 ± 1.2 | 39.8 ± 1.3 | 40.1 ± 1.2 |
| Ni | 77.9 ± 3.8 | 77.3 ± 4.1 | 76.8 ± 4.3 |
| Y | 4.74 ± 0.27 | 1.16 ± 0.13 | 1.18 ± 0.15 |

bd: below detection

| | Trace Element concentration (in µg/g) in augite of Nakhla | | | | | |
|---|---|---|---|---|---|---|
| | core | | | | | rim |
| La | 0.108 ± 0.037 | 0.229 ± 0.049 | 0.135 ± 0.046 | 0.108 ± 0.039 | 0.62 ± 0.1 | 0.79 ± 0.11 |
| Ce | 0.535 ± 0.083 | 1.56 ± 0.16 | 0.76 ± 0.11 | 0.441 ± 0.066 | 2.85 ± 0.16 | 2.89 ± 0.2 |
| Pr | 0.136 ± 0.032 | 0.27 ± 0.054 | 0.123 ± 0.037 | 0.095 ± 0.031 | 0.589 ± 0.083 | 0.52 ± 0.075 |
| Nd | 0.65 ± 0.2 | 1.84 ± 0.36 | 0.74 ± 0.22 | 0.81 ± 0.21 | 4.23 ± 0.52 | 3.54 ± 0.49 |
| Sm | 0.185 ± 0.073 | 0.72 ± 0.16 | 0.38 ± 0.12 | 0.137 ± 0.07 | 1.3 ± 0.21 | 0.82 ± 0.19 |
| Eu | 0.086 ± 0.031 | 0.218 ± 0.039 | 0.107 ± 0.029 | 0.048 ± 0.021 | 0.316 ± 0.052 | 0.337 ± 0.05 |
| Gd | 0.243 ± 0.097 | 0.76 ± 0.19 | 0.266 ± 0.095 | 0.186 ± 0.075 | 1.53 ± 0.22 | 1.13 ± 0.19 |
| Tb | 0.036 ± 0.013 | 0.124 ± 0.024 | 0.063 ± 0.016 | 0.052 ± 0.016 | 0.222 ± 0.029 | 0.164 ± 0.029 |
| Dy | 0.311 ± 0.076 | 0.69 ± 0.13 | 0.259 ± 0.063 | 0.262 ± 0.065 | 1.29 ± 0.19 | 1.19 ± 0.14 |
| Ho | 0.072 ± 0.017 | 0.136 ± 0.025 | 0.076 ± 0.021 | 0.049 ± 0.015 | 0.255 ± 0.041 | 0.269 ± 0.032 |
| Er | 0.12 ± 0.04 | 0.391 ± 0.077 | 0.131 ± 0.049 | 0.155 ± 0.045 | 0.707 ± 0.079 | 0.657 ± 0.093 |
| Tm | 0.0174 ± 0.0094 | 0.051 ± 0.016 | 0.0196 ± 0.0096 | 0.0062 ± 0.0061 | 0.089 ± 0.026 | 0.087 ± 0.019 |
| Yb | 0.137 ± 0.062 | 0.26 ± 0.095 | 0.23 ± 0.087 | 0.141 ± 0.061 | 0.71 ± 0.13 | 0.62 ± 0.11 |
| Rb | bd | bd | 0.08 ± 0.12 | 0.06 ± 0.12 | 0.16 ± 0.14 | 0.91 ± 0.19 |
| Ba | bd | 0.11 ± 0.11 | 0.35 ± 0.19 | 0.31 ± 0.18 | bd | 0.14 ± 0.12 |
| Th | bd | bd | bd | bd | bd | bd |
| Nb | bd | 0.044 ± 0.029 | bd | bd | bd | 0.021 ± 0.02 |
| Sr | 13.82 ± 0.56 | 25.64 ± 0.84 | 15.73 ± 0.54 | 29.6 ± 1.1 | 17.91 ± 0.75 | 27.49 ± 0.93 |
| Zr | 0.28 ± 0.2 | 7.42 ± 0.91 | 0.5 ± 0.25 | 1.52 ± 0.4 | 0.99 ± 0.36 | 5.05 ± 0.84 |
| Ti | 694 ± 16 | 2347 ± 63 | 764 ± 17 | 1705 ± 35 | 952 ± 29 | 2512 ± 52 |
| Sc | 68.7 ± 1.7 | 69.6 ± 2.3 | 69.3 ± 2 | 63.5 ± 1.4 | 73.3 ± 1.8 | 81 ± 2.2 |
| V | 204.5 ± 3.7 | 245.3 ± 5.5 | 217.6 ± 4.9 | 208.8 ± 4.6 | 221.2 ± 4.5 | 308.5 ± 7.7 |
| Cr | 2520 ± 52 | 2445 ± 54 | 2481 ± 56 | 2381 ± 58 | 929 ± 55 | 881 ± 35 |
| Mn | 3470 ± 54 | 3450 ± 73 | 3542 ± 81 | 3600 ± 61 | 4086 ± 85 | 4305 ± 85 |
| Co | 42.1 ± 1.2 | 41.4 ± 1.4 | 40.6 ± 1.3 | 39.5 ± 1.6 | 37.3 ± 1.5 | 39.5 ± 1.5 |
| Ni | 80.4 ± 2.8 | 80.9 ± 4.2 | 84.1 ± 4.1 | 82.4 ± 4 | 47.4 ± 3.8 | 48.4 ± 3.3 |
| Y | 1.42 ± 0.14 | 3.82 ± 0.27 | 1.85 ± 0.15 | 1.43 ± 0.14 | 6.43 ± 0.31 | 5.21 ± 0.35 |

bd: below detection

| Trace Element concentration (in µg/g) Nakhla | | |
|---|---|---|
| | orthopyroxene | melt |
| La | 0.108 ± 0.89 | 31.5 ± 2.1 |
| Ce | 19.6 ± 2.1 | 73.3 ± 5.1 |
| Pr | 2.4 ± 0.32 | 9.06 ± 0.72 |
| Nd | 11.2 ± 1.4 | 36.8 ± 2.6 |
| Sm | 2 ± 0.26 | 6.34 ± 0.61 |
| Eu | 0.264 ± 0.0045 | 1.39 ± 0.13 |
| Gd | 1.81 ± 0.3 | 4.64 ± 0.54 |
| Tb | 0.267 ± 0.032 | 0.615 ± 0.057 |
| Dy | 1.99 ± 0.21 | 3.43 ± 0.31 |
| Ho | 0.397 ± 0.043 | 0.642 ± 0.069 |
| Er | 1.21 ± 0.13 | 1.59 ± 0.18 |
| Tm | 0.157 ± 0.032 | 0.192 ± 0.034 |
| Yb | 1.06 ± 0.19 | 0.87 ± 0.14 |
| Rb | 3.1 ± 1.3 | 9.84 ± 0.77 |
| Ba | 12.9 ± 4.4 | 170.6 ± 8.6 |
| Th | 0.638 ± 0.096 | 2.13 ± 0.18 |
| Nb | 0.084 ± 0.034 | 0.017 ± 0.017 |
| Sr | 24.4 ± 8.2 | 333 ± 15 |
| Zr | 19.7 ± 1.2 | 7.64 ± 0.61 |
| Ti | 1045 ± 58 | 351 ± 21 |

| Trace Element concentration (in μg/g) Nakhla | | |
|---|---|---|
| | olivine | |
| V | 16.7 ± 1.7 | 4.06 ± 0.43 |
| Cr | 52.8 ± 7.8 | 14.7 ± 2.6 |
| Mn | 8110 ± 220 | 8940 ± 170 |
| Co | 109.5 ± 3.6 | 128.6 ± 2.6 |
| Ni | 86.2 ± 3.9 | 222.2 ± 5.5 |
| Zn | 186.5 ± 7.1 | 211.4 ± 8.7 |

| | Trace Element concentration (in µg/g) in augite of NWA 998 | | | | | | |
|---|---|---|---|---|---|---|---|
| La | 0.476 ± 0.076 | 0.189 ± 0.054 | 0.279 ± 0.052 | 0.275 ± 0.067 | 0.287 ± 0.055 | 0.79 ± 0.1 | 0.664 ± 0.092 |
| Ce | 1.87 ± 0.17 | 0.857 ± 0.096 | 1.15 ± 0.11 | 1.34 ± 0.14 | 1.223 ± 0.098 | 2.91 ± 0.24 | 2.06 ± 0.17 |
| Pr | 0.379 ± 0.051 | 0.206 ± 0.049 | 0.232 ± 0.04 | 0.284 ± 0.045 | 0.298 ± 0.048 | 0.635 ± 0.073 | 0.504 ± 0.069 |
| Nd | 1.92 ± 0.32 | 1.1 ± 0.21 | 1.29 ± 0.29 | 1.72 ± 0.26 | 1.49 ± 0.29 | 3.79 ± 0.49 | 2.89 ± 0.44 |
| Sm | 0.49 ± 0.11 | 0.362 ± 0.099 | 0.349 ± 0.092 | 0.59 ± 0.11 | 0.43 ± 0.1 | 0.97 ± 0.19 | 0.93 ± 0.17 |
| Eu | 0.198 ± 0.046 | 0.162 ± 0.041 | 0.168 ± 0.042 | 0.17 ± 0.031 | 0.118 ± 0.035 | 0.307 ± 0.053 | 0.283 ± 0.051 |
| Gd | 0.64 ± 0.14 | 0.402 ± 0.088 | 0.56 ± 0.1 | 0.58 ± 0.13 | 0.53 ± 0.13 | 1.19 ± 0.22 | 0.95 ± 0.16 |
| Tb | 0.183 ± 0.033 | 0.186 ± 0.036 | 0.071 ± 0.017 | 0.075 ± 0.018 | 0.075 ± 0.018 | 0.175 ± 0.028 | 0.181 ± 0.026 |
| Dy | 0.529 ± 0.081 | 0.359 ± 0.069 | 0.487 ± 0.085 | 0.66 ± 0.097 | 0.66 ± 0.097 | 1.2 ± 0.16 | 0.94 ± 0.13 |
| Ho | 0.214 ± 0.031 | 0.123 ± 0.027 | 0.097 ± 0.019 | 0.134 ± 0.022 | 0.134 ± 0.022 | 0.254 ± 0.027 | 0.214 ± 0.036 |
| Er | 0.478 ± 0.071 | 0.237 ± 0.052 | 0.266 ± 0.048 | 0.272 ± 0.059 | 0.272 ± 0.059 | 0.567 ± 0.094 | 0.465 ± 0.079 |
| Tm | 0.111 ± 0.025 | 0.114 ± 0.026 | 0.034 ± 0.013 | 0.033 ± 0.012 | 0.033 ± 0.012 | 0.075 ± 0.022 | 0.063 ± 0.018 |
| Yb | 0.388 ± 0.085 | 0.263 ± 0.076 | 0.155 ± 0.054 | 0.242 ± 0.075 | 0.242 ± 0.075 | 0.48 ± 0.11 | 0.43 ± 0.1 |
| Rb | bd | bd | 0.08 ± 0.12 | 0.01 ± 0.13 | 0.15 ± 0.15 | bd | 0.01 ± 0.13 |
| Ba | 0.13 ± 0.1 | 0.095 ± 0.094 | 0.88 ± 0.36 | 0.4 ± 0.17 | 0.35 ± 0.17 | 1.53 ± 0.48 | 0.053 ± 0.078 |
| Th | 0.084 ± 0.025 | 0.069 ± 0.024 | 0.014 ± 0.009 | bd | bd | 0.017 ± 0.01 | bd |
| Nb | 0.033 ± 0.024 | 0.043 ± 0.026 | 0.017 ± 0.015 | bd | 0.003 ± 0.007 | 0.065 ± 0.029 | bd |
| Sr | 23.47 ± 0.76 | 16.75 ± 0.63 | 21.07 ± 0.86 | 24.87 ± 0.83 | 24.09 ± 0.8 | 23.68 ± 0.88 | 33.8 ± 1.5 |
| Zr | 2.37 ± 0.49 | 0.51 ± 0.23 | 1.14 ± 0.38 | 1.94 ± 0.46 | 1.66 ± 0.37 | 4.12 ± 0.86 | 2.88 ± 0.58 |
| Ti | 1348 ± 31 | 953 ± 23 | 1125 ± 33 | 1369 ± 33 | 1371 ± 36 | 1728 ± 52 | 1847 ± 69 |
| Sc | 63.1 ± 1.4 | 60.5 ± 1.6 | 61.1 ± 2.1 | 65.6 ± 1.7 | 66.6 ± 1.9 | 74.9 ± 2.8 | 173.9 ± 2.9 |
| V | 218.9 ± 5.2 | 201.9 ± 5 | 223.6 ± 6.5 | 228.1 ± 3 | 227.9 ± 18.2 | 249 ± 7.3 | 250.3 ± 9.9 |
| Cr | 2533 ± 61 | 2801 ± 72 | 2668 ± 76 | 2599 ± 55 | 2372 ± 82 | 1640 ± 57 | 3180 ± 130 |
| Mn | 3720 ± 100 | 3493 ± 87 | 3690 ± 120 | 3727 ± 72 | 3850 ± 140 | 4069 ± 96 | 3630 ± 150 |
| Co | 36.8 ± 1.4 | 37.1 ± 1.3 | 39 ± 1.7 | 40 ± 1.4 | 39.4 ± 2 | 37 ± 1.6 | 37.6 ± 1.8 |
| Ni | 65.1 ± 2.9 | 81.3 ± 4 | 84.4 ± 3.6 | 85.1 ± 3.6 | 85.6 ± 5.1 | 64.4 ± 3.5 | 78.3 ± 4 |
| Y | 3.25 ± 0.19 | 1.68 ± 0.14 | 2.42 ± 0.16 | 3.21 ± 0.2 | 2.73 ± 0.19 | 5.38 ± 0.38 | 4.66 ± 0.26 |

bd: below detection

| | Trace Element concentration (in µg/g) in orthopyroxene of NWA 998 | | | | | | |
|---|---|---|---|---|---|---|---|
| La | 0.164 ± 0.042 | 0.052 ± 0.021 | 0.033 ± 0.019 | 0.048 ± 0.021 | 0.067 ± 0.026 | 0.204 ± 0.055 | 0.47 ± 0.12 |
| Ce | 1.05 ± 0.14 | 0.2 ± 0.048 | 0.344 ± 0.059 | 0.2 ± 0.044 | 0.255 ± 0.045 | 0.653 ± 0.085 | 0.24 ± 0.202 |
| Pr | 0.21 ± 0.042 | 0.049 ± 0.017 | 0.028 ± 0.017 | 0.036 ± 0.016 | 0.059 ± 0.021 | 0.09 ± 0.027 | 0.202 ± 0.05 |
| Nd | 1.52 ± 0.26 | 0.42 ± 0.13 | 0.48 ± 0.18 | 0.207 ± 0.095 | 0.32 ± 0.13 | 0.68 ± 0.18 | 1.22 ± 0.28 |
| Sm | 0.55 ± 0.13 | 0.09 ± 0.049 | 0.138 ± 0.057 | 0.104 ± 0.057 | 0.201 ± 0.075 | 0.23 ± 0.069 | 0.329 ± 0.089 |
| Eu | 0.154 ± 0.041 | 0.024 ± 0.014 | 0.042 ± 0.019 | 0.028 ± 0.015 | 0.01 ± 0.001 | 0.035 ± 0.016 | 0.052 ± 0.023 |
| Gd | 0.76 ± 0.14 | 0.221 ± 0.069 | 0.212 ± 0.077 | 0.221 ± 0.081 | 0.228 ± 0.073 | 0.265 ± 0.091 | 0.65 ± 0.16 |
| Tb | 0.13 ± 0.023 | 0.032 ± 0.01 | 0.062 ± 0.015 | 0.054 ± 0.016 | 0.053 ± 0.013 | 0.068 ± 0.019 | 0.084 ± 0.021 |
| Dy | 1.15 ± 0.15 | 0.285 ± 0.066 | 0.452 ± 0.084 | 0.385 ± 0.082 | 0.471 ± 0.096 | 0.481 ± 0.095 | 0.625 ± 0.097 |
| Ho | 0.297 ± 0.029 | 0.11 ± 0.022 | 0.124 ± 0.023 | 0.092 ± 0.019 | 0.1 ± 0.015 | 0.133 ± 0.022 | 0.154 ± 0.026 |
| Er | 0.77 ± 0.1 | 0.312 ± 0.064 | 0.492 ± 0.085 | 0.343 ± 0.066 | 0.419 ± 0.074 | 0.447 ± 0.074 | 0.534 ± 0.079 |
| Tm | 0.106 ± 0.022 | 0.054 ± 0.018 | 0.076 ± 0.018 | 0.071 ± 0.0168 | 0.07 ± 0.016 | 0.076 ± 0.016 | 0.087 ± 0.016 |
| Yb | 0.84 ± 0.013 | 0.53 ± 0.1 | 0.62 ± 0.13 | 0.52 ± 0.012 | 0.56 ± 0.012 | 0.63 ± 0.12 | 0.57 ± 0.12 |
| Rb | 0.32 ± 0.14 | 0.27 ± 0.15 | 0.37 ± 0.16 | 0.04 ± 0.12 | 0.08 ± 0.15 | 0.71 ± 0.18 | 0.97 ± 0.22 |
| Ba | 1.79 ± 0.54 | 6.04 ± 0.67 | 2.89 ± 0.72 | 3.5 ± 1.5 | 1.66 ± 0.47 | 12.6 ± 1.9 | 39.4 ± 6.2 |
| Th | 0.003 ± 0.003 | 0.123 ± 0.028 | 0.074 ± 0.021 | 0.043 ± 0.017 | 0.095 ± 0.021 | 0.271 ± 0.049 | 0.391 ± 0.049 |
| Nb | 0.087 ± 0.029 | 0.093 ± 0.039 | 0.138 ± 0.047 | bd | 0.06 ± 0.028 | 0.059 ± 0.028 | 0.508 ± 0.093 |
| Sr | 2.29 ± 0.23 | 3.41 ± 0.31 | 0.82 ± 0.14 | 0.89 ± 0.24 | 0.45 ± 0.12 | 6.46 ± 0.72 | 18.1 ± 2.7 |
| Zr | 5.93 ± 0.7 | 6.88 ± 0.97 | 5.15 ± 0.68 | 3.34 ± 0.5 | 11.4 ± 1.3 | 18.6 ± 1.7 | 18.6 ± 1.8 |
| Ti | 1229 ± 41 | 492 ± 14 | 493 ± 20 | 436 ± 20 | 434 ± 13 | 569 ± 24 | 607 ± 24 |

bd: below detection

| | Trace Element concentration (in µg/g) in plagioclase of NWA 998 | | | |
|---|---|---|---|---|
| La | 0.96 ± 0.18 | 1 ± 0.15 | 3.14 ± 0.27 | 9.3 ± 1.5 |
| Ce | 1.62 ± 0.25 | 1.8 ± 0.24 | 0.437 ± 0.29 | 18.8 ± 2.8 |
| Pr | 0.096 ± 0.046 | 0.192 ± 0.06 | 0.326 ± 0.072 | 2.22 ± 0.46 |
| Nd | 0.26 ± 0.16 | 0.49 ± 0.22 | 1.12 ± 0.35 | 8.6 ± 1.8 |
| Sm | bd | 0.044 ± 0.052 | 0.128 ± 0.086 | 1.35 ± 0.4 |
| Eu | 1.15 ± 0.21 | 1.11 ± 0.13 | 1.52 ± 0.15 | 0.99 ± 0.14 |
| Gd | 0.003 ± 0.001 | 0.019 ± 0.032 | bd | 0.53 ± 0.2 |
| Tb | bd | bd | bd | 0.08 ± 0.024 |
| Dy | bd | bd | bd | 0.43 ± 0.16 |
| Ho | bd | bd | bd | 0.072 ± 0.026 |
| Er | bd | bd | bd | 0.199 ± 0.078 |
| Tm | bd | bd | bd | 0.028 ± 0.014 |
| Yb | bd | bd | bd | 0.1 ± 0.07 |
| Rb | 2.28 ± 0.48 | 2.36 ± 0.42 | 7.44 ± 0.61 | 66.2 ± 3.6 |
| Ba | 212 ± 23 | 243 ± 19 | 535 ± 20 | 421 ± 21 |
| Th | bd | bd | bd | 1.19 ± 0.12 |
| Nb | bd | bd | bd | 0.81 ± 0.21 |
| Sr | 1119 ± 86 | 1138 ± 67 | 793 ± 32 | 214.8 ± 8.6 |
| Zr | 0.23 ± 0.23 | bd | bd | 16.5 ± 3.1 |
| Ti | 289 ± 29 | 257 ± 15 | 200.5 ± 9.7 | 238 ± 14 |

bd: below detection

| Trace Element concentration (in µg/g) in melt of NWA 998 | | | | |
|---|---|---|---|---|
| La | 0.71 ± 0.12 | 4.21 ± 0.55 | 3.68 ± 0.35 | 3.31 ± 0.42 |
| Ce | 0.9 ± 0.14 | 10.6 ± 1.1 | 10.48 ± 0.66 | 10.3 ± 0.86 |
| Pr | 0.083 ± 0.034 | 1.3 ± 0.2 | 1.5 ± 0.14 | 1.69 ± 0.17 |
| Nd | 0.34 ± 0.34 | 5.46 ± 0.69 | 6.72 ± 0.57 | 7.45 ± 0.79 |
| Sm | 0.004 ± 0.009 | 1.05 ± 0.29 | 1.6 ± 0.27 | 1.88 ± 0.35 |
| Eu | 0.23 ± 0.056 | 0.348 ± 0.08 | 0.474 ± 0.058 | 0.55 ± 0.076 |
| Gd | 0.051 ± 0.04 | 1.01 ± 0.21 | 1.16 ± 0.15 | 1.45 ± 0.26 |
| Tb | 0.003 ± 0.003 | 0.176 ± 0.047 | 0.231 ± 0.038 | 0.257 ± 0.051 |
| Dy | 0.068 ± 0.043 | 1.14 ± 0.25 | 1.5 ± 0.2 | 1.77 ± 0.26 |
| Ho | 0.009 ± 0.007 | 0.167 ± 0.035 | 0.271 ± 0.044 | 0.393 ± 0.061 |
| Er | 0.022 ± 0.022 | 0.44 ± 0.13 | 0.76 ± 0.12 | 0.99 ± 0.14 |
| Tm | bd | 0.053 ± 0.022 | 0.088 ± 0.0121 | 0.116 ± 0.032 |
| Yb | bd | 0.59 ± 0.2 | 0.77 ± 0.15 | 0.93 ± 0.22 |
| Rb | 246 ± 14 | 203 ± 20 | 134 ± 14 | 104 ± 11 |
| Ba | 1100 ± 49 | 340 ± 28 | 245 ± 27 | 181 ± 22 |
| Th | 2.3 ± 0.22 | 12.5 ± 1.3 | 8.9 ± 1.2 | 6.5 ± 1.4 |
| Nb | 19.5 ± 3.5 | 56.9 ± 6.1 | 38 ± 5.6 | 24.9 ± 4.5 |
| Sr | 177.6 ± 6.8 | 1336 ± 12 | 100.5 ± 9.5 | 79.9 ± 8.6 |
| Zr | 136 ± 54 | 365 ± 40 | 278 ± 36 | 215 ± 41 |
| Ti | 2030 ± 330 | 2930 ± 300 | 2560 ± 160 | 2380 ± 180 |

bd: below detection

| Trace Element concentration (in µg/g) in olivine of NWA 998 | | | | |
|---|---|---|---|---|
| V | 4.59 ± 0.37 | 2.86 ± 0.26 | 5.68 ± 0.42 | 2.91 ± 0.25 |
| Cr | 13.9 ± 2.3 | 1.8 ± 1.3 | 18.2 ± 2.7 | 11.9 ± 1.9 |
| Mn | 8360 ± 280 | 7980 ± 360 | 8500 ± 370 | 8410 ± 330 |
| Co | 121.5 ± 4.5 | 126 ± 5.7 | 116.3 ± 4.5 | 125.4 ± 4.7 |
| Ni | 177.8 ± 7.8 | 190.4 ± 9.8 | 178.6 ± 7.9 | 185.3 ± 7.4 |
| Zn | 239.4 ± 9.2 | 208.8 ± 9.1 | 228.3 ± 8.3 | 226.7 ± 7.4 |